



# THE UNIVERSITY *of* EDINBURGH

This thesis has been submitted in fulfilment of the requirements for a postgraduate degree (e. g. PhD, MPhil, DClinPsychol) at the University of Edinburgh. Please note the following terms and conditions of use:

- This work is protected by copyright and other intellectual property rights, which are retained by the thesis author, unless otherwise stated.
- A copy can be downloaded for personal non-commercial research or study, without prior permission or charge.
- This thesis cannot be reproduced or quoted extensively from without first obtaining permission in writing from the author.
- The content must not be changed in any way or sold commercially in any format or medium without the formal permission of the author.
- When referring to this work, full bibliographic details including the author, title, awarding institution and date of the thesis must be given.

# Heterogeneous growth and death of small bacterial populations in microfluidic droplets

Nia Verdon



Doctor of Philosophy  
The University of Edinburgh  
October 2022

# Abstract

Antibiotic resistance is a major global health challenge, and there is still much to learn about how antibiotics work to inhibit the growth of bacterial populations. In many real infections, bacteria grow in small populations where stochastic effects can be important, especially because even a single surviving bacterium can lead to regrowth of an infection. Microfluidic droplets offer an opportunity to study this heterogeneity under well-controlled experimental conditions. Creating numerous, monodisperse microenvironments from the same initial bacterial suspension gives multiple micro-experiments which run in parallel, allowing the study of individual bacterial growth and response to stress (for example, antibiotics). This approach results in a rich data set which can be compared with predictions from both deterministic and probabilistic theoretical models, producing insight into the growth dynamics and antibiotic response of small populations, which are often hidden in conventional large-scale experiments.

In this thesis I present a study of small populations of bacteria using microfluidic droplets and theoretical modelling. Chapter 1 provides motivation for the study of small bacterial populations and background on  $\beta$ -lactam antibiotics (the class of antibiotics investigated in Chapters 5–6) and  $\beta$ -lactamase enzymes.

Chapter 2 outlines the experimental methodology and the image analysis procedure. Principally, this involves encapsulating bacteria into picolitre volumes of growth media and imaging using fluorescence and brightfield microscopy for 4–7 hours. A Matlab workflow is used to count the number of bacteria in each droplet over the course of an experiment. Chapter 3 explores the heterogeneous growth dynamics by comparing hundreds to thousands of growth trajectories of clonal populations of *E. coli*.

Deterministic and probabilistic models were developed to understand the response of small populations of  $\beta$ -lactam resistant bacteria to  $\beta$ -lactam antibiotics, as

described in Chapter 4. The effect of stochastic bacterial loading into droplets as well as stochastic growth are compared to the deterministic case in Chapter 5, in which the survival of bacterial populations under a range of antibiotic concentrations, with different initial numbers of bacteria, is explored. These simulations predict a range of concentrations of antibiotic where stochastic effects lead to the survival of a proportion of the population, while a deterministic mean-field theory would predict success of the antibiotic treatment.

In Chapter 6 these predictions are tested experimentally and it is found that, in droplets, some populations of *E. coli* survive at concentrations of ampicillin beyond the bulk MIC determined by equivalent plate reader experiments. Dormant cells are visible in droplets but not in plate reader experiments, and we propose that some of the growth observed in bulk plate reader experiments might be biomass (filamentous) growth rather than (healthy) division. This implies that bulk experiments may not reveal the whole picture and need to be interpreted with care.

Finally, in Chapter 7 a model is used to investigate the possibility of cooperative behaviour in mixtures of resistant and sensitive bacteria in droplets. This explores the extent to which bacteria with no intrinsic resistance could survive exposure to antibiotics when in the presence of bacteria which produce  $\beta$ -lactamase enzymes, a phenomenon which is of rising ecological interest and clinical concern.

# Declaration

I declare that this thesis was composed by myself, that the work contained herein is my own except where explicitly stated otherwise in the text, and that this work has not been submitted for any other degree or professional qualification except as specified.

*(Nia Verdon, October 2022)*

# Acknowledgements

I have many people to thank.

Firstly, my supervisors, Rosalind and Simon, for their knowledge, patience and encouragement. Secondly, my family, old friends and friends made during the PhD—who believed I would finish even when I did not. In particular, my parents; my sister, Dr W; Dan, who has been there from the start; and Uncle Oliver, for timely financial support. Finally, I would like to give a special mention to Gary the tortoise, whose company has been invaluable throughout the writing of this thesis.

# Lay Summary

In this thesis, I present a study of the growth and death of small populations of bacteria. Generally, when we perform experiments in the biophysics or microbiology lab, we measure billions of bacterial cells growing exponentially. However, this means we average the behavior of all the individual bacteria, and, moreover, the measurement is dominated by fast growing or the fittest bacteria. In contrast, measurements on individual bacterial cells have revealed great diversity, including variation (heterogeneity) in growth rates and response to stresses.

Differences between individual bacteria in a population are especially relevant in the context of antibiotics. Antibiotics are a central part of modern medicine, and are highly effective in killing or inhibiting bacteria. However, some infections are resistant to treatment. Variation in stress responses within genetically identical bacterial populations implies that some bacteria may be able to survive antibiotic exposure, even if the population on average is susceptible. This has clinical consequences of reinfection, as well as increasing the risk of evolving resistant mutations.

Up to now, studies of variation among individual bacteria have mainly focused on tracking single cells. There have been few studies of how bacterial variability plays out in the context of small, growing populations despite this describing many infections. In this thesis, we explore the heterogeneity of small populations by exploiting microfluidic droplet technology and computational modelling.

Droplets containing 1–10 initial bacteria can be used as an intermediate scale between single-cell and traditional large-scale measurements. Droplet methodology has the potential to generate large datasets for statistical analysis of thousands of identically prepared small populations. Encapsulating small numbers of cells into picolitre droplets, we are able to study both how small populations of bacteria grow and how they respond to the presence of antibiotic.

In this thesis, we specifically study the situation where bacteria produce antibiotic-degrading enzymes. Beta-lactamase enzymes are commonly produced as a resistance mechanism to beta-lactam antibiotics (which include penicillins). Previous work has shown that these enzymes can reduce the antibiotic concentration not just for the enzyme producer, but also for other bacteria. Here we

investigate the effects of this on a small population level.

The work reported in this thesis develops and uses microfluidic droplet technology to study small-population growth and death of bacteria. Some of the key results are: (i) that growth of bacteria in the absence of antibiotic can be understood with simple stochastic mathematical models; (ii) antibiotic-resistant, beta-lactamase-enzyme-producing bacteria can survive at higher concentrations of antibiotic in droplets than in large populations of the same average density; (iii) response to antibiotics is complicated, involving bacterial filamentation, which may alter the chances of survival at a local level.



# Contents

Abstract	i
Declaration	iii
Acknowledgements	iv
Lay Summary	v
Contents	vii
<b>1 Background</b>	<b>1</b>
1.1 Overview.....	1
1.2 Studying bacteria in small populations.....	1
1.2.1 Intrinsic heterogeneity within clonal populations of bacteria	2
1.2.2 Traditional study of bulk bacterial populations.....	4
1.2.3 Methods of studying small populations .....	6
1.3 Antibiotic Response and Resistance.....	7
1.3.1 $\beta$ -lactam antibiotics .....	7
1.3.2 Antibiotic resistance.....	11
1.3.3 $\beta$ -lactamase enzymes .....	11
1.3.4 The minimum inhibitory concentration (MIC) .....	12

1.3.5	Inoculum effect .....	13
1.3.6	Single-cell MIC .....	14
1.3.7	$\beta$ -lactamase production as a social interaction .....	14
1.4	Microbiology in droplets .....	15
1.4.1	Forming microfluidic droplets .....	17
1.4.2	Encapsulation of bacteria into droplets .....	20
<b>2</b>	<b>Methods and method development</b>	<b>23</b>
2.1	Overview.....	23
2.2	Experimental method.....	25
2.2.1	Overview of the microfluidic droplet method.....	25
2.2.2	Integrated microfluidic device .....	28
2.2.3	Device chamber.....	32
2.2.4	Surfactant.....	33
2.2.5	Surface treatment .....	35
2.2.6	Introduction of antibiotic.....	35
2.3	Image analysis.....	38
2.3.1	Stitching the fields of view together .....	38
2.3.2	Droplet detection.....	40
2.3.3	Bacteria detection.....	42
2.3.4	Tracking droplets and counting bacteria.....	45
2.4	Image analysis of bacterial cell size.....	46
2.4.1	Filamentation .....	46
2.4.2	Aggregation.....	48

2.5	Validation of the methodology .....	52
2.5.1	Checking for errors in the bacterial count.....	52
2.5.2	Comparing bacterial counting to integrated droplet fluorescence .....	53
2.5.3	Analysis of droplet loading statistics .....	55
2.6	Concentration of bacteria within the droplets .....	62
2.7	Summary .....	64
<b>3</b>	<b>Heterogeneous growth of uninhibited bacteria</b>	<b>66</b>
3.1	Introduction .....	66
3.2	Method.....	68
3.3	Results and analysis .....	68
3.3.1	Data.....	68
3.3.2	Growth rates .....	71
3.3.3	Comparing initial and final bacteria counts.....	76
3.3.4	Stochastic dynamics of bacterial growth.....	78
3.3.5	Non-growing bacteria.....	87
3.4	Discussion .....	88
<b>4</b>	<b>Simulating <math>\beta</math>-lactamase-producing bacterial populations: method</b>	<b>92</b>
4.1	Simulation overview.....	94
4.2	Deterministic droplet filling and bacterial dynamics .....	98
4.2.1	Deterministic distribution of initial bacterial numbers .....	98
4.2.2	Deterministic growth and death dynamics .....	98

4.3	Stochastic droplet filling and bacterial dynamics .....	101
4.3.1	Stochastic distribution of initial bacterial numbers .....	101
4.3.2	Stochastic proliferation and death .....	102
4.4	Modelling $\beta$ -lactamase enzyme action .....	107
4.4.1	Assumption of a well mixed system.....	107
4.4.2	Rate of antibiotic degradation .....	108
4.5	Model specifications, assumptions and parameters .....	110
4.5.1	Technical structure .....	110
4.5.2	Verifying the simulation output.....	111
4.5.3	Parameter values .....	112
4.6	Discussion .....	114
<b>5</b>	<b>Simulating <math>\beta</math>-lactamase-producing bacteria: results</b>	<b>115</b>
5.1	Introduction .....	115
5.2	Predictions of the different model variants for a single parameter set .....	116
5.2.1	Deterministic model .....	117
5.2.2	Stochastic droplet loading.....	117
5.2.3	Stochastic proliferation and death dynamics .....	118
5.2.4	Fully stochastic model .....	119
5.3	Simulating the effect of varying antibiotic concentration, bacterial density, growth and death rates .....	123
5.3.1	Inoculum effect: dependence of the MIC on bacterial density for droplet populations .....	123
5.3.2	Survival probability as a function of antibiotic concentration .....	124

5.3.3	Effect of bacterial loading density of bacteria on survival curves .....	127
5.3.4	Effect of growth and death rate on survival curves.....	129
5.3.5	Dynamical trajectories of droplet population growth and death .....	130
5.4	Discussion .....	134
5.4.1	Future amendments or extension of the simulation .....	135
<b>6</b>	<b>Exposure of <math>\beta</math>-lactamase-producing bacteria to antibiotics: experiments</b>	<b>136</b>
6.1	Introduction .....	136
6.2	Plate reader experiments .....	137
6.2.1	Plate reader procedure.....	137
6.2.2	Plate reader results .....	138
6.3	Droplet experiments .....	142
6.3.1	Droplet experiment procedure .....	142
6.3.2	Droplet experiments: qualitative observations .....	143
6.3.3	Killing dynamics of the droplet populations .....	145
6.3.4	Quantifying kill times .....	151
6.3.5	Analysis of filamentous growth .....	153
6.4	Discussion .....	167
6.4.1	Comparing plate reader and droplet data .....	169
6.4.2	Comparing experimental data to the simulation predictions.	171
<b>7</b>	<b>Simulating mixed populations of <math>\beta</math>-lactamase producers and non-producers</b>	<b>172</b>
7.1	Introduction .....	172

7.2	Method.....	173
7.3	Results .....	176
7.3.1	Simulations with equal starting numbers of resistant and sensitive bacteria .....	176
7.3.2	Varying the initial number of resistant bacteria .....	177
7.3.3	Varying the initial number of sensitive bacteria .....	180
7.3.4	Including stochastic droplet filling .....	181
7.4	Discussion .....	185
<b>8</b>	<b>Conclusions</b>	<b>187</b>
8.1	Perspectives on the work presented in the thesis.....	187
8.2	Suggestions for future work .....	189
<b>A</b>	<b>Extra figures</b>	<b>193</b>
A.1	Uninhibited droplet experiment with no growth .....	193
A.2	Bellman–Harris analysis .....	194
A.3	Ampicillin droplet experiments.....	196
A.4	Bacterial density range .....	198
A.5	Plate reader plots.....	199
A.6	Droplet images .....	206
<b>B</b>	<b>Droplet experimental protocol</b>	<b>208</b>
	<b>Bibliography</b>	<b>215</b>

# Chapter 1

## Background

### 1.1 Overview

This chapter provides context and motivation for the study of small bacterial populations. Background information is given on beta-lactam antibiotics, which is the class of antibiotics investigated in this thesis, and the global antibiotic resistance problem. Droplet-based microfluidics, the experimental methodology used in this thesis, is explained, as well as the advantages of the technique for studying heterogeneity in small populations of bacteria.

### 1.2 Studying bacteria in small populations

The experiments presented in this thesis utilise droplet microfluidics to track the dynamics of small bacterial populations (1–100 cells). This enables us to investigate stochastic aspects of the population growth and death dynamics that would not be accessible in traditional microbiological experiments. Droplets are especially relevant for mirroring the confined environment which occurs when infectious bacteria grow inside human cells (e.g. tuberculosis bacteria inside macrophages [1]).

Many infections start from small numbers of bacteria. Therefore to learn about the early dynamics of infections we need to study the dynamics of small populations. For example, small populations can die out following a few random

death events, while larger populations are very unlikely to randomly go extinct. In the food industry it is highly important to understand how small bacterial populations grow inside food, since even a few contaminating bacteria can cause infection. Small bacterial populations are also relevant in the pores between soil granules and on plant roots and leaves.

### **1.2.1 Intrinsic heterogeneity within clonal populations of bacteria**

In Chapter 3 we explore the uninhibited growth of *E. coli* populations, grown from a single colony. We expect to see a range of behaviours between the small droplet populations because many phenotypic traits vary among clonal cells. Examples include growth rate, cell length, persistence (subpopulations of cells which do not grow) and competence for DNA transformation [2, 3]. In small populations, the effects of this variation will be much more apparent compared to in a large population.

There is growing evidence that this noisy behavior can offer fitness benefits, and is sometimes adaptive [4]. Phenotypic heterogeneity, i.e. noisy gene expression, provides a dynamic source of diversity, in addition to the diversity derived from genotypic changes such as genome rearrangements and mutation. A distribution of states amongst clonal cells or organisms (the ‘survival machines’[5]) can mean some proportion of the population is able to survive a stress (and thus the genome survives and goes on to be reproduced), when a homogeneous population might go extinct (along with the genome). Furthermore, there is growing evidence of evolutionary selection for diversity-generating mechanisms in microorganisms [3, 6]. For example, quorum sensing, originally thought only to direct an entire bacterial population to act in unison, has been shown to also control heterogeneity in gene expression [7, 8].

### **Heterogeneous response to antibiotics**

Antibiotic response is an important theme of this thesis, where survival of a few bacteria can drastically affect the outcome of a population. In Chapter 6 we investigate the response of *E. coli* to ampicillin exposure in small droplet populations.



The survival of low levels of bacteria is important when evaluating, for example, the risk of food contamination and infectious diseases because inoculum sizes of just a few cells can cause infections [9–14]. This is also relevant to reinfections because even a small number of cells surviving antibiotic treatment can regenerate a population. Furthermore, spatially separated infections can act as distinct small populations and respond to local concentrations of antibiotics, particularly notable because a nonuniform drug distribution can accelerate the emergence of resistance [15].

The antibiotic response of small populations can be very different to that of large populations. For example, population level processes such as the inoculum effect (see Section 1.3.5) can result in survival in cases where an isolated bacterial cell would not survive [16]. However there are other environments where phenotypic variation between individual cells offers an advantage over a homogeneous population [17]. In an unpredictable, rapidly changing environment, diversity within genetically identical populations sometimes allows a community to survive a stress that kills the majority of the population (i.e. the cells which are resistant to the temporary stress survive and can repopulate the environment once the stress is gone).

Persistence is one example of phenotypic heterogeneity which can be a mechanism of resistance; where otherwise sensitive bacteria survive antibiotic exposure by simply not dividing. This occurs when a genetically homogeneous microbial population splits into two distinct sub-populations with different growth and survival properties (or strategies) as a result of reversible phenotype switching [18]. Growth bistability, such as this, can be caused by the stochastic production or expression of a protein with detrimental effect on growth, resulting in different growth rates of subpopulations expressing or not expressing the toxic protein [19].

Several studies have investigated the response of small populations of bacteria to antibiotics. Heterogeneous resistance and its evolution in bacteria has been studied in droplets [20], and the effects of different antagonistic drug pairs on single cells has been observed in mother machines [21] (both methods are discussed below). Coates et al. found that low concentrations of antibiotic might be sufficient to eradicate a small bacterial population, especially at the scale when division and extinction are probabilistic. A population will undergo extinction if cells die more frequently than they divide; bactericidal antibiotics induced stochastic fluctuations in the bacterial population size, increasing the probability of extinction [22]. Alexander et al. determined that low concentrations of

antibiotic may also be sufficient to significantly reduce the likelihood of *de novo* emergence of resistance. This is because a cell with a resistant gene must first evolve, but then must also successfully replicate and grow [23]. A study of high and low noise gene expression (for genotypes of *S. cerevisiae*), found each was advantageous under different environmental conditions. Specifically, with increasing concentrations of antibiotic, the strain with more noisy gene expression performed better [4].

These studies have demonstrated the stochastic nature of eradicating bacteria with antibiotics, as well as the importance of studying small population responses in addition to large population responses, because the findings of one cannot always be simply extrapolated to the other. Controlling the heterogeneity which allows partial survival is important for reducing the risk of resistance, food preservation, clinical antimicrobial treatments and understanding natural microbial populations [6].

## **Heterogeneity in evolution**

Although it is not the topic of this thesis, evolution also happens differently in small populations compared to large populations. In particular, ‘genetic drift’, in which mutants take over a population randomly, even when they are not fit, is much more important in small populations. In addition, mutation rates themselves may be subject to stochastic variation among cells in the population. Heterogeneity has been shown to be a factor in spontaneous mutation frequencies not induced by antibiotic treatment [24]. Bacterial competence for transformation (the ability of cells to bind to and to take up exogenous DNA) is another mechanism controlled by heterogeneous molecular fluctuations rather than genetic differences in a population; phenotypic diversity means that only a fraction of the population are competent at a given time [3].

### **1.2.2 Traditional study of bulk bacterial populations**

Bacterial behaviour converges to a homogeneous response as the population size increases, and this response is what is frequently measured. Heterogeneous behaviour is often lost when studying large populations of bacteria because we measure the largest or average response. Bacterial populations which start with over 100 cells appear to behave deterministically, even when the underlying law

is stochastic [2]. However, small microbial populations do not fit deterministic models where heterogeneity is not considered [25].

Standard microbiology methods involve measuring populations of  $10^5 - 10^9$  bacteria and monitoring the growth of cells suspended in well-mixed liquid media or growing as colonies on plates of growth medium solidified with agar.

In large bacterial populations, fluctuations in the population size are negligible, and the growth of the population can be well described using deterministic equations. However, if the population grows exponentially, the fastest-growing subpopulation will dominate these conventional measurements, and phenotypic variations within the initial inoculum will be hidden from view, as data is averaged across thousands or millions of cells in a sample. In addition, dormant subpopulations of cells will not be visible in a traditional growth assay (although they may be detected as persister cells in a killing assay). Measurements which give a good indication of the population as a whole, can miss bacteria which are no longer growing; a particular issue when studying the effect of antibiotics [26]. Antimicrobial susceptibility testing is usually performed either in liquid culture or on plates, i.e. in large bacterial populations. Testing for antimicrobial susceptibility with a population size of  $5 \times 10^5 - 10^9$  CFU mL<sup>-1</sup> does not detect the stochastic response which occurs in small populations.

Optical density (OD) measurements of microbial growth are one of the most common techniques used in microbiology because they are fast and non-destructive. Light is directed through the sample and a detector is used to make a turbidity measurement. However, the OD value is often not proportional to the cell number. The Beer-Lambert law can only be applied for microbial cultures of low densities where there is limited scattering or other interactions. The proportionality constants strongly depend on a number of factors; for example, cell size, shape or refractive index of the growth media [27]. Therefore the interpretation of optical density must be done with care, and with the knowledge that filamentous cells and dormant sub-populations can be missed or misinterpreted.

Homogeneous liquid solutions of bacteria are not representative of most natural environments, and therefore results are not always applicable *in vivo*. Furthermore, results are not always comparable to other laboratory growth methods. The method of growth can affect bacterial behaviour, and this should be considered when concluding the outcome of an experiment. For example, the growth of

crowded bacteria on plates can generate different evolutionary and extinction outcomes than in well-mixed liquid cultures [28].

### **1.2.3 Methods of studying small populations**

Methods which enable the study of small populations of cells are becoming increasingly relevant as the prevalence and impact of individual cell heterogeneity is becoming more recognised [29]. Small bacterial population experiments allow us to distinguish between deterministic and stochastic regulation of bacterial gene expression. This includes confirming the roles of cell ageing, the cell cycle, metabolic rhythms and epigenetic modifications (heritable phenotype changes that do not involve alterations in the DNA sequence) in causing phenotypic heterogeneity [6]. In this thesis, we use microfluidic droplets as a way to study small populations. Other studies have used different methods.

Traditional methods of growth can be adapted to study small populations. Agarose pads can be used with a very diluted cell suspension, and then viewed under the microscope. This has been a very useful technique, but is typically limited to a small number of fields of view, containing few cells. Additionally, after a short time the fields of view fill with cells, such that they can no longer be analysed [30]. Similarly, single cells have been studied using standard well-plate methods, with serial dilutions to ensure only one cell remains. However this can be very labour intensive and the number of populations which can be studied separately is limited [22].

Flow cytometry can be used to detect single cells, coupled with downstream processing, often via fluorescence activated cell sorting (FACS). Cell populations can be sorted based on their fluorescent or light scattering characteristics [31, 32]. Many FACS instruments can then sort single cells into a container—such as a 96-well plate—allowing cells to be isolated and grown. This method requires correctly calibrated, expensive equipment and is a one-time measurement, however, therefore experimental procedures allowing the study of numerous single cells (or small populations) over long periods of time, in parallel, are interesting and promise new insight into the the stochastic nature of biological mechanisms.

Microfluidic techniques allow the study of small volumes and are highly efficient research tools. By creating structures with micrometre dimensions, individual cells can be manipulated and analysed in rapid and low-volume studies and

diagnostics. Mother machines are a popular microfluidic device used for this purpose. Cells are grown single-file within narrow growth-channels that are perpendicularly connected to a main flow-channel that supplies nutrients and washes away cells extruding from the growth channels. The mother cell at the bottom of the growth channel can, in principal, be studied for an unlimited period of time, which means that a mother cell of *E. coli* can divide for hundreds of generations [33].

Mechanical constraints have been shown to effect growth in devices such as the mother machine because bacteria adapt to the constrictions [33, 34]. It has been found that cell dimensions generally decrease as the channel length increases and width decreases. In particular, *E. coli* adapt to the restrictive channel environment by becoming narrower and longer in comparison to the same strain grown in liquid culture. Cell width at birth and average mother cell volume has been shown to increase with channel width, and this also impacts the doubling time, which increases as a function of length [35].

This response to spatial structure must be taken into account when comparing results from mother machine experiments to those from unconfined bulk growth. Droplet-based microfluidics, which address many of the limitations described above, are discussed in Section 1.4.1.

## 1.3 Antibiotic Response and Resistance

Antibiotics are drugs that are used to treat bacterial infections in humans and other animals. Antibiotics either kill microorganisms (bactericidal antibiotics) or stop them from reproducing (bacteriostatic antibiotics), allowing the immune system to remove them. Antibiotics can be grouped into classes based on their chemical structure and their mechanism of action [36]. My thesis focuses on the beta-lactam or  $\beta$ -lactam class of antibiotics, which act by inhibiting bacterial cell wall synthesis.

### 1.3.1 $\beta$ -lactam antibiotics

$\beta$ -lactam antibiotics are the oldest class of antibiotics (the first antibiotic to be discovered, penicillin, is a  $\beta$ -lactam [37, 38]) and they remain amongst the most

### Trend of the consumption in the hospital sector of ATC group J01 expressed in DDD per 1000 inhabitants and per day

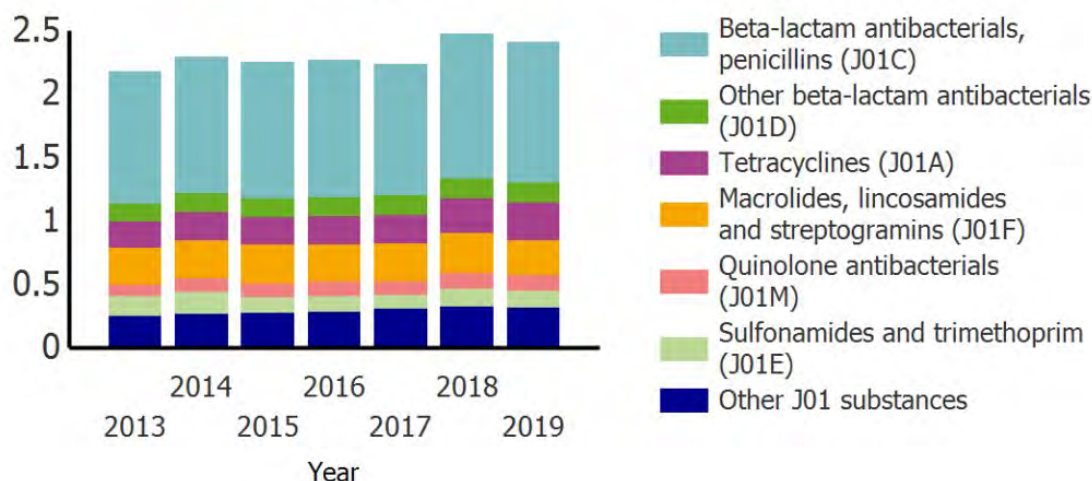


**Figure 1.1** *Hospital sector defined daily doses (DDD) of antibacterials for the UK, showing that  $\beta$ -lactam antibacterials are consistently the most used from 2013–2019 (52% in 2019). ATC group J01 is a therapeutic subgroup of antibacterials for systemic use in the Anatomical Therapeutic Chemical Classification System, developed by the World Health Organization (WHO). Figure generated from ESAC-Net data submitted to The European Surveillance System (TESSy) [40].*

widely used group of antimicrobial agents for the treatment of bacterial disease in humans [39, 40]. In 2013,  $\beta$ -lactams accounted for 65% of the worldwide antibiotics market [41], and they account for half of all antibacterials used systemically in the UK hospital sector (see Figure 1.1).

$\beta$ -lactam antibiotics contain a  $\beta$ -lactam ring in their molecular structure (see Figure 1.2). The first  $\beta$ -lactam antibiotics to be discovered were active only against Gram-positive bacteria, but the development of broad-spectrum  $\beta$ -lactam antibiotics, which are active against various Gram-negative organisms, vastly increased their usefulness and consumption rate. In particular, broad-spectrum penicillins, which are used for management and treatment of bacterial infections, are of major clinical relevance [42–44].

### Mechanism of action

$\beta$ -lactam antibiotics are bactericidal because they inhibit bacterial cell wall synthesis. The targets for  $\beta$ -lactam antibiotics are enzymes involved in synthesis

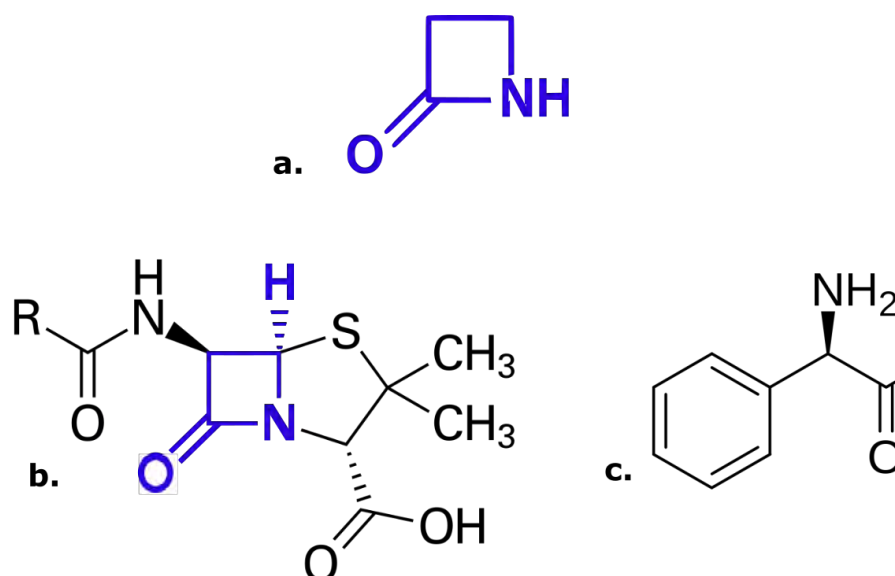


**Figure 1.2** *Skeletal structural formula of (a) the  $\beta$ -lactam ring, (b) the core structure of all penicillins, with the  $\beta$ -lactam ring highlighted in blue, and (c) the R-group for ampicillin. A four-membered lactam ring is a cyclic amide, and here the nitrogen atom is attached to the  $\beta$ -carbon atom, relative to the carbonyl.*

of the peptidoglycan cell wall, known as penicillin-binding proteins (PBPs).  $\beta$ -lactams inhibit the last step in the synthesis of peptidoglycan by binding to (acylating) the transpeptidases which cross-link the peptides which hold together the peptidoglycan mesh. Inhibition of peptidoglycan synthesis causes cell lysis, possibly due to disturbance of the balance between synthesis and hydrolysis of the peptidoglycan. The peptidoglycan layer is important for cell wall structural integrity and for maintenance of turgor pressure, especially in Gram-positive organisms, where this is the outermost and primary component of the cell wall [39]. Because the interior of the cell is under turgor pressure, disruption of the peptidoglycan can cause rapid cell lysis.

## Ampicillin

Ampicillin is the antibiotic we use for the experiments presented in this thesis. Ampicillin is a  $\beta$ -lactam antibiotic which is widely used for the treatment of a variety of infections. It is still featured on The WHO Model Lists of Essential Medicines, since being first listed in 1977 [45].

Ampicillin molecules (shown in Figure 1.2) contain an amino group which helps the antibiotic pass through the pores of the outer membrane of Gram-negative

bacteria. Ampicillin acts as an irreversible inhibitor of the penicillin-binding proteins; transpeptidase, carboxypeptidases and endopeptidases enzymes, which are needed by bacteria to make the cell wall [46].

## Filamentation

It is important to note that *E. coli* uses different peptidoglycan synthesis machinery for cell elongation and for cell division (pole formation)—the elongasome and divisome respectively. Different  $\beta$ -lactam antibiotics bind to different components of the elongasome and divisome, such that they inhibit elongation and division to different extents. Therefore low doses of  $\beta$ -lactam antibiotics can cause changes in cell morphology. Antibiotics that inhibit elongation cause cells to become round (e.g. mecillinam) while antibiotics that inhibit division cause cells to turn into long filaments (e.g. aztreonam and ampicillin) [47]. Images of filamentous cells at various stages of ampicillin exposure are shown in Figure 1.3. Filamentation will become relevant in Chapter 6 of this thesis (Section 6.3.5).

Interestingly, for the antibiotic ampicillin (which is used in this thesis), filamentation can sometimes be a tolerance or persistence strategy. Persisters are a slowly-growing or dormant subpopulation of cells which can survive antibiotic treatment and resume normal growth when the antibiotic stress is lifted. During ampicillin treatment, persister cells have been shown to exhibit filamentous morphology, getting longer over time rather than lysing [48]. Filaments formed under these conditions still often lyse within a few hours [49]. This means that this survival strategy only works if the exposure to antibiotic is short.

Filamentous cells have been found to build up a reserve of ATP (the principal molecule for storing and transferring energy in cells) during antibiotic treatment, perhaps to prepare for when the antibiotic stress is removed [48]. However, the success of this strategy is varied; when the antibiotic is removed, some of these filamenting cells are able to resume growth normally, although some fail to do so. In one study, only 1.5–3% of the analysed filamentous cells recovered and reverted back to normal growth [50]. This means that only a fraction of the filamentous cells can be considered filamentous persisters.



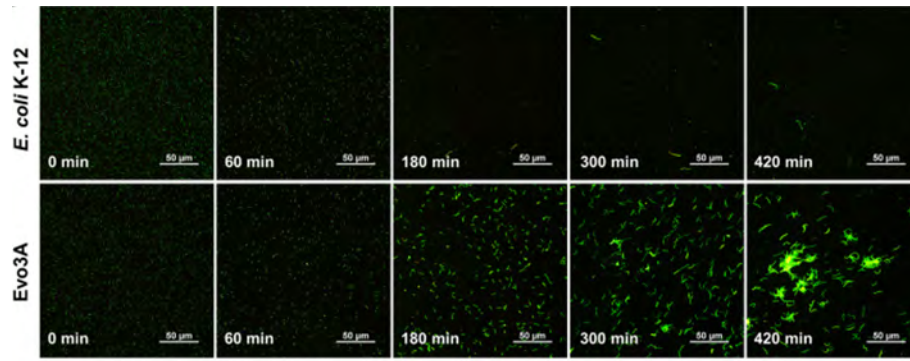


**Figure 1.3** *Epifluorescence microscopy images of *E. coli* K-12 and *Evo3A* cells, which become filamentous during exposure to ampicillin. Image taken from [48].*

### 1.3.2 Antibiotic resistance

Bacteria evolve over time in response to environmental pressures, including antibiotic exposure. Because of the widespread use (and misuse) of antibiotics, there is an increasing selective pressure for resistance. This is a rising threat to global health; antibiotic resistant infections have been predicted to cause 10 million annual deaths by 2050 [51]. As an example of the prevalence of antibiotic-resistant strains, a 2009 study of samples from healthy children found that 40.2% of the 92 *E. coli* strains detected were resistant to ampicillin [52]. In this thesis we will investigate the response of a resistant strain of *E. coli* to ampicillin exposure. This strain is resistant because the bacteria produce beta-lactamase enzymes which degrade  $\beta$ -lactam antibiotics.

### 1.3.3 $\beta$ -lactamase enzymes

In Gram-negative bacteria, the most common mechanism of resistance to  $\beta$ -lactam antibiotics is the production of  $\beta$ -lactamase (beta-lactamase) enzymes which degrade the antibiotic by hydrolysis of the amide bond of the  $\beta$ -lactam ring (see Figure 1.2) [53, 54]. More than 300 types of  $\beta$ -lactamase enzyme have been identified.

As antibiotic degradation can benefit the whole population of bacteria, the production of  $\beta$ -lactamase can result in groups of bacteria surviving concentrations of antibiotic above the concentration that would kill isolated bacterial cells. Therefore,  $\beta$ -lactamase production can be thought of as a cooperative

phenomenon. This inhibition can allow clinical infections to survive antibiotic treatment, sometimes even protecting neighboring cells of sensitive (non- $\beta$ -lactamase-producing) strains [55, 56]. In this thesis I will present experiments and simulations with  $\beta$ -lactamase producing bacteria.

### 1.3.4 The minimum inhibitory concentration (MIC)

The minimum inhibitory concentration (MIC) is a quantitative measure of the effect of an antibiotic on a given strain of bacteria. The MIC is the lowest concentration of antibiotic that, under defined *in vitro* conditions, prevents visible growth of bacteria within a defined period of time [57]. The MIC value indicates the level of susceptibility of the organism to a particular antibiotic agent [58]. Clinically, the procedures and doses for antibiotic therapy are often based on the antimicrobial MIC value [59–61].

From a practical point of view, a standard protocol is used to determine the ability of a micro-organism to produce visible growth when exposed to an antimicrobial agent. This is done either in broth containing serial dilutions of the antimicrobial agent or on a series of agar plates. Careful control and standardisation is required for intra-laboratory and inter-laboratory reproducibility of MIC values. It is generally accepted that broth MIC values are reproducible to within one doubling dilution [57, 58].

### Limitations

The MIC has advantages as a standardised measure of activity of an antibiotic against a microorganism, however, the MIC is an inherently uncertain measurement. An MIC is obtained using an assay that determines *in vitro* the concentration that prevents visible growth. On plates, colonies need to grow large enough to be counted by eye, and in liquid media, visible growth can start at bacterial densities as high as  $10^7 - 10^8$  CFU mL<sup>-1</sup> [59]. The concentration measured as the MIC is therefore not the concentration at which growth is inhibited, but rather the concentration at which observable growth is inhibited. Furthermore, the MIC value does not give an indication of the mode of action of the antibiotic. Even with no visible growth, there may still be viable cells if the drug had a bacteriostatic effect on the bacterial species tested. Growth may resume after the removal of the drug, if persister cells remain. Alternatively,

there may be partial inhibition resulting in impaired and reduced growth rates and consequently no visible growth within the time given [58]. In addition, there was no correlation found between MIC values and resistance mechanisms such as  $\beta$ -lactamase enzyme activity [62]. No direct inference should be made between the bacterial response measured in the laboratory and the *in vivo* response because the MIC is not a good pharmacodynamic indicator for the relationship between antibiotic concentration and antibiotic effect for the range of physiological environments found in the human body [63].

### 1.3.5 Inoculum effect

It is often observed that larger inocula (initial bacterial population size) have higher apparent MIC values, particularly when the strain produces an enzyme capable of destroying the antibiotic. This dependence of antibiotic response on the inoculum size is called the inoculum effect [64].

Inoculum effects have been observed for a wide range of bacterial species and antibiotics [64]. The inoculum effect implies that bacterial populations of different densities can respond differently to the same antibiotic treatment. As a result, antibiotic treatments that would be successful for early bacterial infections may fail to eradicate infections that have reached a critical population density. From a clinical point of view, an inoculum effect is defined as an eightfold or greater increase in the measured MIC, upon testing with a 100-fold higher inoculum than is standard [58].

An inoculum effect is frequently seen when testing the  $\beta$ -lactam antibiotic susceptibility of a bacterial isolate that produces  $\beta$ -lactamase enzymes [58].  $\beta$ -lactamase enzymes inactivate  $\beta$ -lactam antibiotics, reducing the local concentration of antibiotic in the area around an enzyme-producing bacterium. Therefore, the surrounding bacteria experience a lower antibiotic concentration, and are able to survive the exposure. Artemova et al. found that the MIC for *E. coli* expressing  $\beta$ -lactamase varied by three orders of magnitude depending upon the initial cell density [65]. In Chapter 6, we will investigate the responses of small and large bacterial populations to  $\beta$ -lactam antibiotics.

### 1.3.6 Single-cell MIC

It is acknowledged that the MIC is a flawed measure of antibiotic susceptibility because the concentration we measure often depends on the inoculum size. A different metric can be used instead to control for the inoculum effect; the single-cell MIC (scMIC). The scMIC value can be over an order of magnitude smaller than the MIC, as individual bacteria are generally more susceptible to antibiotics than large populations [65]. The single-cell MIC is measured with the same techniques used to find the MIC, but with low density (diluted) initial cultures or very small volumes (such as microfluidic droplets). The lowest concentration of antibiotic which prevents growth is determined, quantifying the inhibitory effect of the antibiotic at low initial bacterial densities [65], or per bacterial cell [20, 66]. It has been shown that both the selection for more resistant pre-existing mutants, as well as selective pressure towards the emergence of new mutations which increase the scMIC, happens at an antibiotic concentration corresponding to the scMIC regardless of the density of the bacterial population. This means the scMIC is a more relevant quantity than the MIC when studying evolutionary dynamics [65].

### 1.3.7 $\beta$ -lactamase production as a social interaction

Social interactions, in which organisms cooperate with one another to mutual benefit, are widespread among humans and animals. A large body of work studies the factors that allow the evolution and stable maintenance of cooperative traits, in which individuals sacrifice some of their fitness to benefit other individuals in the population. These traits are evolutionary stable when the cooperation is between closely-related individuals. It is now widely understood that bacteria can also show cooperative traits and form a crucial part of sustainable ecosystems [67–70].

Cooperating organisms are vulnerable to the emergence of ‘cheaters’, that benefit from the efforts of the cooperator organisms, but do not pay the fitness cost themselves. For example, in *Pseudomonas*, secretion of iron-sequestering molecules benefits not just the secreting cells but also their neighbours [71]. Here, a ‘cheater’ is a bacterial strain that does not produce the iron-sequestering molecule.

Production of  $\beta$ -lactamase enzymes can be viewed as a cooperative trait, since surrounding bacteria benefit from the reduction in antibiotic concentration. In the context of  $\beta$ -lactamase production, ‘cheaters’ are antibiotic-sensitive cells that do not produce  $\beta$ -lactamase enzymes, but benefit from the reduction in antibiotic concentration. As they do not pay the cost of making  $\beta$ -lactamase, the sensitive cells are expected to have a higher fitness in the absence of antibiotic. This concept was explored by Yurtsev et al. who showed that the presence of  $\beta$ -lactamase-producing resistant bacteria allow otherwise sensitive bacteria to thrive at antibiotic concentrations 100-fold higher than their MIC [32].

In Chapter 7 the dynamics of mixed populations of  $\beta$ -lactamase producers and non-producers is explored using simulations. Interspecies interactions can alter antimicrobial sensitivity profiles within polymicrobial biofilm communities, which may in part explain why antimicrobial therapies often fail to eradicate chronic infections [72]. There is clinical evidence to suggest that cooperative  $\beta$ -lactamase production is the cause of an increased failure rate of penicillin therapy in eradicating polymicrobial infections [56]. Coexisting organisms can even have the opposite response to antibiotics in comparison to the isolated species [73].

Since polymicrobial infections are common, it is important to understand these cooperative effects at the interspecies level as well as in populations of the same species.

## 1.4 Microbiology in droplets

Microfluidic droplet methodologies are used in many disciplines to study phenomena in small, isolated volumes. The rapid rate of production (from 0.1–2kHz) results in large numbers (often over 1000 droplets) of picolitre environments with identical conditions; ideal for precise comparative experiments. In these droplets, reagents and reaction products are contained within a controlled microenvironment. The monodispersity of the droplets means that they can be used as effective repeats of biological and chemical assays [74–76].

Droplet microfluidics have many medically relevant applications, such as diagnostics, biomaterial synthesis [77] and in the field of molecular discovery, in screening for new drugs. Initial screening of a chemical library can be done with thousands of droplets, resulting in precise measurements of dose-response relationships using

minimal quantities of reagents [78].

Within microbiology, using microfluidic devices to create monodisperse droplets offers many advantages for quantitative small population or single-cell studies, because they generate numerous, simultaneous, directly comparable environments. This can help remove unwanted biological and environmental variables. Droplets were used by Pan et al. to isolate the effect of varying medium conditions, such as pH and nitrogen concentration, on the growth of *C. reinhardtii* [79]. Encapsulating bacteria in droplets also facilitates long-term population studies, with examples including over 240 hour experiments [80] and those with incubation times of up to 2 weeks [81].

Droplets provide separate compartments in which species or reactions can be isolated and thus enables the analysis of products such as proteins secreted by cells, alongside the cells themselves. Examples of these studies include the detection of antibodies [82]; the detection antibiotics synthesised by actinobacteria [81]; and the synergistic interactions of microbial communities [83].

The micrometre scale of the droplets allows us to observe behaviour that would be masked in large populations (as discussed above in Section 1.2.1). For example, when measuring spatial distribution of motile *E. coli* [84] and growing biofilms in 3D cultures (to observe cellular differentiation within the microstructure) [85].

Microfluidic droplets allow the study of heterogeneity across multiple communities, simultaneously. Such as the heterogeneous evolution of resistance to antibiotics, where droplets make it possible to detect a resistant sub-population that comprises only  $1 \times 10^{-6}$  of the population [20]. Droplets have also been used to encapsulate different species of bacteria together, and characterise microbial communication (e.g. a study into quorum sensing using fluorescence microscopy with a GFP and RFP strain [86]).

Encapsulating bacteria into droplets using microfluidic devices offers several advantages over bulk growth. One of the main advantages is replication: each droplet can be investigated as an independent experiment, allowing parallel study of thousands of replicate populations, in contrast to standard microbiology experiments in which 96 parallel samples (in a microplate) constitutes a high-throughput experiment. Droplets offer advantages over other microfluidic growth methods, which generally use chambers to contain cells (such as the mother machine) because constriction can affect bacterial growth (see Section 1.2.3). In contrast, by encapsulating bacteria in droplets, cells are unconstrained within

a confined environment (showing similar doubling times to bulk growth [34, 79]) and are also unaffected by neighboring droplets (or the bacterial populations they contain).

There are many detailed review articles which give an overview of device fabrication, droplet formation and applications of droplet based microfluidics [74, 76, 87–89].

### **1.4.1 Forming microfluidic droplets**

Microfluidic devices manipulate the flow of liquids inside micrometre-sized channels and chambers. These devices enable the study of small volumes and fluid behaviour on a microscale. Performing experiments at the microscale has additional practical advantages, including easier control of variables (such as temperature), as well as reduced wastage because small volumes of reagents are used. Droplet production using microfluidic devices offers the opportunity to rapidly create numerous isolated environments, with considerable control over droplet size and uniformity, resulting in multiple replicates within a single experiment.

In the majority of cases, droplets are produced by simply engineering the geometry of microscale channels to manipulate input fluids [76, 88]. Most methods for forming droplets are passive, negating the need for moving parts; the most common geometries are shown in Figure 1.4. Droplets are produced in these devices when two immiscible fluids, with independently controlled flows, meet at a junction. Droplets can either be water-in-oil (water-based droplets in a continuous oil medium) or oil-in-water. The specific aqueous phase, oil phase and surfactant combination is selected to optimise droplet properties (such as stability, monodispersity and size) [90]. The fluids are generally driven by syringe pumps or pressure pumps, in which either a volume flow rate or applied pressure is kept constant, respectively. The local flow field is determined by the geometry of the junction, the flow rates and the fluid properties (such as viscosity). Local fluid stresses caused by interfacial tension between the two phases deform the liquid interface at the intersection where the two phases meet and lead to the production of droplets. Capillary pressure acting to resist deformation as well as upstream pressure from restriction at the junction both act to drive ‘pinch off’. The wettability of the nearby channel walls is another important factor, determining which liquid phase is dispersed [91].

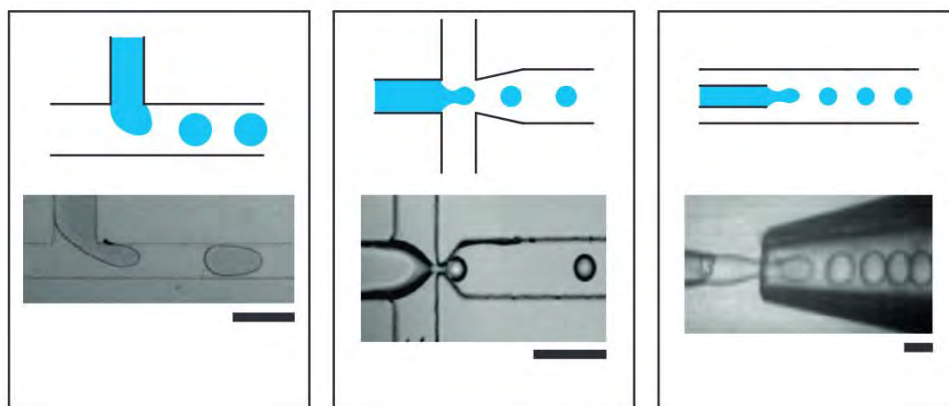


**Figure 1.4** *Schematic paired with an image of the three most common geometries used to generate droplets in microfluidic devices. From left to right these are: cross flow or T-junction (where the fluid of one phase is sheared by a second immiscible phase flowing perpendicularly), flow focusing or elongational flow (where immiscible fluids are accelerated through a small gap) and capillary (a channel inserted inside another, so that the fluid to be encapsulated emerges from the end of the capillary into a parallel flow of the continuous phase). Scale bars show 100  $\mu\text{m}$ . Panel from [74].*

The physical parameters that dominate droplet formation are characterised by the capillary number  $Ca = \frac{\mu U}{Y}$ , where  $\mu$  (Pa s) is the viscosity and  $U$  ( $\text{m s}^{-1}$ ) is the characteristic velocity of the continuous phase and  $Y$  ( $\text{N m}^{-1}$ ) is the surface tension of the water–oil interface. With increasing capillary number, different flow regimes are encountered (squeezing, dripping and jetting regimes). Other non-dimensional quantities are also relevant, especially at high flow rates and when using larger dimension geometries. These include the Weber number,  $We$ , (the relative importance of inertia with respect to interfacial tension), the Bond number,  $Bo$ , (the relative importance of gravitational forces with respect to interfacial tension) and the Reynolds number,  $Re$ , (the relative importance of inertial forces with respect to viscous forces) [88].

Once produced, droplets can be manipulated, incubated and sorted in various ways [74]. Dilutions or changes in concentration can be achieved by splitting or fusing drops—often achieved simply using channel geometries—or with active techniques such as pico-injection—typically triggered by an electrical field, electro-coalescence or electrode-free injection to change the chemical environments of specific droplets [80]. Multiple merging, mixing and re-splitting events can be used to perform serial dilutions, to generate concentration gradients, or to initiate and terminate reactions. This can be used for rapid chemical and biological



screens such as DNA-binding assays, using only nanolitre volumes of sample [92].

Droplets can be sorted by deflection through a variety of forces, both in-device [93] and with external methods such as fluorescence-activated cell sorting (FACS) or mass spectrometry [76]. Fluorescence-activated droplet sorting (FADS), is an in-device method of sorting, using fluorescent markers, often attached to ‘reporter’ bacteria, [81, 88]. A label-free FADS method has been demonstrated for the screening of cyanobacteria and microalgae, using intrinsic chlorophyll fluorescence in photosynthetic cells to measure differences in biomass [94].

In conjunction with the various techniques for manipulation, droplets and their contents are often ultimately imaged in some way. Fluorescence and bright-field microscopy imaging can be used to follow reactions or growth cycles within a microfluidic device over significant time periods, in thousands of individual droplets, for both qualitative analysis and to generate statistics for population studies [95, 96]. Alternatives to optical detection are also used, such as vibrational spectroscopy or mass spectroscopy, allowing a non-destructive measurement of molecular composition and structure [74, 76].

## **Microfluidic device fabrication**

Microfluidic devices are made from inert materials, typically glass or polymers. Polymer-based microfluidic devices offer cost, accessibility and biocompatibility benefits. There are many direct and replication approaches for the manufacturing of microfluidic devices [97]. In this thesis, we use a master mould to create Polydimethylsiloxane (PDMS) devices because once one master is created, it can be used to manufacture numerous devices in a typical biolab setting (without the need for specialist equipment or a clean room).

These master moulds are made by spin coating SU8 to the desired channel depth on a silicon wafer. The wafer is baked and then exposed to UV light through a custom photomask (a mask fabricated with a CAD generated device design). The wafer is baked a second time, and then rinsed in propylene glycol methyl ether acetate (PGMEA) until only the crosslinked SU8 remains, creating a positive mould of the design. Many identical PDMS devices can then be made using this mould. This process is illustrated in Figure 1.5 and detailed elsewhere [98, 99].

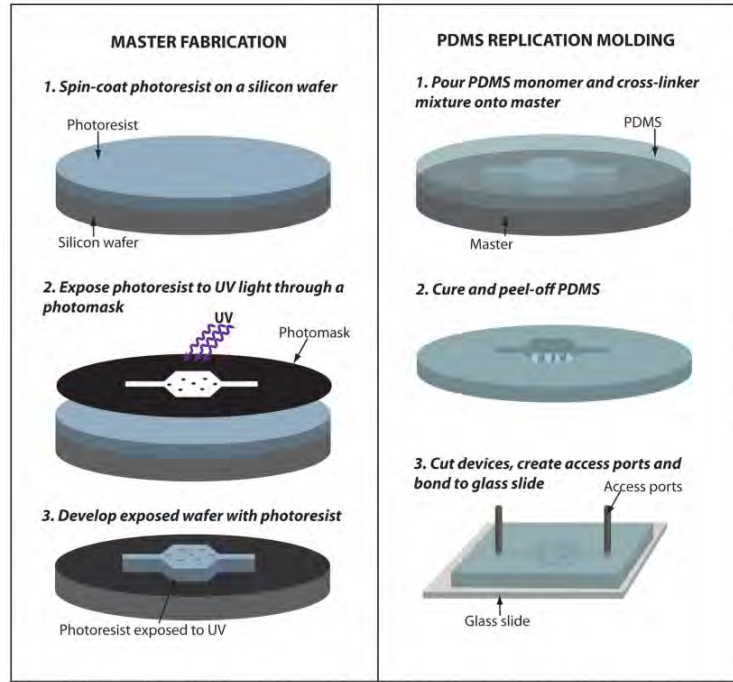


**Figure 1.5** *Schematic of the fabrication of master mould (left) and PDMS replica microfluidic device (right). Figure taken from [98].*

### 1.4.2 Encapsulation of bacteria into droplets

Encapsulating bacteria into monodisperse, picolitre-size droplets can be achieved simply by using a bacterial suspension (in growth media) as the aqueous phase in the methods detailed above. The arrival of cells at the water–oil interface is random while the production of droplets is continuous. The concentration of bacteria in a well-mixed suspension is constant and therefore so is the mean number of bacteria in the droplets. Hence the number of bacteria per droplet is dictated by Poisson statistics, due to the random dispersion of cells within the encapsulated phase.

The Poisson distribution is discrete, and describes the number of events happening at a particular time, when these events are stochastic but happen at a fixed rate (in this case, the number of bacteria arriving at a droplet as it forms). This rate is characterised by an average value,  $\lambda$ :

$$P(k, \lambda) = \frac{\lambda^k e^{-\lambda}}{k!}$$

where, in this context,  $P$  is the probability of a droplet containing  $k$  bacteria,

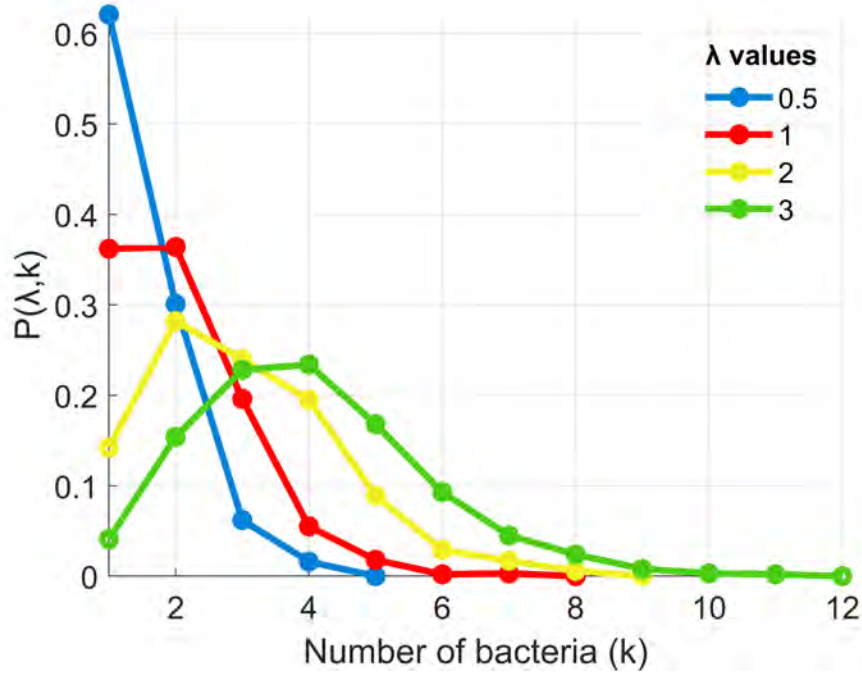


**Figure 1.6** *Poisson distributions.* Graph showing the probability,  $P(k, \lambda)$  of droplets containing  $k$  cells, with plots for  $\lambda$  values of 0.5, 1, 2 and 3. Each line shows an example distribution for 1000 randomly generated values at every  $\lambda$  value.

when using an aqueous phase concentration which gives an average number of  $\lambda$  bacteria per droplet. Figure 1.6 shows a plot of this probability distribution for various values of  $\lambda$ .

Because it is an intrinsic property of encapsulated bacteria, Poisson statistics are often used as a methodological validation of droplet microfluidic techniques [88, 95].

Poisson distributions are also formed with serial dilutions [9], but in droplets, we have a direct measurement of the initial number of cells before growth. The advantage of this passive encapsulation, is that we can study a distribution of initial bacteria encapsulated in the droplets. Growth and antibiotic response can be studied and compared between small populations with different starting sizes.

An additional benefit of stochastic confinement, is that because cell density is increased, the encapsulation process can decrease the time needed to detect bacteria or measure response to antibiotics [100]. There is an inherent inefficiency due to the production of empty droplets, which can be inferred from the Poisson

equation and the resulting distributions (displayed in Figure 1.6). This reduces the number of filled drops when using low concentrations, but empty droplets are useful for checking the results of image analysis and can be used to provide background measurements if required by the image analysis methodology.

Complications arise when there is an experimental requirement for a specific initial number of cells, as in the case of single-cell studies. At low bacterial concentrations, for example at  $\lambda = 0.05$ , the majority of droplets will be empty (95%), but those that do contain cells, 98% of these will only have one [9]. There are numerous methods to overcome this single-cell Poisson limitation, including droplet sorting or organising the bacterial cells prior to droplet formation [88, 101].

In this thesis, we will exploit the Poisson distribution of initial bacterial numbers in Chapters 3 and 6, as it provides a way to sample and compare different bacterial concentrations (i.e. different initial inoculum sizes) within the same experiment.

# Chapter 2

## Methods and method development

This chapter details both the experimental and image processing methodology that are used in this thesis to measure the growth of fluorescent bacteria in picolitre droplets. The methodological starting point of my research was the device detailed in the thesis of previous PhD student, Daniel Taylor [99], and in our joint paper [96], which also contains analysis performed by me on Daniel Taylor’s data. In this chapter, I describe a redesign of the microfluidic device to improve performance, together with improved analysis methods.

### 2.1 Overview

To facilitate the study of the dynamics of small populations, bacteria were put into monodisperse picolitre droplets to form spatially separate communities. The bacterial growth within individual droplets was then tracked over time. Section 1.4 includes a discussion of droplet microfluidics methodologies as well as the microbiological experiments they facilitate.

Specifically, in my work, fluorescent bacteria were diluted such that droplets are filled with 0–10 initial cells. The droplets were stored in a 10  $\mu\text{m}$  deep microfluidic reservoir in which bright-field and fluorescence images are taken every 10 minutes over multiple fields of view, (FoV) for 4–6.5 hours. The experimental method is described in detail below in Section 2.2.

The resulting array of paired images for each field of view (FoV)—bright-field

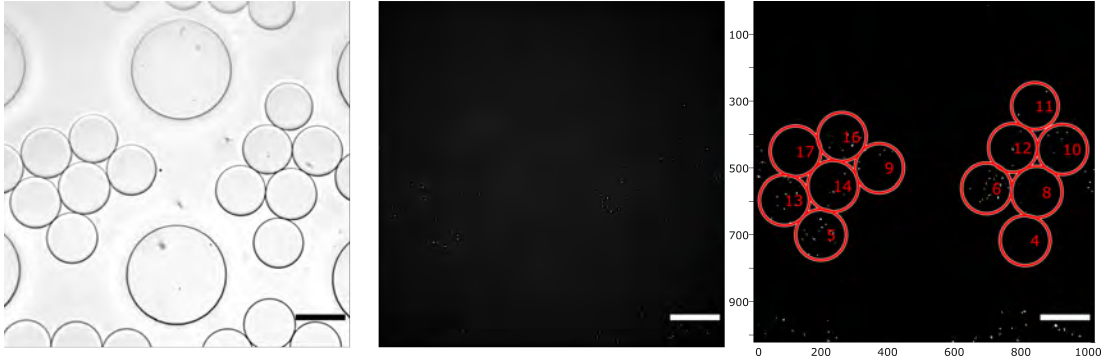


**Figure 2.1** *An example field of view (FoV) in the droplet reservoir. Showing (left to right) a bright-field image, fluorescence image in CFP and a binarised, processed image. In the processed image, the red circles show where the droplet boundaries have been detected using the brightfield image and the bacteria identified from the fluorescent image are shown in white. The numbers indicate the droplet ID, a unique number used to track the droplet throughout the experiment. Droplets on the image boundary are ignored. Scale bars show 100  $\mu\text{m}$ .*

images of the droplets, and fluorescent images of the bacteria—was analysed to obtain counts of bacteria at each timestep, within each droplet (which was assigned a unique ID number). Figure 2.1 shows an example FoV in bright-field, where we can see the droplets; the corresponding fluorescence image, where we can see the bacteria; and the analysed image, where the droplet boundaries and the bacterial cells have been identified. The image analysis methodology is described fully in Section 2.3.

The image processing results in a dataset of droplet radius, droplet location and size of the bacterial population, for each individual droplet at every timestep. This can be used to obtain growth trajectories (as in Figure 3.1) which can then be analysed further. As each data point is linked to a raw image, any unusual trends or outliers in the data can be easily investigated post-analysis by referring back to the original images.

In the following sections, the experimental and image processing methodologies are described in more detail.

## 2.2 Experimental method

I first present an overview of the experimental method, in Section 2.2.1, then, in Sections 2.2.2–2.2.6, I explain and describe novel aspects of the methodology that I established during my PhD research. A more detailed experimental protocol can be found in Appendix B.

Throughout this thesis, each experimental run is referred to using the letters A–D, with the ampicillin concentration given in brackets, in  $\text{mg mL}^{-1}$ . Experiments A(0)–D(0) are uninhibited droplet experiments with no antibiotic, the results of which are explored in Chapter 3. A full list of experiments is given in Table 6.1.

### 2.2.1 Overview of the microfluidic droplet method

#### Device preparation

The microfluidic device was made with PDMS (Polydimethylsiloxane) using a master mould as in described by Taylor et al. [96] (see Section 2.2.2 for a discussion of the device design). Outlets and inlets were created using a biopsy punch and glass capillaries. Channels were created by attaching the PDMS to a large glass slide ( $76 \times 38$  mm). The device was then secured into a customised chamber (see Section 2.2.3), and a surface treatment was applied to make the channels fluorophilic (see Section 2.2.5).

#### Bacterial preparation

Three single colonies were grown up overnight in 6 mL of M9 minimal medium supplemented with glucose at 0.4 wt% (recipe given in [96]). M9-based media was chosen for this study due to its low levels of auto-fluorescence. In the morning, 25  $\mu\text{L}$  of one of the overnight cultures, or 50  $\mu\text{L}$  if using a Y-junction to introduce the aqueous phase (see Section 2.2.6), was used to inoculate 10 mL of M9-glucose media. The diluted culture was incubated at  $37^\circ\text{C}$  with shaking for a further 1.5 hr. This was sufficient time for the bacteria to exit lag phase and we therefore see growth in exponential phase at the start of the droplet experiments (see Figure 3.2).

### **Bacterial strain: RJA003**

The bacteria used in these experiments was RJA003, a strain of *E. coli* carrying a chromosomal cyan fluorescent protein (CFP). It was created by P1 transduction from strain MRR of Elowitz et al. into MG1655 [102, 103]. This strain was sequenced to identify the  $\beta$ -lactamase it produces as blaTEM-116 (a class A broad-spectrum  $\beta$ -lactamase TEM-116) with accession WP\_000027050.1.

### **Device setup**

The device was mounted on the microscope in a chamber that allows it to be surrounded by water to maintain high humidity and a constant temperature (see Section 2.2.3). The oil phase inflow (FC-40 with Pico-Surf<sup>TM</sup> surfactant, see Section 2.2.4) was started at a low flow rate using a NE-300 (one-channel) syringe pump.

After 1.5 hours, the bacterial suspension was removed from the incubator. The optical density (OD) of the bacterial culture was measured immediately before it is used, to check adequate growth. A 1 mL syringe was filled with the bacterial culture. Air bubbles were removed and the syringe was attached to the aqueous inlet of the microfluidic device using tubing. The remaining bacterial culture was then placed back into the 37°C incubator.

Epoxy was applied to secure the tubing to the glass capillaries and to ensure water-tightness. Once the epoxy was dry, the lid of the chamber was secured, the whole chamber submerged in a water bath and a pump engaged to create a closed-system (see Section 2.2.3 for discussion of the chamber). The device was surrounded by water throughout the experiment to maintain high humidity (to prevent droplet evaporation) and a constant temperature.

### **Antibiotic: ampicillin**

Ampicillin was used in the droplet experiments presented in Chapter 6 as an example of a  $\beta$ -lactam antibiotic (see Section 1.3.1).

The stability of ampicillin is highly dependent on environmental factors such as temperature, pH and the solvent [104]. Ampicillin was measured to have a half-life of  $\approx 30$  hours in Citric Acid-Disodium Phosphate Buffer at 35 °C,



with an ionic strength of 0.5 M and pH 6.85 [105]. Pharmacokinetic factors make *in vivo* dynamics more complex; accelerating the degradation. Plasma concentrations of an ampicillin dose decline with a half-life of about 80 minutes in adults (elimination half-life increases to 2.4–5.0 hours in infants) [106].

We expect the conditions of the droplet experiments to result in a half-life between these two values, and therefore we expect some decline of concentration independent of the bacterial  $\beta$ -lactamase action, although we still presume significant antibiotic concentrations throughout the experiment, as 6.5 hours should be below the *in vitro* half-life.

To minimise this degradation, a fresh stock sample (at 100 mg mL<sup>-1</sup>) was removed from the freezer and diluted to the desired concentration shortly before use (see Table B.1). Two separate syringes, one filled with the bacterial suspension and the other with the ampicillin solution, were attached to a Y-connector, which was attached to the aqueous inlet of the device with 1 cm of tubing (see Section 2.2.6). In this case, a two-channel Harvard Apparatus PHD ULTRA™ syringe pump was used to dispense both aqueous phase inputs at the same rate.

## Droplets

To achieve monodisperse droplets of the desired size, flow rates were adjusted once droplet generation was established (i.e. once the oil and aqueous phases were meeting at the flow-focusing junction). A discussion of the flow rates is given in Section 2.2.2. Once monodisperse droplets filled the reservoir, the tubing at both the inlets was cut to stop the flow.

## Microscopy

Images are taken using a Nikon eclipse Ti2 microscope with a 20× plain Apo  $\lambda$  objective (OFN25 Ph2 DM, 0.75 NA, with air immersion) and a Hamamatsu ORCA-flash 4.0 digital camera (model C13440-20CU). The microscope stage was operated with a Nikon TI2-S-JS stage joystick. A magnification of 20× was chosen as a compromise between individual cell resolution and a reasonable scan time (the full reservoir is approximately 400 fields of view at 20× magnification and a scan was completed every 10 minutes). A higher objective would increase the time for a complete scan and would therefore increase the time between data

points for each droplet population. A lower objective would decrease the accuracy of the image analysis and bacterial counts.

Nikon NIS-Elements imaging software [107] was used to operate the microscope and the ND-acquisition (N-dimensional image acquisition) functionality was used to set up automated imaging of the entire device for 4–6.5 hours. After this time, the bacterial count for some droplets in the uninhibited experiments reaches  $\approx 150$  bacteria (see Figure 3.1), after which image analysis starts to fall down [96]. Example images of full droplets are shown in Figures 2.15 and A.13; the bacteria were observed to swim throughout the experiment and were still able to divide exponentially (see Figure 3.2). The length of the experiments was kept consistent for comparative purposes, although it would be possible, and interesting in future to perform longer measurements for the antibiotic experiments presented in Chapter 6 (perhaps with a lower image acquisition rate).

Before each experiment, the microscope was checked for Köhler illumination, calibrated and adjusted for optimum imaging in the bright-field and CFP (Cyan Fluorescent Protein) channels, including  $2 \times 2$  binning. The area of the scan was tested to ensure it was correctly centred and covered the whole reservoir whilst maintaining the Nikon Perfect Focus System (PFS). The ND acquisition was set to image both channels, at each field of view (FoV) in the selected area, every 10 minutes (a multi-channel, multi-point, timelapse image scan).

### **During the image acquisition**

As soon as the image acquisition scan is running, the bacterial culture was again removed from the incubator and a second optical density measurement was taken. This provides a reference for the concentration of the bacterial culture at the start of the droplet imaging. Throughout the 4–6.5 hour experiment, the water flow and temperature were checked intermittently to ensure the droplets were maintained at a constant temperature. The scan focus and the captured microscope images were also checked regularly.

### **2.2.2 Integrated microfluidic device**

In the previous version of the microfluidic device (designed by Dan Taylor [99]), the droplet generator and reservoir were separate, connected by a piece of tubing.

During my PhD, I designed a new integrated two-level device. Combining the reservoir and droplet generator into one device drastically reduced the time difference between droplet generation and the droplets reaching the reservoir; therefore reducing the time gap before imaging. This can now be as low as 3 minutes (see Table 6.1), in comparison to 90 minutes in the original device [96]. Another advantage of this design is that more droplets are pushed into the outer chambers of the reservoir, since they enter over a wide transition zone rather than at a central inlet, as in the previous design. This means that all four reservoir chambers are filled with droplets for imaging, rather than the majority flowing into the central two chambers, as was previously the case.

The new device utilises the established design for the droplet generator, which creates droplets at a flow-focusing junction (see Section 1.4.1 for background).

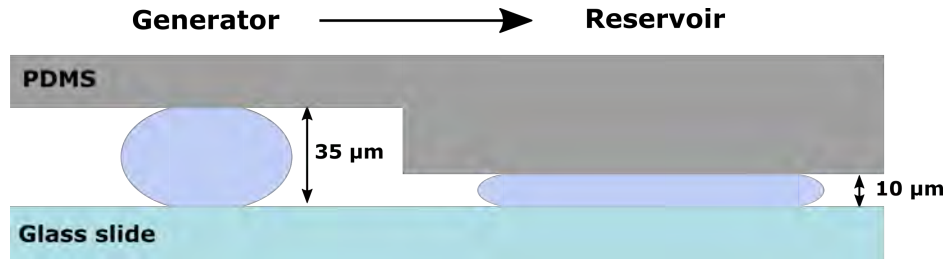


**Figure 2.2** *Schematic demonstrating the droplet shape in the generator and the reservoir on each side of the device step. The flow is from left to right, indicated by the arrow. This is to scale and represents a droplet with a volume of 65 pL with a 25 μm radius.*

The generator and reservoir have different heights, since droplets need to be compressed in the reservoir for optimal imaging of the bacteria. Therefore the integrated device needs to be multi-level, as shown in Figure 2.2. It has been verified using the original device that the bacteria remain in focus in droplets contained in a channel with a height of 11.5 μm [96].

To this end, a multi-layer master mould was made with SU-8 resin on a silicon wafer (manufactured by Micrux technologies [108]). This is a patterned template which can be used to cast numerous PDMS devices (see Section 1.4.1 for description of the fabrication process). Figure 2.3 shows the generator (in pink) and the reservoir (in purple) as separate layers, which were used to make two masks. These masks were used to make channels of different depths, so that there is a step in height between the generator and reservoir which the droplets travel through. Figure 2.4 shows a microscopy image of droplets traversing through the step, from the generator to the reservoir. Figure 2.2 the change in droplet shape

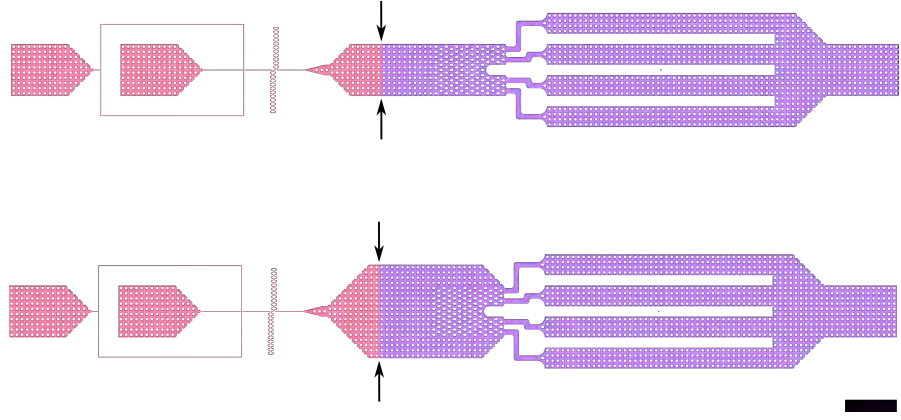


**Figure 2.3** *The CAD of the connected device design used to create the master mould. The generator (in pink) was made with a channel depth of  $35 \pm 5 \mu\text{m}$ , and the droplet reservoir (purple) has a channel depth of  $10 \pm 3 \mu\text{m}$ . The two designs shown are identical, except for the step width (indicated with arrows), which are 4 mm (upper) and 7.2 mm (lower). Scale bar shows 4 mm.*

as it moves through the device.

Two-level master moulds are intrinsically more complex than single-level master moulds. Tension and alignment difficulties result in a higher likelihood of mistakes in fabrication; this can create points of weakness, which are exacerbated with each use, which results in lower reusability than a single-level mould. To mitigate alignment problems in the manufacturing process, a 2 mm overlap between the generator and reservoir layers (the pink and purple layers in Figure 2.3) was included in the design, perpendicular to the step. This means that instead of the masks needing to be positioned exactly where the arrows indicate, there is an allowance for the horizontal position of the step, which reduces the risk of a gap between the layers.

The new design also includes a central reference point in the reservoir to allow the ND acquisition scan to be aligned easily. The microscopy scan is aligned by positioning the central FoV over the objective and then inputting a scan size which surrounds this central point. This is the only support outside of the reservoir chambers, and is therefore easy to identify (see Figure 2.8). Now this alignment step only requires finding the reference point, and creating a grid with covers the area of the whole reservoir.

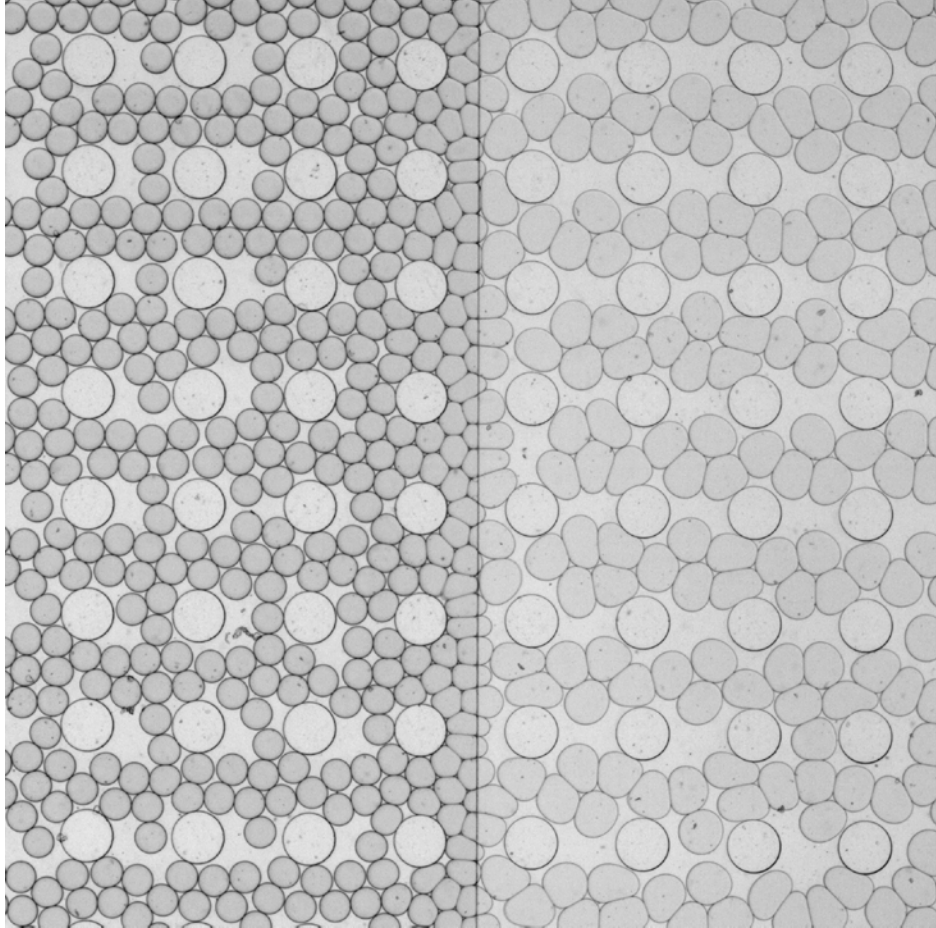


**Figure 2.4** *Microscope image taken of droplets moving through the step of the device. Droplets are moving left to right from the  $35 \pm 5 \mu\text{m}$  layer to the  $10 \pm 3 \mu\text{m}$  reservoir. The droplets appear to increase in diameter in this 2D image, as a constant volume is squashed in the  $z$ -direction. Droplet shape is deformed when moving through a region where the carrier-fluid velocity is changing.*

## Flow rates

Two versions of the two-level device were made, with different lateral widths of the zones in which droplets transition from generator to reservoir. Both versions are shown in Figure 2.3, with arrows indicating the transition steps. In the device with the narrower, 4 mm transition step (the upper design), the flow rate used for the oil phase was  $120 \mu\text{L hr}^{-1}$  while in the device with the wider, 7.2 mm transition step (the lower design), it was  $160 \mu\text{L hr}^{-1}$ . The flow rate for the aqueous phase (containing the bacteria) was set at  $35 \mu\text{L hr}^{-1}$  if a Y-junction was used or  $60\text{--}70 \mu\text{L hr}^{-1}$  if there was only one aqueous syringe. These flow rates can be adjusted if needed (for example, if blockages impede the flow).

### 2.2.3 Device chamber

As part of my PhD research, I designed a custom chamber to maintain the microfluidic device in a humid temperature-controlled environment on the microscope stage. Previously an 3D-printed open chamber was used, which the device was secured into using a silicon glue [99]. Because the microscope slide had to be supported on all sides, this restricted how much of the device was accessible for imaging. In the new chamber, the slide was fastened along just two lengths using a perspex clamp secured with screws onto an O-ring beneath. Photos B.1 and B.2 show the chamber and how the microfluidic device (which is mounted in the centre of a glass slide) was secured.

Combining this new chamber design with larger than standard glass slides ( $76 \times 38$  mm) allowed the whole droplet reservoir to be imaged; specifically, we were able to image  $25 \times 16 = 400$  FoV, compared with  $14 \times 18 = 252$  FoV in the old device [96]. This increases the number of imaged droplets from 300–1000 to 1000–5000.

A lid was added to prevent splashing of water onto on the microscope (since the stage moves whilst scanning) and maintain a consistent temperature. Inlets and outlets were inserted to connect the water pump. Small holes were made in the lid for the microfluidic device tubing and a bubble trap was included. The chamber was made in the School of Physics mechanical workshop at the University of Edinburgh by technician Andy Garrie.

We also needed to ensure that bacteria are maintained at the desired temperature before they enter the microfluidic device. The syringe containing the bacterial

suspension was not heated but at least 8 cm of the tubing leading to the device was kept inside the chamber (when using a Y-junction, this could be reduced to 4 cm). The maximum time from syringe start to droplet production of the experiments presented in this thesis is 34 minutes (see Table 6.1). This means that all bacteria that end up in droplets had been at the desired temperature as soon as the water bath was started (since at  $70 \mu\text{L hr}^{-1}$ , the fluid in the 0.8 mm ID tubing moves 14 cm per hour).

## 2.2.4 Surfactant

Pico-Surf<sup>TM</sup> is a proprietary biocompatible surfactant which can stabilise water-in-oil droplets up to a size of  $110 \mu\text{m}$ , or  $700 \text{ pL}$  [109].

In the two-level device, droplets experience a step in the device height as they travel from the generator to the reservoir, illustrated in Figure 2.2. Droplets travel through a step junction rather than a glass capillary and a tube, as in the previous version of the device. In comparison to the original protocol, the surfactant concentration was increased from 2.5% to 6–7% to ensure that the droplets could withstand the stresses of travelling from the generator ( $35 \mu\text{m}$  in depth) to the reservoir level of the device ( $10 \mu\text{m}$  in depth). These stresses are visualised in Figures 2.4 and 2.5 which show deformation of droplets due to the step in channel height and collisions with channel supports. The flow rate of the carrier fluid (the oil phase) was also increased in comparison to the original methodology, since in the connected device higher flow rates are required to push the droplets under the step.

To create a solution of Pico-Surf<sup>TM</sup>, 6–7 % of Pico-Neat<sup>TM</sup> by weight was mixed with FC-40 (a fluorocarbon oil immiscible with water). Pico-Neat<sup>TM</sup> is highly viscous, so to dissolve it completely into the FC-40, it was left overnight on a magnetic stirrer.

Each solution of Pico-Surf<sup>TM</sup> can behave slightly differently because it is a polymer mixture. Each new lot of Pico-Surf<sup>TM</sup> was therefore checked to tune the conditions (primarily the flow rates) of the experimental setup to ensure reproducibility [109].

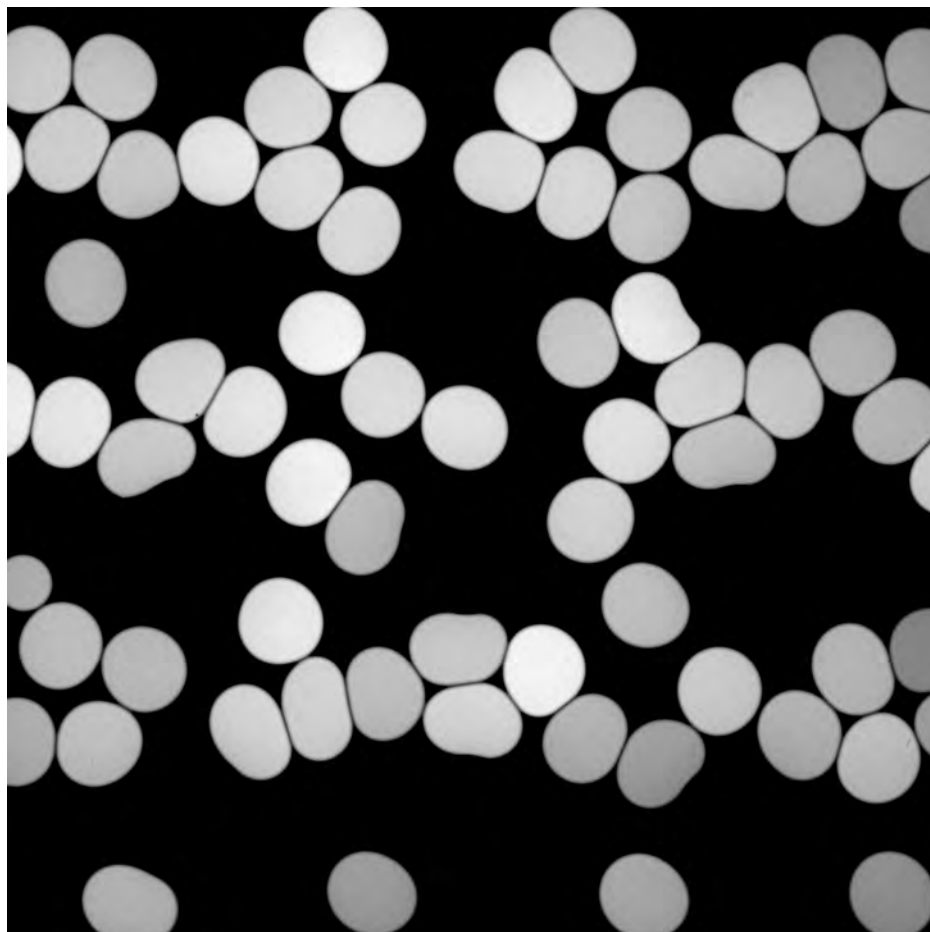


**Figure 2.5** *Fluorescent image of moving picolitre droplets (from left to right) filled with fluorescein, taken using a 10× objective. We can see the droplets deforming as they move around each other and the microfluidic supports.*



## 2.2.5 Surface treatment

Pico-Glide™ is a surface coating agent that is used to enhance the performance of droplet-generating microfluidic devices and ensure stability of the droplets. It is a specialised chemical solution containing 0.5% (w/w) functional, fluororous polyether polymer that is chemically reactive to plasma-etched glass and polydimethylsiloxane (PDMS) surfaces. Pico-Glide™ forms a uniform and dense fluorophilic layer which is covalently bonded to the microfluidic channel surfaces [110].

Prior to using a device for an experiment, a syringe was half filled with air, and 0.05 mL of Pico-Glide™ was gently pushed into the channels through the outlet of the device. In the integrated device design (Section 2.2.2), this fills quickly (in less than 90 s) and so could be done the day of the experiment if required. It was left to sit in the channels for at least 30 minutes to allow the fluorophilic layer to form.

## 2.2.6 Introduction of antibiotic

To introduce the antibiotic immediately before droplets are formed, we used a Y-connector to combine separate inflows of a solution of antibiotic and dispersion of bacteria just before the aqueous inlet. In the original protocol, developed by previous student Dan Taylor, antibiotic was added to the bacterial culture before it was loaded into the syringe [96]. However this does not allow the study of early-time responses to antibiotic. Using the Y-connector method, droplets that reach the reservoir have been in contact with the antibiotic for between 3–37 minutes at the start of imaging (see Table 6.1). The antibiotic and bacterial suspension are both pushed through the Y-junction at the same rate to ensure both are flowing evenly. It was then attached to the aqueous inlet of the device using epoxy.

### Validation of the Y-junction

It is important that every droplet contained the same concentration of antibiotic. Both the bacterial suspension and the antibiotic solution were pushed through a Y-junction through a short length of tubing and then into the aqueous inlet section of the device, so there was opportunity for mixing prior to the droplet

formation at the flow-focusing junction. However because the tubing dimensions are so small (0.8 mm ID), the flows meeting at the Y-junction were well within the laminar range, with a Reynolds number of 0.006 (flow is considered laminar below 2300)<sup>1</sup>. This is not necessarily a problem, as mixing can occur when both flows are forced together at an angle. Furthermore, even if the two fluids are not well mixed when they reach the flow-focusing junction where droplets are created, we would still expect the bacteria and antibiotic to be combined in the right proportions.

To test the function of the Y-junction experimentally, I performed an experiment where droplets were filled with fluorescein, a widely used fluorescent dye. Firstly, droplets were made from a 100% solution of fluorescein. A second device was then used to generate droplets using a Y-junction connected to the same solution of fluorescein and a syringe filled with water. By using the same flow rates for both, as in the experimental protocol, generated droplets should each contain 50% of the fluorescein.

Using fluorescence microscopy I then measured the fluorescence intensity per pixel within the droplets, as a measure for fluorescein concentration. Figure 2.6 shows the distribution of fluorescence per pixel taken for droplets filled with 100% fluorescein compared to droplets made using a Y-junction with a 50:50 mixture of water and fluorescein.

The low value of the coefficients of variation for the measured intensities (0.049 and 0.068 for 100% and 50% fluorescein, respectively) are an indication that the Y-junction combines the two fluid streams homogeneously. Unfortunately there is a non-linear dependence between the measured fluorescence intensity and fluorescein concentration, which means that this measurement does not quantitatively confirm the 1:1 dilution ratio at the Y-junction. The dilution ratio was instead validated by considering the details of the Poisson distribution of droplet populations, as discussed in Section 2.5.3.

---

<sup>1</sup>The values for velocity were taken for a flow rate of  $35 \mu\text{L hr}^{-1}$ , and the dynamic viscosity and density values were used for water at  $37^\circ\text{C}$  [111].

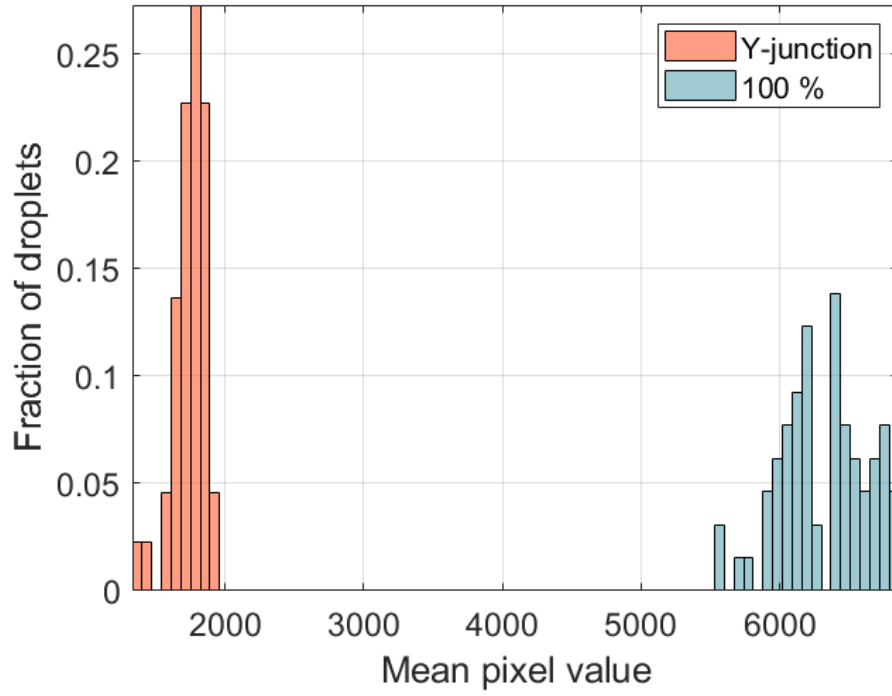


**Figure 2.6** *Histograms from the Y-junction experiment with fluorescein. Pixel values were normalized by the area of the droplets. The mean pixel values for each histogram are 1750 (Y) and 6316 (100% fluorescein). This is for a sample of 44 and 65 droplets respectively. The mean of the background distributions were 152 (Y) and 366 (100% fluorescein). Images were taken with a 10× objective and 20 ms exposure.*

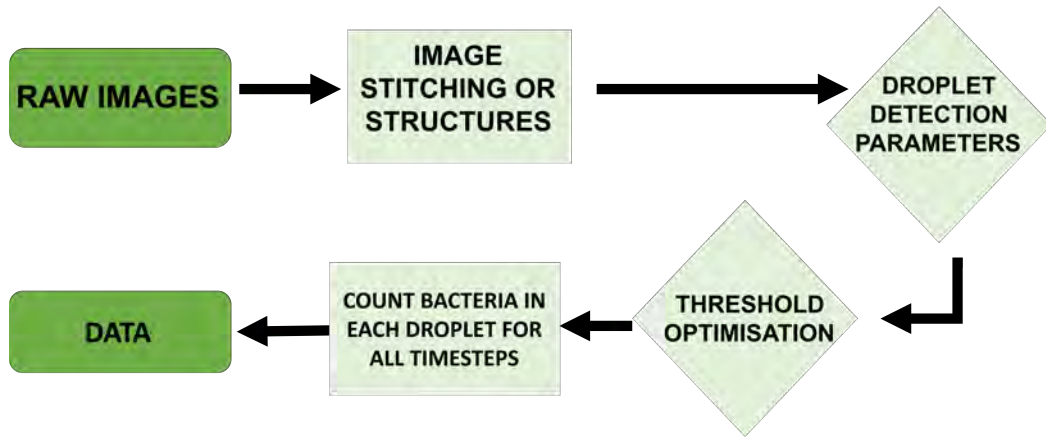


**Figure 2.7** *Flow chart of the image analysis process for an experimental dataset. Raw bright-field and fluorescent images are analysed to generate data for each droplet population. Diamonds indicate manual optimisation, and squares indicate steps which are executed with algorithms written in Matlab.*

## 2.3 Image analysis

Each droplet experiment produces thousands of bright-field and fluorescence microscopy images of droplets and bacteria in the reservoir. Our image analysis protocol must match the bright-field boundary of the droplets with the corresponding fluorescent bacteria. The images were stitched or structured together to combine fields of view (FoV), after which the images were processed to detect droplets and count the bacteria in each droplet population, for every timestep. In my work, I built upon the image analysis protocol developed by previous PhD student, Daniel Taylor [96, 99]. In the following sections, I describe this protocol and highlight the improvements that I made to it.

### 2.3.1 Stitching the fields of view together

An early stage of the image processing was the stitching together of multiple fields of view (FoV) into a single image. A typical scan of the reservoir (with a  $20\times$  objective) has at least 240 FoV. This process was not trivial because there is typically a small overlap between adjacent fields of view (due to the way the microscope scans the device). This can be done in several ways.

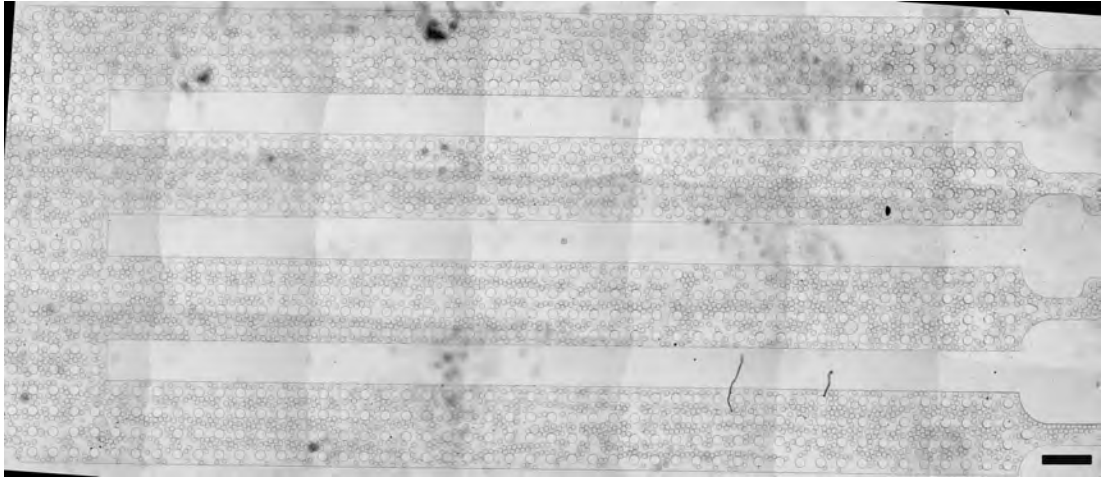


**Figure 2.8** *A stitched bright-field image of the whole reservoir which was generated using the Nikon NIS-Elements software. This was stitched from 33 separate FoV taken with a 4 $\times$  objective. This reservoir is filled with 4600 droplets. The scale bar shows 1mm.*

### Stitching with Nikon NIS-Elements

We can process the raw microscopy images using the inbuilt microscope software, Nikon NIS-Elements [107]. First, the raw Tiff files need to be imported as a sequence. The sorting is automated if the files are saved in the format ‘t\_xy\_c\_’, which gives each image a unique number for time (t), field of view (xy) and channel (c). This sequence can then be converted into an ND2 format (a file type used by Nikon software), which can then be stitched to a ‘large image’. Figure 2.8 shows a fully stitched image using this method. Stitched files are very large as it contains images for all FoV, for every time step, for both channels. Therefore it needs to be split into smaller files, which each contain multiple ( $\approx 10$ ) FoV for every timestep. This generally results in 20-30 stitched files which we export in a Tiff format. Once these sections have been exported, they can then be downloaded from the microscope computer and processed as arrays of (x, y, t) for each channel.

### Stitching with Matlab

Sometimes the Nikon software stitching fails (or the experiment was performed on a different microscope with a different software). In this case, one option was to stitch with an in-house Matlab code developed by previous student Dan Taylor [99]. This places the individual images in the correct position, (x, y), for each

timestep,  $t$ , into a 3D array of  $(x, y, t)$  for both the bright-field and fluorescence channels. As with the software stitching above, the set of images from a full experiment was too large to process as one array, so the FoV were split into sections.

This method relies on a good calibration of the stage position, although some alignment errors can be fixed if they are consistent over the full set of images.

### **Analysis without stitching**

The main advantage of stitching the fields of view together is that droplets which cross the boundary of a FoV can be included in the analysis. However these boundary droplets are somewhat prone to errors. In the new two-level device I was able to image many more droplets than with the old device, meaning that it became less important to analyse every droplet. For most of my experiments, I therefore performed the analysis without any stitching. Here, I arranged the fields of view into a structure, and then simply processed the FoV individually, discounting any droplets that crossed the boundary of the image (see Section 2.3.2).

Other benefits include: only having to store one set of raw data (and not the additional stitched arrays); saving time by not having to stitch and load large files; and the fact that we can adapt our thresholding of the fluorescence images for different fields of view (see Section 2.3.3). It was also easier to match droplet images to the data when investigating possible errors or unusual bacterial counts, because each FoV had a bright-field image, a fluorescence image and a data structure with the same field name.

### **2.3.2 Droplet detection**

As established by previous student Dan Taylor [96, 99], droplet outlines were detected using a circular Hough transform (CHT), an intensity-gradient based approach which remains robust in the presence of noise or varying illumination in an image. Matlab has an inbuilt function for this, called ‘`imfindcircles`’. The application ‘Circle Finder’ was used to visualise the fitting parameters.

We use a dark object polarity because the droplet outlines are darker than the background. A Two-Stage or 2-1 CHT method was used, where the normal to

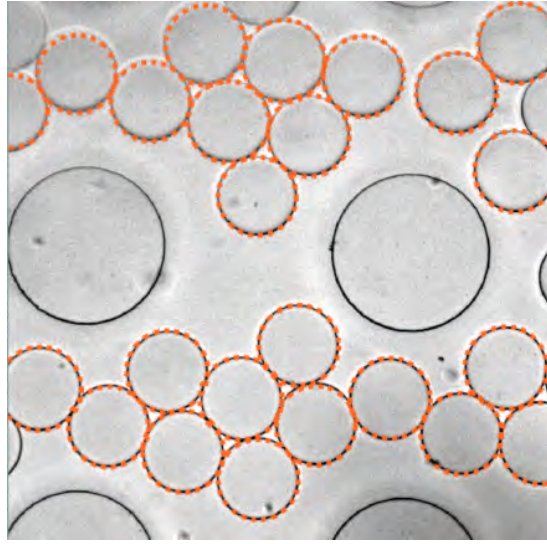


**Figure 2.9** *Image of the droplet boundary detection for one FoV using the Circle Finder application, a UI for the ‘imfindcircles’ Matlab function. 24 droplets are detected (outlined in dashed orange). We see the droplets are much smaller than the reservoir supports, allowing them to be easily distinguished. The range of radius values were selected to be 65–85 pixels, the edge threshold was 0.06 and the sensitivity was 0.95.*

each detected edge point is calculated, and the common intersection point is used to find the centre of the circle. A radius histogram of the distances from this centre point to the detected edge points is used to identify the most probable radius [112].

The radius range, edge threshold and sensitivity are manual parameters for the droplet detection algorithm. The radius range indicates the range of acceptable droplet radii (in pixels). The upper limit of the range must be smaller than 140 pixels to avoid detecting the microfluidic channel supports (see Figure 2.9). The edge gradient threshold sets the gradient threshold for determining edge pixels in the image, it is a scalar value in the range 0–1. More circular objects are detected as we lower the threshold value. The sensitivity factor is the sensitivity for the circular Hough transform accumulator array, it is also a scalar value in the range 0–1. More circular objects are detected with a higher sensitivity factor, however higher sensitivity values also increase the risk of false detection. The Matlab code ‘imfindcircles’ does not find circles with centers outside the domain of the image, which helped reduce the number of partial boundary droplets detected in the analysis.

## Outside bounds

A boundary check was used to remove objects that appear to be partial droplets. This is particularly important when using the FoV analysis with no stitching, as there are more boundaries per experiment. Droplets detected outside the perimeter of the image (the FoV or stitched array) were removed. Figure 2.9 shows 4 detected droplets which would be removed from the dataset. Overall this reduces uncertainty in the analysis as droplets on the boundary are more likely to be tracked incorrectly and could be counted twice if split across two FoV. This also avoids imprecise or fluctuating bacteria counts, as bacteria can swim in and out of the part of the droplet which is imaged.

### 2.3.3 Bacteria detection

Individual bacteria were detected by first thresholding the fluorescence microscopy images. Groups of pixels in these binary images were then labelled as objects, and counted as bacteria. The optimisation of these two steps are described below. The aim was to get as accurate a count as possible, using automated methods, to create large datasets with thousands of droplet populations. There will always be some uncertainty in this process; even counting manually has an associated error (it is easy to miss a bacterial cell at the edge of a droplet, and it is sometimes difficult to distinguish cells due to aggregation etc.).

#### Thresholding

Thresholding is a type of image segmentation, where we binarize the pixel intensities of an image to make the image easier to analyse. After thresholding the fluorescence images, each group of bright pixels is counted as an individual bacterial cell. This removes the need for sophisticated background subtraction. The original image analysis process used a single absolute threshold value for the entire stitched dataset, which was optimised by minimising the difference between a manually counted sample and the output of the algorithmic count [96, 99].

In my research, I investigated instead the use of adaptive thresholding, including Otsu's method and integral image thresholding. In Otsu's method, the grey-level histogram of a greyscale image is normalized and regarded as a probability



distribution. For a 16-bit greyscale image there are 65,536 levels of grey. Otsu’s method aims to separate the histogram of grey-scale values into two classes, in the optimum way. The algorithm searches for the threshold that minimizes the intra-class variance, defined as a weighted sum of variances of the two classes [113]. Unfortunately, when used on the raw fluorescent images, the result is biased towards very bright fluorescent dust and anomalies, which make the threshold not sensitive enough to the bacteria. This was especially the case with stitched images (containing multiple FoV), where in almost all cases, the accuracy of the counts was found to be lower than using an absolute threshold.

Integral image thresholding is a form of thresholding that takes into account spatial variations in illumination. Here, a different threshold value is computed for each pixel in the image. The Matlab function ‘`adaptthresh`’ computes a locally adaptive threshold that can be used with the ‘`imbinarize`’ function to convert an intensity image (the raw fluorescent array) into a binary image. The result is a matrix the same size as the image array containing normalized intensity values in the range 0–1. The threshold is based on the local mean intensity (using first-order statistics) in the neighborhood of each pixel [114]. This technique for thresholding makes the assumption that the image contains primarily background pixels and that the foreground pixels are distributed spatially across the image. This makes the individual FoV images from the droplet experiments a particularly good candidate for this type of thresholding. The integral image thresholding allows for variation in bacterial brightness and in background lighting across the device—particularly as each FoV is binarised individually—where an absolute threshold does not.

A manually selected sensitivity value determines which pixels get thresholded as foreground pixels, specified as a number in the range 0–1. High sensitivity values reduce the contrast needed to threshold a pixel as foreground, at the risk of including some background pixels. The range of sensitivity values (from 0–1) used to analyse the experiments in this thesis was 0.44–0.501. This relatively small range of sensitivity values indicates that the algorithm is appropriate for our experiments, since the optimal parameter is similar across different experimental runs.

In both the adaptive and absolute thresholding methods, a sensitivity or threshold value was selected for each experiment by comparing a sample of manually counted droplet populations to a range of algorithmic counts. This sample was taken from 2–4 different timesteps in a minimum of 4 different FoV. The method

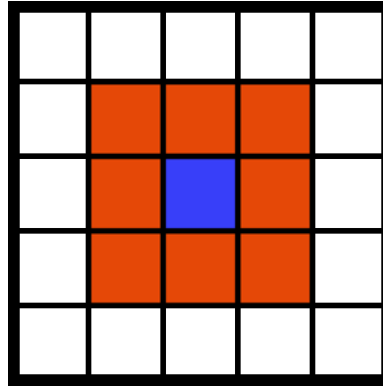


**Figure 2.10** *Schematic showing the 8-connected pixels (highlighted in orange) to a central (blue) pixel. Pixels are considered connected if their edges or corners touch.*

of least squares was then used to select the optimum sensitivity value.

In future work, there are other methods which could be explored to improve the bacterial image analysis. Watershed transformations could be used to eliminate the effect of bacterial clumps by segmenting the images of the cells. Machine learning or basic object detection could be used to replicate the manual identification of fluorescent objects as bacteria. Movement of the living bacteria between frames could be used as a check to distinguish between fluorescent artefacts and live bacterial cells.

### **Bacteria as objects**

Once the images had been thresholded, bacteria were detected as connected-pixel objects in the binarised image. Two adjoining pixels are considered part of the same object if they are connected along the horizontal, vertical, or diagonal direction. Figure 2.10 shows the 8-connected pixels in orange. The minimum number of pixels that were counted as a bacteria object is the final manual parameter to be optimised. For my experiments with *E. coli* using a 20 $\times$  objective, this was mostly set at 2 pixels, or 3 if the images were particularly noisy. The optimality of this parameter was checked using the same least squares method used for the threshold sensitivity value (and should be checked in combination with the threshold value); by minimizing the sum of the difference between the algorithmic and manual counts from a set of sample of images.

### 2.3.4 Tracking droplets and counting bacteria

Once all the parameters were optimised (as discussed above), each FoV (or stitched section) was passed in turn through the circle-finding, tracking and bacterial counting codes in Matlab. The array of brightfield images for all timesteps were input into the ‘`imfindcircles`’ function, along with the manually optimised sensitivity, threshold edge and radius range values. This function detects circles using a Hough Transform and stores their respective positions and size. The output of this is an array of circle (droplet) centres in (x, y) co-ordinates, with the corresponding timestep and radii (see Section 5.2.2 of Daniel Taylor’s thesis [99]).

This array was then input into ‘`track.m`’ [115], a Matlab tracking code which constructs trajectories from a scrambled list of particle coordinates determined at discrete times. An estimate of the maximum distance that a droplet can move in a single time interval (movement of droplets between frames) is set at 75 pixels for all the analysis presented in this thesis. The output gave a list containing the original data rows with an additional column containing a unique ID number corresponding to each identified droplet trajectory; (x, y, t, ID, radius).

The corresponding fluorescence images were then thresholded (see 2.3.3). We were now able to count the bacteria within the detected droplets by using the position and radius of the droplet to create a mask area. The Matlab function ‘`bwlabel`’ returns a label matrix that contains labels for the 8-connected objects found in the masked binarised image [116]. A Matlab script then counted number of labelled 8-connected objects (the bacteria) for each droplet.

This resulted in an array of droplet coordinates and radii, with a corresponding bacterial count at each timestep, for every droplet in the FoV; (x, y, t, ID, radius, count). Every droplet was represented by an individual row for each timestep. The final data array was contained in a Matlab structure which has a field corresponding to each FoV.

This structure could then be manipulated for graphical interpretation or data analysis. For example, it was converted into an array of bacteria counts over time, as shown in Figure 2.11, to plot growth curves for each droplet.

	FOV	FOV	FOV	...
	ID	ID	ID	...
T0				
T1				
T2				
T3				
T4				
...				

**Figure 2.11** *The structure of an output array, with the FoV number and droplet ID number labelled on row 1 and 2 for every column. This allows easy comparison of the data and the original images. Each column displays the bacterial count for an individual droplet, where each row is a different timestep (T0, T1, T2,...).*

## 2.4 Image analysis of bacterial cell size

A parallel image analysis protocol was developed to quantify the size of bacterial cells in each droplet in addition to the number of cells. This is particularly relevant for the ampicillin experiments presented in Chapter 6, where we observe filamentous growth.

Our main image analysis method involves counting a group of pixels as an object, and each object as a bacterial cell. We set a minimal bacterial size of 2–3 pixels in order to remove noise, but we do not set a maximal size. Therefore, larger groups of pixels can be used to identify phenomena like aggregation (where multiple bacteria are counted as a single object) or filamenting (where a given bacterial cell has a larger pixel area than normal).

Figure 2.12 shows the distribution of the object (bacteria) sizes, in pixels, for a dataset of uninhibited bacteria. The peak size in the distribution occurs at 9 pixels and the vast majority of the detected objects are smaller than 100 pixels. The ratio of pixels to  $\mu\text{m}$  in 1D is  $0.68 \mu\text{m}/\text{px}$  (see Section 2.6), and therefore each pixel represents an area of  $0.46 \mu\text{m}^2$ . The modal object area is therefore  $9 \times 0.46 = 4.2 \mu\text{m}^2$ , which we attribute to the projected area of a single bacterium in uninhibited conditions.

### 2.4.1 Filamentation

Filamentous cells are found in many populations of *E. coli*, particularly in stationary phase or when the population is exposed to stress [48–50], see Section 1.3.1 for background. In microfluidic mother machine experiments, Wang et al.

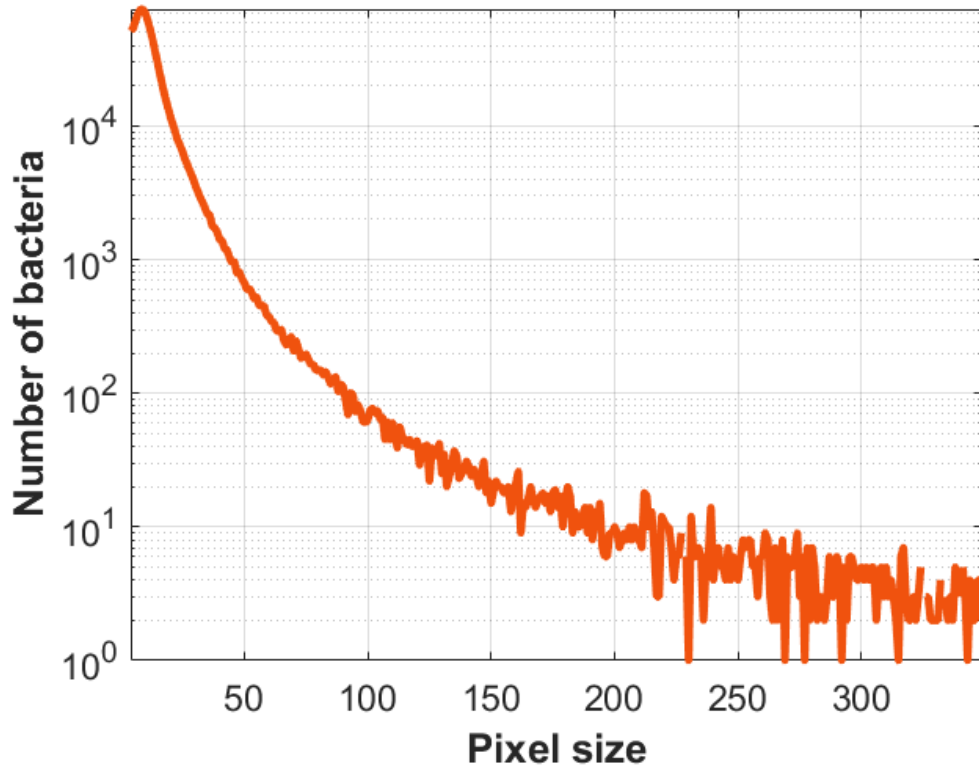


**Figure 2.12** *Distribution of bacterial cell size (in pixels). A sample of 870464 bacterial cells taken from experiment A(0), from droplet images throughout the experiment (33 timesteps, corresponding to a cumulative time of 5.5 hours). The frequency is plotted on a log scale to show the full range of the data.*

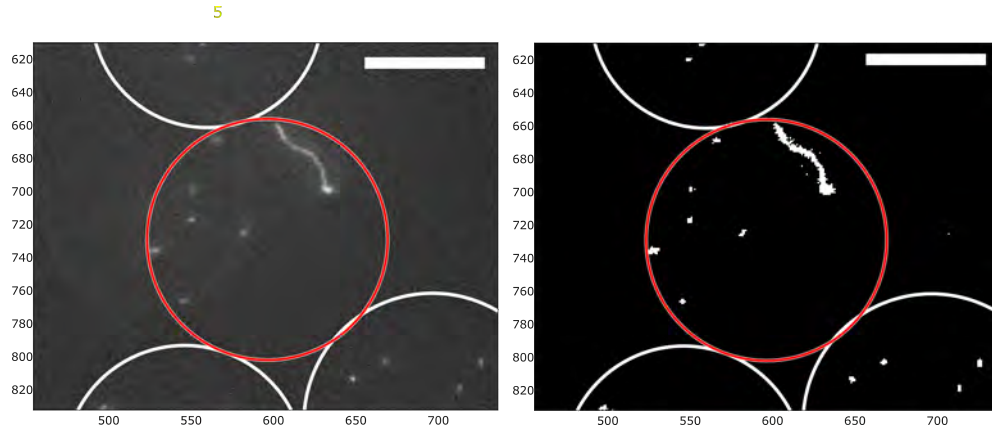


**Figure 2.13** *Filamentation of a bacterial cell in a droplet after 3.3 hr of uninhibited growth. The red circle shows the droplet boundary. The raw CFP image is shown on the left, and the thresholded image is shown on the right. We can see that the filamentous cell is one mass of connected pixels, and therefore counted as one cell in the thresholded image. This droplet image is from zero-antibiotic experiment A(0). Scale bars show 50  $\mu\text{m}$ .*

found that the rate of filamentation significantly increased as bacteria aged for more than 50 generations [33]. As the growth rates in our droplet experiments were slow (see Table 3.2) and the bacteria are only observed for up to 6.5 hours, we do not reach this threshold and therefore we see relatively few filamentous cells in the uninhibited droplet experiments. However, filamentous cells were common in our experiments when low concentrations of ampicillin are added (see Section 6.3.5).

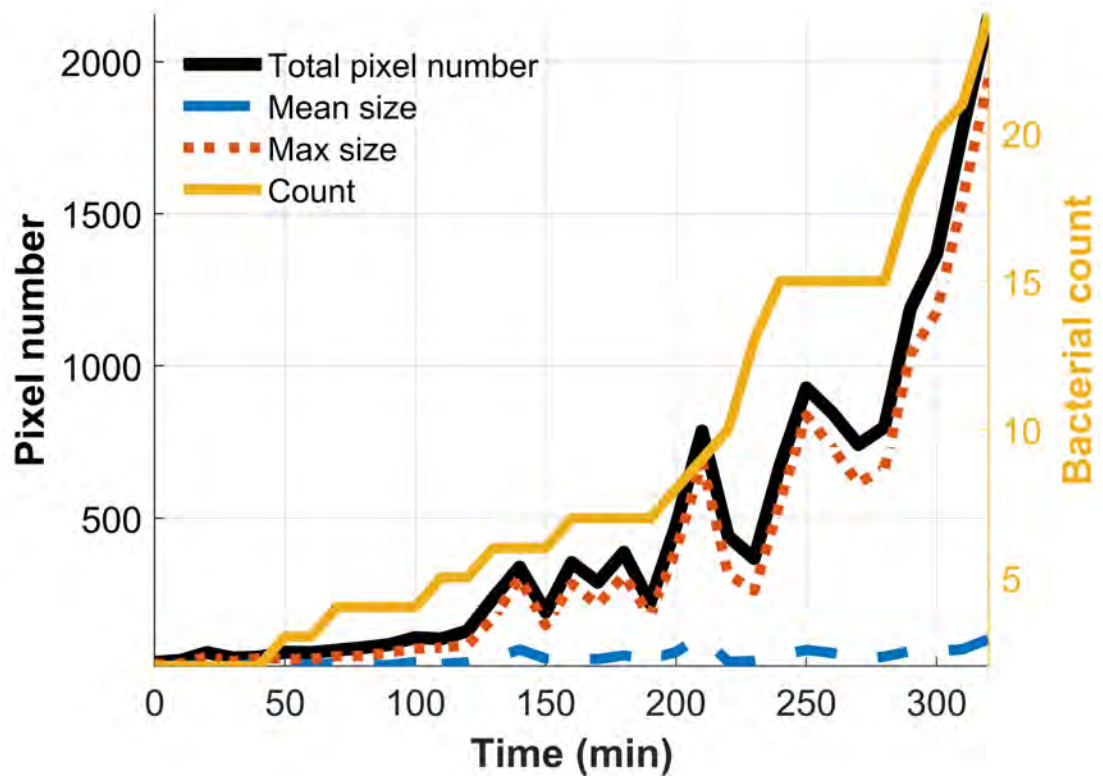
Individual cells of *E. coli* are rod-shaped and are approximately  $0.8\ \mu\text{m}$  wide (corresponding to 1–2 px) and  $2.5\ \mu\text{m}$  long (corresponding to 4–5 px), which is consistent with our observation of a modal projected area of 9 px [117]. Filaments are observed in the droplet experiments with a pixel size ranging from 55–1000 pixels. The number of pixels which represent a single bacterium depends on the length of the cell, the orientation in 3D, overlapping or clustering of bacteria, the focus of the image (blurring can make the bacteria appear bigger) and threshold value. Fluctuations of these factors between successive timesteps can cause transient drops in the pixel number associated with a given cell, which do not represent an actual fluctuation in filament length (for example, the maximal size shown in Figure 2.14).

Figure 2.13 shows a filamentous cell in a droplet which also includes many non-filamentous cells. For simplicity, a lower cut-off of 70 pixels was used to sort the data into filamentous cells and non-filamentous cells. A 70-pixel bacterial cell covers an area of  $32\ \mu\text{m}^2$ .

Figure 2.14 displays the image analysis output for the droplet shown in Figure 2.13, of bacterial count, the summed size (in pixels) and the maximal size of all detected objects. For this filament-containing droplet (shown in Figure 2.13), the maximum bacterial size follows the same trend as the count and the total pixel sum. The maximum cell size is almost as many pixels as the combined pixel size of all the bacteria, because the filamentous cell is far larger than the other non-filamentous cells (which we can infer from the low mean size).

## 2.4.2 Aggregation

Aggregation between bacteria of the same type (autoaggregation or flocculation) is a common phenomenon for many types of bacteria. Autoaggregation is also often among the first steps in forming biofilms and suspended bacterial aggregates



**Figure 2.14** *Example plot for a droplet containing a filamentous cell (a droplet from uninhibited experiment A(0)). The LH axis shows the total sum, the mean and the maximum bacterial pixel size within the droplet over the course of the experiment. The RH y-axis shows the bacterial count (yellow). The total pixel sum, maximum cell size and bacteria count all increase at a similar rate throughout the experiment. An image of the droplet is shown in Figure 2.13.*

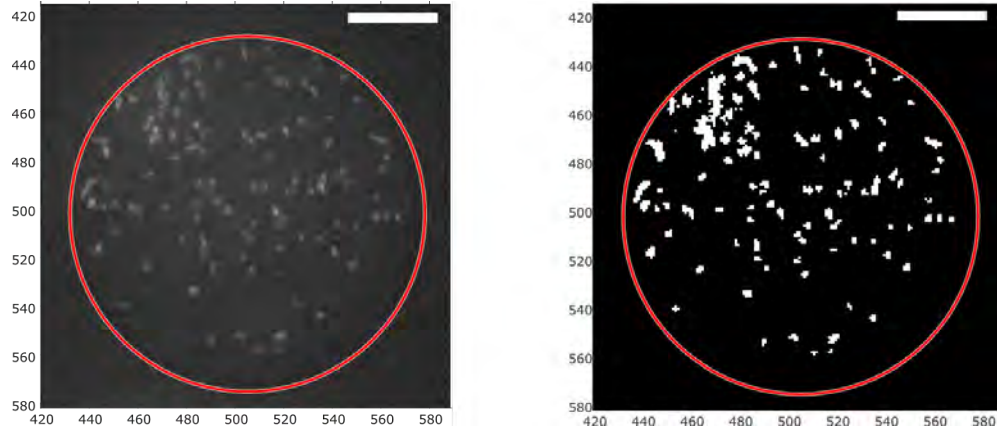


**Figure 2.15** *Image of a droplet after 5 hr of growth, showing overcrowding or aggregation of bacteria. The red circle shows the droplet boundary. The image on the left shows the raw CFP image, and the image on the right shows the binary thresholded image. The algorithmic count found a bacteria number of 78. This droplet image is from zero-antibiotic experiment  $A(0)$ . Scale bars show 25  $\mu\text{m}$ .*

can offer protection from environmental stresses whilst maintaining mobility [118]. In droplets, aggregation (a biological or chemical phenomenon) or over-crowding (the breakdown of the image segmentation and analysis at high densities), both mean that particularly at later times, the count can fluctuate [96]. Figure 2.15 shows a fluorescence image of a droplet containing bacteria after 5 hours of growth. We can see that in the thresholded image, some of these bacteria are grouped as one object where they will be counted by the algorithm as one (large) cell. Figure 2.16 illustrates the effect of this on the image analysis output by plotting the bacterial count, the summed size (in pixels) and the maximal size of all detected objects, for a droplet population in an experiment without antibiotic. In particular, we can see that the maximal object size is sometimes very large due to bacterial aggregation, and fluctuates significantly as bacteria swim in and out of proximity to each other, in contrast to the maximal object size given by the red dashed line in Figure 2.14, which can be attributed to a filamentous bacterium. The mean size remains constant throughout the experiment, indicating that the individual bacterial size is not increasing. This analysis of object sizes as well as bacterial counts could allow us to identify filamentation or aggregation without manually looking at every image. Note that this identification process is not utilised for the filamentation analysis presented in Chapter 6 (Section 6.3.5) because we do not observe aggregation or high bacterial densities in droplets containing antibiotic. We therefore simply treat high-pixel-number cells as filamentous.



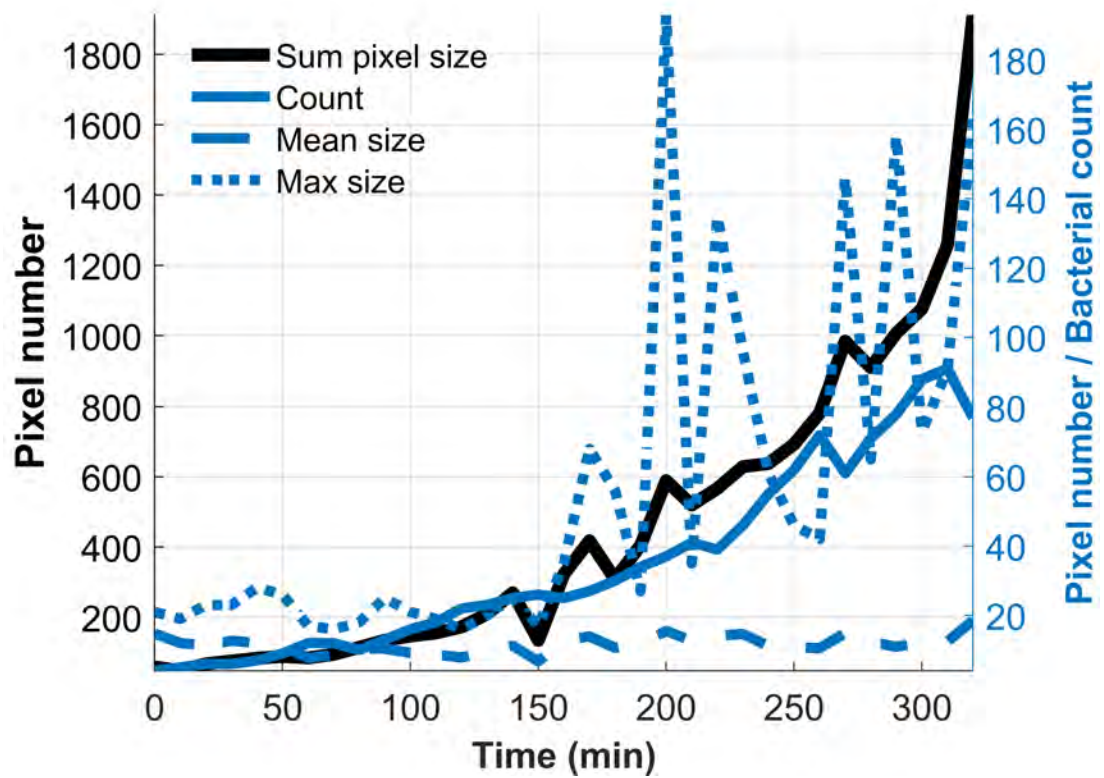


**Figure 2.16** *A plot of a single droplet population throughout the experiment  $A(0)$ . The sum of the thresholded pixels is shown in black on the LH axis, and grows in a comparable curve to the count, shown in blue on the RH axis. The average size of each bacterial cell (RH axis) is consistent throughout, whereas the maximum size (RH axis) fluctuates as the bacteria move and aggregate. Fluorescence image of the droplet is shown in Figure 2.15.*

## 2.5 Validation of the methodology

As part of my PhD research, I developed several different procedures to ensure both the image analysis and device were performing as expected.

### 2.5.1 Checking for errors in the bacterial count

In every experiment, the output data was checked for count accuracy. A minimum of 5% of droplets in each dataset were checked, and these were selected to represent the entire spatial and temporal range of the experiment.

A Matlab script was used to find columns in the dataset with unexpectedly high counts (using a cut-off value). If a systematic error was seen, this was corrected and the whole detection and counting code was run again on the raw images. For example, sometimes it was necessary to have different threshold parameters for different time periods, which may not have been identified in the initial optimisation. Other obvious outliers (such as rapidly changing counts) were manually identified and either corrected or deleted.

Counting errors can be caused by many different factors; several bacteria in close proximity can be counted as one; a dim bacterial cell can be missed by a high threshold value; the droplet boundaries can be misaligned; or fluorescent dust can be incorrectly counted as a cell. I performed an extensive analysis of the origin of counting errors for a sample dataset for *E. coli* grown in the original microfluidic device. The results are presented in [96].

For selected datasets presented in this thesis, I compared the algorithmic count to a manual count. I observe a 2% error in the bacterial count per droplet in a 45 droplet sample from experiment A(10), and a 3.5% error in a sample of 81 droplets from experiment A(0). None of these errors were caused by droplet fitting issues, suggesting that the analysis with individual fields of view and the removal of boundary-crossing droplets improves accuracy (for a stitched dataset 6% of errors were caused by droplet detection issues [96]).

In general, the percentage error is higher for lower bacterial counts, since a miscount of one cell represents a large deviation from an actual population of zero, one or two bacteria. This is sometimes hard to spot, and is more important in droplet experiments with antibiotic, where number of bacteria is low. To

increase the accuracy of the death dynamics we report, a droplet population is defined to have died if the bacterial count is equal to zero for two consecutive timesteps.

### **2.5.2 Comparing bacterial counting to integrated droplet fluorescence**

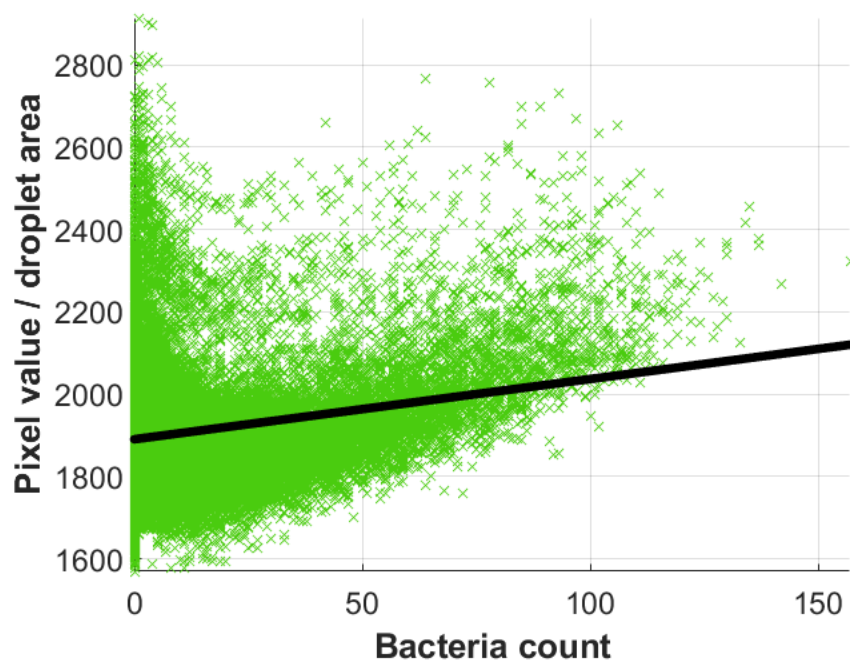
In previous droplet studies [66, 80, 81, 94, 95, 119], growth trajectories of bacteria in droplets were measured using the integrated fluorescence intensity of the droplet as a proxy for bacterial number. Therefore I compared the results of our automatic bacterial counting algorithm to measurements of integrated droplet fluorescence, as well as analysing the variation in fluorescence levels among individual bacteria.

Figure 2.17 shows a comparison of bacterial counts measured using our algorithmic method, to total droplet fluorescence values. A similar analysis is shown in Figure 3b in [96]. To evaluate total fluorescence, pixel values are summed over an entire droplet and this sum was normalised by the droplet area to control for background fluorescence, which scales with area. There is a weak correlation between droplet count and integrated fluorescence, with significant noise.

Our image analysis process results in counts of bacteria by using thresholding and counting each group of binarised pixels as a cell (as described in Section 2.3.3). This avoids the noise which occurs when quantifying intensity or integrating fluorescence output [120] and the pitfalls associated with binning and proxy methods.

#### **Pixel intensity for objects identified as bacteria**

The noisy total droplet fluorescence data in Figure 2.17 is potentially caused by the different fluorescence levels of individual bacteria, due to intrinsic variation in the expression of fluorescence genes. There may also be artefacts associated with imaging, e.g. due to differing depths within a droplet. Figure 2.18 shows distributions of the fluorescence of individual bacterial cells. To obtain this data, the bacteria in the raw fluorescent images were segregated using a mask of the thresholded sections. These masked sections were then labelled as objects, as in the standard counting protocol (described in Section 2.3.3). However, instead



**Figure 2.17** *Plot of integrated droplet fluorescence, normalised by droplet area, against our algorithmic bacteria count. The data points represent 1245 droplet populations tracked over the entire experimental run (therefore different data points can represent images taken at different timesteps). The Pearson correlation coefficient is 0.21 (with a  $p$ -value  $< 0.001$ ). The best fit line is shown in black; with equation  $y = 1.46x + 1890$ .*

of each group of thresholded pixels being counted as one bacterial cell, the thresholded section was used as a mask to identify the corresponding pixel values in the raw images. This produced a summed fluorescence value for every bacterial cell in every droplet. These values are plotted as a histogram in Figure 2.18 (a). There was a wide range of summed fluorescence pixel values, and some of this variation is due to the range of bacterial sizes.

In panel (b) of Figure 2.18, the fluorescence values are normalised with respect to the size of the bacterial objects, giving an average fluorescence value per pixel for each identified bacterium. When compared to the background, we see that the pixels in objects identified as bacteria have a generally higher fluorescence value and show more variation. The fact that some bacterial pixels are lower in fluorescence than the background arises from the adaptive thresholding method (see Section 2.3.3). The fact that the fluorescence varies between individual bacteria justifies our use of discrete bacterial counting rather than integrated fluorescence, as in previous studies.

### 2.5.3 Analysis of droplet loading statistics

When bacteria are initially loaded into the droplets, we expect the numbers of bacteria per droplet to follow a Poisson distribution. This is because at the flow-focusing junction, the encapsulation of each bacterium into a droplet is an independent random event. The concentration of the bacterial culture controls the mean number of bacteria per droplet (the control parameter of the Poisson distribution, which we call  $\lambda$ ), see Section 1.4.2. Checking whether encapsulation numbers follow the expected Poisson distribution is a common validation method for encapsulation studies [88, 95]. I therefore investigated the distribution of initial bacterial numbers per droplet to check whether the image analysis and the Y-junction method of introducing antibiotic (see Section 2.2.6) was operating correctly. Poisson statistics can also confirm that the delay between droplet generation and is droplet imaging is negligible.

Figure 2.19 shows the relationship between the mean and the variance of the initial bacterial numbers for the experiments performed in the absence of antibiotic (see Chapter 3). For a theoretical Poisson distribution, these should be equal (indicated by the dotted red line). For our datasets, we find that the variance is greater than the mean, suggesting that there is another factor at play.

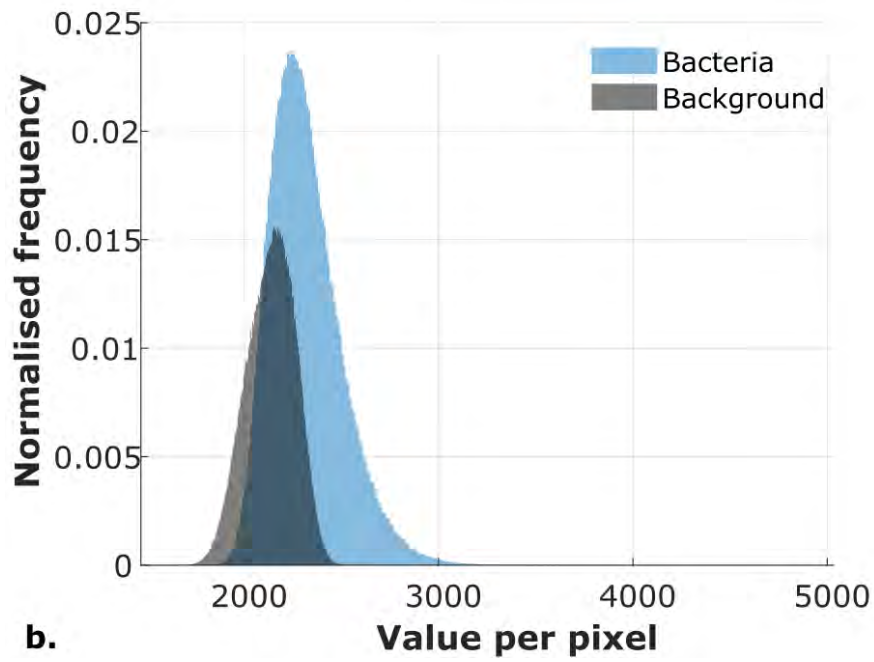
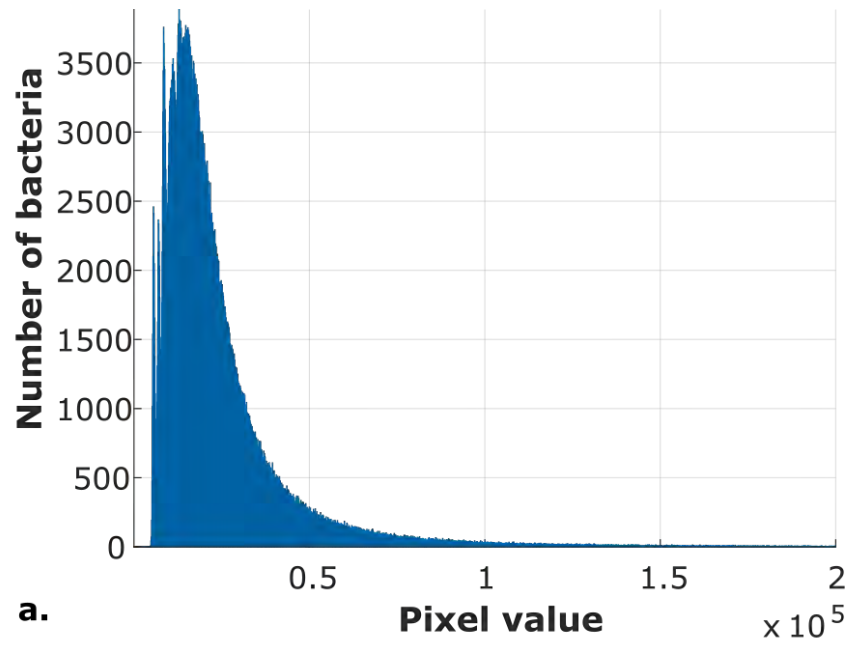


**Figure 2.18** *Histograms of pixel values for individual bacterial cells. (a) Distribution of the pixel values of bacteria taken from the raw TIFF fluorescence images. This is a sample of 808488 bacteria across all 33 timesteps from  $\approx 1500$  droplets in 166 different FoV. (b) Distribution of pixel values normalised by the pixel size of each bacterial cell. This sample contains 546661 bacteria, detected over all timesteps. The background is taken from empty droplets and the surrounding areas from 3 separate FoV (a sample of  $5.4 \times 10^5$  pixels). This data is a subsection of experiment A(0) (see Table 3.1).*

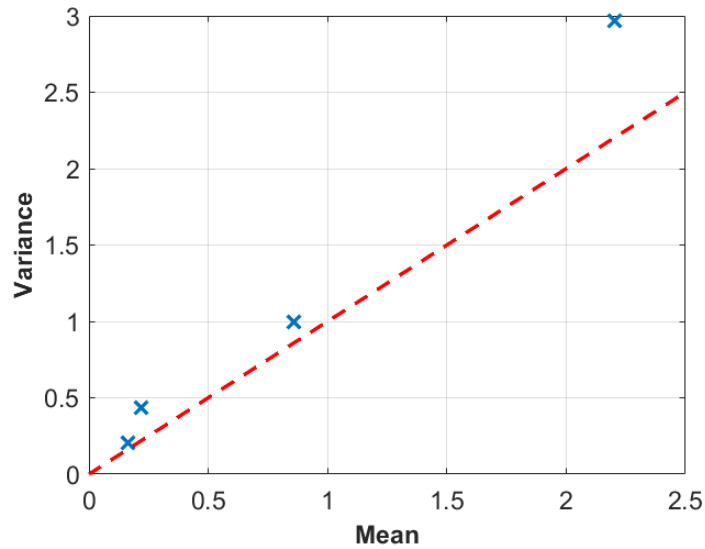


**Figure 2.19** *Plot of mean vs. variance of the initial bacteria distributions for experiments with no antibiotic. For a Poisson distribution the mean and the variance should be equal; the dotted red line shows the expected 1:1 trend.*

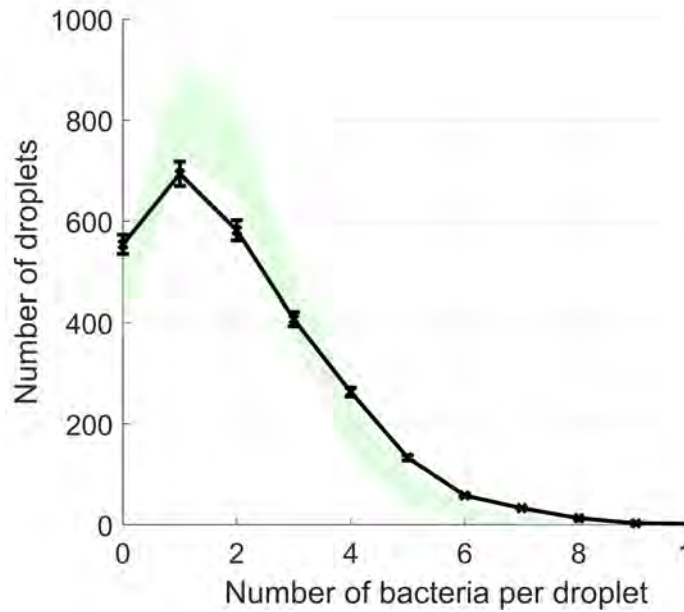


**Figure 2.20** *The initial bacterial counts of uninhibited growth experiment A(0), which had 2743 tracked droplets, shown in black. The shaded green area is the range of 10,000 repeated samples of Poisson distributions (of size 2743) computationally generated with a fitted  $\lambda$  value of 1.79 (see Table 2.1). This method was chosen to include the variation caused by drawing from a finite sample size. Error bars show a 3.5% uncertainty in the experimental bacterial counts.*

To see whether our data was produced by a Poisson process we compared the distribution of initial bacterial numbers to Poisson distributed values. The  $\lambda$  parameter is found using a Matlab script which iteratively compares the least squares difference between the initial distribution of the data and generated Poisson distributions for a range of  $\lambda$  values. Table 2.1 shows the fitted parameter values.

Figure 2.20 shows the range of computer-generated Poisson values compared to the experimental data. The uncertainty in the bacterial count (see Section 2.5.1), is displayed as 3.5% error bars on the number of droplets containing each count of bacteria. Although visually the Poisson fit is quite good for droplet populations of 0, 1 and 3, the measured frequency of more populated droplets (5–9 bacteria) is higher than the Poisson fitted range.

A Pearson’s chi-squared test was used to establish the goodness-of-fit, using a custom R script developed by Alexander et al. [23]. Deviation from a Poisson distribution was determined at a 5% significance level, with degrees of freedom equal to the number of categories (defined here as subsets containing at least five droplets) reduced by two. According to the goodness-of-fit test, the experimental data showed significant deviation from a Poisson distribution when compared to expected distributions with both a  $\lambda$  value equal to the mean ( $\lambda=2.02$ ,  $\chi^2_7 = 312$ ,  $p < 1 \times 10^{-10}$ ) and the fitted value ( $\lambda=1.79$ ,  $\chi^2_7 = 590$ ,  $p < 1 \times 10^{-10}$ ). Thus we reject the null hypothesis that this data represents a Poisson distribution. We discuss in the next section how this deviation can be accounted for by considering bacterial growth.

### **Poisson distributions with growth**

In our experiments, the first measurement of bacterial counts is taken 3–37 minutes after encapsulation into droplets (see Table 3.1). Therefore the bacteria have some time to proliferate after they are encapsulated and before the first image is taken. We therefore tested whether a model which includes growth after Poisson encapsulation could explain our initial count data.

To do this, I used a simulation approach. In the simulation, an initial bacterial number is chosen for each droplet from a Poisson distribution, then exponential growth of that population is simulated using the experimentally determined growth rate. Growth was simulated in discrete timesteps using a tau-leaping



Experiment	OD (600 nm)	Y	Total droplets	NZ droplets	Mean	Fitted $\lambda$
A(0)	0.1034	y	2743	2189	2.02	1.79
B(0)	0.0573	n	1524	201	0.164	0.14
C(0)	0.0667	n	385	45	0.218	0.09
D(0)	0.0362	n	592	484	3.33	N/A*
E(0)	0.0315	y	626	626	0.860	0.81

**Table 2.1** *Initial parameters for the zero antibiotic experiments, presented in Chapter 3. The (post) OD value of the bulk bacterial suspension is given. The Y column indicates whether a Y-junction was used for the introduction of bacteria (y, yes or n, no). The NZ (non-zero) droplets indicates the number of droplets containing bacteria. The mean is the calculated mean number of initial bacteria per droplet (calculated over all analysed droplets). Fitted  $\lambda$  values were tested in increments of 0.01, by comparing 100 computer-generated Poisson samples, the size of the corresponding droplet number, to the experimental distribution. \*Experiment D(0) is omitted from the fitting as the image analysis was started at 50 minutes, and so the populations of bacteria are no longer Poisson distributed.*

method to account for the stochastic nature of growth. The output parameters of this model are the best fitting Poisson parameter  $\lambda$  and the time of growth (or delay).

Minimisation of the residual sum of squares (RSS) (the difference between the experimental frequency and the simulated value) was used to find the optimal  $\lambda$  value and growth time. Figure 2.21 shows the dependence of the RSS and therefore the fit quality of  $\lambda$  for different growth times. The minima of these curves shifts left as the growth time increases, as would be expected. For longer growth times (50 and 60 min) we see the minima are at higher values than the non-grown fits. Whereas for shorter amounts of simulated growth (5–25 min), the minima values are lower than for the non-grown fits.

Figure 2.22 shows an example of the resulting distributions of the fits compared to the experimental bacterial counts, with (in purple) and without (in green) growth. This plot shows that Poisson loading plus exponential growth appears to explain the data better than the Poisson distribution alone; see, for example, the data for droplets containing 2 bacteria. When we account for 15 minutes of exponential growth in the model, we are able to fit the entire dataset. This is a reasonable growth time, as the actual experimental delay between droplet loading and imaging for this dataset was between 21–31 minutes (see Table 3.1).

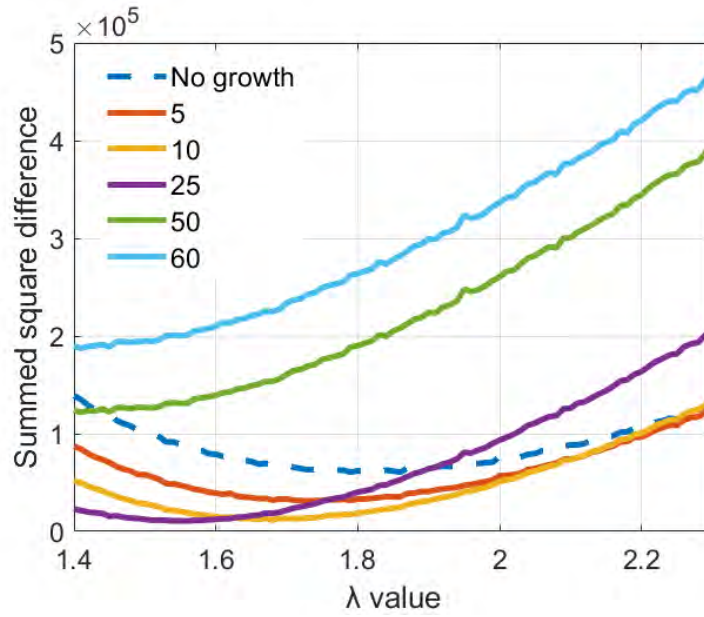


**Figure 2.21** *Minimising curves of the residual sum of squares between generated Poisson distributions and the initial population numbers. The x-axis shows the tested  $\lambda$  value. The dotted line shows the fit without growth, the coloured lines show the fit for various growth times, in minutes. Growth was simulated in discrete 5 minute intervals.*

### Characterising the impact of the imaging delay

The delay between the droplet generation and droplet imaging is important. If this gap is too long, then bacteria could start to grow or die in the droplets before the first images are taken, and they would be characterised with an incorrect initial population number. This would obscure inferences we could make about our results. The delay for each experiment is given in Table 6.1. These values are calculated as the difference between the time the tubing is cut (when droplets stop being produced) and the start of the scan. A range of 10 minutes is given to account for the range of travelling times for droplets in different areas of the reservoir, as well as the difference between the start and end position of the scan.

We can use the initial distribution of bacteria to verify that we are capturing the important early death dynamics. Figure 2.23 shows the bacterial count per droplet for the first timestep of experiment A(10), with an overlay of randomly generated Poisson distributions (as in Figure 2.20), using the mean bacterial number per droplet as the  $\lambda$  value.

According to a Pearson's chi-squared goodness-of-fit test (implemented identically

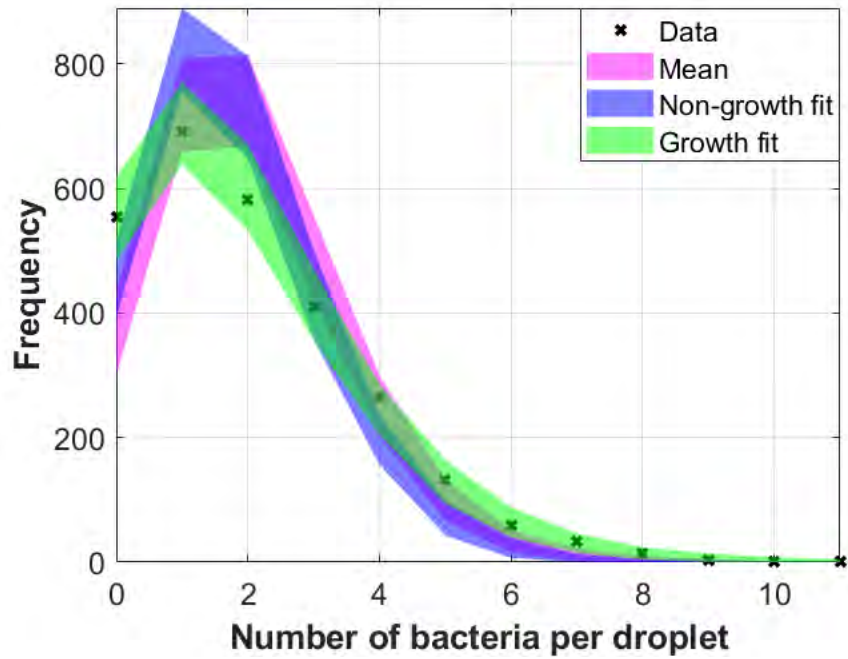


**Figure 2.22** *This plot shows the initial bacterial count (data) for experiment  $A(0)$ , in crosses. Poisson-distributed samples were generated in Matlab, with a size corresponding to the number of droplets in the dataset (here, 2743). This was repeated 100 times to calculate the ranges shown. The  $\lambda$  values used were; the calculated mean of the data, 2.02 (magenta); the best fitted  $\lambda$  value, 1.79 (blue); and the best fitted with growth  $\lambda$ , 1.62, with 15 minutes of simulated growth (green).*

as for the dataset  $A(0)$ , described above), the deviation from a Poisson distribution is not significant ( $\lambda=0.496$ ,  $\chi^2_2 = 1.33$ ,  $p = 0.515$ ) and thus we do not reject the null hypothesis that the data was drawn from a Poisson distribution. This gives us confidence that the death rate isn't so high such that we miss the early dynamics. For this experiment, the time delay between the droplet generation (i.e. the Poisson distribution) and the first measurement was 16–26 minutes.

As well as showing that this order of time delay is negligible for our experiments, the good fit for a Poisson distribution also indicates the Y-junction methodology is working as expected (the mean number of bacteria reaching the junction is constant).

Furthermore, we can compare Figure 2.23, which shows a dataset of bacterial populations under antibiotic stress, where we do not see bacterial proliferation, to Figures 2.20 and 2.22, which show a dataset of uninhibited bacterial growth. We see a good fit to Poisson statistics for the droplet populations with suppressed growth, whereas the datasets for bacteria with uninhibited growth do not show a good fit without growth in the model. This supports our hypothesis that the bacterial proliferation is the underlying cause of the deviation from a Poisson distribution.

## 2.6 Concentration of bacteria within the droplets

The small volumes we use to encapsulate the bacteria result in a high inoculum concentration even when there is only one cell. Picolitre-volume droplets containing a small number of bacteria have similar (or higher) concentrations of bacteria per mL to the concentrations used in traditional bulk microbiology experiments (see Figure A.5). This is useful to calculate for comparisons between the two.

The average droplet radius in the reservoir is  $81 \pm 6.5$  pixels (calculated using the mean droplet size of 3 different experiments presented in Chapter 6). Pixel to  $\mu\text{m}$  ratio was calculated using the known diameter of the device supports (which are  $200 \mu\text{m}$ ) as  $0.68 \mu\text{m}/\text{px}$ . This means the average droplet (reservoir) radius is  $55 \pm 4.4 \mu\text{m}$ . For some experiments with polydisperse droplets, this range will be far greater. For the experiments in this thesis, we analyse a maximum droplet

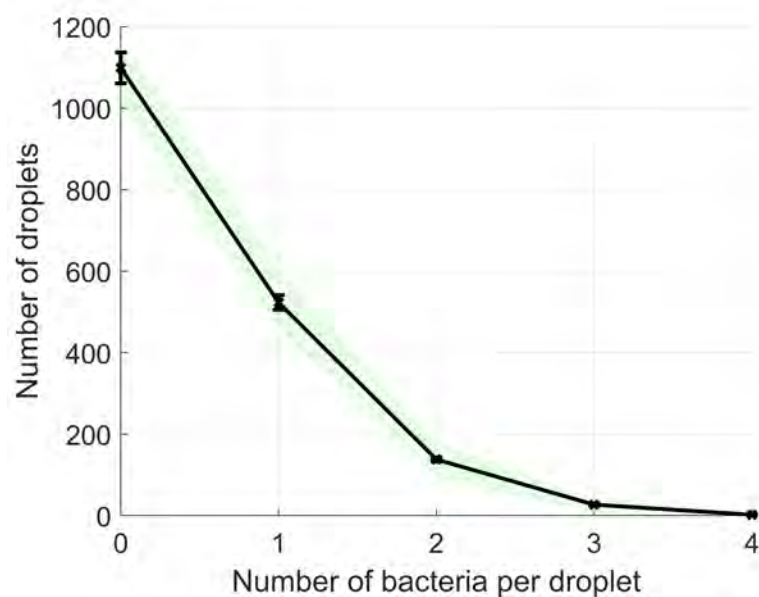


**Figure 2.23** *Initial bacterial counts from experiment A(10) (at  $10 \text{ mg mL}^{-1}$  of ampicillin, the highest concentration tested in droplets), for 1789 droplets, shown in black. The shaded green area shows the range of values generated from 10,000 computer-sampled (size 1789) Poisson distributions using the mean experimental bacterial number (per droplet) as the  $\lambda$  value ( $\lambda = 0.496$ ). This representation was chosen to include the variation caused by drawing from a finite sample size. Here we see a consistent overlap between the Poisson distributions and the experimental data. Error bars show a 3.5% uncertainty of the experimental bacterial counts.*

Number of bacteria	1	2	3	4	10
Concentration (mL <sup>-1</sup> )	$1.1 \times 10^7$	$2.2 \times 10^7$	$3.3 \times 10^7$	$4.4 \times 10^7$	$1.1 \times 10^8$

**Table 2.2** *Bacterial concentrations for a range of population sizes contained in a droplet with a volume of 91 pL ( $9.1 \pm 1.5 \times 10^{-8}$  mL).*

radius range of 60–140 pixels (40.8–95.2  $\mu\text{m}$ ).

Droplets in the reservoir are squashed and therefore are not circular (see schematic in Figure 2.2). We approximate the shape as a cylinder of height,  $h$ , equal to the channel depth, surrounded by half a torus. We can use the second theorem of Pappus to calculate the volume of the half torus shape; the volume of a solid of revolution is the product of the revolution distance ( $2\pi R$ ), and the area of the planar cross section ( $\frac{\pi r^2}{2}$ ). We can therefore calculate the droplet volume as:

$$Volume = \pi r_c^2 h + \frac{1}{4} \pi^2 h^2 r_c.$$

In all the droplet experiments, we use the same microfluidic master mould (see Section 2.2.2), so channel height,  $h$  is fixed at 10  $\mu\text{m}$ . The radius of the cylinder, variable  $r_c$  is determined by subtracting  $\frac{h}{2}$  from the total radius (measured from microscopy images). The average droplet therefore, has an  $r_c$  value of  $55 - 5 = 50 \pm 4$   $\mu\text{m}$ . This gives a volume of  $90877 \pm 14500$   $\mu\text{m}^3$ ,  $91 \pm 15$  pL or  $9.1 \pm 1.5 \times 10^{-8}$  mL per droplet. This is slightly less than the volume of a cylinder with radius 55  $\mu\text{m}$ , and height 10  $\mu\text{m}$ :  $\pi \cdot 55^2 \cdot h = 95033$   $\mu\text{m}^3$ , 95 pL or  $9.5 \times 10^{-8}$  mL, as we would expect.

We can use this volume to calculate the concentration of bacteria in a droplet with a given population number. Table 2.2 shows the concentration of the inoculate for a range of example population numbers. We can see that even with one bacterial cell, the droplet concentration is far higher than the standard inoculum for measuring the MIC.

## 2.7 Summary

This chapter has outlined the experimental method for making microfluidic devices and using these to create and image thousands of picolitre droplets containing bacteria. Section 2.3 described the image analysis procedure used to convert these images into datasets of droplet populations and Section 2.4 describes

how I used the same images to additionally assess the extent of filamentation and aggregation. This data allows us to obtain large numbers of population growth trajectories. Section 2.5 validated the methodology, finding that the bacterial count results were accurate to within an error of 3.5%.

Bacterial population data generated using these methods is presented and further analysed in Chapters 3 and 5. An investigation of filamentation is used in Chapter 6 to fully understand the impact of antibiotic on the growth dynamics of these small populations.

# Chapter 3

## Heterogeneous growth of uninhibited bacteria

### 3.1 Introduction

Intrinsic noise fundamentally limits the precision of the regulation of gene expression. This means that bacterial division and survival include stochastic processes. Stochastic effects in gene expression account for the large amounts of cell-to-cell variation observed in isogenic populations [102]. Heterogeneity can be a beneficial part of many biological processes, and can allow the survival of a genome in times of stress. See Section 1.2.1 for discussion of intrinsic heterogeneity within clonal populations of bacteria and its relevance.

Experimental techniques which take averages of large populations, such as absorbance measurements or counting colonies on an agar plates, can mask distributions and variability in the growth of individual cells; thus obscuring the heterogeneous behaviour of the bacteria. It is known that individual cells systematically deviate from population-level growth laws, and therefore are not represented well by these measurements [95, 121].

Instead, new methods have been developed to study the heterogeneous behaviour of individual microorganisms. Mother machines are a popular microfluidic device used for this purpose. Here the mother cell can, in principal, be studied for an unlimited period of time. This means that a mother cell of *E. coli* can be observed for hundreds of generations [33]. See Section 1.2.3 for a review of methods used



to study small populations.

For the experiments in this thesis, we have chosen to use droplets in order to study the dynamics of small populations of cells that are not subjected to the geometrical constraint imposed by the mother machine. Imaging bacteria growing in multiple replicate droplets can improve our ability to understand and quantify stochastic behavior within small populations. See Section 1.4 for a discussion of the advantages of using droplets.

In this chapter, the results and analysis of four microfluidic droplet experiments are presented. Small populations of bacteria were encapsulated in droplets to study the growth dynamics over many hours. Analysis of this bacterial growth without antibiotic or other environmental stresses shows heterogeneous growth within the inoculating culture, grown from single a colony of *E. coli*. We are able to directly measure the distribution of droplet-population growth rates (Section 3.3.2) and see heterogeneity in the final population sizes of the droplets (Section 3.3.3). We find a significant distribution of droplet-population growth rates; and that the population growth rate of some droplets to be lower than the bulk rate, because the faster growing cells dominate these large-population experiments. We also identify a number of droplet populations which do not grow at all (Section 3.3.5).

We use this data to investigate the possible inheritance of growth rate. If there is a growth rate distribution of fast and slow growing *E. coli* cells at the start of the experiment and this trait is inherited, then we might expect droplets with larger initial populations to have higher overall growth rates (since a droplet starting with more bacteria would have a higher probability of containing a fast-growing cell). However, we find that the droplet-population growth rates do not follow this trend (see Figure 3.5), and this therefore suggests no (or weak) inheritance of growth rate for the strain of *E. coli* tested.

Furthermore, because we can precisely count the number of bacteria in each droplet population (at multiple timesteps), we have large datasets which we can use to compare to theoretical predictions. Here we use an analysis based on the Bellman–Harris model to investigate whether our experimental data fits this framework (Section 3.3.4). This also gives us a way to determine single-cell division time statistics from our population-level measurements.

This analysis helps demonstrate the vast potential of the rich experimental datasets to generate biological insight, particularly alongside the raw images of

the droplet populations obtained from every experimental run.

## 3.2 Method

The experimental and image analysis methodologies are detailed comprehensively in Chapter 2. These are briefly summarised below.

Uninhibited growth experiments were completed with an ampicillin resistant, CFP strain of *E. coli* (RJA003). The data presented below is from four repeat experiments, with different inoculates, completed on different days.

A single colony was taken from an agar plate and grown overnight in 6 mL of M9+gl media. On the day of the experiment, 25  $\mu$ L of this bacterial suspension was further diluted in 10 mL of media and placed in a 37°C incubator for 1.5 hr to ensure that the bacteria were in the exponential growth phase. The optical density (OD) was checked at this stage; the OD (at 600 nm) of the initial bacterial suspensions for the experiments in this chapter range from 0.009–0.023. This suspension was then used as the aqueous input for a microfluidic device to create picolitre droplets. The design for the microfluidic device is explained in Section 2.2.2. The device was secured in a water bath which ensured humidity and a temperature of 37°C throughout the experiment (see Section 2.2.3). The droplets were then imaged within the device every 10 minutes using brightfield (to image the droplet boundaries) and CFP fluorescence (to image the bacteria) microscopy, for 5.5–6.6 hr. See Appendix B for a step-by-step experimental protocol.

These microscopy images were then converted into a dataset of bacterial number per droplet, for each timestep. The image analysis process is explained in Section 2.3.

## 3.3 Results and analysis

### 3.3.1 Data

---

<sup>1</sup>See Figure A.1 for the growth curves from experiment E(0), which were not included here as we did not observe growth in droplets.

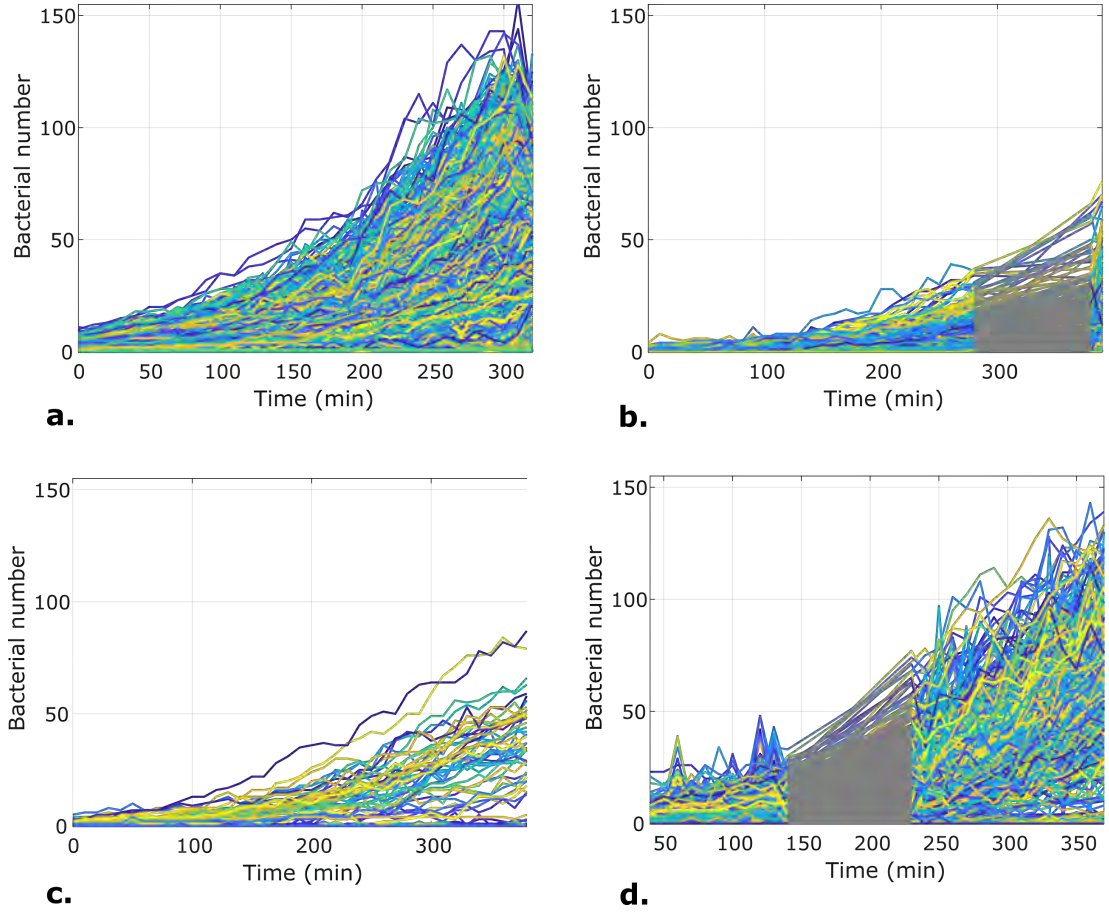


**Figure 3.1** *Growth curves of the droplet populations in the experiments with zero antibiotic. Panels show data from experiments: (a)  $A(0)$ , (b)  $B(0)$ , (c)  $C(0)$  and (d)  $D(0)$ , which are detailed in Table 3.1<sup>1</sup>. Each line corresponds to the number of bacteria in a particular droplet over the course of an experiment. Grey sections of the growth curves indicate a range of time when images were either not taken or unable to be analysed. Note that the data for  $D(0)$  begins from 40 minutes.*

Figure 3.1 displays raw data extracted from the droplet experiments once the image analysis is complete and manual error checks have been performed. Each panel of Figure 3.1 shows the growth curves measured of all the individual droplets for each experiment (A–D). These growth tracks represent the number of bacteria at each timestep, in the populated droplets that were able to be tracked for the complete experiment, which is up to a maximum of 2189 droplet populations in A(0).

Table 3.1 lists the experiments, which are each coded with a letter to distinguish them and the concentration of antibiotic given in brackets. The total number of droplets is listed, but it is important to note that some of these are empty, and so the number of populated droplets is also given, which corresponds to the number of lines on the corresponding panel in Figure 3.1. The range in fractional occupancy is due to the range of concentrations of the bacterial suspension used to make the droplets. There is an intrinsic delay between when the droplets are formed and the imaging (measurement) begins. This has been drastically reduced in comparison to previous methods (see Section 2.2.2), but is still relevant on the scale of bacterial division. The delay time is listed in Table 3.1 for each experiment.

The image analysis for experiment D(0) is started from 40 minutes as there was droplet movement within the device at the fourth timestep. This interrupted the droplet tracking and so the data presented is from after this movement had stopped.

The droplet trajectories exhibit a wide range of population growth rates, even within an individual experiment. This represents heterogeneous growth rates of subpopulations of the same clonal inoculum. This is explored in Section 3.3.2. There is also a wide range of final population numbers (from 0 to 135 bacteria) resulting from the diverse growth rates, as well as the Poisson distribution of initial population sizes. In Section 3.3.3 we separate these factors to confirm that the population size is heterogeneous even between droplets with the same initial number of bacteria.

For completeness, an example of an experiment where there was no observed growth is included in Appendix A, in Figure A.1. This is likely due to choosing a single colony from the plate to grow the overnight culture, which then by chance didn't grow any further. This is an example of the heterogeneous nature of bacterial colonies.

Experiment	Total droplets	Populated droplets	Delay (min)
A(0)	2743	2189	21–31
B(0)	1524	201	3–13
C(0)	385	45	27–37
D(0)	592	484	9–19
E(0)	1126	626	1–10

**Table 3.1** *Zero-antibiotic experiments. Total droplets is the number of droplets tracked for the entire time range of the experiment (at least 5 hours, which is 31 timesteps). The delay is calculated as the difference between the time the tubing is cut (and droplets stop being produced) and the start of the scan. A range of 10 minutes is given to account for the range of travelling times for droplets in different areas of the reservoir, as well as the difference between the start and end position of the scan.*

### 3.3.2 Growth rates

With thousands of individual growth tracks, we are able to investigate the heterogeneity of growth dynamics between these populations. Bacteria are geometrically unconstrained within droplets and growth is conducted under uninhibited growth conditions. Therefore growth is expected to be in the exponential phase. Figure 3.2 shows the natural logarithm of the growth curves from experiments A–D (which are plotted in Figure 3.1). A simple linear regression was performed on the straight section of the data, from 0–240 minutes, to assign an exponential growth rate for each droplet population.

A distribution of population growth rates is observed between droplets within each experiment. This heterogeneity is present despite the bacteria being from a single colony and all droplets being kept under identical growth conditions. Figure 3.3 shows these distributions. Each colour of histogram represents the growth rates for droplet populations from each experiment. The mode of the data is similar across all the experiments, as the histogram peaks only differ by  $1.5 \times 10^{-3} \text{ min}^{-1}$ .

A second level of comparison can be made between the growth rates for the droplet populations between experiments, A–D. Table 3.2 shows the mean droplet-population growth rate for each experiment, as well as the standard deviations and the absolute range (the difference between the maximum and minimum) of the growth rates. The simple average of the mean population growth rate for all droplet experiments (discarding the non-growing experiment, E(0)) is

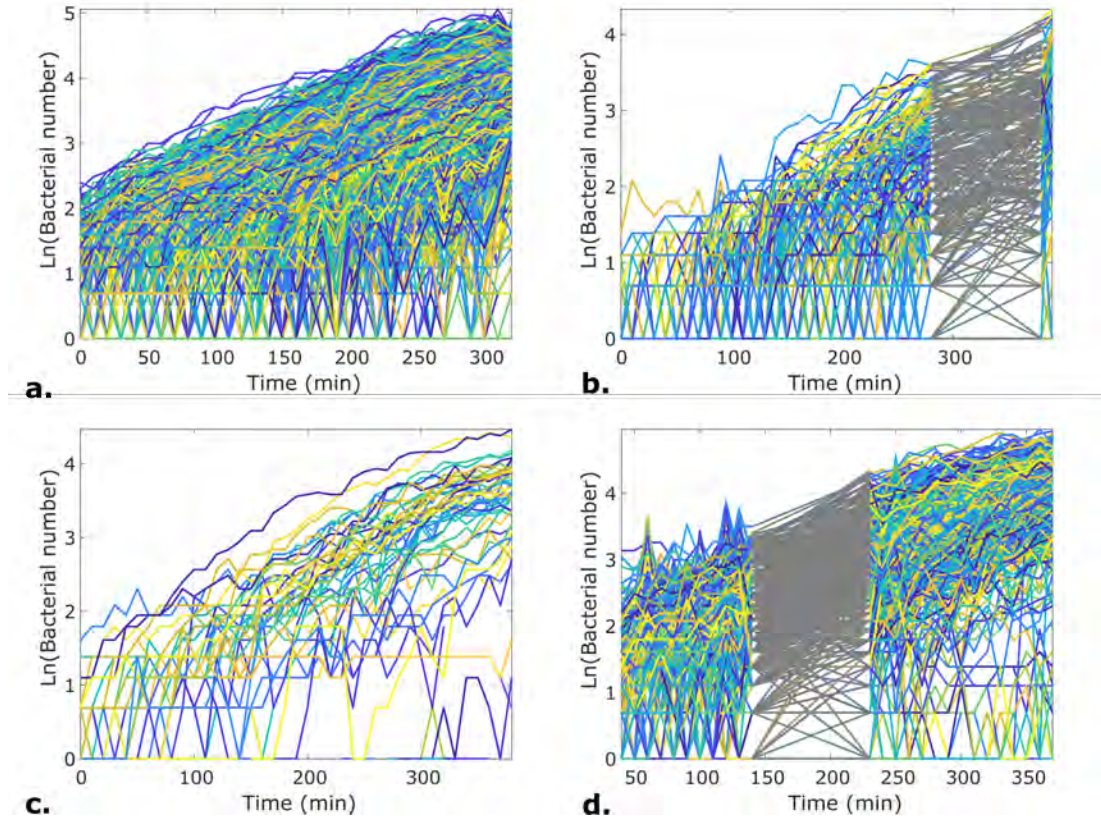


**Figure 3.2** Log plots of the growth tracks for experiments (a)  $A(0)$ , (b)  $B(0)$ , (c)  $C(0)$  and (d)  $D(0)$ . Growth rate is calculated by fitting the first 240 minutes of data for each droplet population growth tracks to a straight line (except for  $D(0)$  which is fitted to a straight line using data from 40–140 minutes). Grey sections of the growth curves indicate a range of time when images were either not taken or unable to be analysed.

Exp.	Mean GR ( $\text{min}^{-1}$ )	DT (min)	Range ( $\text{min}^{-1}$ )	SD ( $\text{min}^{-1}$ )	CV
A(0)	0.0099	70	0.0183	0.0017	0.17
B(0)	0.0073	95	0.0194	0.004	0.55
C(0)	0.0088	79	0.0130	0.0024	0.28
D(0)	0.0085	81.5	0.0330	0.0044	0.52
E(0)	0.00058	1201	0.0177	0.0022	3.2

**Table 3.2** *Growth rates (GR) of each zero-antibiotic experiment (Exp.), determined using linear fits to the natural log of the bacterial number for data from 0–240 minutes (except for D(0), which is taken between 40–140 minutes, as this is the available data). The doubling time (DT) is calculated using the mean growth rates. The range is calculated by subtracting the minimum droplet population growth rate from the maximum. Coefficient of variance (CV) is calculated by dividing the standard deviation (SD) by the mean growth rate.*

$0.0086 \pm 0.0012 \text{ min}^{-1}$ . It is interesting that we see a fairly consistent mean droplet-population growth rate across the experiments, but a high variance between the growth rates of droplet populations within these experiments. The coefficient of variation (CV) in population growth rates for experiments A(0), B(0), C(0) and D(0) are between 0.17–0.55. However the CV between the four mean population growth rates of the droplet experiments is 0.11. Therefore the spread of population growth rates differs more between clonal droplet populations than between repeats of the experiment with different initial colonies. By sampling thousands of bacteria, we converge towards an average value. The two experiments with the fastest mean growth rates, A(0) and C(0), have the lowest CV values, whereas the slower growing experiments, B(0) and D(0), have a much larger spread with CV values of over 0.5.

This data is in contrast to bulk optical density (OD) measurements where a single growth rate is measured for the whole population. Using a plate reader we determined the typical bulk growth rate for RJA003 in M9 minimal media to be  $0.0066 \pm 0.002 \text{ min}^{-1}$ . The plate reader results are plotted in Figure A.11. Perhaps surprisingly, the mean bulk growth rate is lower than the mean droplet growth rate, when we would expect the fastest growing bacteria to dominate the plate reader. However these two values are equivalent within the uncertainty of the measurements, so we cannot draw a meaningful conclusion from these two values.

We can compare the variation that we observe between droplet populations to growth variation measured from single cells using time-lapse microscopy. Stewart

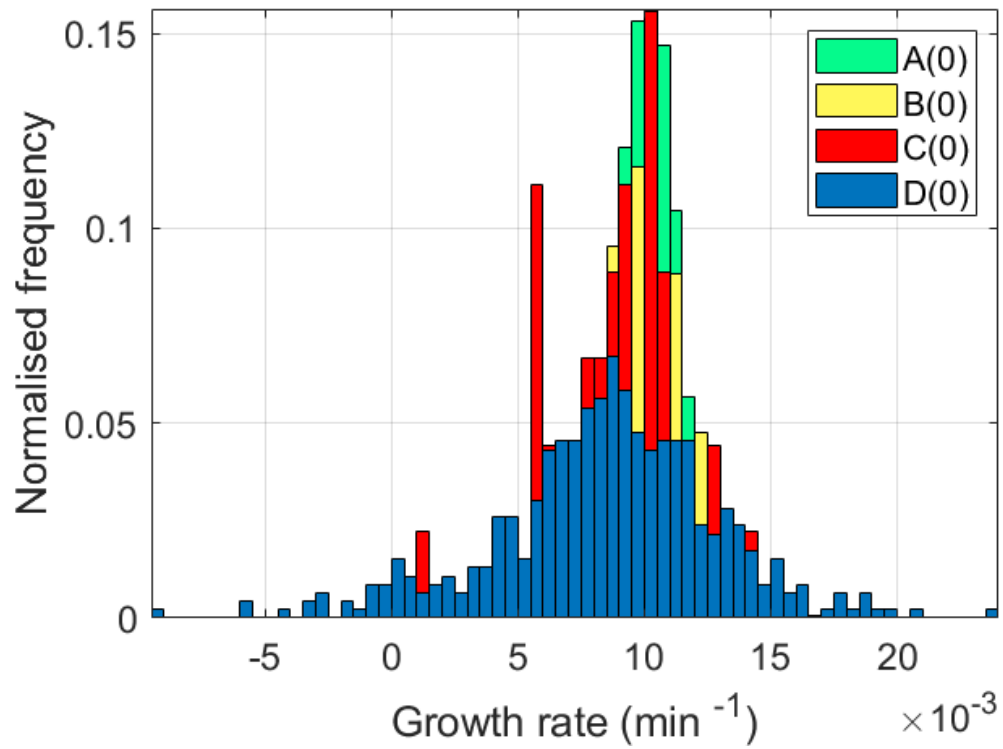


**Figure 3.3** *Histograms showing the distribution of growth rates for the droplet populations. Colours indicate the experiments A(0), B(0), C(0) and D(0). The mean and range of the growth rates are given in Table 3.2*



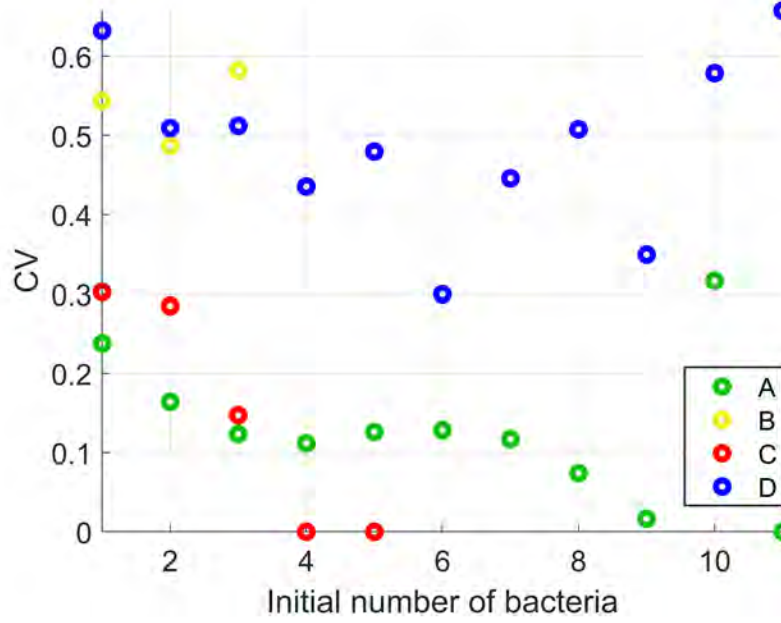


**Figure 3.4** The coefficient of variation ( $CV$ ) values of droplet population growth rates, separated by initial population size ( $N_0$ ), for experiments  $A(0)$ – $D(0)$ . The  $CV$  was calculated by dividing the standard deviation of the droplet population growth rates by the mean droplet population growth rate, for each subset of data.

et al. measured repeated cycles of reproduction by individual *E. coli* cells, finding a difference of up to 5% between the growth rates of sibling pairs. This arises from intrinsic sources of stochasticity and reproductive asymmetry, where upon division, the cell that inherits the old pole grows slower than the cell with the new pole [30]. Koutsoumanis et al. measured the growth rate, for 213 microcolonies of *Salmonella Typhimurium*, originating from a single cell. They found a range of 0.005 to 0.022  $\text{min}^{-1}$ , with a  $CV$  of 0.205 (20.5%), demonstrating high variability in the growth dynamics [2]. Whilst not directly comparable to the droplet-population growth rates, these single-cell measurements demonstrate the underlying stochasticity which is likely to be a source of the variability we measure amongst the droplet populations, in addition to the added dispersion of Poisson distributed initial bacterial numbers.

We can explore the effect of the initial population size on the heterogeneity of the growth rate by separating the experimental data into subsets. Figure 3.4 shows the  $CV$  values for the growth rates of droplets with the same initial population number. This plot indicates that the heterogeneous growth rates of the droplet populations do not simply result from the range of initial population sizes. In particular, droplets which begin with one bacterial cell do not have a lower

variance in population growth rate than those which start with more bacteria. Although we note that the sample sizes vary significantly between the subsets, due to the Poisson distribution of the bacteria, therefore at higher values of  $N_0$  there may only be 1–2 droplet populations available to include in the comparison.

We can also utilise the subsets of data to see if there is any correlation between initial number and population growth rate. One could hypothesise that if the growth rate is dictated by an initial distribution of fast and slow growing cells, we might expect droplets with larger initial populations to have higher growth rates; since a droplet starting with more bacteria would have a higher probability of containing a fast-growing cell.

As we can see in Figure 3.5, we do not see faster growth in populations with more initial bacteria, as we might expect if fast division was inherited. Instead we see shallow gradients (a slight negative correlation between initial number and growth rate for experiments A(0), B(0) and D(0), and a slight positive gradient for the fit to experiment C(0)), which indicates there isn't a correlation. This is consistent with mother-machine experiments which show that a cell forgets immediately upon division how fast it was growing in the previous cell cycle [33], although there is evidence for weak growth rate correlations under certain conditions [122], this is not detectable in these droplet experiments.

Overall, our results suggests that the heterogeneity between droplet population growth rates has a nuanced and intrinsic underlying source.

### 3.3.3 Comparing initial and final bacteria counts

The distribution in growth rates, discussed above, naturally causes a distribution in population size over time. The effect of initial population size on final population size is shown in Figure 3.6. There is a consistently positive correlation, however we can see that the final population size data is noisy; droplets that start with two bacteria are less than twice as populated by the end of the experiment than those that started with a single cell (and so on). This indication of saturation could due to competition for nutrients within the droplet (as minimal media was used). Correlation values for each experiment are shown in Table 3.3. The wide distribution of population sizes is presumably an effect of cell-to-cell variability, amplified by exponential growth. Growth rate variability between individual cells has been shown to, in general, lower population growth [122], so perhaps this has

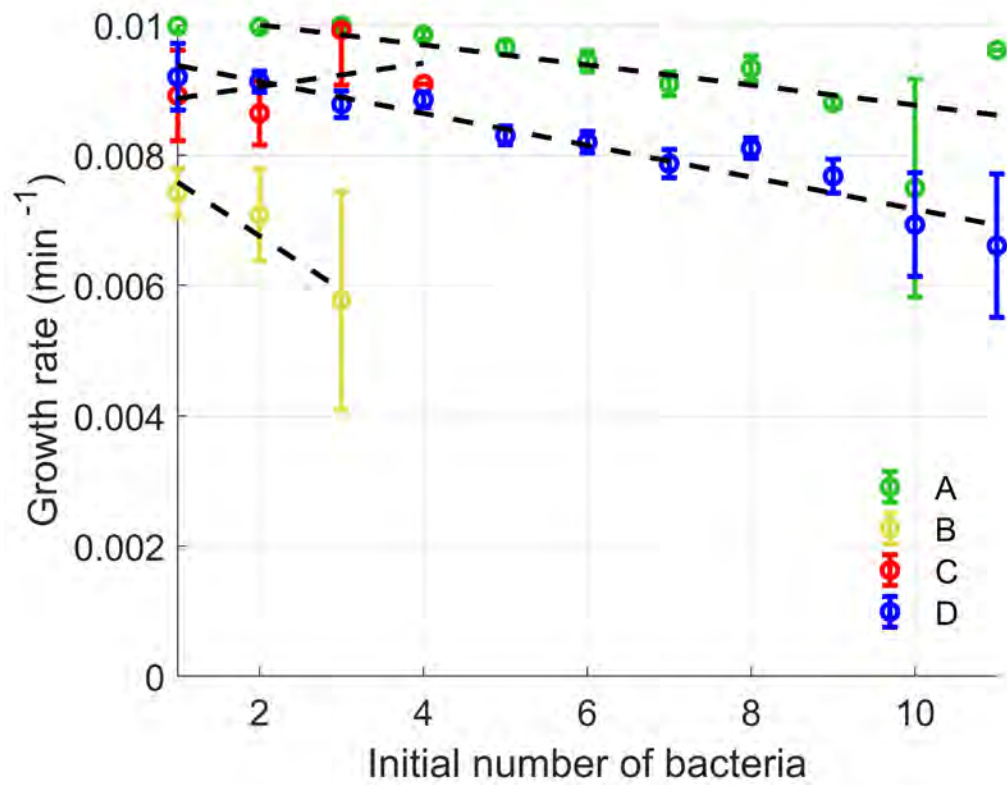


**Figure 3.5** Population growth rate as a function of initial population size ( $N_0$ ), for experiments A(0)–D(0). Each point represents the mean population growth rate of each subset of droplets (separated by initial bacterial number). The black dashed lines show the linear fit for each set of data. Error bars show the standard error of the mean.

Experiment	Gradient	R-value	P-value
A(0)	11.4	0.676	$1.06 \times 10^{-292}$
B(0)	6.25	0.187	0.0079
C(0)	9.98	0.478	0.0009
D(0)	5.66	0.527	$6.14 \times 10^{-36}$

**Table 3.3** *The fit gradient between the initial and final droplet populations of bacteria. The R-value is the correlation coefficient between the initial and final counts per droplet. The P-values correspond the probability of obtaining results at least as extreme as the observed results, assuming that the null hypothesis (that there is no correlation between initial and final population numbers) is correct. Values close to 0 correspond to a significant correlation and a low probability of observing the null hypothesis.*

Experiment	Initial number	Final number	Factor
A(0)	5538	126001	22.8
B(0)	241	5328	22.1
C(0)	83	1807	21.8
D(0)	1951*	30947	15.9

**Table 3.4** *The total initial number of bacteria and the total final number of bacteria for each experiment. This was done by summing over all droplets. The factor is the final number divided by the initial number. \*Initial number for D(0) starts at 40 minutes.*

an effect on the final population numbers. There is also an uncertainty in the initial division time (as the bacteria are not synchronised), which will have the greatest impact on the first observed divisions.

Reassuringly, when we look at the experiments as a whole and we compare the final and initial bacterial populations, we find that the bulk population increases by a similar factor across the experiments (see Table 3.4)<sup>2</sup>. This suggests that the heterogeneity we see in Figure 3.6 is a result of droplet-to-droplet variation which we observe only by measuring and analysing individual small populations.

### 3.3.4 Stochastic dynamics of bacterial growth

Thousands of droplets observed over multiple hours enable us to observe heterogeneity in growth amongst clonal populations. The distributions of droplet-

---

<sup>2</sup>We exclude experiment D(0) as here the initial bacterial numbers are calculated after 40 minutes of growth.

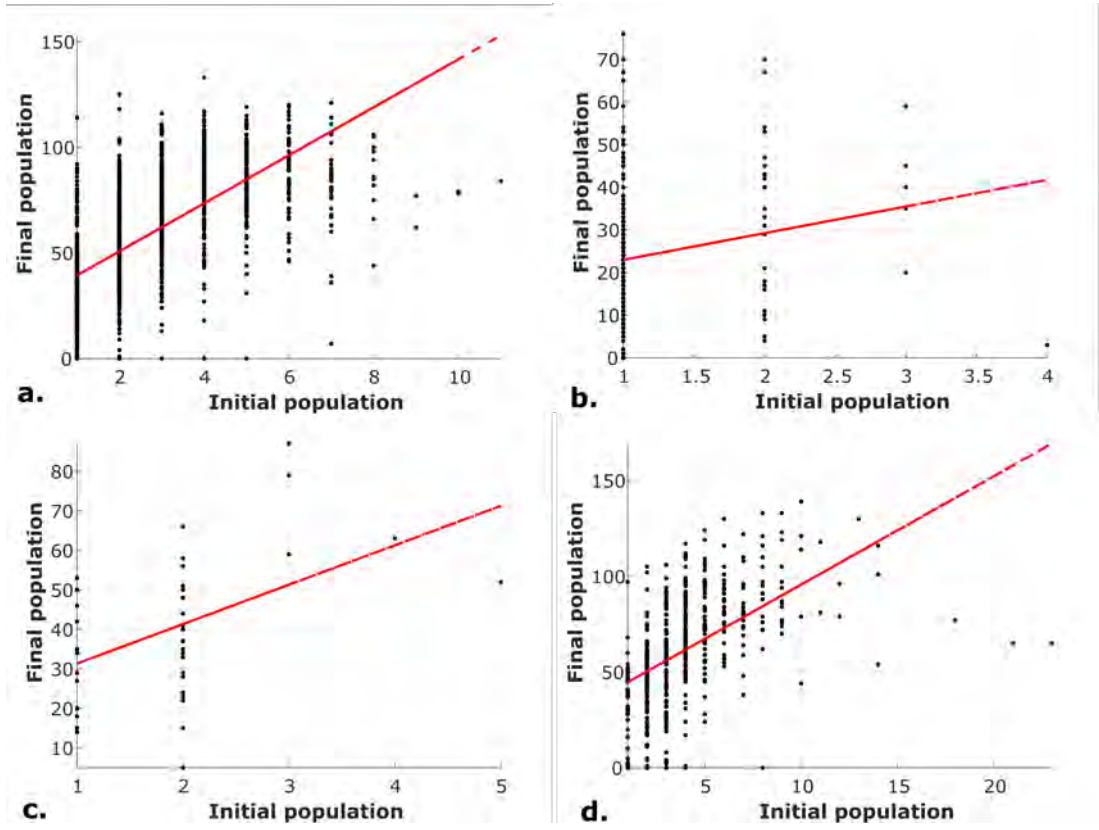


**Figure 3.6** *Plots of initial population number per droplet against the final population number (each data point represents a droplet). Each panel shows the data for experiments (a)  $A(0)$ , (b)  $B(0)$ , (c)  $C(0)$ , (d)  $D(0)$ . The linear fit to each set of data is shown in red. The linear regression values are given in Table 3.3.*

population growth rate and final population number (Figures 3.3, 3.5 and 3.6) are some ways to quantify the heterogeneity, but do not provide much insight into the origin of this stochasticity. In this section we use a theoretical framework developed by Barizien et al., which takes into account various contributions to stochastic growth dynamics probabilistically and allows us to investigate single-cell behaviour from our population-level measurements [95]. This analysis has also been performed on a previous set of experimental droplet data [96].

### Bellman-Harris branching process

The analysis is based on the classical Bellman–Harris (BH) model, which describes a stochastic branching process [123]. A single bacterium is born at time  $t = 0$  and lives for a random time,  $\tau_i$ , drawn from a fixed cumulative distribution function. In our work we assume a birth process where, at time  $\tau_i$ , each bacterium splits into two daughter cells. These descendants have the same properties as the original bacterium and are independent of its predecessor and each other; there is no memory or inheritance of division time. From this model, a distribution of population size at a given time,  $t$ , can be derived.

The BH model predicts that both the mean and the standard deviation of the bacterial number,  $N(t)$ , grow exponentially with the same exponent,  $\alpha$ , tending to  $n_1 e^{\alpha t}$  and  $n_2 e^{\alpha t}$  at long times. The values of the constants  $\alpha$ ,  $n_1$  and  $n_2$ , depend on the underlying distribution of division times. For droplets which start with a single bacterium, the coefficient of variation,  $CV_1$ , is given by the standard deviation of  $N(t)$  divided by the mean of  $N(t)$ , which tends to a constant value  $\frac{n_2}{n_1}$ . For droplets with an initial population of  $k$  bacteria, the coefficient of variation,  $CV_k$ , for the number of bacteria in these droplets is described by [95]:

$$CV_k \rightarrow \left( \frac{1}{\sqrt{k}} \right) \frac{n_2}{n_1} = CV_1 \left( \frac{1}{\sqrt{k}} \right). \quad (3.1)$$

Furthermore, for the case where the initial bacterial numbers are Poisson-distributed (as for the droplet experiments), the coefficient of variation of  $N(t)$ ,  $CV_\lambda$ , (computed over non-empty droplets) obeys the relation [95]:

$$CV_\lambda^2 = \frac{1 - e^{-\lambda}}{\lambda} \left( \frac{n_2}{n_1} \right)^2 + \frac{1 - (\lambda + 1)e^{-\lambda}}{\lambda} = \frac{1 - e^{-\lambda}}{\lambda} CV_1^2 + \frac{1 - (\lambda + 1)e^{-\lambda}}{\lambda}, \quad (3.2)$$

where  $\lambda$  is the parameter of the Poisson distribution (the mean initial bacterial

number, computed over all droplets including the empty ones). The coefficient of variation,  $CV$ , is a statistical measure of the dispersion of data points in a data series around the mean. It allows us to make comparisons between our droplet experiments and other growth studies which might have (very) different mean values for the growth rates and sample size.

### Comparing the experimental data to the Bellman-Harris model

Using our datasets of bacterial count over time, we can see whether the BH model represents the growth dynamics in the droplets. Firstly, I divided the droplet trajectories into groups according to their initial population size. Otherwise, the dominant effect on the variance of the number of cells at a given time is the variance due to the initial distribution, and not the heterogeneity of the division times. For each group of trajectories, the mean, standard deviation and the coefficient of variation of population size, were computed as functions of time. Figure 3.7, shows the mean (a) and standard deviation (b) to be exponential over time, for subsets of droplets with each initial bacteria number,  $k$ . Figure 3.8 shows the  $CV$  of population size at each timestep for droplets with different initial starting numbers. We can see that the  $CV$  values are constant over time (with very low gradients between  $-1 \times 10^{-1}$  and  $2.1 \times 10^{-4} \text{ min}^{-1}$ ), consistent with the BH model. Statistical tests were performed to confirm these datasets do not show an upward or downward trend. These results are given in Table A.1. A Mann-Kendall test [124] showed that there is insufficient evidence to reject the null hypothesis (that there is no trend, as expected) for all subsets apart from those for  $k = 5$  and 7. Using a Lilliefors test, we found all datasets to be normally distributed, signifying that the values are symmetric and clustered about the mean.

A linear fit of these  $CV$  values was taken to compare the experimental variance of the population size with the BH prediction, shown in Figure 3.9. Each point represents a measured  $CV$  of population size for each subset of initial number,  $k$ . We see good agreement with the theoretical relationship given in Equation 3.1.

We can also assess whether the BH model accounts for the variance in population size across the whole dataset by utilising Equation 3.2, which incorporates the variance in population size from both the Poisson distribution and the intrinsic BH stochasticity. This gives us a value for  $CV_\lambda$  which we can then compare to the  $CV$  value from the full dataset ( $CV_{tot}$ , calculated using a linear fit of mean

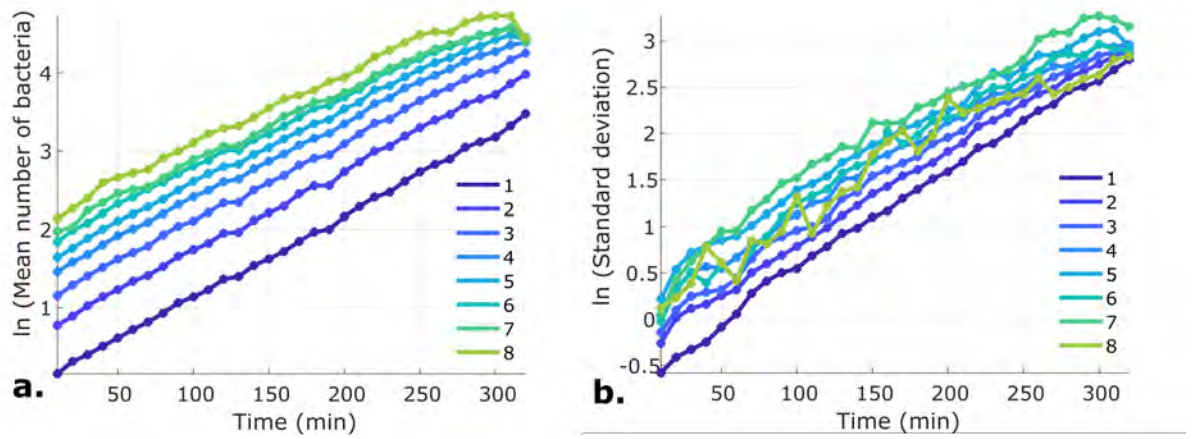


**Figure 3.7** Plots showing the exponential increase over time of (a) mean number of bacteria and (b) standard deviation of the population number. Different colours correspond to different initial population numbers of the droplets,  $k$ . This data is from experiment  $A(0)$ .

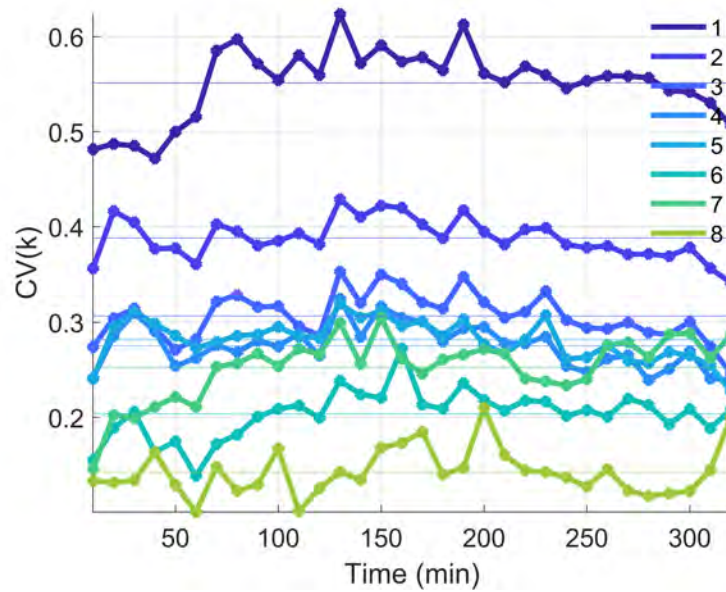


**Figure 3.8** Coefficient of variation (CV) value plotted against time, for droplets starting with 1–8 bacteria, indicated with different colours (droplets with 9–11 starting bacteria were omitted due to having less than 4 samples). These are expected to be approximately constant. This data is from experiment  $A(0)$ .



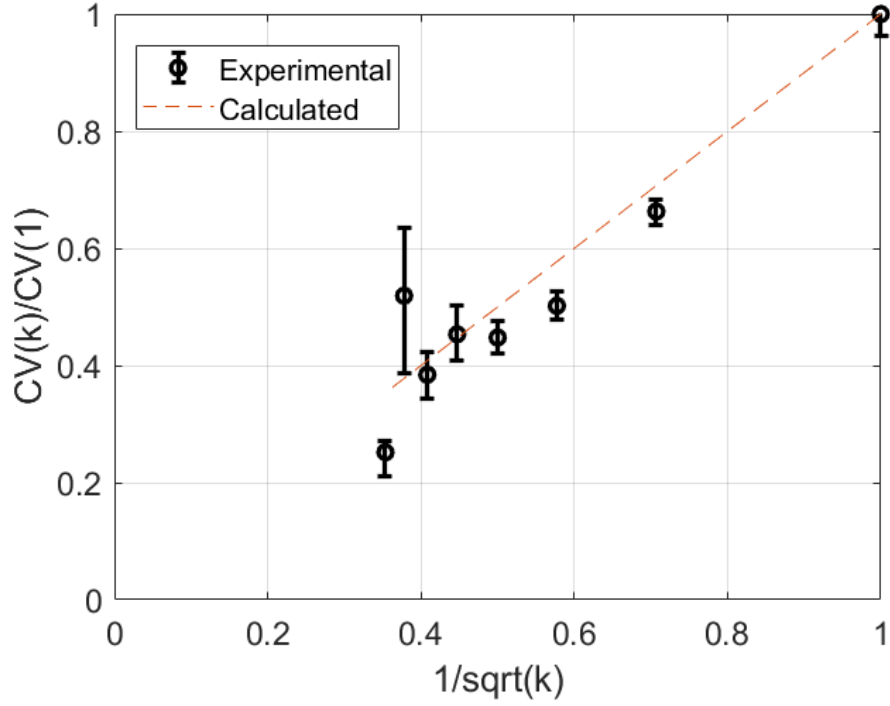


**Figure 3.9** Coefficient of variation ( $CV$ ) values of population size for droplets starting with 1–8 bacteria ( $k$ ) scale with  $\frac{1}{\sqrt{k}}$  as predicted by Barizien *et al.*'s generalisation of the Bellman-Harris theory. Droplets with 9–11 initial bacteria were omitted as there were less than 4 samples.  $CV$  values were calculated using a linear fit of standard deviation over mean, for 5.8 hr (350 min) of data collection. The dashed line shows the theoretical correlation as predicted by the BH model (Eq. 3.1). The error bars were calculated using bootstrapping with 1000 resamplings. This plot shows the results of the Barizien analysis for dataset A(0). The corresponding plots for experiments B(0)–D(0) are shown in Figure A.2.

and standard deviation of the population size over time, within all of the non-empty droplets). Evaluating the coefficient of variation across all the non-empty droplets in the A(0) dataset (2189 droplets), we find that  $CV_{tot} = 0.758 \pm 0.04$ . The value for  $CV_1$  is calculated using a linear fit of mean and standard deviation of the data from droplets with an initial population of 1 bacterium and the mean initial bacterial number for experiment A(0) is  $\lambda = 2.02 \pm 0.11$  (see Table 2.1), therefore  $CV_\lambda = \sqrt{0.418} = 0.65 \pm 0.2$ , which is in agreement with  $CV_{tot}$ .

### Inferring single-cell division time statistics

Although we don't track individual bacteria within the droplets, application of the BH analysis allows us to infer single-cell division time statistics. We can calculate population-level parameters using the experimental datasets;  $\alpha$  is the exponential growth rate for the subset of droplet populations that start with 1 cell ( $k = 1$ );  $n_1$  and  $n_2$  are the prefactors of the mean and standard deviation of the distribution of population size. Assuming that the single-cell division times are Gaussian distributed, Barizien et al. [95] showed that the values of these constants depend on the underlying distribution of division times:

$$\alpha = \frac{\ln(2)}{\tau} \frac{2}{1 + \sqrt{1 - 2\ln(2)cv^2}}, \quad (3.3)$$

where  $\tau$  is the mean single-cell lifetime and  $cv$  is the coefficient of variation of the single-cell division time distribution,  $cv = \frac{\sigma}{\tau}$  (which is distinct from  $CV_1(t)$ , the coefficient of variation of the population number of droplets which start with a single-cell). The population growth rate,  $\alpha$ , is therefore a function of the growth rate when the heterogeneity of division times is neglected ( $\frac{\ln(2)}{\tau}$ ), multiplied by a factor which increases with  $cv$  (a larger cell-to-cell variability of the division times increases the apparent growth rate of the whole population).

In addition, the relationship between  $cv$ ,  $CV_1$  and the prefactors  $n_1$  and  $n_2$  is:

$$\exp \left[ \frac{(2 \ln 2)cv}{1 + \sqrt{1 - (2 \ln 2)cv^2}} \right] = \frac{1 + \left( \frac{n_1}{n_2} \right)^2}{\frac{1}{2} + \left( \frac{n_1}{n_2} \right)^2} = \frac{1 + \left( \frac{1}{CV_1} \right)^2}{\frac{1}{2} + \left( \frac{1}{CV_1} \right)^2}. \quad (3.4)$$

Table 3.5 shows the calculated values for  $\alpha$  and  $\tau$  for each uninhibited droplet experiment. Alpha ( $\alpha$ ) was determined using a linear fit to a log plot of the  $k = 1$  droplet population count;  $CV_1$  is taken from Figure 3.7; and Equation

Experiment	$k = 1$	$\alpha$	$\pm$	$cv$	$\pm$	$\tau$	$\pm$
A(0)	694	0.0105	0.0001	0.167	0.02	66.7	0.72
B(0)	168	0.0087	0.0006	0.282	0.04	81.9	3.6
C(0)	15	0.0092	0.0008	0.146	0.08	75.8	6.5
D(0)	47	0.0091	0.0008	0.282	0.114	78.4	5.5

**Table 3.5** *Values for each zero antibiotic experiment of  $\alpha$ , the exponential growth rate for the droplet populations that start with one bacterium ( $k = 1$ );  $cv$ , the coefficient of variation single-cell division-time distribution; and  $\tau$ , the mean single-cell lifetime. Errors calculated by bootstrapping 1000 resamples of the  $k = 1$  dataset. Column 1 gives the number of droplets in each experiment which start with one cell.*

3.4 was then solved for the coefficient of variation of the single-cell division-time distribution,  $cv$ . The values for  $cv$  and  $\alpha$  were then used to calculate the mean single-cell lifetime,  $\tau$ , by rearranging Equation 3.3. The relationship between the population-scale growth rate and single-cell-division can be visualised in Figure 3.10, where we can see that the values from the droplet experiments are close together, which means that the individual cells had similar division times across the experimental replicates, as we might expect.

## Summary

By using this BH theoretical framework, I have demonstrated that we can infer individual-cell parameters from the population-level data measured in the droplet experiments. This enables the study of heterogeneity in cellular response to external factors, without the need to distinguish between cells in the analysis. Furthermore, our image analysis methodology offers more accurate data for this analysis than was originally presented by Barizien et al. (where fluorescence was used as a proxy for the size of the bacterial population and droplets could not be sorted according to the initial population size) [95].

A good fit with the BH model suggests that the growth dynamics we observe in the droplets is possibly a Markov process, in which the probability of each division event depends only on the state attained in the previous event, meaning that we do not observe the inheritance of growth rate. We find that growth dynamics are congruent with the Bellman-Harris model, and also with other measurements of single cell growth dynamics from literature. We determine values of  $cv$  in a range of 0.167–0.282, which can be compared to a  $cv \approx 0.19$ , calculated from

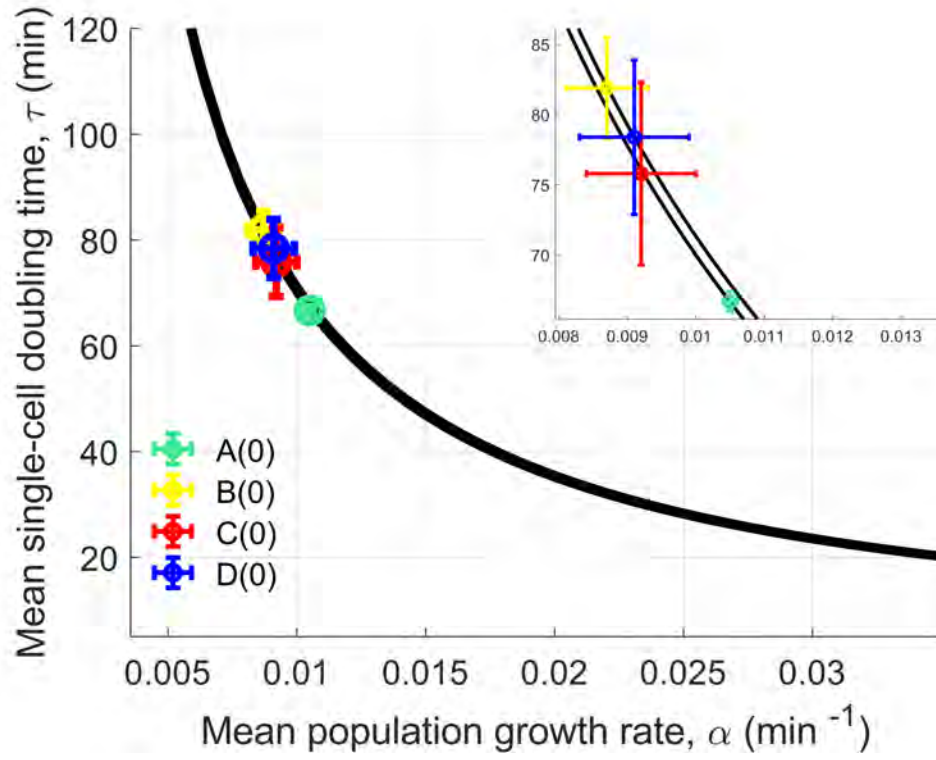


**Figure 3.10** Plot illustrating the relationship between  $\alpha$ , the exponential growth rate for the droplet populations and  $\tau$ , the mean single-cell division time (values given in Table 3.5). Equation 3.3 is plotted in black (different experimental values of  $cv$  have overlapping lines on this scale, inset shows the theoretical range in black). Corresponding values of  $\alpha$  and  $\tau$  are shown in circles for each experiment (A–D).

growth data of *E. coli* on agarose pads [122, 125]. Wallden et al. measured the growth rates of single cells in fast, intermediate, and slow growth conditions using a microfluidic device. The division time ( $\tau$ ) for experiment A(0) is equivalent to a growth rate of  $0.01 \text{ min}^{-1}$ , which corresponds to the intermediate growing conditions in this experiment, which had a *cv* of 0.234 in a sample of 1217 cells. They found that cell-to-cell variation in division timing and cell size was mainly driven by variations in growth rate [126].

### 3.3.5 Non-growing bacteria

Very few droplet populations die when there is no antibiotic stress. Survival fractions of the uninhibited droplet populations are between 0.955–0.99 (see Figure 6.6). Here we define survival fraction as the proportion of droplets with any surviving bacteria (representing a subpopulation which could hypothetically repopulate or reinfect a larger volume). However, not all these surviving bacteria grow.

Table 3.6 shows the number of non-growing droplet populations in each experiment. Droplets with growth rates less than  $0.0005 \text{ min}^{-1}$  for the first 4 hours were categorized as slow (or non) growing. Sustained fluorescence was used to distinguish between non-growing cells and dead cells; this classification was supported by observing the movement of non-growing bacteria between timesteps. When checking the images of a sample of 30 droplets, I found 35% of these populations were filamentous (such as in Figure A.13), 60% were slow growing populations and the remaining 5% were dying populations.

The slow-growing populations we observe in the zero-antibiotic droplet experiments are interesting because they are potential persister populations. As we observe them in the absence of imposed environmental stress, this suggests that the existence of a small fraction of non-growing bacteria is a stochastic or spontaneous phenomenon, rather than necessarily a direct response to antibiotic (or other environmental stress).

Persisters are phenotypic variants that survive antibiotic treatment in a dormant state. Persistence could be a bet-hedging strategy, part of the phenotypic heterogeneity generated under uncertain conditions. Antibiotic-tolerant persister cells are thought to cause relapsing infections and antibiotic treatment failure in various clinical setups [127, 128].

However, the proportions of non-growing populations we observe in the uninhibited droplets are small compared to the large number of non-growing populations we find when we expose the bacteria to ampicillin (see Section 6.3.3 and Figures 6.3 and 6.6). Therefore we can conclude that they probably do not play a major role as persisters in the response to antibiotic stress. Although it is possible that some non-growing cells within growing droplet populations would be masked by this analysis.

Persistence is generally categorised into two types; spontaneous persistence and stationary phase-induced persistence [129]. Spontaneous persisters are a rare phenotypic phenomenon in most strains; only a small fraction of bacteria, typically  $10^{-3}$ – $10^{-6}$ , switch to a persister state during exponential growth and survive exposure to antibiotics, which allows the population to regrow [130]. Therefore the non-dividing bacteria we see here are unlikely to be persisters in this sense.

Stationary phase-induced persistence, however results from delayed growth resumption when stationary-phase bacteria are diluted in fresh media. An increase of the persister subpopulation is observed when cells enter stationary phase. Variation in recovery time can be due to cell damage or could represent an ecological survival strategy [18]. These cells could also be regarded as contamination from the original overnight growth which failed to reenter the exponential growth phase. It has been demonstrated that the majority of persisters in batch culture experiments come from the stationary-phase inoculum. These bacteria do not divide after dilution in fresh medium and throughout antibiotic treatment but resume growth and form colonies when plated [127].

In addition, older cells cease growing after approximately 100 divisions (a study by Stewart et al. found this at a frequency of  $4.6 \times 10^{-4}$  [30]). This is another potential cause of the non-growing cells, but it is unlikely to be a major source in the droplet experiments due to the short time-scale over which we observe the bacteria.

### 3.4 Discussion

The microfluidic device and image analysis protocol allows us to count individual bacteria during unconstrained growth in droplets. This facilitates a study of small

Experiment	Number	Fraction
A(0)	10	0.005
B(0)	9	0.04
C(0)	0	0
D(0)	27	0.06

**Table 3.6** *Droplets with slow growing populations (or with no growth within the experiment). The numbers have a high uncertainty of  $\pm 30\%$ , as these low counts and low gradient fits are prone to error. The fraction is calculated by dividing the number of slow growing populations by the number of populated droplets.*

bacterial populations, without the need for proxy measures of population size such as integrated droplet fluorescence. This chapter demonstrates the potential for analysis on the data generated from droplet experiments. Variability can be obscured in large population studies, and the system can seem to behave deterministically, even though the underlying law is stochastic [2]. Whereas with these large, precise datasets we can quantitatively and statistically investigate the growth dynamics of small populations.

We can plot the growth trajectories for multiple small populations of *E. coli* bacteria (Figure 3.1), and measure the distributions in population growth rates (Section 3.3.2) and final population sizes (Section 3.3.3). We have found that the heterogeneity we see between droplet populations is exacerbated by, but not solely due to the initial Poisson distribution. These results can provide a baseline measure of the variability in growth in uninhibited environments to which comparisons can be made for the cases in which ampicillin is present in the environment (Chapter 6).

We identified a fraction of non-growing bacterial populations (Section 3.3.5), which cannot be detected in bulk experiments. These cells could be in a persister state, which is an important phenomenon to study as this behavior reduces the effectiveness of antibiotic treatments. The proportion of these non-growing bacteria when there is no antibiotic stress allows us to differentiate between spontaneous behavior and reactive behavior when comparing to the antibiotic experiments (in Chapter 6). Droplets could a good candidate for future persister studies, particularly because our experimental methodology allows us to easily check the raw images associated with each data point. This means we can distinguish between bacteria which are alive, filamentous or dead, and confirm that a data point is not an artefact in the image.

We find good agreement with the Bellman–Harris model, which assumes that individual cell lifetimes are independent. We are also able to infer parameters of the single-cell lifetime distribution from population trajectories. This type of analysis shows it is possible to extract single-cell information from our population-level measurements. This type of analysis could help distinguish between different stochastic growth models.

We assume in the BH model that cell division events are independent, and the division times are drawn from a fixed Gaussian distribution. This means that each bacterium divides after a time selected from a Gaussian distribution of single-cell division times, with a fixed mean and standard deviation. Our results fit this model well, but not exactly. Figures 3.9 and A.2 show approximately linear trends for droplets starting with different numbers of bacteria (which should follow the same asymptotic behavior as the droplets that start with one bacteria, if each cell acts independently). Loose growth rate correlations between generations or a non-Gaussian distribution of division times could be the cause of this, and might obstruct other underlying mechanisms.

We infer that the inheritance of growth rate is not strong, as a system with inherited growth rates would not fit the BH model. This conclusion is supported by Figure 3.5, which shows that the growth rates of subpopulations of the droplet data do not appear to be dependent on  $N_0$ , and so a larger sample of initial bacteria (with a higher probability of containing a fast-growing cell) does not seem to impact the ultimate population growth rate, as we would expect if this trait was inherited. This is consistent with other studies of inter-generational memory [2].

Instead, there are many other hypotheses for the underlying causes of heterogeneous growth in bacteria, for example, due to the asymmetric behavior of the new and old poles of the daughter cells [30]. Although other studies have found no clear dependence between the age of a cell and the growth rate [33]. In addition, different rates of growth can display different mechanistic behavior; *E. coli* can appear as a ‘sizer’ during slow growth and an ‘adder’ during fast growth [126]. Another study found a link between cell size and the single-cell growth rate [131]. This all implies that the underlying growth mechanisms are complex and intertwined with other processes.

It would be interesting to design an experiment using droplet methodology—and the large, precise datasets which are produced—to investigate and distinguish



between these different underlying behaviors.

## Chapter 4

# Simulating $\beta$ -lactamase-producing bacterial populations: method

In this chapter, deterministic and probabilistic models are developed to understand the response of small populations of  $\beta$ -lactamase-producing bacteria to  $\beta$ -lactam antibiotics.

Computer simulations allow us to explore the behavior of complex systems and provide a mathematical framework for the underlying mechanisms. The results of simulations can be compared to experimentally measured values or responses, to gain insight into the factors which might determine a particular outcome. A model can provide a way to test a hypothesis that is difficult to directly measure with experiments. Alterations to a model can often be made with a shorter time commitment and smaller financial investment than would be required for the equivalent change in an experimental setup or procedure. Therefore, simulations can be used to inform the planning of future laboratory experiments, indicating parameters which are most likely to result in the desired outcome. In addition, simulations can usually generate far larger amounts of data than can be achieved experimentally.

Due to these advantages, many models have been developed to investigate biological systems, including the behavior of resistant bacteria. Disease outcome models can be used to estimate the infection rate, as well as the clinical and public health consequences of antibiotic-resistant bacteria [132]. Models have also been used to study the connection between single-cell growth dynamics and population fitness. Lee et al. present a stochastic model to find a mechanistic

interpretation of population-level responses to antibiotic exposure, which predicts a proportionality between bacterial growth rate and the lysis rate [133]. Yurtsev et al. use a model to describe the cooperative population dynamics of resistant and sensitive bacteria [32], which is the starting point for the model presented in this chapter.

Using mathematical models, I aim to simulate an experiment in which resistant bacteria are exposed to antibiotic stress whilst encapsulated in multiple droplets in order to track the population dynamics over time. Microfluidic droplets provide multiple replicate enclosed environments, enabling the study of multiple small populations of bacteria. Careful matching of the parameters between the simulations and our experimental setup should offer insight into the results we obtain experimentally.

In this model, the effect of the  $\beta$ -lactamase enzymes is modelled implicitly by including degradation of the antibiotic (i.e. decreasing antibiotic concentration) when there are resistant bacteria present. It is expected that this will make survival more likely in more populated droplets, since more antibiotic is degraded if there are more  $\beta$ -lactamase-producing bacteria in a droplet. Therefore droplets containing greater numbers of bacteria could potentially survive at a higher concentration of antibiotic than droplets containing fewer bacteria. The effect of stochastic bacterial loading into droplets and stochastic growth are compared to the deterministic cases. I explore these different growth dynamics to allow us to investigate under what circumstances a group of bacteria can ‘save itself’ when exposed to a  $\beta$ -lactam antibiotic. The key result is that stochasticity can result in some droplets surviving at higher concentrations than would be possible in a deterministic population.

The model is based on previous work by Yurtsev et al. [32], who simulated the growth of mixtures of resistant and sensitive bacteria in the presence of antibiotics. They used deterministic models to study the evolution of resistance via the spread of a plasmid that encodes a  $\beta$ -lactamase enzyme. This work showed that coexistence between resistant and sensitive cells is possible at antibiotic concentrations above the MIC of the sensitive cells, because  $\beta$ -lactamase production by the resistant cells acts as a cooperative trait, protecting the sensitive cells.

Here, however, our purpose is different. We seek to understand the behaviour of small populations encapsulated in microfluidic droplets, rather than a large pop-

ulation evolution study. These droplet populations mimic some natural habitats, especially in spatially structured environments where bacterial populations are initially small. I adapted one of the models proposed by Yurtsev et al. (Model 4 in reference [32]) to simulate multiple small populations (or droplets) on a time scale similar to the droplet experiments in this thesis, where we grow multiple encapsulated small populations of bacteria (Chapter 6). I use the same rate equation for the degradation of antibiotic (see Section 4.4), as well as a Heaviside step function to determine a state of either exponential growth or exponential death, depending on a defined antibiotic concentration (see Section 4.2.2). My simulations include a death condition for the resistant strain which is not present in the original paper and I also introduce Poisson-distributed initial bacterial numbers (see Section 4.3.1) as well as Tau-leaping growth and death dynamics (Section 4.3) to investigate the impact of stochasticity on survival.

This chapter provides a detailed description as well as validation of the model. The results of the simulations are presented in Chapter 5, where we explore the survival of bacterial populations under a range of antibiotic concentrations, with different starting numbers of bacteria. A further aim of these simulations is to make predictions for the possible outcomes of the droplet experiments that will be discussed in Chapter 6. The model is adapted in Chapter 7 to include a sensitive strain of bacteria and model cooperation between small populations of resistant and sensitive strains.

## 4.1 Simulation overview

### Starting conditions

In our simulations, we model a resistant ( $\beta$ -lactamase producing) strain of *E. coli* bacteria. The population is characterised by a starting number of cells ( $N_0$ ), a growth rate ( $\gamma_G$ ), a death rate ( $\gamma_D$ ), and a single-cell MIC ( $scMIC$ ). If the local antibiotic concentration is above the single-cell MIC, the bacteria will die, and below this  $scMIC$  threshold, the bacteria will grow.

## Droplets

To mimic our experimental setup, we simulate multiple discrete populations or droplets. Essentially, this simply means running the simulation multiple times, each time modelling a different droplet population. Within a droplet, the input antibiotic concentration is converted from  $\mu\text{g mL}^{-1}$  into molecules per droplet (see Section 4.5.3). We assume each droplet is well-mixed system and therefore treat the antibiotic concentration as uniform (see Section 4.4).

## Growth and death dynamics

Bacterial growth and death are implemented either deterministically or stochastically in our simulations. Deterministic growth and death dynamics give us an insight into the behavior of large populations, and comparison with stochastic dynamics can reveal the impact of heterogeneity on the survival of replicate droplet populations. Deterministic growth and death are modeled by integrating a set of differential equations with a defined timestep,  $dt$  (given explicitly in Section 4.2.2). Stochastic growth is modeled using Gillespie’s tau-leaping algorithm [134], which is detailed in Section 4.3.2.

## Effect of $\beta$ -lactamase

Each resistant bacterium is assumed to contain a fixed number of  $\beta$ -lactamase enzyme molecules, which degrade the antibiotic at a fixed rate. Therefore the total degradation rate is proportional to the number of resistant bacteria that are present (see Section 4.4). This implies that population size has a direct impact on survival, as a greater number of bacteria results in a lower concentration of the antibiotic over time. This is an inoculum effect, which plays out at the small-population-level of droplets, when some droplets have different starting numbers of bacteria than others.

This small-population inoculum effect can be seen in Figure 4.1, where the larger populations of bacteria are able to survive an antibiotic treatment which kills the smaller population of bacteria (with identical antibiotic susceptibility, growth and death rates). Figure 4.1 also shows that for surviving populations, antibiotic degradation reduces the level of antibiotic to a concentration below the scMIC, allowing regrowth of the population.

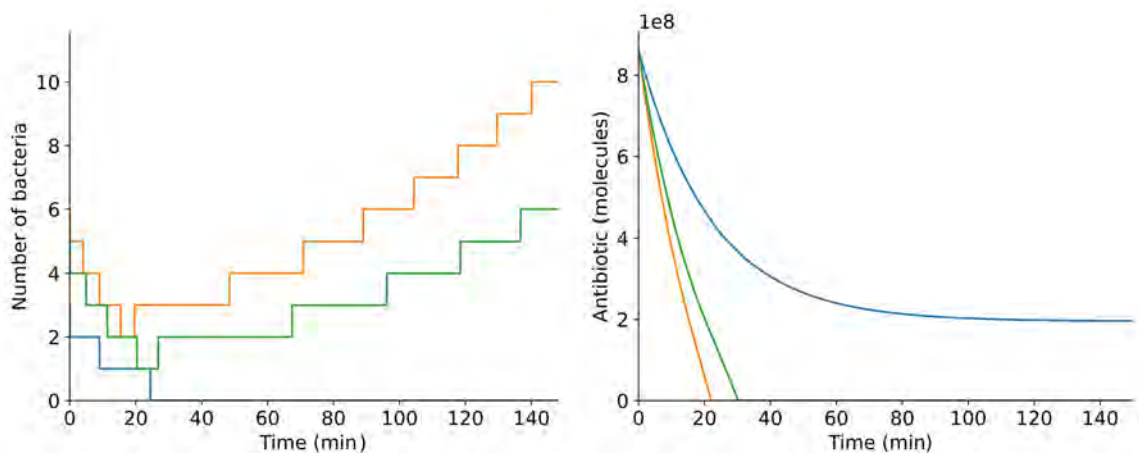


**Figure 4.1** *Three examples of growth simulations of a strain with a scMIC of  $1 \mu\text{g mL}^{-1}$  (the equivalent of  $1.72 \times 10^8$  molecules per 100 picolitre droplet), with different initial starting numbers of bacteria ( $N_0 = 6, 5$  and  $3$ ). The plots show number of bacteria (left) and the corresponding amount of antibiotic (right) against time, for simulations run with a starting antibiotic concentration of  $5 \mu\text{g mL}^{-1}$  ( $5 \times \text{scMIC}$ ). In 2/3 simulations (shown in orange and green, starting with 6 and 5 bacteria, respectively <sup>1</sup>), the population survives; in the other simulation (starting with 3 bacteria) it does not. Growth and death are modelled deterministically (see Section 4.2.2).*

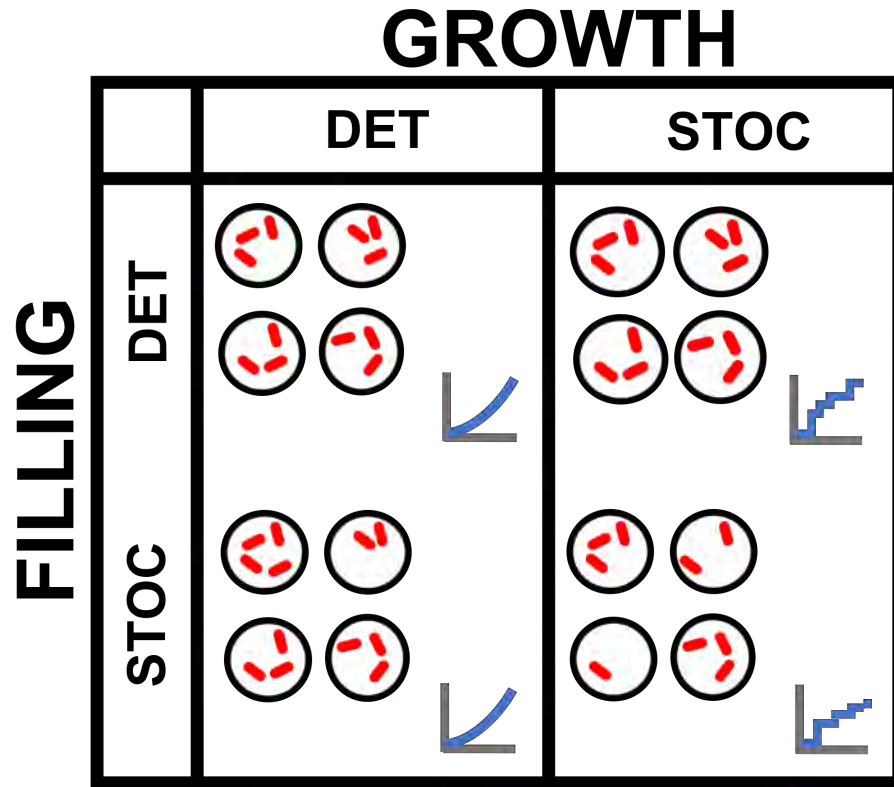


**Figure 4.2** *Schematic illustrating the four categories of droplet simulations. The top left corner shows the fully deterministic (DET) case, and the bottom right shows the fully stochastic (STOC) case. Filling refers to the initial bacterial number distribution within the droplets (deterministic or Poisson distributed). Growth is modelled either exponentially (deterministic) or modeled with tau-leaping (stochastic).*

### Sampling of droplet populations

In our droplet experiments, bacteria are distributed according to Poisson statistics since the encapsulation of each bacterium is an independent event (where the mean is controlled by the overall bacterial density; see the background discussion of Poisson distributions was given in Section 1.4.2). Poisson encapsulation means that within a single experiment, some droplets have smaller initial populations while others have larger initial populations. To investigate the effects of Poisson encapsulation, the model was designed to enable comparison between deterministic (homogeneous) and stochastic (Poisson-distributed) initial population sizes. This is outlined in Sections 4.2.1 and 4.3.1 below. Figure 4.2

<sup>1</sup>Note that each droplet population immediately drops by one bacterium after the first timestep.

illustrates the four classes of model that we investigate with our simulations, which include the two types of population distributions and the two types of growth methods.

## 4.2 Deterministic droplet filling and bacterial dynamics

Deterministic models are appropriate for modelling bulk populations. They also provide a useful baseline for comparison to stochastic models, which allows us to assess the effects of stochasticity on the growth and survival of small populations.

### 4.2.1 Deterministic distribution of initial bacterial numbers

If we assume that droplets are populated deterministically, then all our replicate simulations start with the same initial number ( $N_0$ ) of bacteria, input by the user. From an experimental point of view, this can be interpreted as the bulk concentration of bacteria in the inoculating culture, multiplied by the droplet volume. This scenario is represented in the top row of the schematic in Figure 4.2.

### 4.2.2 Deterministic growth and death dynamics

We model growth exponentially, from an initial bacterial number ( $N_0$ ) with a fixed growth rate of  $\gamma_G$ :

$$N(t) = N_0 e^{\gamma_G t}. \quad (4.1)$$

Death is modelled identically, with a fixed death rate of  $\gamma_D$ . Therefore the deterministic growth and death processes can be expressed as differential equations:

$$\frac{dN}{dt} = \begin{cases} \gamma_G N & a < scMIC \\ -\gamma_D N & a \geq scMIC \end{cases}, \quad (4.2)$$

where  $a$  is the concentration of antibiotic. Bacteria grow exponentially at rate  $\gamma_G$  if the antibiotic concentration ( $a$ ) is below the single-cell MIC ( $scMIC$ ), and they die exponentially if the antibiotic concentration is above the single-cell MIC.



We note that the death rate takes a single fixed value,  $\gamma_D$ , if the antibiotic concentration, is above the single-cell MIC; it does not depend on the amount by which  $a$  exceeds  $scMIC$ .

We model  $\beta$ -lactamase enzymes implicitly, and it is assumed that they are able to uniformly decrease the concentration of antibiotic within a droplet (see Section 4.4). Therefore the antibiotic concentration,  $a$ , is reduced at a rate which is dependent on the number of resistant bacteria,  $N$ :

$$\frac{da}{dt} = -DN, \quad (4.3)$$

where  $D$  is the degradation rate constant.

Growth and death are simulated in discrete time steps ( $dt$ ) and so Equations (4.2) are solved approximately using a first order Taylor expansion. The bacterial population,  $N$ , is increased each timestep by  $dN = N \times \gamma_G \times dt$ , where  $\gamma_G$  is the growth rate (in  $\text{min}^{-1}$ ) and  $dt$  is the timestep (in minutes). For death, the population is decreased as  $dN = -N \times \gamma_D \times dt$ , where  $\gamma_D$  is the death rate (in  $\text{min}^{-1}$ ). We do not allow the population size to become negative ( $N > 0$ ).

When counting bacteria or plotting trajectories of bacterial population size, bacterial numbers are rounded down to the nearest whole integer. However the simulation algorithm operates with fractional numbers of bacteria.

We assume that the bacteria are always in exponential growth phase with no saturation, since our aim is to characterise small population dynamics. Inherently these dynamics occur at early times, where we do not experimentally observe saturation of growth.

### **Solving the deterministic growth model analytically**

The deterministic model is simple enough that we can solve it analytically, without the need for simulations. If the initial antibiotic concentration  $a_0$  is high, such that  $a_0 > scMIC$ , the bacterial population density decreases exponentially according to Eq. (4.4):

$$N(t) = N_0 e^{-\gamma_D t}. \quad (4.4)$$

The size of the bacterial population at the start of the experiment is fixed for every droplet at  $N_0$ . Substituting this into Eq. (4.3), for the antibiotic degradation, we

find that:

$$\frac{da}{dt} = -DN_0e^{-\gamma_D t}, \quad (4.5)$$

which can be integrated to give:

$$a(t) = a_0 - \frac{DN_0}{\gamma_D} (1 - e^{-\gamma_D t}). \quad (4.6)$$

Therefore, as expected, the antibiotic concentration decreases in time. Since the antibiotic degradation is assumed to be constant (per resistant bacterium), we can solve for the time,  $\tau$  at which the antibiotic concentration becomes lower than the single-cell MIC. Setting  $a = scMIC$  in Eq. (4.6) we find:

$$e^{-\gamma_D \tau} = 1 - \frac{\gamma_D(a_0 - scMIC)}{DN_0} \quad (4.7)$$

and hence,

$$\tau = -\frac{1}{\gamma_D} \ln \left[ 1 - \frac{\gamma_D(a_0 - scMIC)}{DN_0} \right]. \quad (4.8)$$

We can see from this that if  $\gamma_D(a_0 - scMIC) > DN_0$  then  $\tau \rightarrow \infty$ , i.e. the antibiotic concentration never becomes lower than the scMIC, and the bacterial population will all die. To get eventual regrowth of the population we need  $\tau$  to be finite, i.e.  $\gamma_D(a_0 - scMIC) < DN_0$ . This implies that the initial bacterial population,  $N_0$ , has to be greater than a threshold value,  $n_T$ :

$$n_T = \frac{\gamma_D(a_0 - scMIC)}{D} \quad (4.9)$$

We can use this result to verify our numerical implementation of the deterministic growth dynamics. Figure 4.1 shows population trajectories for three simulations at an initial antibiotic concentration of  $5 \mu\text{g mL}^{-1}$ , with initial bacterial population sizes of  $N_0 = 3, 5$  and  $6$ . For a droplet volume of  $V_d = 10^{-7} \text{ mL}$  (100 pL), and a degradation rate of  $D = 5.8 \times 10^{-9} \mu\text{g min}^{-1}$  (parameter values are discussed in Section 4.5.3); we see that  $n_T = \frac{0.045(5-1)V_d}{D} = 3.1$  bacteria. And indeed, we see that the droplet population where  $N_0 = 3$  does not survive, whereas the other populations, where  $N_0 > n_T$ , survive the antibiotic exposure. Solving for  $\tau$ , we find that when  $N_0 = 5$ ,  $\tau = 21.5 \text{ min}$  and when  $N_0 = 6$ ,  $\tau = 16.2 \text{ min}$ . The plots in Figure 4.1 show that the minimal population size occurs at these calculated  $\tau$  times.

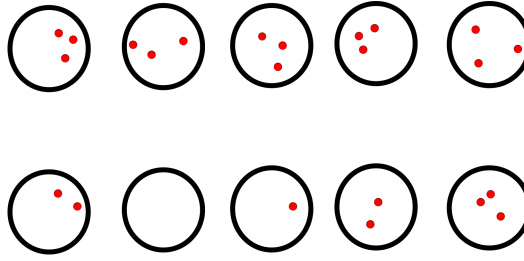


**Figure 4.3** *Schematic of droplets filled with bacteria. The top row illustrates deterministic filling; with each droplet containing 3 cells, and the bottom row illustrates a Poisson-distributed population; with a  $\lambda$  (mean) value of 3.*

## 4.3 Stochastic droplet filling and bacterial dynamics

By implementing stochastic droplet filling and dynamics we can better represent the true experimental conditions; where different droplets are generated containing different numbers of bacteria, and the bacterial growth and death dynamics can also be stochastic. This will allow us to assess whether stochasticity can change the survival outcome of the droplet populations when exposed to antibiotic.

### 4.3.1 Stochastic distribution of initial bacterial numbers

To mimic the experimental procedure of creating droplets from a well-mixed suspension of bacteria in media, in the simulations we select the initial number of bacteria from a Poisson distribution. A mean value for the number of bacteria per droplet ( $\lambda$ ) is input by the user, which represents the concentration of bacteria in the inoculating culture, multiplied by the droplet volume. Varying the value of  $\lambda$  in the simulations corresponds to varying the density of bacteria in the inoculating culture in the experiment. The schematic in Figure 4.3 illustrates the difference between droplets filled with a fixed (deterministic) or Poisson distributed (stochastic) number of bacteria. For stochastic filling, some droplets have more bacteria than the average while others have fewer bacteria than average. We hypothesise that stochastic droplet filling may allow survival at higher antibiotic doses, since droplets with a higher initial number of bacteria will benefit from a ‘droplet-level’ inoculum effect, making them harder to kill.

## Analytical prediction for bacterial survival in the stochastically distributed model

Building on our analytical calculations for the deterministic model (Section 4.2.2), we can also solve for the probability that the initial population number  $N_0 > n_T$ , the threshold value for survival (see Eq. (4.9)) when the droplets are filled stochastically. As discussed above, the initial population size,  $N_0$ , of each droplet is sampled from a Poisson distribution. Therefore the probability of a droplet being filled with a given value of  $N_0$  is  $P(N_0) = \frac{\lambda^{N_0} e^{-\lambda}}{N_0!}$ , where  $\lambda$  is the mean bacterial number. If bacterial growth is deterministic then for a given value of  $\lambda$ , the fraction of droplets that survive antibiotic treatment is equal to the fraction of droplets for which  $N_0 > n_T$ , or in other words, the Poisson probability of getting  $N_0 > n_T$ . This is given by:

$$P(N_0 > n_T) = 1 - e^{-\lambda} \sum_{i=0}^{\lfloor n_T \rfloor} \frac{\lambda^i}{i!} = 1 - \frac{\Gamma(\lfloor n_T + 1 \rfloor, \lambda)}{\lfloor n_T \rfloor!}, \quad (4.10)$$

where  $\Gamma$  is the upper incomplete Gamma function. Eq. (4.10) is plotted in Figure 4.4 and compared with the outcome of simulations in which the initial bacterial number is sampled from a Poisson distribution (while bacterial growth is modelled deterministically). There is good agreement between the simulation results and the analytical prediction for the 1000 simulated droplet populations. This validates our implementation of the stochastic filling model.

### 4.3.2 Stochastic proliferation and death

Bacterial proliferation and death are themselves stochastic processes, since individual bacteria show heterogeneous cell lifetimes and response to antibiotics. This has been studied in experiments with mother machines [121] as well as in other microfluidic growth chambers [22].

In our simulations, we model stochastic bacterial proliferation and death dynamics using the tau-leaping or  $\tau$ -leap method [134]. The  $\tau$ -leap algorithm was originally developed to model the time evolution of a well-stirred chemically reacting system. It provides an efficient way to simulate Markovian systems (systems in which the possible events are independent Poisson processes). To model bacterial proliferation and death using  $\tau$ -leaping, we assume that the birth and death processes have no memory, i.e. they are Poisson processes with a

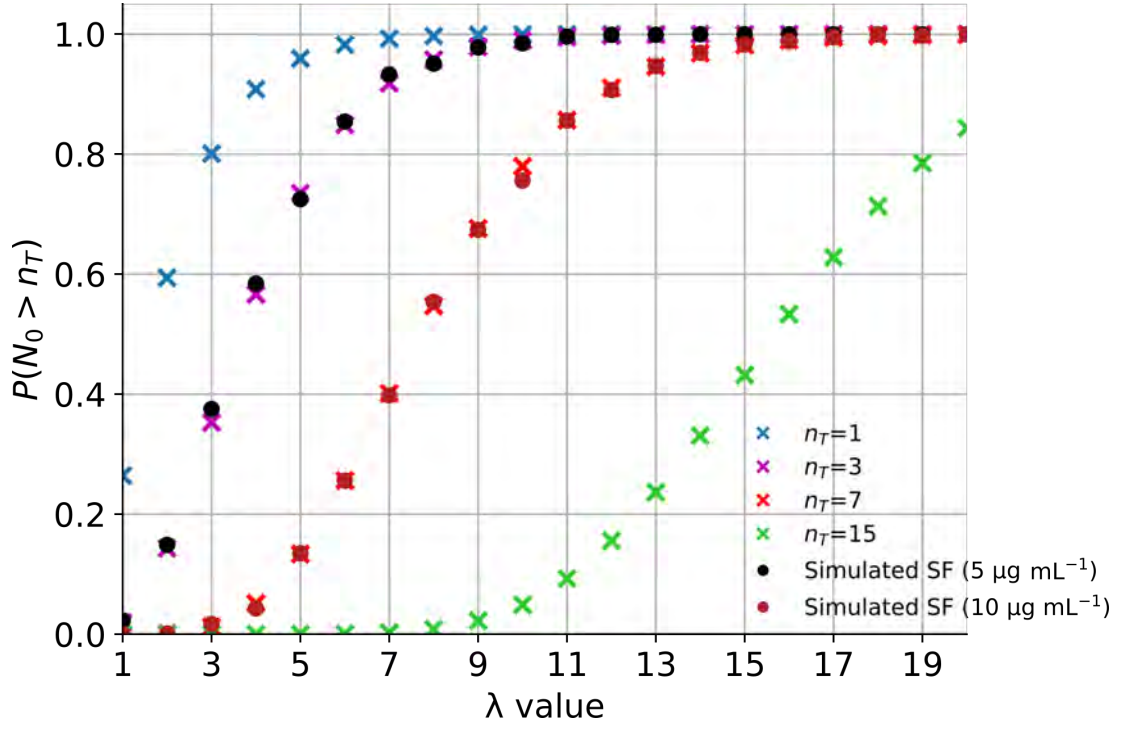


**Figure 4.4** Plot of Eq. (4.10), showing the probability that the initial bacteria number ( $N_0$ ) is larger than  $n_T$  ( $P(N_0 > n_T)$ ), for different values of  $\lambda$ . The survival fractions (SF) for simulations of 1000 droplets are plotted alongside. These simulations were performed with Poisson-loading and deterministic growth and death, with a scMIC of  $1 \mu\text{g mL}^{-1}$ , at initial ampicillin concentrations of  $5 \mu\text{g mL}^{-1}$  and  $10 \mu\text{g mL}^{-1}$ . The  $n_T$  values for the simulated parameters were  $n_T = 3.1$  for  $5 \mu\text{g mL}^{-1}$  and  $n_T = 6.98$  for  $10 \mu\text{g mL}^{-1}$ .

constant rate. In other words, a bacterium is equally likely to proliferate or die at any point in its lifetime. This assumption, although incorrect, is commonly made in modelling bacterial dynamics.

In the deterministic model, the rate of population growth is directly proportional to population size. In this stochastic model, the infinitesimal deterministic increase,  $dN$ , is replaced by the probability of a proliferation event ( $N \rightarrow N + 1$ ) during an infinitesimal time interval [134, 135]. In our model we use the Estimated-Midpoint  $\tau$ -leap Method [134], so we compute the expected state change ( $dN$ ) during each simulation timestep using a Poisson distribution with a mean value equal to the state change that would happen in the deterministic model (outlined above in Section 4.2.2).

The  $\tau$ -leap method requires  $dt$  to be small because we assume that none of the propensities change appreciably during one timestep. In our model, a timestep that is too large would mean that we would not capture accurately the feedback between proliferation/death and changes in antibiotic concentration. Therefore we bound the relative change of  $N$  in each  $dt$  by a specified tolerance. If  $dN > N$  then a warning appears during the simulation, indicating that  $dt$  should be decreased for simulations with those parameters. For the results presented in this thesis, a  $dt$  of 0.1 minutes (6 seconds) is used, which is small enough to satisfy the conditions for the tau-leaping algorithm when simulating small populations, while still allowing for computational efficiency (see Section 4.5.3).

Figure 4.5 shows growth curves for bacteria simulated with  $\tau$ -leap dynamics, in the absence of antibiotic. We see varied growth trajectories and a range of final population numbers, unlike in the deterministic model.

### **Validation of stochastic growth dynamics using the Yule-Furry process**

Our  $\tau$ -leaping growth was validated by comparing the simulation results to analytical predictions for the case of a bacterial population undergoing stochastic growth (with no death). This stochastic growth process, in which the proliferation of each bacterium is modelled as an independent Poisson event, is known as a Yule-Furry (YF) process, starting from a single bacterium. For the YF process an analytical result is available for the probability of obtaining  $N$  bacteria at a given time:  $P_N(t) = e^{-\gamma_G t} (1 - e^{-\gamma_G t})^{N-1}$  [136], where  $P_N(t)$  is the probability of  $N$  bacteria at a given time,  $t$ , and the parameter  $\gamma_G$  is the

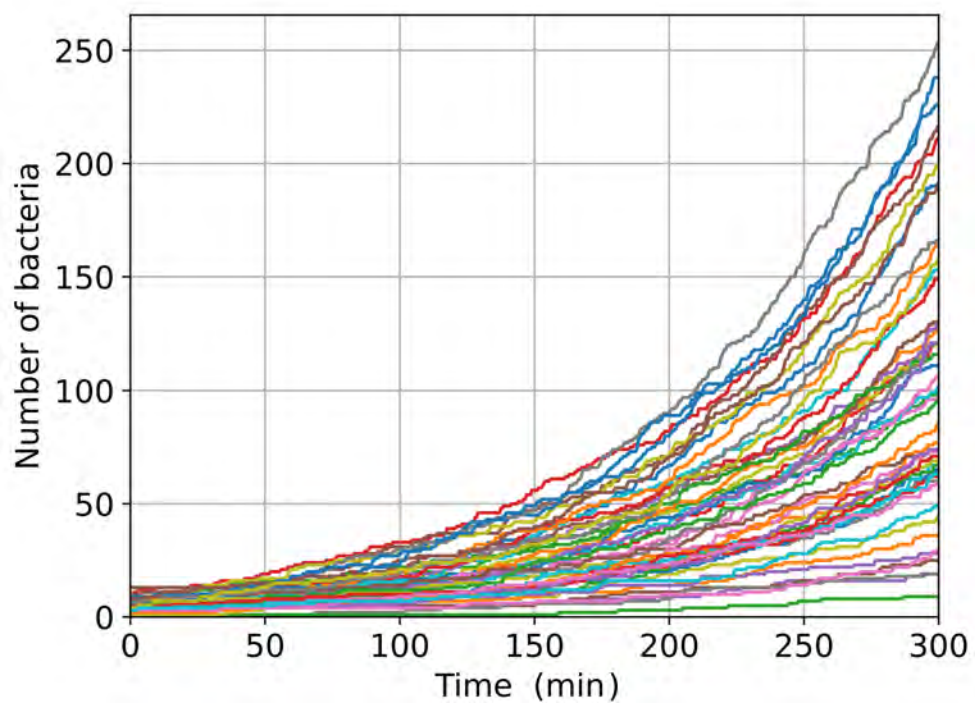


**Figure 4.5** *Tau-leaping growth of 50 droplet populations, simulated with a mean growth rate of  $0.01 \text{ min}^{-1}$ . Initial starting numbers were selected from a  $\lambda=5$  Poisson distribution. Final bacterial counts range from 9 to 253 bacteria after 300 minutes of simulated time.*

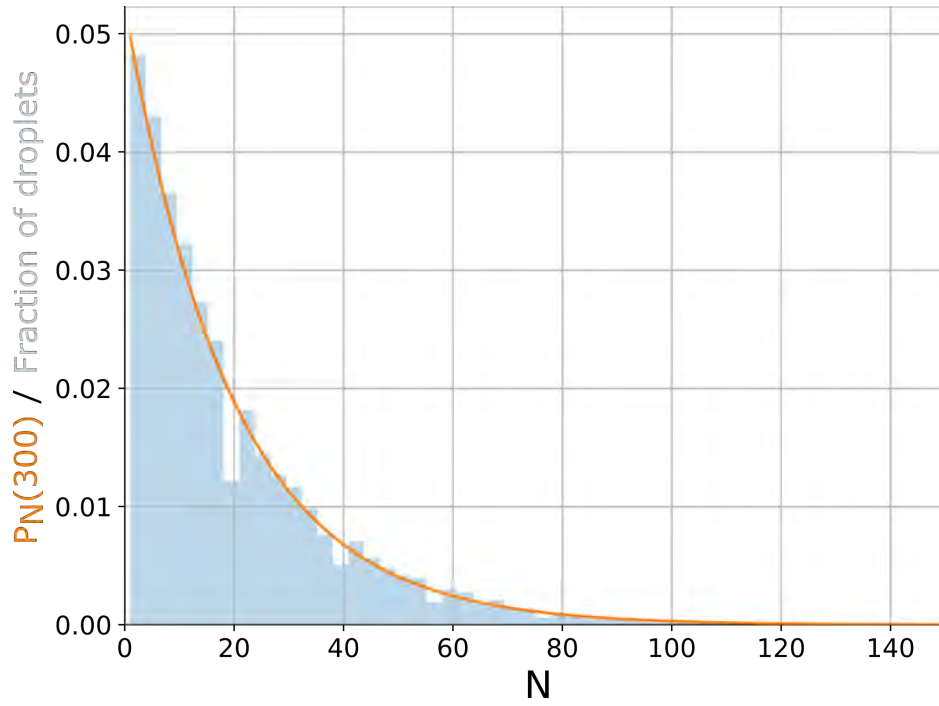


**Figure 4.6** *Histogram showing the number of droplets with a population of  $N$  bacteria after 300 minutes of  $\tau$ -leaping growth (in blue), compared to the Yule-Furry prediction for the probability distribution,  $P_N(300)$  (in orange). The simulation was run for 10,000 droplets, each starting with a single bacterium, and  $dt = 0.01$  minutes. At 300 minutes of deterministic growth,  $N = e^{(0.01 \times 300)} = 20.09$ . The mean of the YF distribution is 20.005 bacteria and the mean of the simulated data is  $20.38 \pm 0.43$  bacteria (the uncertainty given here is the standard deviation, calculated using bootstraps of resampled data).*

proliferation rate. For populations that start with more than a single bacterium (i.e.  $N_0 > 1$ ), this probability distribution can be extended because we can regard each individual bacterium as undergoing an independent YF process [136]:  $P_{N_0, N}(t) = \binom{N-1}{N_0-1} e^{-N_0 \gamma_G t} (1 - e^{-\gamma_G t})^{N-N_0}$ .

In Figure 4.6 we compare the results of simulations run with only growth and no death (i.e. with no antibiotics), to the YF analytical prediction. The droplets were all deterministically filled with  $N_0=1$  bacterial cell. The histogram of simulated bacterial numbers (in blue) is in good agreement to the YF prediction (shown in orange) and the mean of the simulated data ( $20.38 \pm 0.43$  bacteria) within the range of the YF calculated mean (20.005 bacteria).



## 4.4 Modelling $\beta$ -lactamase enzyme action

The action of the  $\beta$ -lactamase enzymes is modelled implicitly through a degradation rate for the antibiotic, and it is assumed that these enzymes uniformly decrease the concentration of antibiotic within a droplet. The antibiotic concentration is reduced at a rate that is proportional to the number of resistant bacteria in the droplet (see Equation 4.3).

### 4.4.1 Assumption of a well mixed system

A key assumption of our model is that there is good mixing such that the antibiotic molecules and  $\beta$ -lactamase enzyme activity are distributed evenly throughout each droplet. A back-of-the-envelope calculation can be used to justify this. In the following calculation we show that the time it would take for an antibiotic molecule to diffuse across a droplet is less than the simulation timestep,  $dt$ .

We use the Stokes-Einstein relation for the diffusion constant,  $d_a$  of an antibiotic molecule:  $d_a = \frac{k_B T}{6\pi\eta r}$ , where  $r$  is the size of an antibiotic molecule and  $\eta$  is the viscosity of the media. We can approximate the size of an ampicillin molecule,  $r$ , as one nanometre, and we assume a temperature,  $T$ , of 37°C (310 K). We suppose that the viscosity,  $\eta$ , of the media is similar to water at this temperature ( $7 \times 10^{-4}$  Pa s). This results in a diffusion constant,  $d_a = 6.5 \times 10^{-10}$  m<sup>2</sup>s<sup>-1</sup>, which is similar to the literature value of  $3 \times 10^{-10}$  m<sup>2</sup>s<sup>-1</sup> for a nanometre sized particle [137].

For diffusive motion the mean square displacement ( $msd$ ) scales linearly with time as:  $msd(\tau) = 6d\tau$ , so that the typical time to cross the entire droplet of size ( $r \approx 50$   $\mu$ m) is the diffusion time  $\tau = 0.64$  s. This is smaller than the timestep,  $dt = 0.1$  min, used in the simulations, and is much smaller than the timescales of bacterial growth or death dynamics. Therefore it is reasonable to take the antibiotic concentration as homogeneous.

Furthermore, in reality, we expect there to be active mixing in the droplet caused by the motility of the bacteria, so the homogenisation of the antibiotic concentration would actually be faster than that predicted with diffusion alone.

#### 4.4.2 Rate of antibiotic degradation

The degradation of antibiotic by  $\beta$ -lactamase is an enzymatic reaction. Such reactions are usually described by Michaelis-Menten (MM) theory. In our case, Michaelis-Menten theory would suggest that the rate of antibiotic degradation,  $\frac{da}{dt}$ , should be given by:

$$\frac{da}{dt} = \frac{k_{cat}ba}{a + K_M}, \quad (4.11)$$

where  $a$  is the antibiotic concentration,  $b$  is the enzyme concentration, and  $k_{cat}$  and  $K_M$  are the Michaelis-Menten parameters. The parameter  $k_{cat}$  represents the turnover number of the enzyme; the maximum number of enzymatic reactions catalysed per unit time, which can be defined as the maximum reaction rate,  $V_{max}$ , per enzyme:  $k_{cat} = \frac{V_{max}}{b}$ . The other MM parameter,  $K_M$  represents the substrate concentration at which half the active sites of the enzymes are filled by antibiotic substrate molecules. It describes the affinity of the antibiotic to the active site of the enzyme [138].

If  $K_M$  is small, we are in a regime where the enzymes are saturated with antibiotic, and the rate of degradation will remain constant. In this regime we can simplify Equation 4.11 by taking  $K_M \ll a$ :

$$\frac{da}{dt} = k_{cat}b. \quad (4.12)$$

We take the enzyme concentration,  $b$  as proportional to  $N_R$  since we assume each bacterium contains an equal amount of  $\beta$ -lactamase. Therefore we can write the degradation rate in terms of the number of resistant bacteria present,  $N_R$ , and combine the constants into a single value,  $D$ :

$$\frac{da}{dt} = -DN_R(t), \quad (4.13)$$

where  $D = Ek_{cat}$  and  $N_R = \frac{b}{E}$ , if  $E$  is the number of enzymes per bacterium. Eq. (4.13) is now identical to Eq. (4.3), used in the simulations. Therefore our approach is equivalent to Michaelis-Menten kinetics in the case where the enzymes are saturated.

The actual value of the degradation rate constants are heavily dependent on the specific properties of the  $\beta$ -lactamase enzyme, the particular  $\beta$ -lactam antibiotic, and the environment in which the catalytic reaction takes place. Furthermore,

these parameters can be difficult to experimentally measure, particularly those which are interdependent.

In our model, we use a value of  $D = 10^7$  ampicillin molecules per resistant cell per minute, following Yurtsev et al. [32] in which the degradation rate ( $V_{max}$ ) was determined to be  $10^6$  molecules  $\text{s}^{-1}\text{cell}^{-1}$ . This is consistent with Lee et al. [133], in which the maximum rate of hydrolysis was taken to be  $1 \times 10^5$ – $1 \times 10^6$  per enzyme hour ( $1.7 \times 10^3$ – $1.7 \times 10^4$   $\text{min}^{-1}$ ).

Below we briefly consider other literature reports of the kinetic parameters for ampicillin degradation, to assess the possible range of plausible values for  $D$  and the accuracy of our assumption that  $K_M < a$ .

$k_{cat}$  is a measure of the rate of hydrolysis per enzyme ( $\frac{V_{max}}{b}$ ) and is thus a constant for an enzyme under given conditions. The value of  $k_{cat}$  for  $\beta$ -lactamase vary widely depending on the strain of bacteria, the type of  $\beta$ -lactamase enzyme, and the antibiotic it is hydrolysing. A study by Nikaido et al. reported  $k_{cat}$  values ranging from 0.01 to 1900  $\text{s}^{-1}$  ( $0.6 - 1.14 \times 10^5$   $\text{min}^{-1}$ ) depending on the  $\beta$ -lactam antibiotic studied. Ampicillin degradation rates were found to vary from 6.5 to 1160  $\text{s}^{-1}$  ( $390 - 7 \times 10^4$   $\text{min}^{-1}$ ), for different bacterial strains [139]. Another study found a range of  $k_{cat}$  values from 200 to 2417  $\text{s}^{-1}$  ( $12000$ – $1.45 \times 10^5$   $\text{min}^{-1}$ ) for two types of class A  $\beta$ -lactamase enzymes [140].

$K_M$  is a measure of affinity between the enzyme active site and the antibiotic molecules. The value of  $K_M$  depends on the specific enzyme–substrate system under particular reaction conditions (such as temperature, pH and ionic strength). For  $\beta$ -lactamase and ampicillin,  $K_M$  has been measured at 0.9–37  $\mu\text{M}$  for  $\beta$ -lactamase produced by *E. coli* [139], 122–255  $\mu\text{M}$  for  $\beta$ -lactamase produced by *Staphylococcus aureus* [141],  $15 \pm 2 \mu\text{M}$  for CTX-M-15 from *Enterobacter cloacae* and 124–290  $\mu\text{M}$  for class A  $\beta$ -lactamases, SHV-1 and S130G [140]. We have chosen to make the assumption  $K_M < a$  for mathematical simplicity. This characterises a system where the enzymes have a high affinity for the antibiotic molecules.

It would be interesting in future work also to investigate the case where  $K_M > a$ , for which we would need to use the full Michaelis-Menten form in the dynamical equations. However we don't expect that this would significantly change the main results of the study.

To obtain our parameter  $D$ , we multiply  $k_{cat}$  by the number of enzymes per cell,

*E. Lee et al.* [133] have suggested that  $\beta$ -lactamase is produced at a maximum rate of  $0.1 \mu M hr^{-1}$  (approximately  $10^5$  enzymes per minute in a  $100 pL$  droplet), implying that for a generation time of  $\approx 60$  min (on poor media), a cell could contain up to  $6 \times 10^6$  enzyme molecules. However, the protein copy number per cell for *E. coli* has been found to peak at  $3 \times 10^5$  [142]. Therefore, using the  $k_{cat}$  values above, the range of possible values for  $D$  is  $\approx (10^5 \cdot 0.6 \text{ to } 10^5 \cdot 1.45 \times 10^5)$ , or approximately  $6 \times 10^4 - 1.5 \times 10^{10}$  antibiotic molecules degraded per resistant cell, per minute. The value that we use,  $D = 10^7$  antibiotic molecules per resistant cell per minute, falls within this range.

## 4.5 Model specifications, assumptions and parameters

### 4.5.1 Technical structure

The simulation code is written using object orientated programming in Python. It is based around three classes; Strain, Droplets and Experiment.

An instance of a strain population object is created with inputted attributes of mean initial number of bacteria ( $\lambda$ ), a growth rate ( $\gamma_G$ ), death rate ( $\gamma_D$ ) and single-cell MIC ( $scMIC$ ). An instance of the droplet object is then defined with total number of droplets, the resistant strain object, the initial antibiotic concentration ( $a_0$  in  $\mu g mL^{-1}$ ), the time increment ( $dt$ ) and the duration ( $T_{end}$ ) of the experiment. The mean initial bacterial number,  $\lambda$  is converted within the simulation into an initial bacterial population number for every droplet,  $N_0$ .

We can then call the method ‘run’ which needs inputs for the growth type (see Section 4.3.2) and loading type (see Section 4.3.1). This method initiates a growth experiment object with the input parameters, and runs the simulated experiment for each droplet. The number of bacteria,  $N$ , is updated as an attribute of Strain (Strain.N), after every  $dt$ .

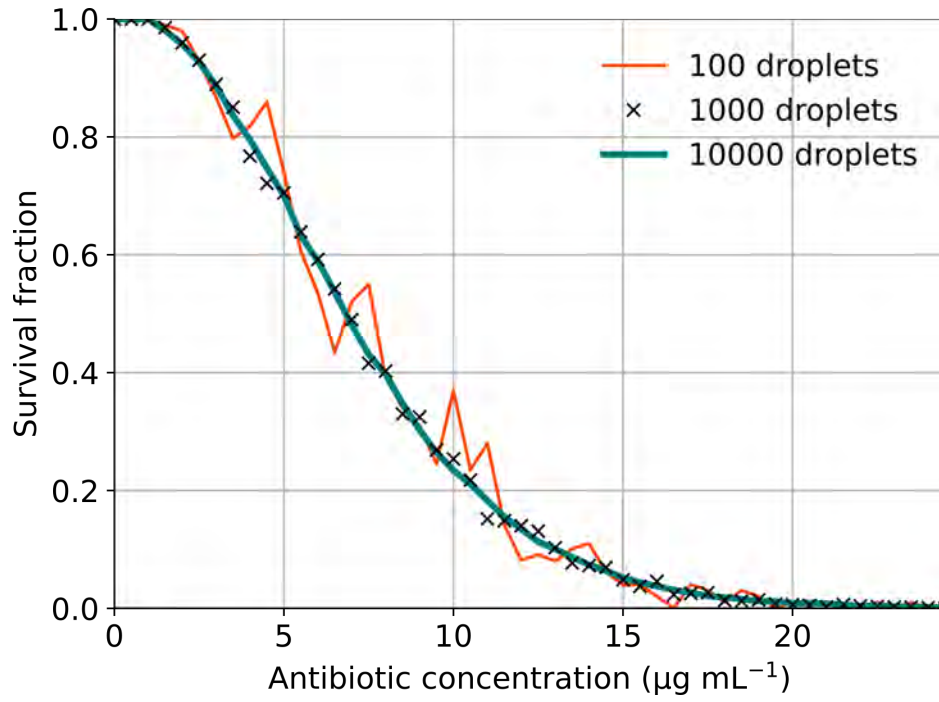


**Figure 4.7** *The survival fraction for fully stochastic simulations of 100, 1000 and 10000 droplet populations. Each simulation was run for 300 simulated minutes with the same initial conditions;  $\lambda = 5$  at concentrations of antibiotic 0–25  $\mu\text{g mL}^{-1}$ , in intervals of 0.5  $\mu\text{g mL}^{-1}$ .*

#### 4.5.2 Verifying the simulation output

Figure 4.7 shows typical outputs from our replicate simulations, for samples of 100, 1000 and 10000 droplets. We plot the fraction of droplets that survive (defined as the fraction of droplets with a non-zero population after 300 minutes of simulated time), as a function of the antibiotic concentration. As expected the survival fraction decreases as the antibiotic concentration increases above the single-cell MIC (which here is 1  $\mu\text{g mL}^{-1}$ ) with a tail of surviving droplets at high concentrations. Although noisier, the same trend is visible even for the fractions of the 100-droplet simulations.

In the following results chapter (Chapter 5) the data presented is for simulations with 1000 droplets, as this is the same order of magnitude as the number of droplets measured experimentally (see Table 6.1).

Parameter	Value	Unit	Source
$\lambda$	5	bacteria	n/a
$scMIC$	1	$\mu\text{g mL}^{-1}$	n/a
Droplet volume	$1 \times 10^{-7}$	mL	Experiment
$T_{end}$	300	min	Experiment
Growth rate, $\gamma_G$	0.01	$\text{min}^{-1}$	Sec. 4.5.3
Death rate, $\gamma_D$	0.045	$\text{min}^{-1}$	Sec. 4.5.3
AB deg. rate, $D$	$1 \times 10^7$	$\text{cell}^{-1} \text{min}^{-1}$	Sec. 4.4
Simulation timestep, $dt$	0.1	min	Sec. 4.3.2

**Table 4.1** *Default parameters for all droplet simulations. Chosen to be comparable to experimental values, to run the simulation correctly or to be consistent to aid comparison. The survival of the droplet populations is calculated at  $T_{end} = 300$  simulated minutes.*

### 4.5.3 Parameter values

Parameter values were selected to mirror the experimental conditions as far as possible. Unless otherwise stated, all simulations were run for 1000 droplets, similar to the experimental number, and the survival of a bacterial population in a droplet was evaluated after 300 minutes of simulated time (5 hours). The droplet experiments are run for a comparable length of time, with microscope images taken every 10 minutes over the course of 4–7 hours.

Droplets created in the microfluidic device are of picolitre size, see Section 2.6. Measurements of our experimental droplets show an average volume of  $91 \pm 15$  pL. For the model, we round this up to be  $1 \times 10^{-7}$  mL.

Our simulated growth rate,  $\gamma_G$  and death rate,  $\gamma_D$  are fixed in the deterministic case, and are used to calculate the mean  $dN$  for the  $\tau$ -leap calculation in the stochastic model.

The simulation timestep is set to 0.1 minutes (6 seconds) for all simulations, which is small enough to satisfy the conditions for the tau-leaping algorithm (see Section 4.3.2) while still allowing computational efficiency. A  $\lambda$  value of 5 was chosen to fill the droplets with a range of low initial population numbers (1–10). This is slightly higher than the initial populations in the droplet experiments we present (see Table 2.1). Table 4.1 shows the default parameter values used for the simulations presented in Chapter 5. More details are given in the subsections below.

## Growth rate

The growth rate,  $\gamma_G=0.01 \text{ min}^{-1}$  was chosen to match the highest experimental droplet growth rate measurement in our uninhibited droplet experiments (see Table 3.2). Changing the growth rate does not impact the survival of the droplet populations in this model, although it does affect the population size. This is discussed in Section 5.3.4. Using a fixed growth rate is a simplification since we know that individual bacteria show variable growth rates (see Chapter 3). Including a growth rate distribution would be an interesting avenue to explore in future work.

## Death rate

In these simulations, we use a value of  $-0.045 \text{ min}^{-1}$  for the antibiotic-mediated death rate,  $\gamma_D$ . This is based on the work of Yurtsev et al. who experimentally measured a death rate of  $2.8 \text{ hr}^{-1}$  ( $0.046 \text{ min}^{-1}$ ) for a sensitive strain of *E. coli* exposed to ampicillin [32]. This value for the death rate is higher than the measured death rates from our droplet experiments, which reached a maximum of  $-0.0095 \pm 0.002 \text{ min}^{-1}$  (see Figure 6.9). The effect of using different death rates is investigated in Section 5.3.4.

Experimentally, it has been shown that bacterial growth rate can affect the efficacy of antibiotics. The lysis rate of a bacterial population has been shown to depend linearly on the instantaneous growth rate of the population [133, 143] (faster growing bacteria are generally killed faster by  $\beta$ -lactam antibiotics). For simplicity, and because we did not vary growth rate in our experiments, the relationship between growth rate and death rate was left out of our model. This dependence could be implemented in future work.

We also note that in our model, the death rate does not depend on the antibiotic concentration. This simplifies the model, but it is widely accepted that death rate typically increases with antibiotic concentration [144]. Including a dependence of death rate on antibiotic concentration would be another useful extension in future work.

## Antibiotic concentration

In our model, the antibiotic concentration is tracked in units of molecules per droplet volume, rather than  $\mu\text{g mL}^{-1}$ . Ampicillin is used as the  $\beta$ -lactam antibiotic in all the simulations presented since this antibiotic was used in our experiments. The molar mass of ampicillin is  $349.406 \text{ g mol}^{-1}$  [145], which is equivalent to  $5.8 \times 10^{-16} \text{ }\mu\text{g}$  per molecule. The user-defined initial antibiotic concentration ( $a_0$ ), in  $\mu\text{g mL}^{-1}$  is converted into molecules per droplet using:

$$a_{\text{molecules}} = \frac{a_0 V_{\text{droplet}}}{5.8 \times 10^{-16}} \quad (4.14)$$

where  $V_{\text{droplet}}$  is the droplet volume in mL.

## 4.6 Discussion

The model presented in this chapter is designed to mirror a droplet experiment, to allow us to explore underlying small-population dynamics. In the following chapter, the simulation model is used to understand the effects of stochasticity in droplet loading and bacterial dynamics on the survival of antibiotic treatment.

Using our simulation method, we can easily run multiple replicate droplet simulations and predict the number of droplets with a surviving population after a chosen time. We can then repeat this procedure for different parameter values, in particular, varying the average droplet loading,  $\lambda$ , and the initial antibiotic concentration,  $a_0$ . These parameters are also easy to vary experimentally, but simulations offer the advantage that many more parameter values can be tested in a short time, allowing a wider exploration of the system's behaviour. Moreover, in the simulations we can track how the antibiotic concentration changes in time, which we cannot do in our experiments. We can also run many more replicate simulations than the number of replicate droplets we can track experimentally.

Features of the model which could be changed in future work to increase its accuracy and breadth include; adding saturation of the growth dynamics to mimic the effects of nutrient depletion within the droplets; adding heterogeneity in the growth and death rates; introducing a dependence between death rate and the antibiotic concentration; and including a more detailed model of the enzyme kinetics.



# Chapter 5

## Simulating $\beta$ -lactamase-producing bacteria: results

### 5.1 Introduction

Small populations of  $\beta$ -lactamase-producing bacteria were simulated in the presence of  $\beta$ -lactam antibiotics. This chapter presents the simulation results, leading to predictions for the droplet experiments presented in Chapter 6. The methodology and parameters of the model are outlined in Chapter 4.

In Gram-negative bacteria, such as *E. coli*, the most common mechanism of resistance to  $\beta$ -lactam antibiotics is the production of  $\beta$ -lactamase enzymes, which degrade the antibiotic molecules by hydrolysing the amide bond of the  $\beta$ -lactam ring [53, 54]. The degradation of the antibiotic by enzyme-producing bacteria reduces the antibiotic concentration for the entire population (assuming rapid diffusion of the antibiotic). This can result in a population of bacteria being able to survive treatments of antibiotic above the single-cell minimum inhibitory concentration (scMIC). Consequently, the observed MIC, when measured at the standard population size of  $5 \times 10^5$  CFU mL<sup>-1</sup>, is higher (often by an order of magnitude) than the concentration that inhibits the growth of smaller population sizes [65]. This dependence of antibiotic effect on the initial size of the bacterial population is a well-studied phenomenon known as the inoculum effect. The MIC and scMIC are defined and discussed in Section 1.3.4. The inoculum effect is discussed in Section 1.3.5.

In our simulations, we capture the inoculum effect by modelling a well-mixed system in which the antibiotic concentration decreases at a rate that is proportional to the number of resistant bacteria. Furthermore, our simulations allow us to explore the effects of stochasticity in both initial population size and growth/death dynamics. For small droplet populations, these stochastic effects can be very significant. In particular, stochasticity can lead to some droplets having a higher-than-average population size, which in turn allows these droplet populations to survive at higher antibiotic concentrations than would be predicted for a bulk system.

Therefore our simulations predict a range of concentrations of antibiotic where stochastic effects in a population that is subdivided into droplets, lead to the survival of part of the population, while a deterministic mean-field theory would predict the success of the antibiotic treatment, i.e. complete elimination of the bacterial population. Thus, we show that splitting the population gives an extra survival benefit on top of the regular inoculum effect.

We first discuss results for a single parameter set (with a fixed bacterial density and antibiotic concentration), comparing the various deterministic and stochastic versions of the model (Section 5.2). Next, we vary the parameters of the model to explore the effects of changing bacterial density and antibiotic concentration (Section 5.3).

## 5.2 Predictions of the different model variants for a single parameter set

A droplet experiment starts with many identically prepared populations, each with the same concentration of antibiotic. Comparisons between droplet populations allow us to see heterogeneity in the survival responses and growth outcomes of clonal populations of bacteria. In our model, a single parameter set is analogous to a single droplet experiment.

In this section we compare simulation predictions for the four categories of the model (shown in Figure 4.2). To allow comparison of survival probabilities between the various model types, these simulations were all run for 10 droplet populations, with an initial antibiotic concentration of  $5 \mu\text{g mL}$  ( $5 \times scMIC$ ), and a mean initial population size of 5 bacteria per droplet.

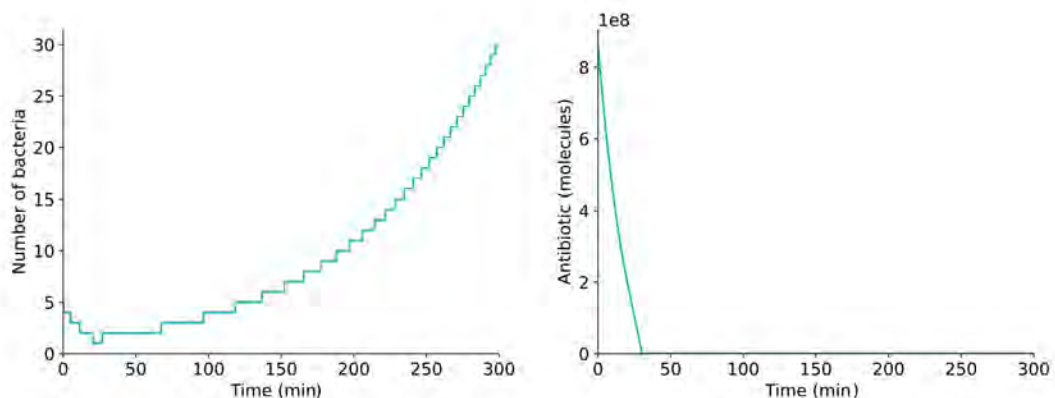


**Figure 5.1** *Example of a fully deterministic 10-droplet simulation, with an initial antibiotic concentration of  $5 \mu\text{g mL}^{-1}$  ( $5 \times \text{scMIC}$ ). The simulations start with exactly 5 initial bacteria per droplet, with a  $\text{scMIC}$  of  $1 \mu\text{g mL}^{-1}$  (the equivalent of  $1.72 \times 10^8$  molecules per 100 pL droplet). The graphs show the number of bacteria (left) and the corresponding amount of antibiotic (right) against time. All 10 droplet populations follow identical exponential growth and death dynamics.*

### 5.2.1 Deterministic model

In the fully deterministic version of the model we fill each droplet with an identical number of bacteria and simulate growth and death as deterministic first order processes. Figure 5.1 shows an example of a deterministic simulation output: all the droplet populations show identical dynamics for both the bacteria and antibiotic. Furthermore, we can see that all droplet populations survive the antibiotic treatment even though the concentration is  $5 \times$  the single-cell MIC value (displaying a small-population version of the inoculum effect). In these simulations, the bacterial population initially decreases, but once the antibiotic concentration has been reduced below the single-cell MIC, the growth of bacteria is no longer inhibited and the population shows regrowth. The antibiotic concentration continues to decrease whilst the droplet population regrows.

### 5.2.2 Stochastic droplet loading

Understanding the effects of the stochastic encapsulation of bacteria in a microfluidics experiment was one of the motivations for constructing the model.

In our model, the rate of antibiotic degradation differs between droplets based

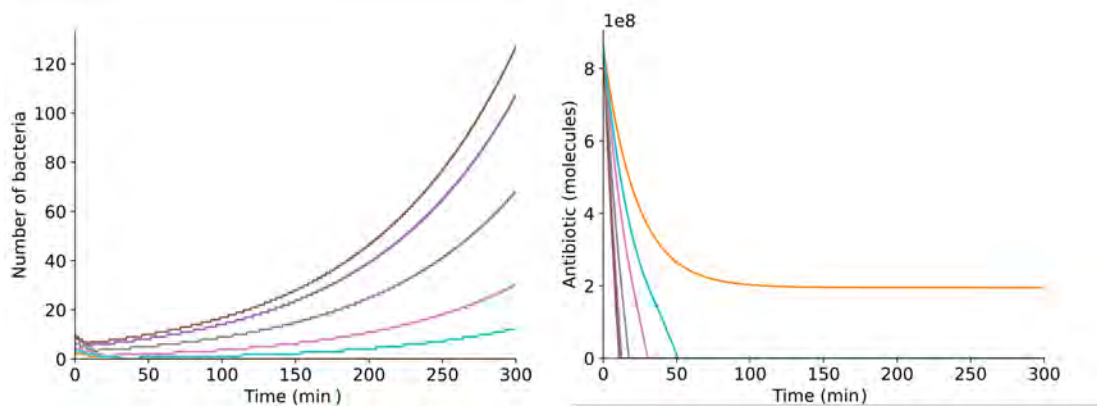


**Figure 5.2** *Example of a 10-droplet experiment, with deterministic dynamics, but Poisson-distributed initial population numbers (with a  $\lambda$  value of 5). The single-cell MIC was  $1 \mu\text{g mL}^{-1}$  (the equivalent of  $1.72 \times 10^8$  molecules per 100 picolitre droplet) and initial antibiotic concentration was  $5 \mu\text{g mL}^{-1}$  ( $5 \times \text{scMIC}$ ). The graphs show number of bacteria (left) and the corresponding amount of antibiotic (right) against time.*

solely on the initial population size,  $N_0$  (see Section 4.2 for the mathematical representation of this dependence). In a simulation of 10 deterministically loaded droplet populations, shown in Figure 5.1, each droplet contains exactly 5 initial bacteria, a total of 50 bacteria. In the simulation of 10 Poisson-loaded droplet populations, shown in Figure 5.2, the total initial population is still  $\approx 50$  bacteria. From an experimental perspective, this is equivalent to an initial suspension of  $5 \times 10^8 \text{ cells mL}^{-1}$ , distributed in droplets of volume 100 pL.

The key difference between the simulations in Figures 5.1 and 5.2, is that in the fully deterministic model, all the populations behave identically, which results in the survival of either all or none of the populations. Whereas when we introduce Poisson loading, the survival outcome diverges between droplet populations.

In the example plotted in Figure 5.2, the survival fraction of the droplet populations is 0.9 (9/10 droplets survive the antibiotic treatment). However for this set of parameters, the survival fraction could range from 0.3–1, depending on the distribution of the bacteria amongst the 10 droplets.

### 5.2.3 Stochastic proliferation and death dynamics

In reality, individual proliferation and death events are stochastic. Therefore we included stochastic dynamics in the model via a tau-leaping algorithm, as

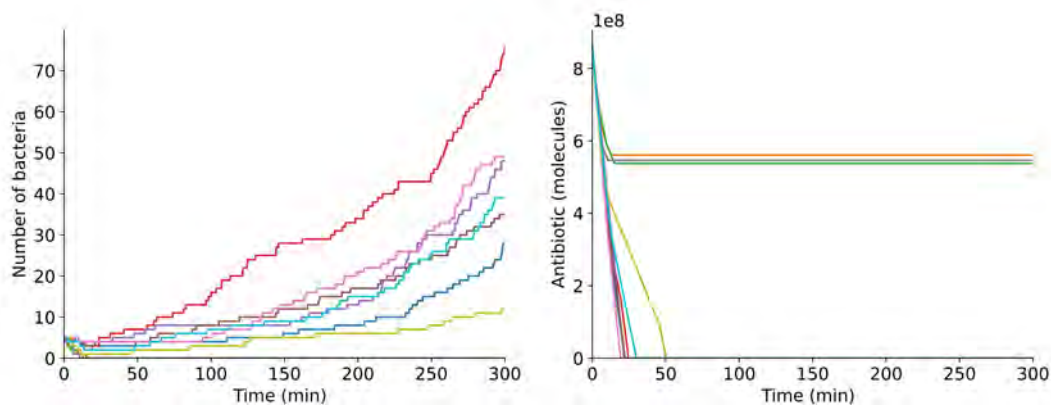


**Figure 5.3** *Example of a 10-droplet experiment, with stochastic dynamics, but fixed initial population numbers (each droplet starting with 5 bacteria). The scMIC was  $1 \mu\text{g mL}^{-1}$  (the equivalent of  $1.72 \times 10^8$  molecules per 100 picolitre droplet) and initial antibiotic concentration was  $5 \mu\text{g mL}^{-1}$  ( $5 \times \text{scMIC}$ ). The graphs show number of bacteria (left) and the corresponding amount of antibiotic (right) against time.*

discussed in Section 4.3.2.

Figure 5.3 shows simulation trajectories of 10 droplet populations, all with fixed initial  $N_0 = 5$  bacteria, i.e. with deterministic droplet loading, but simulated with stochastic proliferation and death dynamics. In this particular example we obtain a survival fraction of 0.7 (as 7 droplet populations survive the antibiotic exposure). However for this set of parameters, the survival fraction for 10 simulated droplets can range from 0.4–1.

With stochastic dynamics, in Figure 5.3, we observe a broad range of final population sizes, from 0 to 130 bacteria, in comparison to the deterministic dynamics of Figure 5.1, where all droplets finish with 30 bacteria.

## 5.2.4 Fully stochastic model

Incorporating both the stochastic bacterial loading and stochastic proliferation/death dynamics, demonstrated above, leads us to the fully stochastic version of the model, which is also the most realistic representation of the droplet experiments.

Running the fully stochastic model for 10 droplets at  $5 \mu\text{g mL}^{-1}$  and average loading,  $\lambda = 5$  bacteria per droplet, we obtain a wide range of final population

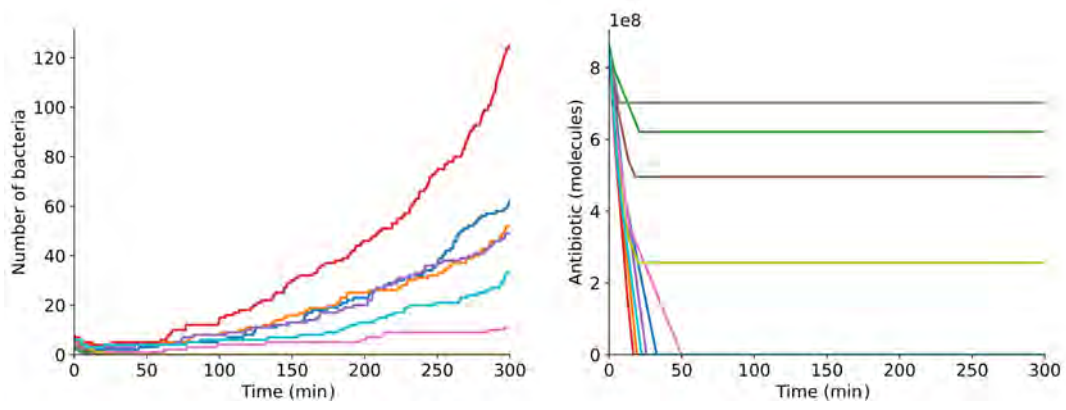


**Figure 5.4** *Example of a 10-droplet experiment, with stochastic dynamics and stochastic initial population numbers. The initial antibiotic concentration was  $5 \mu\text{g mL}^{-1}$  ( $5 \times \text{scMIC}$ ), with 5 initial bacteria per droplet, each with a  $\text{scMIC}$  of  $1 \mu\text{g mL}^{-1}$  (the equivalent of  $1.72 \times 10^8$  molecules per 100 picolitre droplet). The graphs show number of bacteria (left) and the corresponding amount of antibiotic (right) against time.*

sizes, as well as final antibiotic concentrations, as shown in Figure 5.4. In this example we obtain a survival fraction of 0.6. However for simulations with these parameters, the survival fraction for 10 droplet populations can range from 0.3–1, due to the stochastic nature of the model.

The final number of bacteria, after 300 minutes of simulated time, is  $\approx 320$ , which is higher than for the deterministic case ( $30 \text{ bacteria} \times 10 \text{ droplets} = 300 \text{ total bacteria}$ ), despite 4 of the stochastically grown droplet populations dying. The final number of bacteria can vary due to the different initial droplet populations, as well as the stochastic death and growth dynamics. Figure 5.5 shows the distribution of the final bacterial number for the fully stochastic simulation (for 500 repeats of the 10-droplet simulation). The final population sizes are distributed around the deterministic value of 300 bacteria, but 72.6% of the stochastic simulations result in a higher final number.

To explore the behaviour of the fully stochastic model, we investigated how the survival fraction depends on the droplet loading. Figure 5.6 shows the outcome of a single simulated droplet experiment, in which 1000 droplets were initialised with stochastic loading, with a mean value  $\lambda = 5$ . The replicate simulations were then binned by the initial number of bacteria, and survival probability was computed as a function of the initial droplet loading. The blue curve shows the distribution of initial population sizes (which follows a Poisson distribution with  $\lambda = 5$ ). The

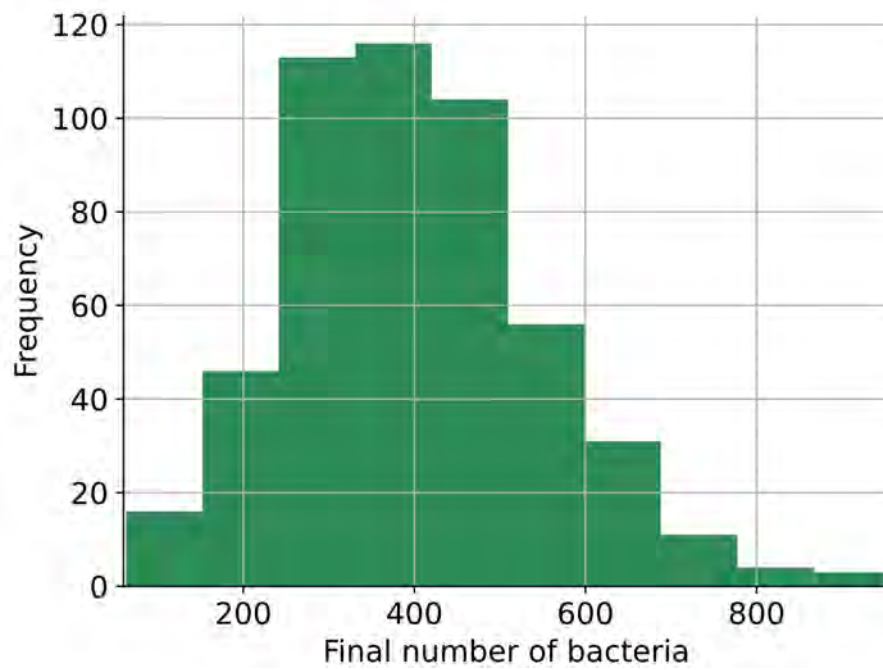


**Figure 5.5** *This histogram shows the final number of bacteria, over all 10 droplets, from 500 repeats of the fully stochastic simulation at an initial antibiotic concentration of  $5 \mu\text{g mL}^{-1}$ . In the equivalent deterministic case, the final number of bacteria is always 300.*

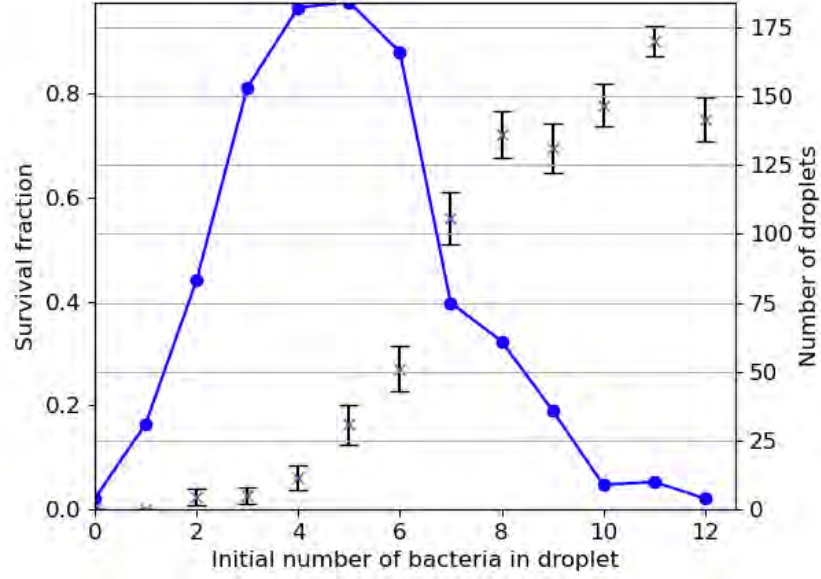


**Figure 5.6** *The fraction of droplets which survived a fully stochastic growth simulation with an initial antibiotic concentration of  $10 \mu\text{g mL}^{-1}$ , plotted as a function of the initial number of bacteria in the droplet. This simulation of 1000 droplet populations included stochastic filling and stochastic dynamics. The blue curve shows the distribution of the number of droplets with a given initial population size (right-hand axis). The crosses show the survival fraction of the droplet subpopulations, with error bars showing the standard deviation of 1000 bootstrap resamplings of the data. For the corresponding deterministic model,  $n_T=6.98$  (see Section 4.2.2).*

crosses show the fraction of surviving droplets for a given initial loading. Clearly, the initial loading strongly impacts the survival fraction. Survival probability increases for droplets with more initial bacteria, but we also see that these highly loaded droplets are rare.



## 5.3 Simulating the effect of varying antibiotic concentration, bacterial density, growth and death rates

Next we present results for many different simulated droplet experiments, in which we vary the key parameters. This allows us to determine the effect of different initial antibiotic concentrations and different initial bacterial densities. We first discuss the inoculum effect: dependence of the apparent MIC on bacterial density. Next, we discuss the survival probability of the resistant bacteria under increasing antibiotic stress, followed by the results for different values of the bacterial loading density. Finally, we investigate the impact of varying the bacterial growth and death rates within our model.

### 5.3.1 Inoculum effect: dependence of the MIC on bacterial density for droplet populations

In our model, bacteria in a droplet survive if the antibiotic concentration is less than the user-defined single-cell MIC parameter (*scMIC*). We can define an apparent MIC, for a population that is encapsulated into droplets, as the concentration of antibiotic for which only a small percentage<sup>1</sup> of droplet populations survive. This apparent MIC is not expected to be the same as the *scMIC*. In fact, in the fully deterministic case, due to the way that we model antibiotic degradation (see Section 4.4), we observe a proportionality between the apparent MIC and the density of  $\beta$ -lactam-producing bacteria for the small population sizes we are studying (as more bacteria are able to produce more enzymes which degrade more antibiotic molecules per timestep). We therefore find a positive, linear relationship between the inhibitory concentration and bacterial density for the fully deterministic case; this is shown in Figure 5.7 (in dark green).

This result fits well with a study of a  $\beta$ -lactamase-carrying *E. coli* strain by Scheler et al., who found that the amount of antibiotic needed to inhibit growth remained approximately constant when normalised to the antibiotic concentration per bacterium, over a wide range of bacterial densities [66]. We also measured the

---

<sup>1</sup>The effect of defining the MIC with different percentages is explored below in Figure 5.7.

inoculum effect experimentally; Figure A.12 shows the results for a set of plate reader experiments, where higher bacterial densities survive higher antibiotic concentrations.

This relationship is perturbed when stochastic filling and stochastic dynamics are added to the simulations. Figure 5.7 plots the apparent MIC at each bacterial loading density for partially and fully stochastic simulations. The relationship between apparent MIC and bacterial density is still linear, but the data shows a shift, in that the apparent MIC is higher for the stochastic simulations compared to the deterministic case. The shift is greatest for the fully stochastic model (in red), compared to the cases of only stochastic loading or only stochastic dynamics. In panel (a), we have chosen to define the MIC as the concentration of ampicillin that reduced the number of droplet populations by 90% (a commonly used cutoff, sometimes referred to as MIC<sub>90</sub> [146]). Panels (b) and (c) show that whilst the deterministic result is the same regardless of the cutoff percentage, the stochastic response is highly dependent on how one defines, or indeed, is able to measure ‘survival’. In particular, the choice of defining the apparent MIC at less than 50% of droplet populations (panel (b)) leads to almost no difference between deterministic and stochastic results. It should be noted, however, this definition is not relevant for the following results presented in this Chapter, which are reported as absolute survival fractions of droplet populations, without a percentage cutoff (although one could imagine a non-zero survival fraction representing the sensitivity of a laboratory measurement).

Therefore, our simulations show (i) an inoculum effect in which the apparent MIC has a linear relationship with the bacterial density, as shown experimentally [66], and (ii) an additional shift in the apparent MIC that is caused by the stochasticity of bacterial loading into droplets and the stochasticity of bacterial growth and death dynamics. Our results strengthen previous suggestions [65] that the single-cell MIC is a more reliable parameter for describing intrinsic bacterial resistance to antibiotics than the MIC, as it is typically measured.

### 5.3.2 Survival probability as a function of antibiotic concentration

Next, we perform a series of 1000-droplet simulations, for antibiotic concentrations in the range 0–25  $\mu\text{g mL}^{-1}$ . In each simulation, we record the fraction

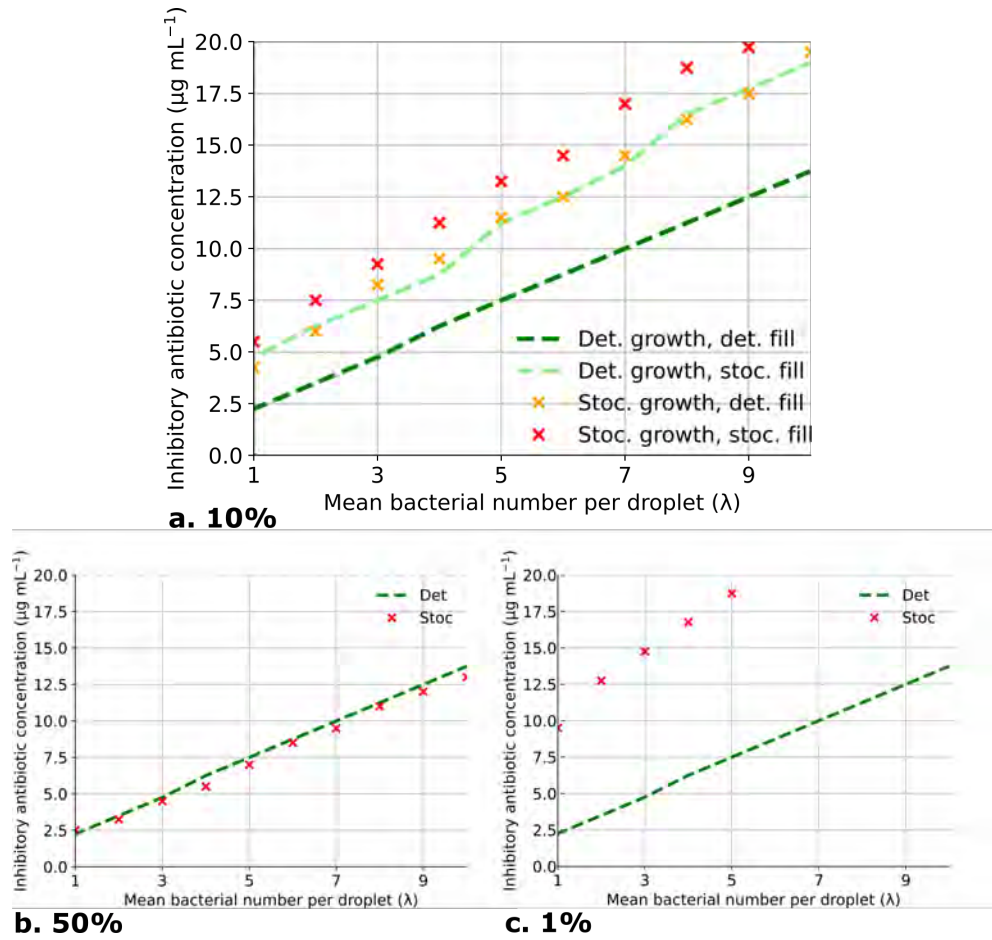


**Figure 5.7** *The dependence of the apparent MIC on the mean number of initial bacteria,  $\lambda$ , per droplet for each mode of the model. This dependence is linear for the deterministic case (the dark green dashed line). The relationship is still approximately linear in the simulations with added stochasticity (in growth/death and bacterial distribution), but the apparent MIC is increased. Each simulation was run for 1000 droplets and the inhibitory concentration was taken as the concentration where less than (a) 10%, (b) 50% and (c) 1% of droplet populations survive.*

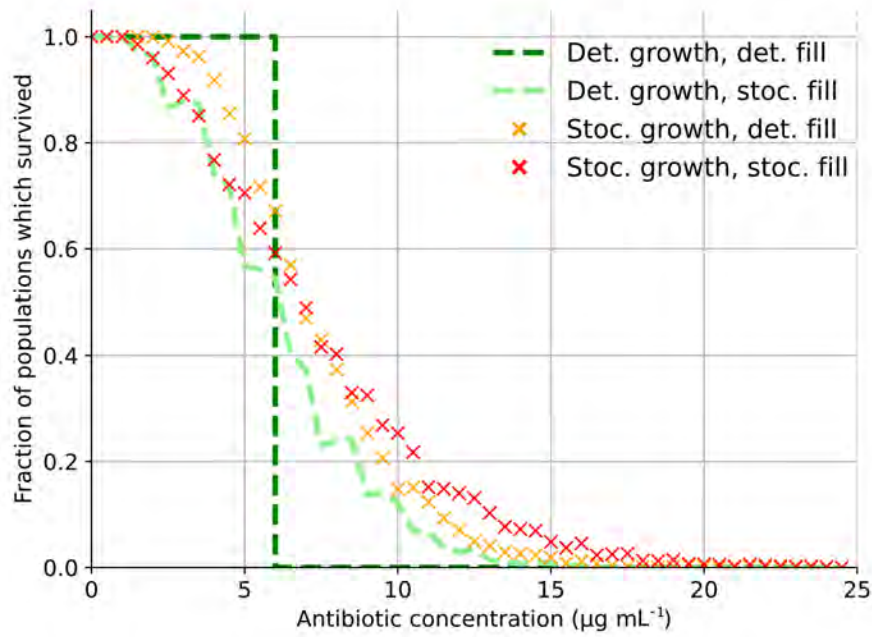


**Figure 5.8** *The survival fraction of droplet populations at different concentrations of antibiotic. Survival is defined as any number of bacteria in a droplet and is calculated at 300 minutes of simulated time. All droplets started with a bacterial population of  $\lambda=5$ . Separately, both stochastic bacterial filling (light green ‘- -’) as well as stochastic growth (orange ‘×’) have a positive effect on survival probability. Combining Poisson distributed bacteria and stochastic growth (red ‘×’) leads to the potential of survival at the highest concentrations of antibiotic.*

of surviving droplet populations after 300 minutes. This mirrors the droplet experiments presented in Chapter 6.

We compare the survival curves for simulations with both deterministic and stochastic filling and dynamics (see Figure 4.3), whilst keeping the mean bacterial loading density constant ( $\approx 5$  bacteria per droplet, or  $\approx 5000$  cells per 1000-droplet simulation). In Figure 5.8 we see that, in the deterministic case, there is a sharp cutoff for survival at  $7 \mu\text{g mL}^{-1}$ . This is much higher than the scMIC concentration of  $1 \mu\text{g mL}^{-1}$ . This is because for concentrations in the range  $1\text{--}7 \mu\text{g mL}^{-1}$ , the antibiotic degradation is fast enough to reduce the concentration in the droplet to below  $1 \mu\text{g mL}^{-1}$  before all the bacteria die, and therefore the population can start to regrow. The effect is a manifestation of the same inoculum effect that was discussed in the previous section.

Furthermore, adding stochastic elements to the simulation changes the shape of the survival curve. Rather than being a step function, it acquires a stretched out ‘tail’. Importantly, we now see surviving droplets at concentrations that are more than double the apparent MIC of the deterministic simulations. We also see that separately, stochastic dynamics and stochastic filling have similar effects on the survival probabilities. These effects are in some way additive, since we find that the fully stochastic model results in the highest survival fractions.

We also note that the stochastic simulations show notably lower survival fractions at concentrations below the deterministic MIC (i.e. below  $7 \mu\text{g mL}^{-1}$ ). In the deterministic case, all droplet populations survive for concentrations lower than this apparent MIC value, whereas up to 50% of these populations do not survive in the stochastic models. This is because some droplets have bacterial densities below the average of 5 bacteria per droplet in the stochastic case.

### 5.3.3 Effect of bacterial loading density of bacteria on survival curves

As discussed above, increasing the number of bacteria per droplet increases the rate at which the antibiotic is degraded and therefore increases the apparent MIC. Figure 5.9 shows survival curves as a function of antibiotic concentration for different values of the droplet loading parameter,  $\lambda$ . As expected, higher droplet loading leads to increased survival, both in the deterministic case (dashed lines in Figure 5.9) and in the stochastic case (crosses in Figure 5.9). By increasing

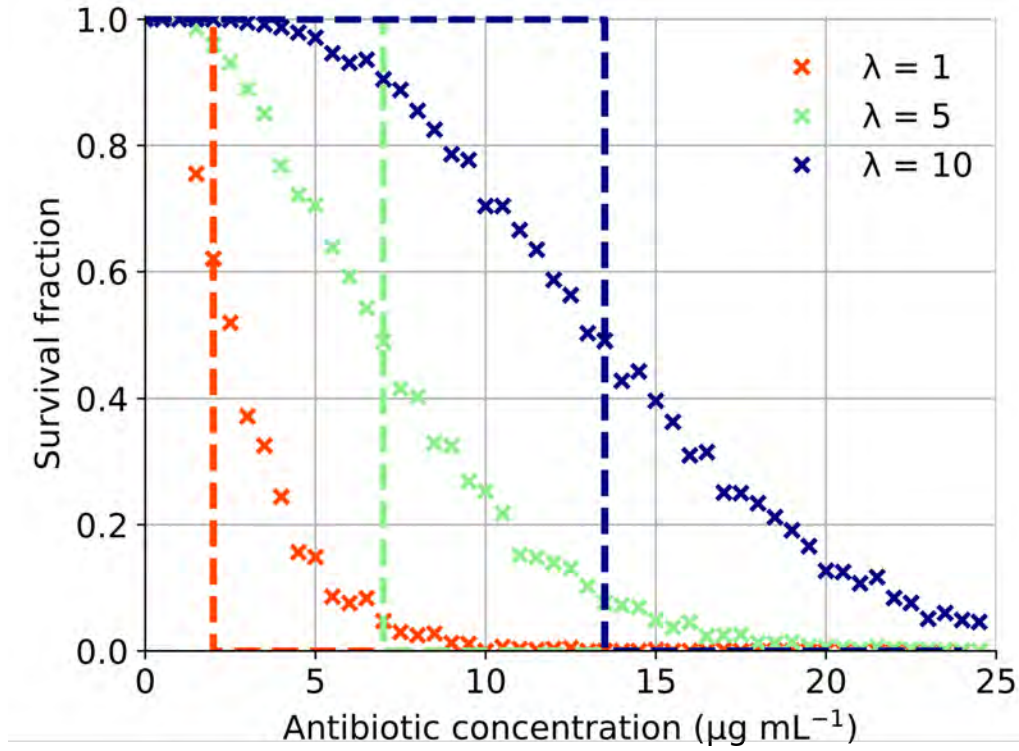


**Figure 5.9** *Survival fraction vs. antibiotic concentration at three different  $\lambda$  values. Survival fraction of the droplet populations was calculated after 300 minutes of simulated time. The deterministic case, where the initial number of bacteria is identical in every droplet and equal to  $\lambda$ , is shown with dashed lines. The survival fraction for the fully stochastic case (growth and loading), is shown with crosses. Each simulation was run for 1000 replicate droplets and the scMIC was kept constant at  $1 \mu\text{g mL}^{-1}$ .*

the  $\lambda$  value we can see the protective effect that the resistant strain is able to achieve when in more populated droplets, i.e. higher concentrations of bacteria are able to survive higher concentrations of antibiotic.

Once again, we are able to see that the stochastic model results in survival at far higher concentrations of antibiotic than the deterministic model. For high densities of bacteria (on the order of bulk microbiology experiments), we would expect the effects of stochasticity to disappear.

### 5.3.4 Effect of growth and death rate on survival curves

The results presented above were obtained for simulations with constant growth and death rates for comparative purposes. Next, we explore how our results depend on the bacterial growth and death rates. Growth rate, for example, could be changed experimentally by changing the growth medium, while death rate might be affected by factors including the osmolarity of the medium. Moreover, faster-growing bacterial populations also show faster lysis rates when exposed to antibiotic [133].

Figure 5.10 shows that in this model, the survival of a droplet population is independent of the bacterial growth rate. Figure 5.10 shows a plot of survival fractions for multiple 1000-droplet simulations, for a range of growth rates, where all other parameters were kept constant. For this parameter set, the antibiotic concentration is below the (apparent) deterministic MIC value, so the survival probability is 1.0 for all the deterministic simulations, and it is somewhat lower (0.8) for the stochastic simulations. In both cases, the survival fraction is independent of the bacterial growth rate. This is because within each droplet the bacteria do not grow when the antibiotic concentration is over the single-cell MIC.

We note that the growth rate does affect the final population sizes in the surviving droplets. However, because we define survival as the presence of any number of living bacteria, this does not influence the survival fraction.

Survival of the droplet population is sensitive to the death rate, however. Figure 5.11 shows this dependence for the stochastic and deterministic case. For the deterministic case, there is a threshold death rate below which all droplet populations survive; above this threshold no bacteria survive. For the stochastic

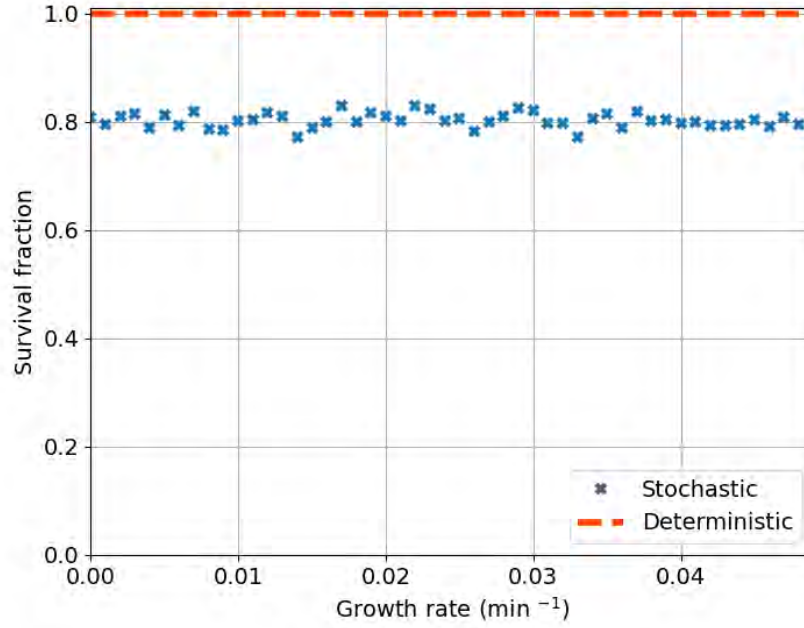


**Figure 5.10** *Dependence of survival fraction on the bacterial growth rate. Simulations were run for growth rates of  $0$ – $0.05 \text{ min}^{-1}$  in intervals of  $0.001$  (doubling times of  $\infty$ – $14$  minutes). Each simulation was repeated for 1000 droplets with  $\lambda = 5$ ,  $\text{scMIC} = 1 \mu\text{g mL}^{-1}$ , at an initial antibiotic concentration of  $5 \mu\text{g mL}^{-1}$  and a fixed death rate of  $0.045 \text{ min}^{-1}$ .*

case, the survival fraction varies smoothly from 1 to 0 upon increasing the death rate. This is because in the model, survival depends on the degradation of the antibiotic to below a threshold single-cell MIC value, before the bacterial population is all killed. The slower the death rate, the longer the  $\beta$ -lactamase enzymes have to degrade the antibiotic molecules before the population becomes extinct.

### 5.3.5 Dynamical trajectories of droplet population growth and death

It is also interesting to investigate how the bacterial numbers in each droplet change prior to the defined ‘survival cutoff time’ of 300 minutes. To this end, we performed 1000-droplet simulations for an average loading of 5 bacteria per droplet, and recorded the distribution of population sizes,  $N(t)$ , across the droplets. This simulation was then repeated for a range of antibiotic



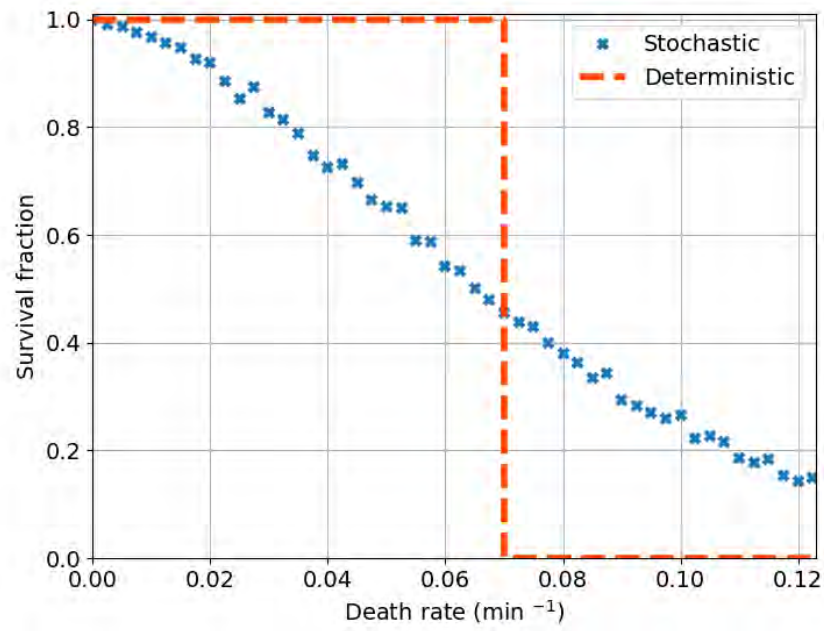


**Figure 5.11** *Dependence of survival fraction on the bacterial death rate. Simulations were run for death rates of  $0\text{--}0.125\text{ min}^{-1}$  in intervals of  $0.0025$  (half times of  $\infty\text{--}5.5$  minutes). Each simulation was repeated for 1000 droplets with  $\lambda = 5$ ,  $scMIC = 1\text{ }\mu\text{g mL}^{-1}$ , at an initial antibiotic concentration of  $5\text{ }\mu\text{g mL}^{-1}$ , and a fixed growth rate of  $0.01\text{ min}^{-1}$ .*

concentrations, from 0 to  $25 \mu\text{g mL}^{-1}$ . Figure 5.12 shows the results, presented as heatmaps. Each panel shows the distribution for a different time point in the simulations, to give an indication of the growth and death dynamics prior to the survival count at 300 minutes (which is shown in Figure 5.8). We can see a spread in population sizes at all times for the fully stochastic case, which can be compared to the deterministic case indicated by the black dotted line (where all 1000 droplets have the same population size at any given time).

On the first panel, at T1, we can see that all the deterministically filled droplets start with 5 bacteria (represented by the vertical dotted line). Whereas the for the stochastically filled droplets, a Poisson distribution with  $\lambda = 5$  is shown in green; with the darkest greens (the highest proportion of droplets) at 5 bacteria. At T30 we can see that growth is suppressed for the majority of droplets above the antibiotic concentration of  $5 \mu\text{g mL}^{-1}$ , and this trend continues for T60 and at T180. At later times the growth trajectories are spread in the stochastic model, particularly for droplets containing low antibiotic concentrations. However, at high concentrations of antibiotic (above  $20 \mu\text{g mL}^{-1}$ ), we see that almost all the droplet populations are zero.

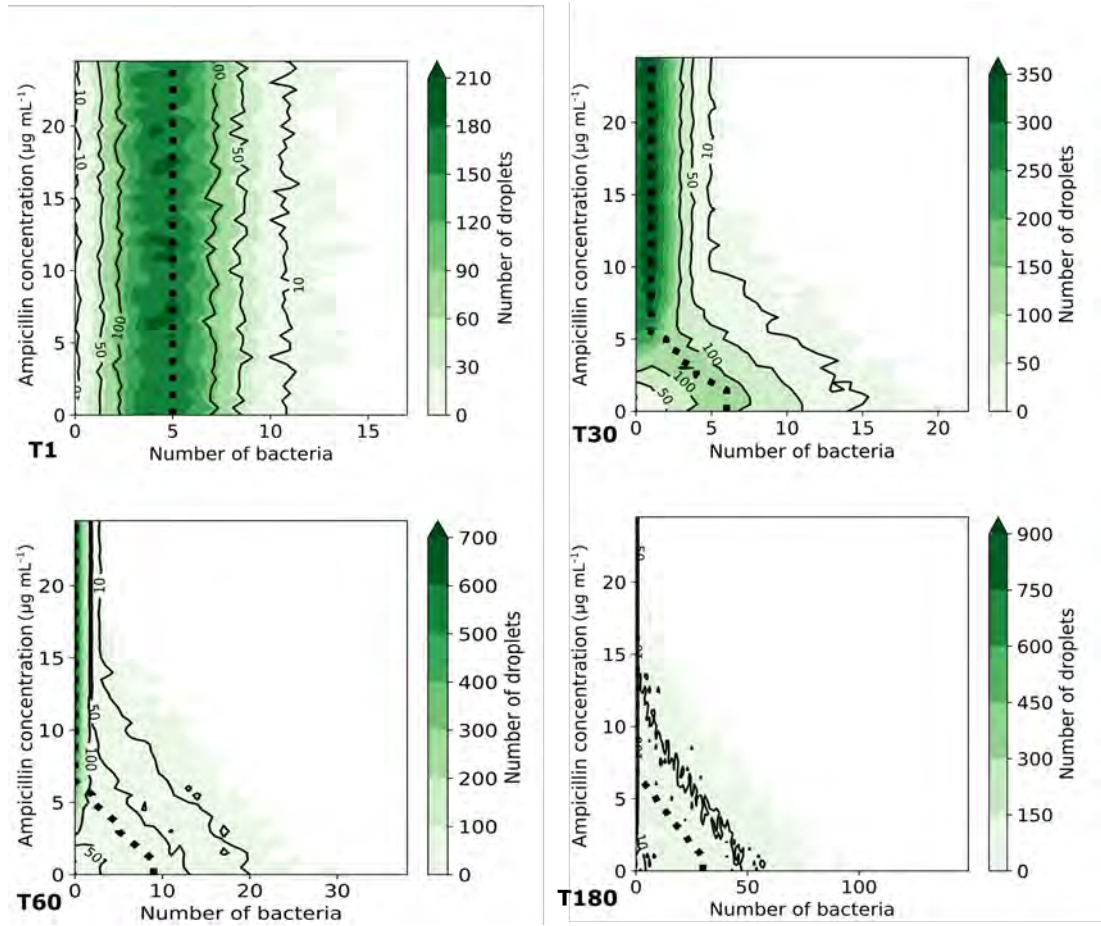


**Figure 5.12** Heatmap showing the number of bacteria ( $x$ -axis) at four time points ( $T$ , in minutes) of the simulation. A simulation of 1000 droplets was run with a starting population  $\lambda=5$ , for each antibiotic concentration (in steps of  $0.5 \mu\text{g mL}^{-1}$ ), shown on the left hand axis. The colour shows the number of droplets at each population size (colourbar scale shown on the right) for droplets simulated with stochastic growth and filling. The dotted black line shows the deterministic case.

## 5.4 Discussion

This model indicates that the survival probability of a droplet population is heavily dependent on both the antibiotic concentration ( $a_0$ ) and the initial number of bacteria ( $N_0$ ), in that particular droplet (see Figure 5.9).

Populations that initially contain more than one bacterium are able to survive at concentrations above the single-cell MIC (as shown for the populations in Figures 5.8 and 5.12 which start with an average of 5 bacteria). As suggested by previous work [65], by growing together, resistant bacteria are able to cooperate with each other and increase the collective apparent MIC above the single-cell MIC. Thus, in both the deterministic and stochastic cases, our model predicts a strong small-population inoculum effect. The addition of simple stochastic elements to the model leads to increased survival in comparison to the deterministic cases. Figure 5.8 shows that either stochastic filling or stochastic growth has a dramatic effect on the probability of survival beyond the (apparent) deterministic MIC. As is clear in Figure 5.12, there is survival in the stochastic case when there is none in the deterministic case.

Subdivision of a population into ‘droplets’ mimics spatial heterogeneities that are found in natural environments. Therefore we might expect real bacterial populations in spatially structured environments to survive higher antibiotic concentrations than suggested by bulk MIC experiments. Our results suggest that in the face of  $\beta$ -lactam antibiotics, bacteria are stronger in groups, and that structural stochastic effects should be taken into account as they lead to a range of survival probabilities that are not seen when we only consider a deterministic model. This means an infection might unexpectedly survive treatment, especially in situations where there is structure, such that small bacterial populations are isolated from one another and the bacteria exist in isolated communities.

A key feature of our model is the definition of a fixed single-cell MIC for individual bacterial cells. Experimental work suggests that antibiotic efficacy is determined by the amount of antibiotic per bacterial colony forming unit (CFU), not by the absolute antibiotic concentration [66]. In addition, it has been shown (both *in vitro* and *in vivo*) that the scMIC is the level of antibiotic concentration which leads to the selection of resistant mutants [65]. Therefore our model helps us translate from the dynamics of individual cells to the population level, which is important to predicting the response and evolution of the larger population.

The results presented in this chapter provide motivation for the small population droplet experiments that we discuss in Chapter 6. The model predicts that with Poisson loading we expect some droplet populations to survive at higher antibiotic concentrations than in a bulk experiment with the same average bacterial density. Moreover, survival of individual droplets should be correlated with their initial bacterial number,  $N_0$ . In reality, we do see survival of droplet populations in Chapter 6, but this is only correlated with the initial population number, at certain antibiotic concentrations (see Figure 6.6). This suggests different or additional underlying dynamics than those we have assumed for this model, at least for the particular strain of bacteria and the  $\beta$ -lactam antibiotic studied.

### 5.4.1 Future amendments or extension of the simulation

There are a number of ways which we might extend the current model, which could perhaps better represent and aid the understanding of the experimental data. Currently, growth and death are modelled at fixed rates (see Sections 4.5.3 and 4.5.3). However experimentally we see a distribution of growth and death rates between droplet populations (see Figure 3.3 and Figure 6.9), so it would be interesting to include growth rate heterogeneity among the individual bacteria. Another observable difference between the simulation and the experimental results in Chapter 6, is the suppression of division when the bacteria are exposed to antibiotics. Therefore, it would be interesting to investigate the effect of including persistence or filamentation responses in the model. Additionally, as discussed earlier in Chapter 4, we could explore in more detail the modelling of the antibiotic degradation using a full Michaelis-Menten model.

# Chapter 6

## Exposure of $\beta$ -lactamase-producing bacteria to antibiotics: experiments

### 6.1 Introduction

The production of  $\beta$ -lactamase enzymes is the most common defense mechanism against  $\beta$ -lactam antibiotics in Gram-negative bacteria. This is relevant clinically as  $\beta$ -lactam antibiotics are amongst the most widely used classes of antibiotic in medicine.  $\beta$ -lactamase production is an intrinsically cooperative form of resistance, as the hydrolysis of the  $\beta$ -lactam antibiotic molecules reduces the global concentration and therefore benefits any surrounding sensitive organisms. This is consistent with observations that the inoculum effect is known to be particularly pronounced for  $\beta$ -lactamase-producing strains, such that the density of a culture has a significant impact on the MIC [64]. Section 1.3 includes a background discussion of  $\beta$ -lactam antibiotics and  $\beta$ -lactamase-mediated antibiotic resistance.

In this chapter I present an experimental investigation of the population dynamics of  $\beta$ -lactamase-producing bacteria in the presence of a  $\beta$ -lactam antibiotic. In my experiments I used the  $\beta$ -lactam antibiotic ampicillin and a  $\beta$ -lactamase-producing strain of *E. coli*, RJA003, which is fluorescent in the cyan channel (see Section 2.2.1).

Bulk-scale 96-well plate experiments were performed using a plate reader for a range of bacterial starting densities to measure the inoculum effect in large

populations. These results were then complemented by droplet experiments, which allowed us to measure the dynamics of small populations under the same range of antibiotic concentrations. In the droplet experiments, the direct observation of individual bacterial cells using fluorescent microscopy allowed us to detect the survival of even a single bacterium in a droplet. It is important to understand the effect of antibiotics on this scale as infections can be caused by very small populations, with infectious doses sometimes as low as a single bacterial cell [13, 14].

Passively distributing the bacterial suspension into droplets allowed us to sample a range of initial population sizes and therefore to test how initial bacterial number affects survival as well as other dynamics of the small populations.

The results of the plate reader and droplet experiments can be compared to the simulation predictions that were presented in Chapter 5. Our simulations pointed to the existence of a small-population inoculum effect, where droplets containing higher numbers of resistant bacteria contained more  $\beta$ -lactamase and therefore showed faster rates of antibiotic degradation; making them more likely to survive antibiotic treatment. Here, we will compare our bulk plate reader experiments to the predictions of the deterministic simulation model, and we will compare our droplet experiments to the predictions of the stochastic version of the simulations.

## 6.2 Plate reader experiments

Bulk-scale growth experiments in a plate reader were performed to assess the large-population response of a  $\beta$ -lactamase-producing *E. coli* strain, RJA003, to ampicillin. Experiments were performed over a range of antibiotic concentrations and a range of starting bacterial densities to allow us to observe the inoculum effect as well as the MIC.

### 6.2.1 Plate reader procedure

A microplate reader was used to measure the growth response of RJA003 at various bacterial densities to a range of ampicillin concentrations, using optical density (OD) measurements every 10 minutes over 24 hours. Optical density measurements are a frequently used, well-documented method for measuring

bacterial growth [27]. To avoid the selection of an atypical variant clone, bacteria from 4–5 colonies on an agar plate were mixed and incubated in M9+gl (0.4%) media to prepare an overnight bacterial suspension [58]. On the day of experiment, 200  $\mu\text{L}$  of the overnight suspension was diluted in 10 mL of fresh M9+gl (0.4%) media and placed back in the 37°C incubator for 1.5 hours. The 96-well plate was prepared with media and ampicillin (see Figure 6.1) and was placed on ice. The bacterial culture was then diluted with fresh medium to achieve 4 different bacterial densities. The bacterial suspension was then pipetted into the wells as shown in Figure 6.1, so that each well contained 200  $\mu\text{L}$  of liquid. The plate setup was designed to achieve 3 replicate wells for each combination of bacterial density and antibiotic concentration .

The 96-well plate was then placed into the microplate reader (BMG CLARIOstar Plus) and incubated at 37°C, taking OD readings at 600 nm, every 10 minutes for 13–24 hours. Between readings, the 96-well plate was shaken at 600 rpm in a double-orbital mode to maintain aerobic conditions throughout the experiment. Three sets of plate reader experiments were performed (PR1–3), for different ranges of antibiotic concentration.

To calibrate the bacterial densities, we also took an additional OD measurement for each of the inoculating suspensions (using a Cary 4000 UV-Vis spectrometer), before performing a series of dilutions on agar plates for colony counting (CFU measurements). Figure A.5 shows the results of this calibration.

### 6.2.2 Plate reader results

The three plate reader experiments, PR1–3, showed consistent results. For clarity, we focus here on the results of experiment PR3. Analysis of the other plate reader experiments can be found in Appendix A. The plate reader results all display a clear inoculum effect. As shown in Figure 6.2, growth is observed at all concentrations of ampicillin (up to 1.25 mg mL<sup>-1</sup>) for every replicate of the highest bacterial density (B1,  $5.05 \times 10^6$  CFU mL<sup>-1</sup>), indicated in green on the schematic. However for the lower densities of bacteria (B2–B4), no growth is observed at the higher antibiotic concentrations, indicated in red on the schematic. To verify that our plate reader experiments show a real inoculum effect, we also tested whether the growth rate of uninhibited (antibiotic-free) populations depended on initial bacterial density. Figure A.11 shows that there is no such dependence.



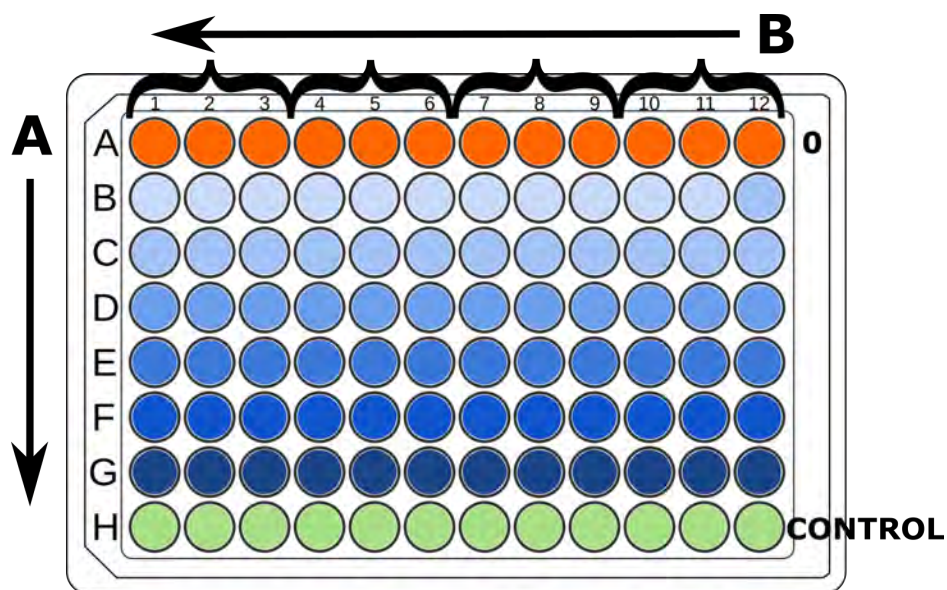


**Figure 6.1** *Diagram of 96-well plate setup used in the three experiments, PR1–3. Each colour represents a different antibiotic concentration (A) (this range was different for each experiment). Columns 1–3, 4–6, 7–9 and 10–12 contain bacterial suspensions of decreasing cell density (B). Each well contained 200  $\mu$ L of liquid; for rows B–G, 100  $\mu$ L of ampicillin and 100  $\mu$ L of the bacterial suspension at the appropriate dilutions; row A (orange) was filled with 100  $\mu$ L of the bacterial suspension and 100  $\mu$ L of media, and row H (green) was a control, with 200  $\mu$ L of M9+gl media.*

Susceptibility to antibiotic stress strongly depends on the bacterial strain and type of antibiotic. Even for a given antibiotic, effectiveness can vary drastically; for example, in a test of 9 antimicrobials on 27 *E. coli* ATCC 25922 strains, ampicillin was found to have the widest MIC range of  $1\text{--}\geq 128\text{ }\mu\text{g mL}^{-1}$  [147]. For the strain used in these experiments, we expected to find a high MIC value, because RJA003 is resistant to  $\beta$ -lactam antibiotics (see Section 2.2.1). Standard MIC assays are conducted using bacterial suspensions of  $\approx 5 \times 10^5\text{ CFU mL}^{-1}$  to minimise variability (the CLSI recommends testing between  $2\text{--}8 \times 10^5\text{ CFU mL}^{-1}$  [58]). In my plate reader experiments, this bacterial density lies between B3–B4 in PR3 and PR2 (Figures 6.2 and A.7). Therefore we find the MIC, as defined in the standard way, to be  $0.375\text{--}0.625\text{ mg mL}^{-1}$ . We note that even at the highest bacterial density tested, no growth was detected in the plate reader for concentrations of ampicillin higher than  $1.25\text{ mg mL}^{-1}$  (see Figure A.6).

We also note that Figure 6.2 shows an apparent increase in the lag time (delay before the start of growth) as the bacterial density decreases. However this is likely to be caused by the detection threshold for the OD measurements, rather than an actual change in lag time.

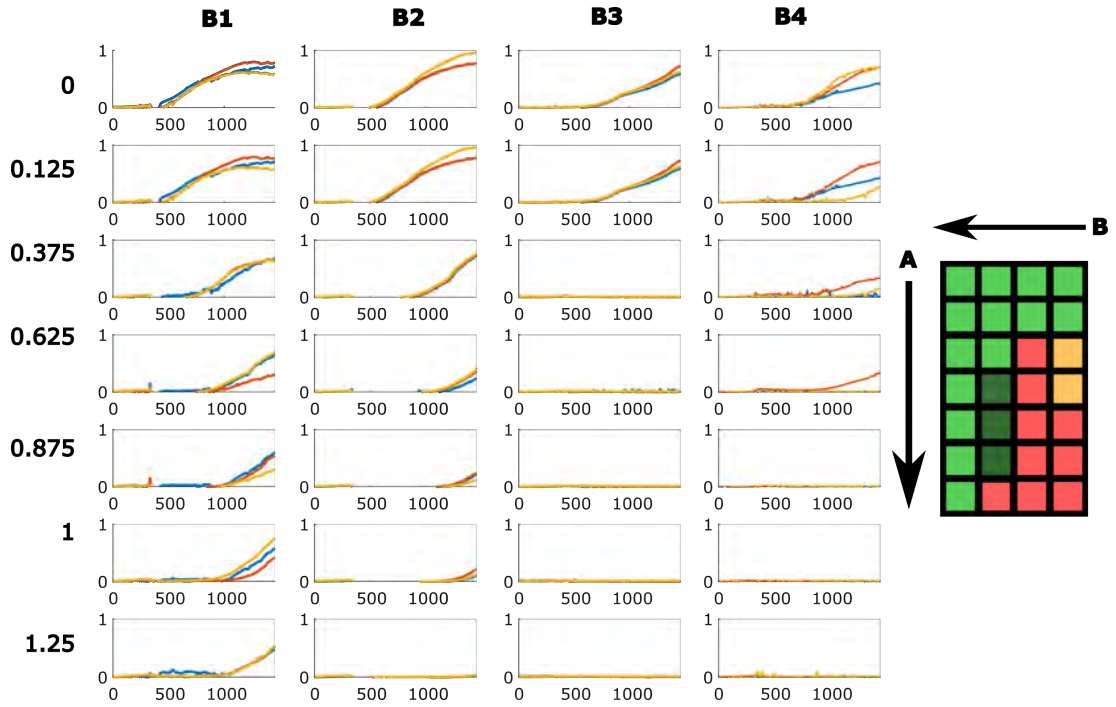


**Figure 6.2** Grid of plate reader ( $OD_{600}$ , y-axis) growth curves over time (in minutes, x-axis) from experiment PR3. Each plot shows 3 replicates for each combination of initial bacterial density and ampicillin concentration. Ampicillin concentration is increasing top to bottom (values given in  $\text{mg mL}^{-1}$ ). The top row shows uninhibited growth. Bacterial density is decreasing left to right (from B1 to B4), with initial concentrations of  $5.05 \times 10^6$ ,  $1.65 \times 10^6$ ,  $7 \times 10^5$ ,  $2 \times 10^5$   $\text{CFU mL}^{-1}$ . The OD values were corrected with the corresponding control subtracted as a baseline. The schematic shows growth as green, while late growth (that starts after 1000 minutes) is shown in dark green; yellow shows growth for some, but not all of the replicate wells; red indicates no growth. The arrows show increasing ampicillin concentration (A) and bacterial density (B).

## 6.3 Droplet experiments

Next, I performed a set of droplet experiments, in which small populations of bacteria exposed to ampicillin were individually monitored over the course of 4–6.5 hours. I used the same strain of *E. coli* as in the plate reader experiments above, and a similar range of ampicillin concentrations. For comparison of the bacterial densities in the droplet and plate reader experiments it is useful to note that a single bacterial cell in a droplet corresponds to  $\approx 1.1 \times 10^7$  CFU mL<sup>-1</sup> (see Section 2.6). The droplet experiments aimed to investigate how the inoculum effect observed in the plate reader plays out in small populations. The droplet experiments produce a far richer data set than our plate reader experiments, with thousands of replicates for each condition, as well as images that can be analysed to determine possible physiological changes in response to antibiotic.

One motivation for our droplet experiments was the simulation predictions of Chapter 5. In these simulations, stochastic encapsulation of bacteria in droplets allowed bacteria to survive at higher antibiotic concentrations than would have been possible in bulk populations. This was because some droplets had a higher than average bacterial density, hence cooperative degradation of the antibiotic was predicted to be more effective in these droplets. As we shall see, however, the results of our droplet experiments are considerably more complex than the simulation predictions.

### 6.3.1 Droplet experiment procedure

The experimental method was the same as that outlined in Chapter 2, and used in Chapter 3 to study uninhibited growth in droplets, except that in this chapter, ampicillin is introduced prior to bacterial encapsulation, via a Y-junction. The Y-junction methodology was introduced in Chapter 2, Section 2.2.6.

In contrast to the plate reader experiments, for the droplet experiments we did not vary the density of the starting bacterial inoculum. Instead, the Poisson loading of the droplets (discussed in Sections 1.4.2 and 2.5.3) led naturally to a range of initial population sizes within each experiment.

The procedure was as follows. A single bacterial colony was picked from a plate and grown overnight. On the day of the experiment, the overnight culture

suspension was diluted into fresh media (50  $\mu\text{L}$  into 10 mL) and placed in a 37°C incubator for 1.5 hr, after which the bacteria grow exponentially. A 1 mL syringe was filled with this culture and attached to a Y-junction along with a solution of ampicillin (prepared at  $2\times$  the desired experimental concentration). The microfluidic device was mounted onto a microscope and a second syringe containing a mix of oil and surfactant was attached to the oil inlet. The Y-junction was then fixed to the aqueous inlet of the microfluidic device, and the fluids were pushed through the channels using syringe pumps to create picolitre droplets (see Section 2.2 for description and justifications of the microfluidic methodology and detailed experimental procedure). The droplets were then imaged every 10 minutes in brightfield (to image the droplet boundaries) and in the CFP channel (to image the bacteria), for up to 6.5 hours. Appendix B provides a step-by-step protocol.

These microscopy images were then converted into a dataset containing the numbers of bacteria in each droplet (as well as other quantities such as total biomass), for each timestep, using the image analysis methods explained in Section 2.3.

### 6.3.2 Droplet experiments: qualitative observations

In total, fifteen droplet experiments were performed for ampicillin concentrations in the range 0.625–10  $\text{mg mL}^{-1}$ ; these are listed in Table 6.1. Repeat experiments are labeled A–D and the ampicillin concentration, in  $\text{mg mL}^{-1}$ , is given in brackets. Each experiment involved the observation of 385–5999 droplets which were able to be tracked throughout the entire experiment. This includes empty droplets which did not contain any *E. coli*. Delay refers to the time between droplet production and the first image acquisition. A range of 10 minutes is given to account for the range of travelling times for droplets in different areas of the reservoir, as well as the difference between the start position and end position of the scan. Baltekin et al. were able to detect inhibited growth of *E. coli* from ampicillin after 11 minutes [148]. Of the experiments presented in this thesis, 53% (8/15) are within this time (see Table 6.1). The impact of the imaging delay is further discussed in Section 2.5.3.

Figure 6.3 shows trajectories of the bacterial count, for hundreds of replicate droplets, for each of the experiments. The range of initial bacterial counts, arising from the Poisson loading, can be seen in the variation in the bacterial counts (on

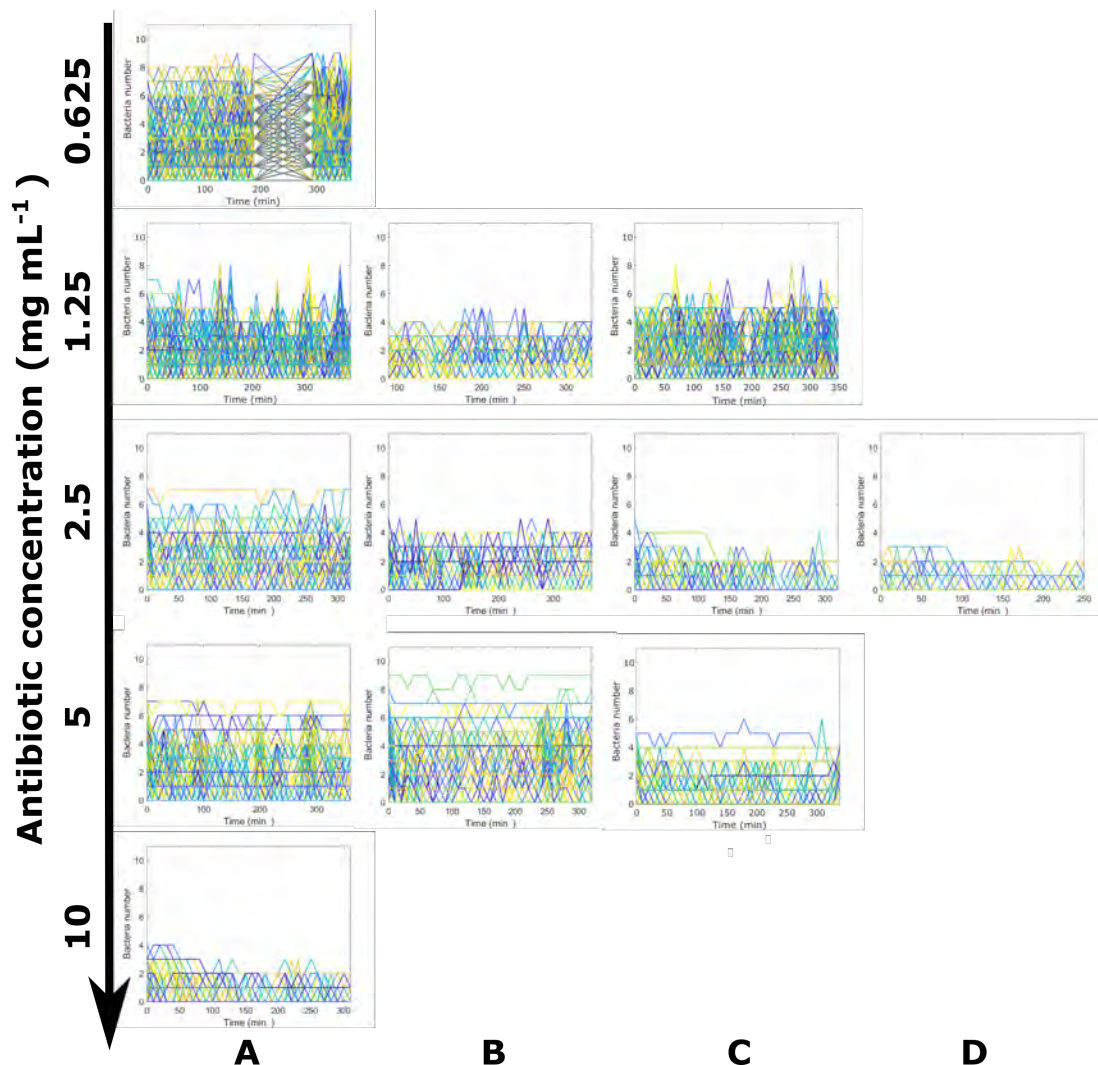


**Figure 6.3** *Growth curves for the ampicillin droplet experiments, each panel corresponds to a separate droplet experiment (listed in Table 6.1). Each line represents a droplet population. Antibiotic concentration is increasing down the left column in  $\text{mg mL}^{-1}$ , and repeat experiments are labelled A–D. We see there is no division when there is ampicillin present.*

the y-axis of each panel) at time zero. The most obvious observation that emerges from Figure 6.3, is that the bacterial count does not increase over time for any concentration of ampicillin, even though the bacterial density in the droplets is higher than in the plate reader experiments, for which we did see growth up to concentrations of  $1.25 \text{ mg mL}^{-1}$  (see Section 2.6). Apart from a very small number of divisions observed within the first hour during experiments with the lowest antibiotic concentration, the fluctuation in bacterial counts are artefacts from the image analysis (amplified by the hundreds or thousands of droplet populations represented in each plot), and do not represent division. This apparent paradox is somewhat resolved when we examine images of the bacteria in our droplets. Figure 6.4 shows three example droplets—these images clearly show that the bacteria are filamenting, i.e. growing without dividing.

Filamentous growth can be detected by plotting the total bacterial area (which we term ‘pixel sum’) as a function of time, rather than the bacterial count. Figure 6.5 compares this ‘pixel sum’ to the bacterial count, for experiment A(0.625) with an ampicillin concentration of  $0.625 \text{ mg mL}^{-1}$ . It is clear that the total biomass in the droplet is increasing, i.e. growth is happening, even though the bacterial count is not increasing. Filamentous growth in the droplets will be analysed in more detail in Section 6.3.5.

### 6.3.3 Killing dynamics of the droplet populations

In droplets we are able to count individual fluorescent bacteria. If we assume that bacteria which fluoresce are alive (whereas killed bacteria lyse, such that they no longer appear in the fluorescence channel), then we can count the number of surviving bacteria at different times in our experiment. This gives a much more detailed picture of antibiotic killing than would be possible in a bulk (e.g. plate reader) experiment. For ease of quantification, we define ‘survival’ as follows: a droplet containing a non-zero number of bacteria after 5 hours of antibiotic exposure<sup>2</sup> is classed as a surviving population. The survival fraction (SF) is then calculated as the number of droplets with surviving populations divided by the number of droplets containing bacteria at the start of the experiment. Figure 6.6

---

<sup>1</sup>Exceptions due to technical problems that arose during the runs are; experiment D(1.25), which has 26 timesteps; A(0.625), which has 28 timesteps (spanning over 5 hrs); and B(1.25), which has 24 timesteps (spanning over 5 hrs).

<sup>2</sup>Five hours corresponds to 31 timesteps in the complete datasets. The survival fraction for D(2.5) is calculated at T26 or 4.3 hr.

Experiment	Total droplets	Delay (min)
A(0)	2746	11–21 (+10)
B(0)	1524	3–13
C(0)	385	27–37
A(0.625)	2439	27–37
A(1.25)	925	6–16
B(1.25)	5999	10–20 (+90)
C(1.25)	747	3–13
A(2.5)	1997	24–34
B(2.5)	1309	5–15
C(2.5)	1068	12–22
D(2.5)	1316	17–27
A(5)	2661	9–19
B(5)	988	9–19
C(5)	477	9–19
A(10)	1789	18–28

**Table 6.1** *A list of the droplet experiments presented in this thesis, with the ampicillin concentration given in brackets in  $\text{mg mL}^{-1}$ . ‘Total droplets’ refers to the number of droplets that were tracked over the entire experimental run (at least 5 hours or 31 timesteps)<sup>1</sup>. ‘Delay’ is calculated as the time delay between when the tubing is cut (when droplets stop being produced) and the start of the scan. The additional time in brackets is due to discarding of initial timesteps during image analysis.*

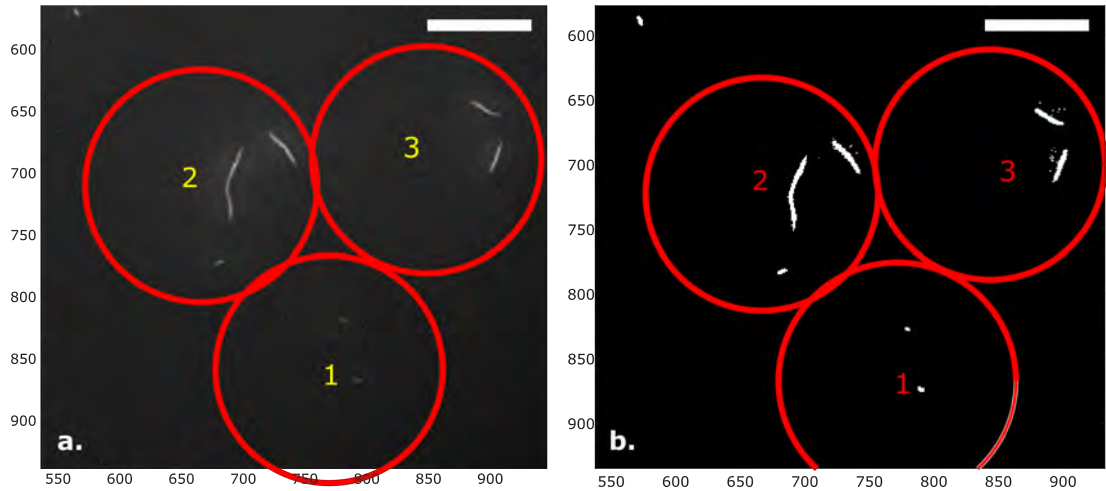


**Figure 6.4** *Three example droplets from experiment A(0.625), at 333 minutes. Panel (a) shows the raw CFP image and (b) shows the binary processed image. Droplet 1 has a bacterial count of 2 and a pixel sum of 26. Droplet 2 has a bacterial count of 3 and a pixel sum of 349. Droplet 3 has a bacterial count of 2 and a pixel sum of 200. Scale bars show  $50 \mu\text{m}$ .*



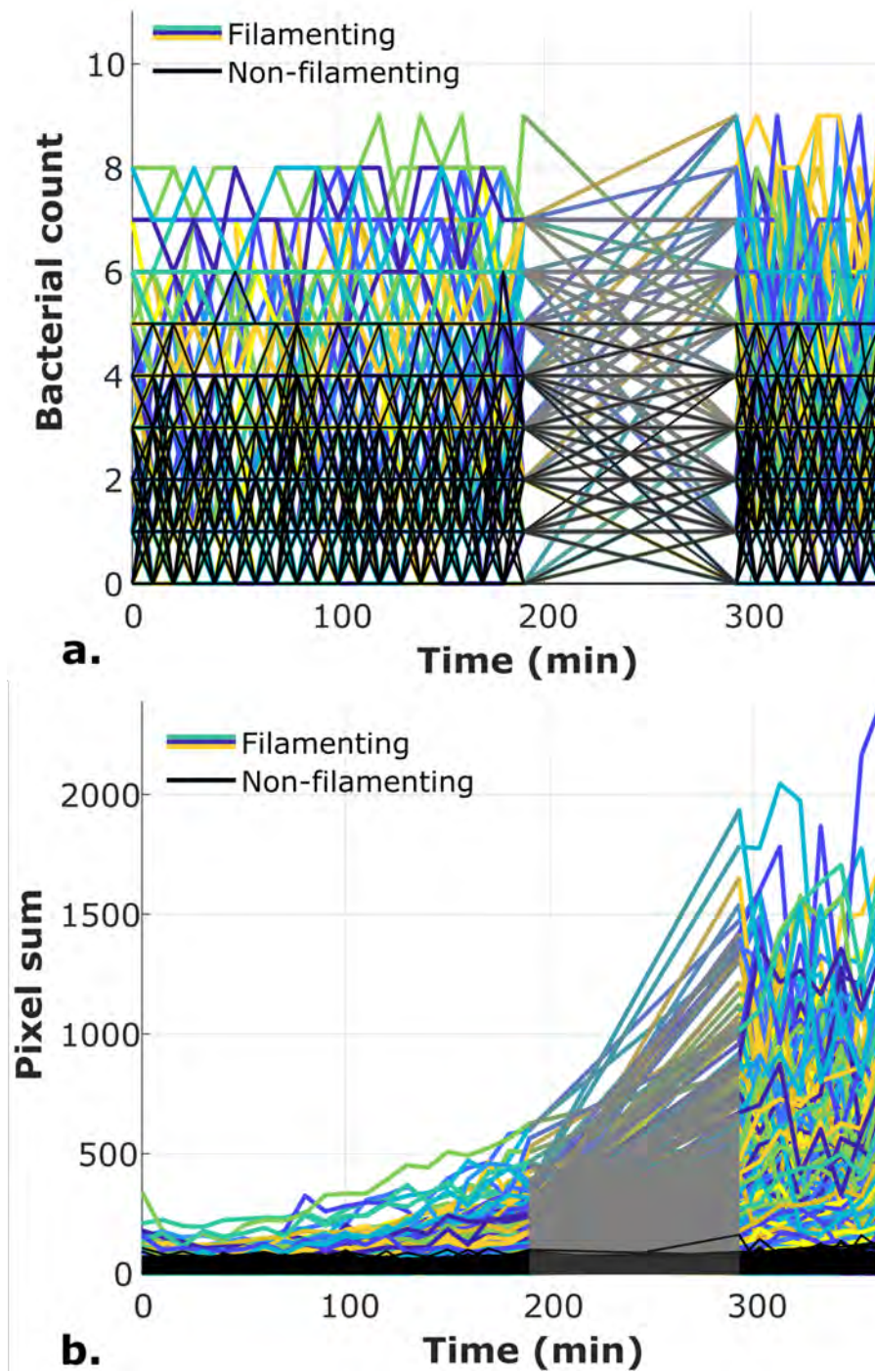


**Figure 6.5** Trajectories of bacterial count, (a), and pixel sum (total area occupied by bacteria), (b), for the droplet experiment at  $0.625 \text{ mg mL}^{-1}$  ampicillin (experiment A(0.625)). Droplet trajectories in which filamentation was observed are shown in colour, while trajectories in which no filamentation was observed are shown in black. The grey area indicates a gap in the measurements due to a technical problem.

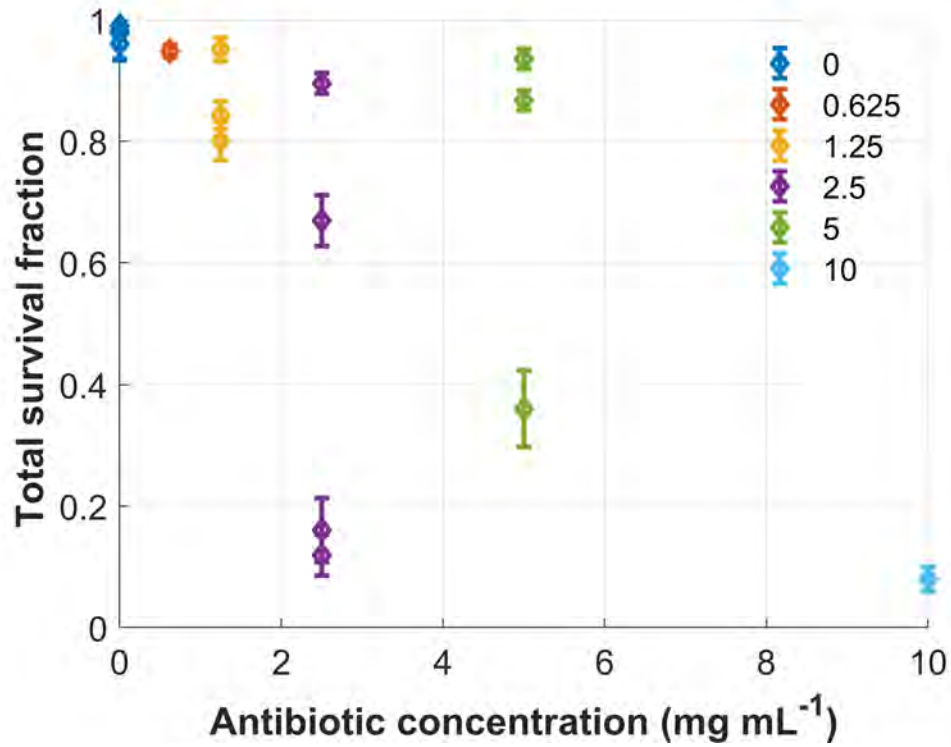


**Figure 6.6** *Total survival fraction (of droplet populations) plotted as a function of initial ampicillin concentration. For clarity, the antibiotic concentration is also indicated by colour (see legend), where different points of the same colour represent experimental replicates. Error bars show a 95% confidence interval based on binomial statistics.*

shows the survival fraction as a function of the antibiotic concentration, for all the droplet experiments. Unsurprisingly, we find that the higher the antibiotic concentration, the lower the survival fraction for the droplet populations.

Interestingly, however, we see a non-zero number of surviving droplet populations even at the very highest concentration ( $10 \text{ mg mL}^{-1}$ ), and many droplet populations survive well above the classical MIC value, which from our plate reader experiments can be estimated as  $0.375\text{--}0.875 \text{ mg mL}^{-1}$  (see Section 6.2.2).

Figure 6.6 also shows that there is significant variation in the droplet survival fractions between replicate experimental runs. This is particularly evident for ampicillin concentrations of  $2.5$  and  $5 \text{ mg mL}^{-1}$  (in purple and green), which have large ranges of total survival fractions.

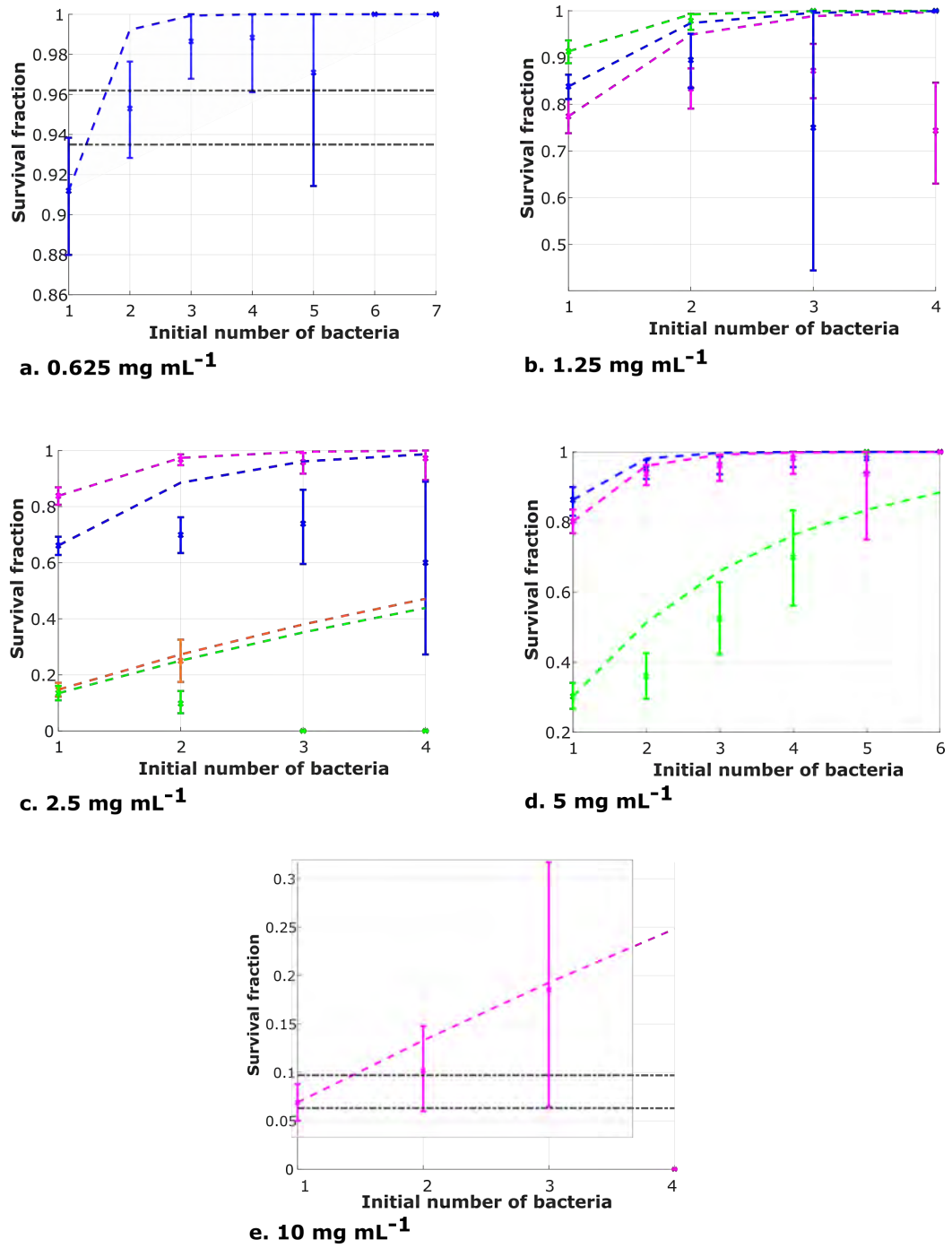


**Figure 6.7** *Survival fraction displayed as a function of initial number of bacteria per droplet. Each panel shows data from experiments with a different antibiotic concentration; different colours indicate replicate experiments. The coloured dashed lines show the theoretical prediction for the null model. The ampicillin concentrations and total survival fractions, were as follows: (a) 0.625 mg mL<sup>-1</sup>: 0.9489, (b) 1.25 mg mL<sup>-1</sup>: 0.8007, 0.8428, 0.9512, (c) 2.5 mg mL<sup>-1</sup>: 0.8955, 0.6694, 0.1193, 0.1604, (d) 5 mg mL<sup>-1</sup>: 0.8675, 0.9358, 0.3604, (e) 10 mg mL<sup>-1</sup>: 0.0797. Black dotted lines indicate the total survival fraction across all droplets (removed from some panels for clarity). Error bars show a 95% confidence interval, given by 1000 bootstrapped resamples of each dataset.*

## Testing for collective effects in bacterial survival

If bacteria are able to protect each other via antibiotic degradation, then we might expect the bacteria in droplets which are more highly populated to have better survival chances. To test this, we separated the droplet data into subsets of initial number ( $N_0$ ). Figure 6.7 shows survival fractions, plotted versus initial bacterial population size, for all the ampicillin droplet experiments. The dashed lines indicate the theoretical survival fraction predicted by a null model in which there is no cooperativity, i.e. each bacterium has an equal chance of being killed, irrespective of initial population size. In this model, the probability that a droplet population with  $N_0$  bacteria survives would scale as  $1 - (1 - SF_1)^{N_0}$ , where  $SF_1$  is the survival probability for droplets with 1 initial bacterium, in that experimental run. This is because the probability that all bacteria are killed, i.e. that the droplet population does not survive, is  $(1 - SF_1)^{N_0}$ . Positive deviations from the theoretical model—particularly for droplets with higher initial bacterial numbers—might indicate cooperative survival effects.

Figure 6.7 shows fairly good agreement between the experimental data and the null theoretical model for the lowest antibiotic concentration (panel (a)  $0.625 \text{ mg mL}^{-1}$ ) and the higher concentrations (panels (d)  $5 \text{ mg mL}^{-1}$  and (e)  $10 \text{ mg mL}^{-1}$ ), suggesting that there is no measurable cooperativity in these environments.

However for the intermediate antibiotic concentrations (panel (b)  $1.25 \text{ mg mL}^{-1}$  and (c)  $2.5 \text{ mg mL}^{-1}$ ), some of the datasets deviate from the theory. In particular, in some experiments, the survival fraction appears to decrease with the initial number of bacteria (although this would need to be confirmed with statistical testing). Intriguingly, this is the case only for some replicate experimental runs: other replicates do seem to follow the theoretical prediction.

The heterogeneity between replicate experimental runs, which is apparent in Figure 6.6 and Figure 6.7 merits careful consideration. At first, we thought this heterogeneity might arise from differences in the optical density of the inoculating culture. Despite following a standardised protocol (Section 2.2.1), the initial OD can vary between runs. Therefore in Figure 6.8 we plot the survival fraction as a function of the initial OD of the inoculating culture, for all droplet experiments. This plot shows no clear trend, suggesting that the initial OD does not explain the variability between replicate runs. In our experiments, the inoculating bacterial cultures originate from single *E. coli* colonies (see Section 6.3.1). It is possible

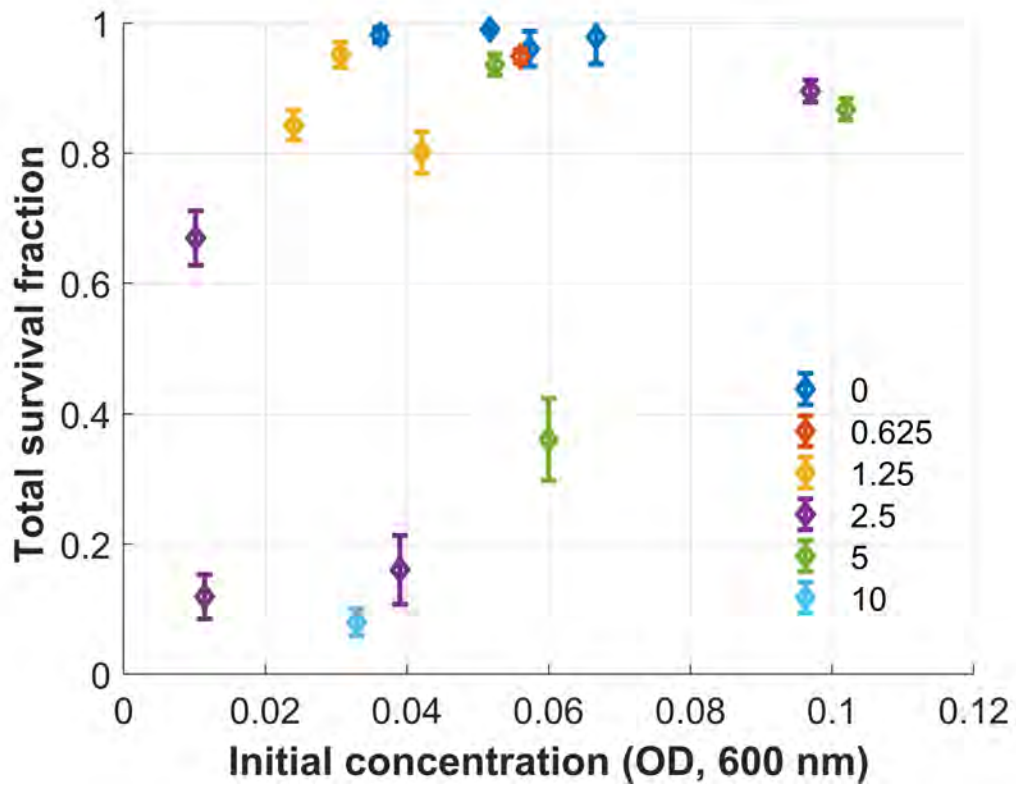


**Figure 6.8** *Total survival fraction plotted against the initial bacterial density of the inoculating culture (an  $OD_{600}$  measurement taken separately at the start of each experiment; see Section 2.2.1). Different colours represent experiments with different ampicillin concentrations, in  $\text{mg mL}^{-1}$ . For experiments using the Y-junction<sup>3</sup>, the OD reported here is half the value measured of the bacterial dispersion, to take into account the 1:1 dilution that occurs when the bacterial dispersion is mixed with the antibiotic solution at the Y-junction prior to the droplet forming junction. Error bars represent a 95% confidence interval based on binomial statistics.*

that differences between these initiating colonies has carried over into our droplet experiments. This issue will be discussed in more detail later.

### 6.3.4 Quantifying kill times

While at least some droplet populations survive in all our experiments, many of the bacteria die when exposed to ampicillin. It is useful to quantify the rate of killing by antibiotic since this could be compared, for example, to classical kill

<sup>3</sup>All antibiotic droplet experiments use a Y-junction to introduce the bacteria and ampicillin, however some of the uninhibited droplet experiments do not (see Table 2.1).

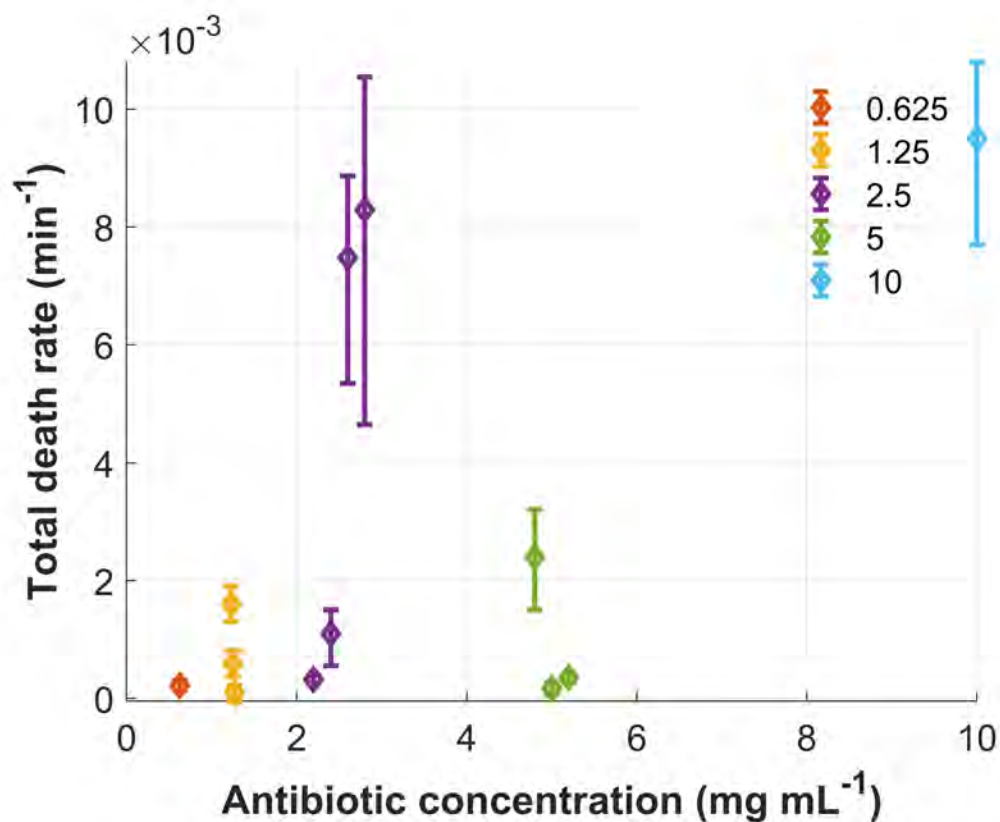


**Figure 6.9** Rate of decline of the total bacterial population (summed across all droplets), for each droplet experiment. Death rate was calculated by fitting the bacterial count to an exponentially decreasing function. Colours represent experiments with different ampicillin concentrations in mg mL<sup>-1</sup> (concentration values are offset on the x-axis for clarity). Error bars indicate the range of fits made with 1000 sets of bootstrap resampled data.

curves for bulk populations. One way to quantify the killing rate is by tracking how the bacterial counts decrease in time. By fitting the total bacterial counts to an exponentially decreasing function, we can extract a killing rate for each droplet experiment. Figure 6.9 shows these killing rates, using the bacterial number, summed across all (initially non-empty) droplets.

The highest death rate occurred for the experiments A(10), D(2.5) and C(2.5); these correspond to experiments where the survival fraction was below 0.16 droplet populations (see Figure 6.7). The maximum total death rate was  $0.0095 \pm 0.0018 \text{ min}^{-1}$ , equivalent to a rate of  $0.57 \pm 0.1 \text{ hr}^{-1}$ . The uncertainty represents the large range of death rates between droplet populations, and the heterogeneous response to the ampicillin. Due to the low population sizes, these values don't fully represent the lysis dynamics.

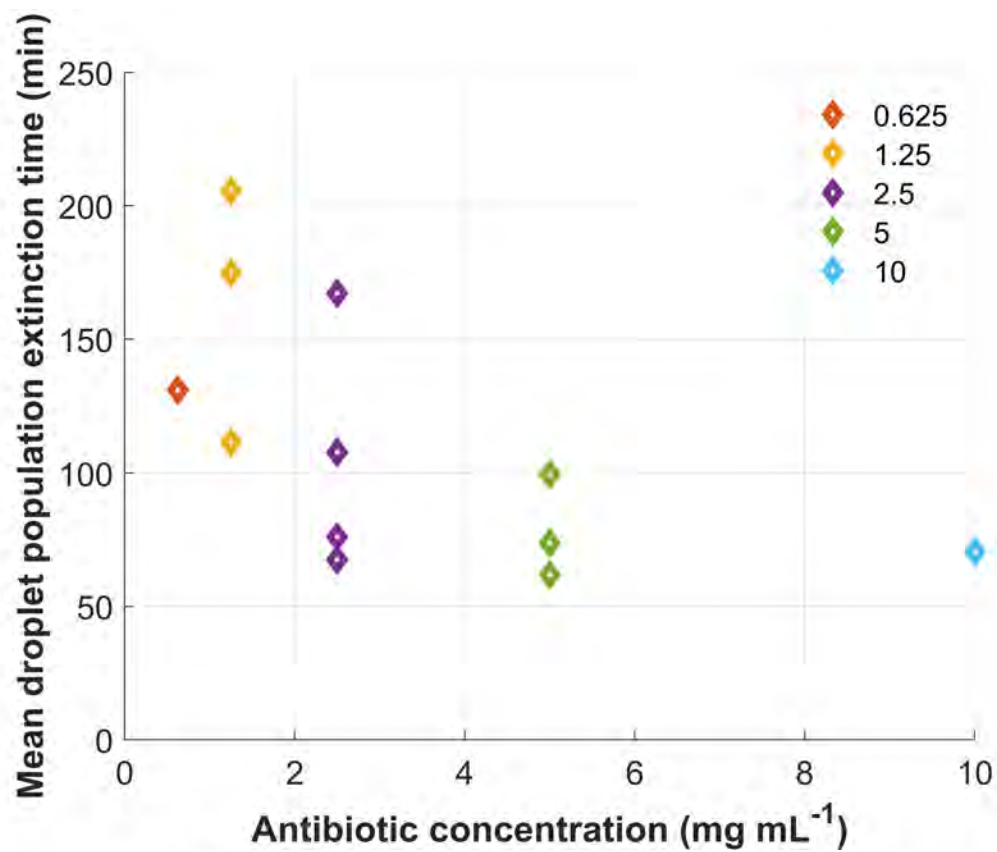
As an alternative way to quantify killing, we also measured the time taken for extinction of individual droplet populations. We define a droplet population as being extinct when the bacterial count is measured to be zero for two consecutive timesteps. Figure 6.10 shows the plot of mean extinction time (across droplets) for each experiment. As might be expected, we observe a general trend of a shorter time to extinction with increasing antibiotic concentration. Indeed, ampicillin has been shown to kill faster at higher concentrations in previous studies with bulk populations. In future work it would be interesting to compare the extinctions times measured in our droplets with bulk kill curves performed under comparable conditions [26, 143].

Figure A.4 shows the distribution function for the times at which a droplet population can be characterized as extinct; the mean of each of these distributions is shown as a separate point at the relevant concentration on Figure 6.10. For antibiotic concentrations 1.25, 2.5 and 5  $\text{mg mL}^{-1}$ , repeat experiments at each concentration yielded a variety of distributions, shown in different colours on panels (b)–(d), which illustrates the heterogeneous response between the droplet populations.

### 6.3.5 Analysis of filamentous growth

As mentioned earlier, bacterial counts do not tell the full story, since we also observe filamentous growth at low levels of antibiotic exposure; where cells continue to elongate but do not divide (see Section 1.3.1). We also sometimes





**Figure 6.10** Plot showing the average time to droplet population extinction as a function of antibiotic concentration. Each point represents the mean time of death for droplet populations within an individual droplet experiment (different points of the same colour represent experimental replicates). This data is the mean of the time distributions shown in Figure A.4.



observe filamentous cells in the droplet experiments with no antibiotic (see Section 2.4), but they are seen much more frequently in the presence of ampicillin. In this section we will quantify the likelihood of filamentation in the presence of ampicillin compared to the uninhibited experiments. The fact that we detect this filamentation demonstrates the benefit of our microfluidic droplet methodology, where we observe cells directly with microscopy, compared to bulk experiments, e.g. with the plate reader, where we only detect overall biomass density.

To quantify filamentation in our image analysis protocol, we assign a cell size in pixels for every bacterial cell in the droplets. We then use a cutoff size of 70 pixels to distinguish between filamentous and non-filamentous cells. The measured cell size is dependent on the chosen threshold value, the image quality and a number of other factors (see Section 2.4.1). The risk of mis-identifying an aggregate (or multiple cells) as a filament is low for the experiments with ampicillin as there is no aggregation observed and almost no division so the bacterial number remains low throughout.

Figure 6.4 shows example droplets to illustrate the shapes and sizes of the filamentous and non-filamentous cells, and how they relate to the 70-pixel cutoff. By thresholding the fluorescent image of the bacteria in panel (a), we obtain a mask of each cell. The number of pixels which represent each cell (cover the area of the cell in the microscopy image), is used to give an approximate measure of size. Droplet 2 is an example of a droplet population containing filamentous and non-filamentous cells. At this time, the filaments cover an area of 197 and 129 pixels, whereas the non-filamentous cell is represented by 23 pixels. Droplet 1 contains no filamentous cells despite having the same antibiotic concentration as its neighboring droplets, with bacterial sizes of 10 and 16 pixels. Since each pixel represents  $0.46 \mu\text{m}^2$  (Section 2.4), our 70-pixel cutoff size corresponds to an area of  $32 \mu\text{m}^2$ . See Figure A.3 for example distributions of bacterial sizes.

### **Quantifying the abundance of filamentous cells**

In our experiments, ampicillin appears to induce filamentation at low concentrations, but not at higher concentrations. Table 6.2 shows the number of filamentous bacteria detected in experiments with different antibiotic concentrations. To ensure accurate counting of the number of filamentous cells, we incorporated a checking procedure, in which we compare the trajectory of the number of objects larger than 70 px (i.e. potential filaments), with the trajectory of the

number of non-filamentous-bacteria, i.e. objects smaller than 70 px. To create a new filament, a non-filamentous bacterium needs to transition into a filament. Therefore, we expect the number of filamentous cells (small objects) to decrease by 1 in the same timestep as the number of filaments (large objects) increases by 1. If this happens, then the new large object is counted as a filament. This checking procedure reduces errors due to artefacts (e.g. debris) being mistaken for a filamentous cell.

Table 6.2 shows that the experiment with the highest fraction of filamentous cells, when compared to the initial bacterial count, is the droplet experiment with the lowest ampicillin concentration tested;  $0.625 \text{ mg mL}^{-1}$ , at 24%. We note that this fraction was calculated by dividing the observed number of filaments (produced at any time during the experiment) by the number of bacteria that were present at the beginning of the experiment. We consider this a good approximation because we see almost no division in the presence of antibiotic (see Figure 6.3). However, the situation is different for the uninhibited growth experiment, where we see bacterial growth, and little or no death. For the uninhibited growth experiment, therefore, the fraction of filaments was calculated by dividing the number of filamentous cells by the total bacterial count at the end of the experiment.

Figure 6.11 shows the biomass plots for two repeat droplet experiments at  $1.25 \text{ mg mL}^{-1}$ ; A(1.25) and B(1.25)<sup>4</sup>. We can see that A(1.25) (panel (a)) is a noisier dataset, and the pixel sum within any droplet population (each indicated by an individual trajectory) reaches a maximum of only 300 pixels. B(1.25) (panel (b)) contains clearer subsets and shows growth for the populations in the filamentous subset. However, compared to experiment A(0.625), even the biggest filamentous populations cover an area a factor of  $\approx 2$  lower than the area covered by the bacteria in A(0.625) (see Figure 6.5), again suggesting that the conditions for filamentous growth are optimised at lower antibiotic concentrations.

The mean time to filamentation is similar for all the ampicillin concentrations tested, including the uninhibited experiment (see Table 6.2). This indicates that although the concentration of ampicillin affects the probability of a bacterial cell filamenting, it does not greatly impact the time it takes to filament.

---

<sup>4</sup>The repeat C(1.25) was not included because some images have focus or halo-ing issues, making the object-size analysis noisy (see Figure A.14).

Experiment	$N_0$	$N_f$	Fraction	Rate ( $\text{min}^{-1}$ )	Mean time (min)	SD (min)
A(0)	5537	2799	0.022*	5.9	240	68
A(0.625)	4323	1041	0.24	3.2	232	80
A(1.25)	1104	90	0.081	0.24	242	99
B(1.25)	1111	106	0.095	0.47	225	64
A(2.5)	2077	0	0	0	n/a	n/a
A(10)	888	0	0	0	n/a	n/a

**Table 6.2** *The total number of filaments ( $N_f$ ) is defined as the number of bacteria we see transition from the non-filamentous to filamentous subset. The fraction of filaments is calculated by dividing the number of filaments by the initial bacterial count ( $N_0$ ), \*apart from the uninhibited case in which we instead divide by the final bacteria count (which for A(0) is 126001 bacteria). Rate of filamentation, in  $\text{min}^{-1}$  was calculated using a linear fit to the cumulative sum of filaments counted over time. The mean time to filamentation is the average of the times at which we identify a switch from the non-filamentous to filamentous subset (this is granular as images are taken every 10 minutes). The standard deviation (SD) of these times is also given.*

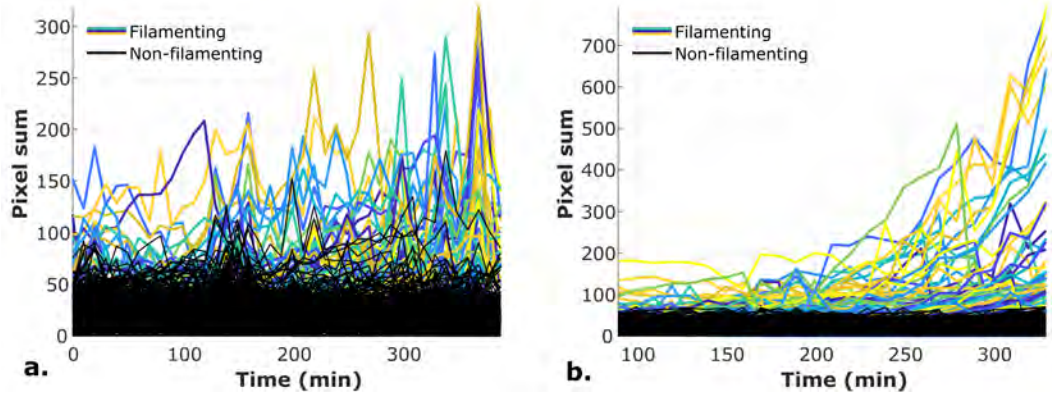


**Figure 6.11** *Trajectories of pixel sum (the total area occupied by bacteria) for two repeat experiments performed at  $1.25 \text{ mg mL}^{-1}$ ; (a) A(1.25) and (b) B(1.25). Droplet trajectories in which filamentation was observed are shown in colour while populations in which no filamentation was observed are shown in black.*

## Rate of biomass growth for filaments

We observe in our experiments that filamentous cells grow in the presence of antibiotic, even though there is no cell division (Figure 6.5). Therefore it is useful to measure the growth rate in terms of increase in biomass, or area, rather than in terms of division rate. Previous work has suggested that ampicillin-induced filaments grow exponentially [26]; our data also suggests exponential growth (see, e.g., Figure 6.11(b)). Therefore we can extract a growth rate by fitting a straight line to the natural log of the cell area (in pixels) as a function of time.

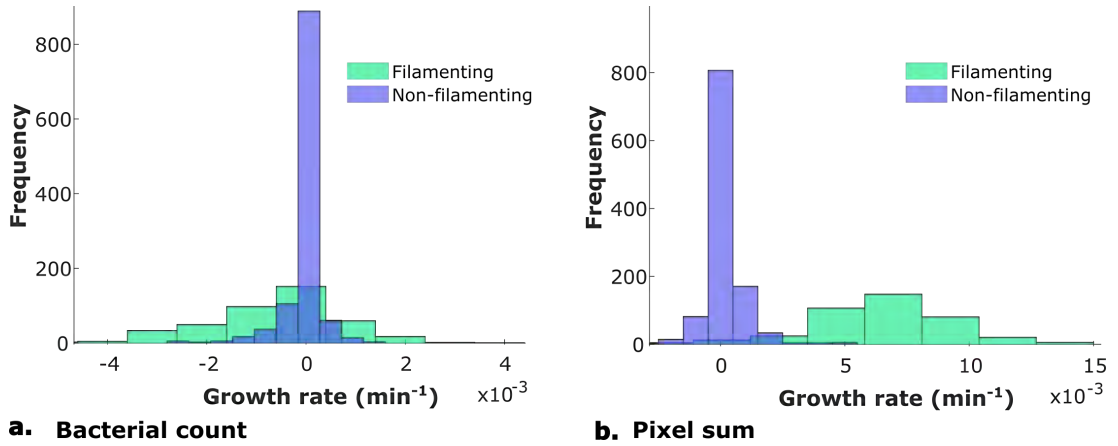
It is also useful at this stage to classify droplets according to whether or not they show filamentation. Any droplet which contains a cell of size 70 pixels or more, at any time, will be labelled as a ‘filamentous’ droplet population (shown in coloured trajectories in Figure 6.5 and Figure 6.11). It is important to note that this label does not mean that all of the bacteria contained in the droplet are filamentous, nor that filaments are present for all timesteps.

Figure 6.12 compares growth rates calculated for bacterial count (panel (a)) and pixel sum (panel (b)). In each panel, growth rate histograms are shown for the filamentous droplet populations (in green), and the non-filamentous droplet populations (in blue). For growth rates computed from bacterial counts (panel (a)), both filamentous and non-filamentous droplet populations show approximately zero growth on average. However the difference between filamentous and non-filamentous subsets is evident in the pixel sum growth in panel (b). For growth rates computed using the pixel area, filamentous droplets show a positive model growth rate of  $6.4 \times 10^{-3} \text{ min}^{-1}$  while non-filamentous droplet populations show approximately zero average growth.

Interestingly, the model growth rate for the filamentous droplets is comparable to the average uninhibited population growth rate,  $8.6 \pm 1.2 \times 10^{-3} \text{ min}^{-1}$ , which is discussed in Section 3.3.2.

## Probability of filamentation

The probability of filamentation for a given bacterial cell seems to depend on whether other bacteria (or filaments) are present. This is shown in Figure 6.13, where we track the dynamics of the filamentous and non-filamentous cells, for droplets with different starting population sizes ( $N_0$ ). In this figure, the solid



**Figure 6.12** Histograms of the growth rates of individual droplet populations at an ampicillin concentration of  $0.625 \text{ mg mL}^{-1}$  (experiment  $A(0.625)$ ), using (a) bacterial count and (b) pixel sum as a proxy for biomass growth. Each droplet was categorised as ‘filamentous’ or ‘non-filamentous’ according to the criteria described in the text. The green data corresponds to filamentous droplets, while the blue data corresponds to non-filamentous droplets. Growth rates were calculated using linear fits to the natural log of the growth curves shown in Figure 6.5. The mean growth rates in panel (a) are  $-6.2 \times 10^{-4} \text{ min}^{-1}$  for the filamentous subset and  $-5.3 \times 10^{-5} \text{ min}^{-1}$  for the non-filamentous subset (i.e. net population decline), but in (b) the mean pixel sum growth rates are positive;  $6.4 \times 10^{-3} \text{ min}^{-1}$  and  $2.2 \times 10^{-4} \text{ min}^{-1}$  for filamentous and non-filamentous respectively.

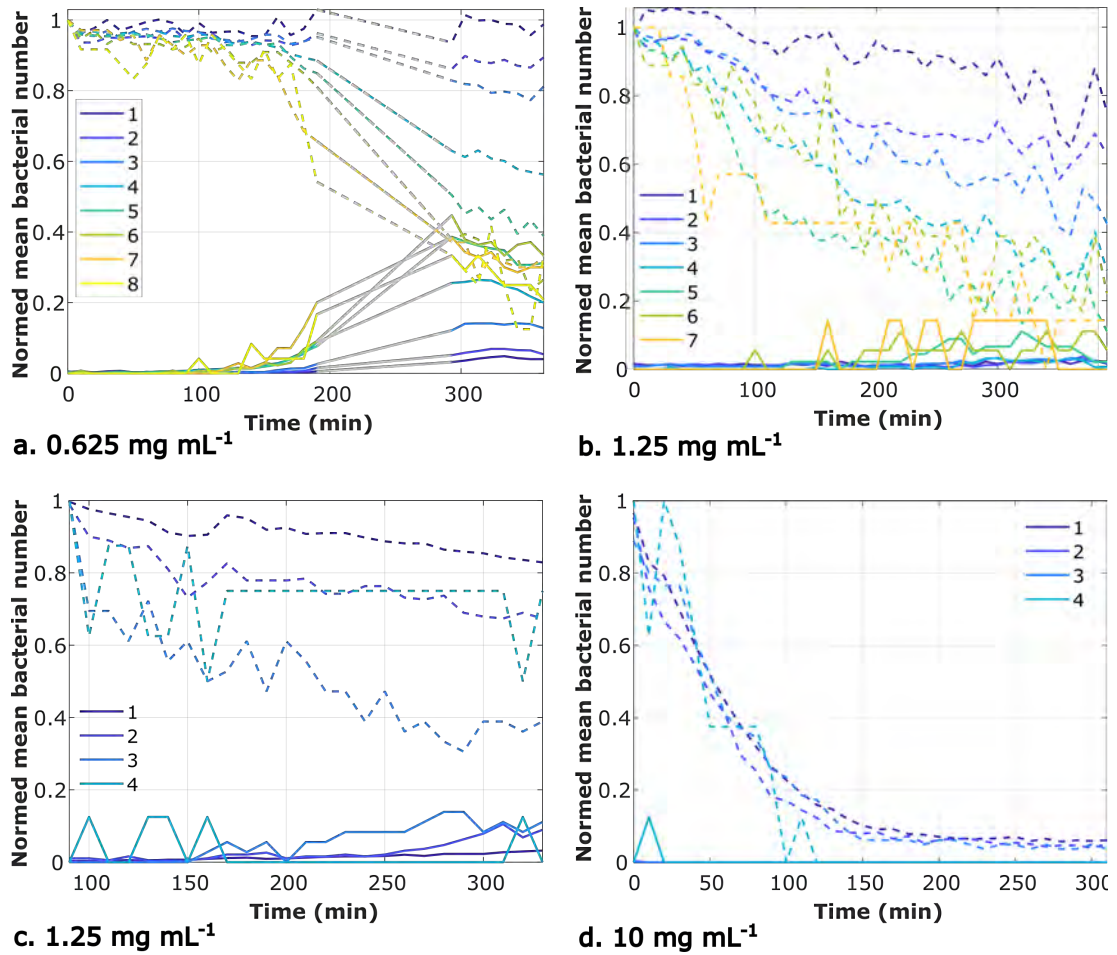


**Figure 6.13** This figure displays subsets of experimental data, separated into initial population size,  $N_0$  (indicated with colours). The number of filamentous and non-filamentous bacterial cells over time are indicated with straight and dashed lines, respectively. The number of bacteria is normalised by  $N_0$  for each subset. Each panel represents data from experiments: (a)  $A(0.625)$ , (b)  $A(1.25)$ , (c)  $B(1.25)$  and (d)  $A(10)$ . The grey sections indicate a gap in the experimental data.

lines show the number of detected filaments, which increases in time, and the dashed lines show the number of detected non-filamentous cells, which decreases in time, as non-filamentous cells either die or change into filaments. The colour coding indicates the initial population size. All datasets have been scaled by the initial population size for ease of comparison. This figure indicates that bacteria in droplets with higher initial population numbers ( $N_0 = 5-8$ ) are more likely to become filamentous. This is particularly evident in panel (a), which shows data from droplets exposed to an ampicillin concentration of  $0.625 \text{ mg mL}^{-1}$ . Panels (b) for A(1.25) and (c) for B(1.25) are noisier, with less filamentation overall, but again they show less filamentation in the droplets that start with only a single bacterium.

In panel (d) for A(10) there is no filamentation or division, therefore in panel (d) the dotted lines show just the killing dynamics of the non-filamentous population.

The effect of initial population size on the probability of filamentation can be quite drastic. For example, for experiment A(0.625), in panel (a), after 190 minutes of exposure to ampicillin, an individual bacterial cell is  $25\times$  more likely to show filamentous growth if it is randomly sampled from a droplet with  $N_0 = 7$  vs. a bacterial cell that is sampled from a droplet with  $N_0 = 1$ . Continuing to focus on experiment A(0.625); of the 4323 total initial bacteria, 1041 showed filamentous growth during the experiment. These filamentous cells were all contained within 482 droplets, out of the 2439 non-empty droplets in the experiment.

Figure 6.14 analyses the probability of filamentation at the level of whole droplets. Here droplets are categorised as filamentous or non-filamentous (using the criterion described earlier), and according to their initial population size. It is clear from Figure 6.14 that droplet populations that start with more bacteria are more likely to show filamentation. For example, the fraction of filamentous droplets within the subset of  $N_0 = 1$  is only 0.049. As there is no division (see Figure 6.5), these droplets start with one bacterium, which either filaments (with probability 0.049) or does not. For droplets that contain 2 bacteria initially, we might expect that the chance of observing filamentation in these populations is  $\approx 0.049 \times 2 = 0.098$ , if the bacteria behave independently. However Figure 6.14 shows that the probability of these droplets containing a filament is actually higher, 0.14 for droplets that start with 2 bacteria. Indeed, almost all droplets with  $N_0 > 5$  contain a filament, while the expected proportion for droplets with  $N_0 = 5$  would be  $\approx 0.049 \times 5 = 0.245$ . This implies that the presence of other bacteria has a strong effect on the filamentation probability.

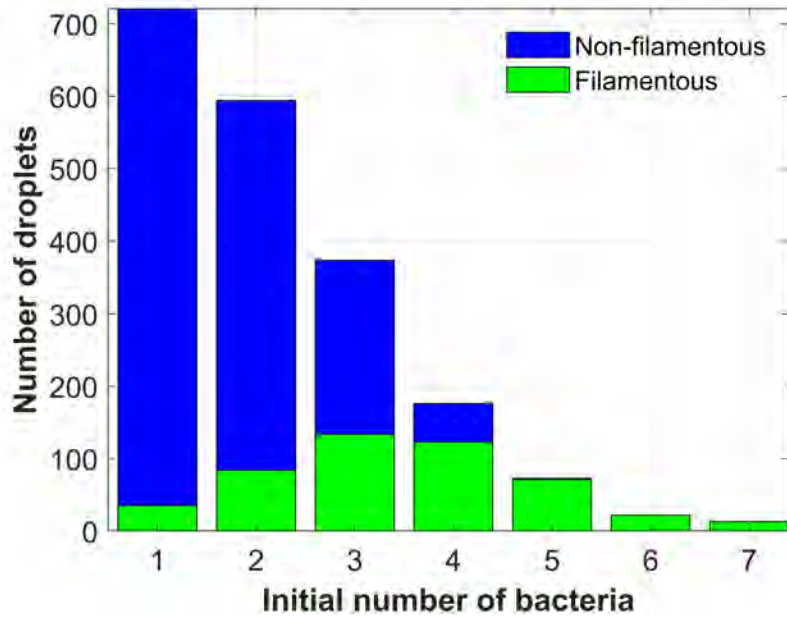


**Figure 6.14** *Stacked bar graph showing the fate of droplet populations depends on the initial population size. Data is shown from experiment A(0.625). Droplets that showed filamentation (at any time during the experiment) are shown in green, while droplets in which no filamentation happened (at any time) are shown in blue. Filamentation predominantly happens in droplets that start with higher population sizes. From 2439 droplets, 482 show filamentation, 1490 contain only non-filamentous bacteria, and the rest (467) are empty. The fraction of droplets in which filamentation happens (of droplets which contain bacteria) is 0.24, these 482 droplets account for 39% of the of the total initial bacteria.*



## A simple theoretical model for filamentation dynamics

We can construct a null model of the dynamics of non-filamentous cells in a simple way, if we assume that non-filamentous cells can either convert to filamentous cells at rate  $f$  or lyse (i.e. die) at rate  $d$ . We will assume that both of these are independent Poisson processes, i.e. that there is no population-size dependence of the filamentation rate. Therefore the number of non-filamentous cells follows a simple death process, with rate  $d + f$ . The mean number of non-filamentous cells,  $M(t)$ , at a given time,  $t$ , therefore should be:

$$M(t) = N_0 e^{-(d+f)t},$$

and the variance,  $V$  should be:

$$V(t) = N_0 e^{-(d+f)t} \cdot (1 - e^{-(d+f)t}).$$

And therefore:

$$V(t) = M \cdot (1 - \frac{M}{N_0}). \quad (6.1)$$

This can be understood by considering the switch of each of the initial bacteria,  $N_0$ , as an independent stochastic event that happens in time  $t$ , with probability  $\exp^{-(d+f)t}$ . Therefore the variance can be found by considering a binomial sampling of  $N_0$  trials with the same probability.

Figure 6.15 tests this theoretical prediction against our experimental data. The number of non-filamentous bacteria was counted at every time point, for all droplets. The variance of the data is plotted versus  $M \cdot (1 - \frac{M}{N_0})$ , with colour coded datasets, according to the initial population size of the droplet,  $N_0$  (each cross corresponds to a different timestep). The ‘total’ result for each experiment, displayed in black crosses, was calculated using the mean and variance of the non-filamentous bacterial count over all the non-empty droplet populations. Here,  $N_0$  was taken as the sum of the initial bacterial number measured over all droplets. The dashed line shows the theoretical prediction from Eq. 6.1. For the highest antibiotic concentration,  $10 \text{ mg mL}^{-1}$ , we do not see any filamentation; this dataset (panel (d)), appears to fit the theoretical model well, showing that bacterial death can be treated as a Poisson process. However, the datasets for lower antibiotic concentrations, where there is significant filamentation, deviate from the model, especially for droplets with larger numbers of initial bacteria.

This supports our previous observations that filamentation is more likely when more bacteria are present in a droplet (because subsets of higher  $N_0$  deviate more from the null model where filamentation occurs at an independent rate).

### **Does filamentation affect the survival chances of droplet populations?**

It has been suggested that filamentation could increase the survival chance of bacterial populations in the face of environmental challenges [50]. Therefore it is interesting to ask whether droplets containing filamentous cells are more or less likely to survive the exposure to ampicillin in our experiments and also, whether they are able to offer protection for other bacteria.

Figure 6.16 addresses this question, by plotting the survival fractions as a function of initial droplet population size, for ‘filamentous’ droplets, i.e. droplets where filamentation happened during the experiment, and ‘non filamentous’ droplets, i.e. non-empty droplets where no filamentation happened. Panel (a) shows data for experiment A(0.625) with  $0.625 \text{ mg mL}^{-1}$  ampicillin. Here it appears that filamentous droplets are actually somewhat less likely to survive than non-filamentous ones, across all initial population sizes. From my experimental measurements, we are unable to distinguish here between cause and correlation. Perhaps filamentation offers no particular advantage in terms of population survival (it may even be detrimental), and does not provide enhanced cooperative benefits. Or alternatively, these filaments could have formed as a (possibly beneficial) response to a higher environmental stress, and therefore the lower survival fractions could be a result of the more stressful conditions rather than the filamentous response.

Panels (b) and (c) show data from the two experiments with  $1.25 \text{ mg mL}^{-1}$  ampicillin. Here the results for the filamentous and non-filamentous droplets are indistinguishable. Once again it appears that filamentation does not increase the survival chances of a population.

It would be interesting to investigate in more detail the process by which filaments die. For example, do filaments always reach a fixed size before dying? Qualitatively, we observe a wide range of cell sizes (see Figure A.3) and the lysis of filaments at different times and different sizes throughout the experiment. These size and time distributions would be interesting to quantify in future work.

---

<sup>5</sup>Data for experiment B(1.25) begins at 90 minutes (see Table 6.1).

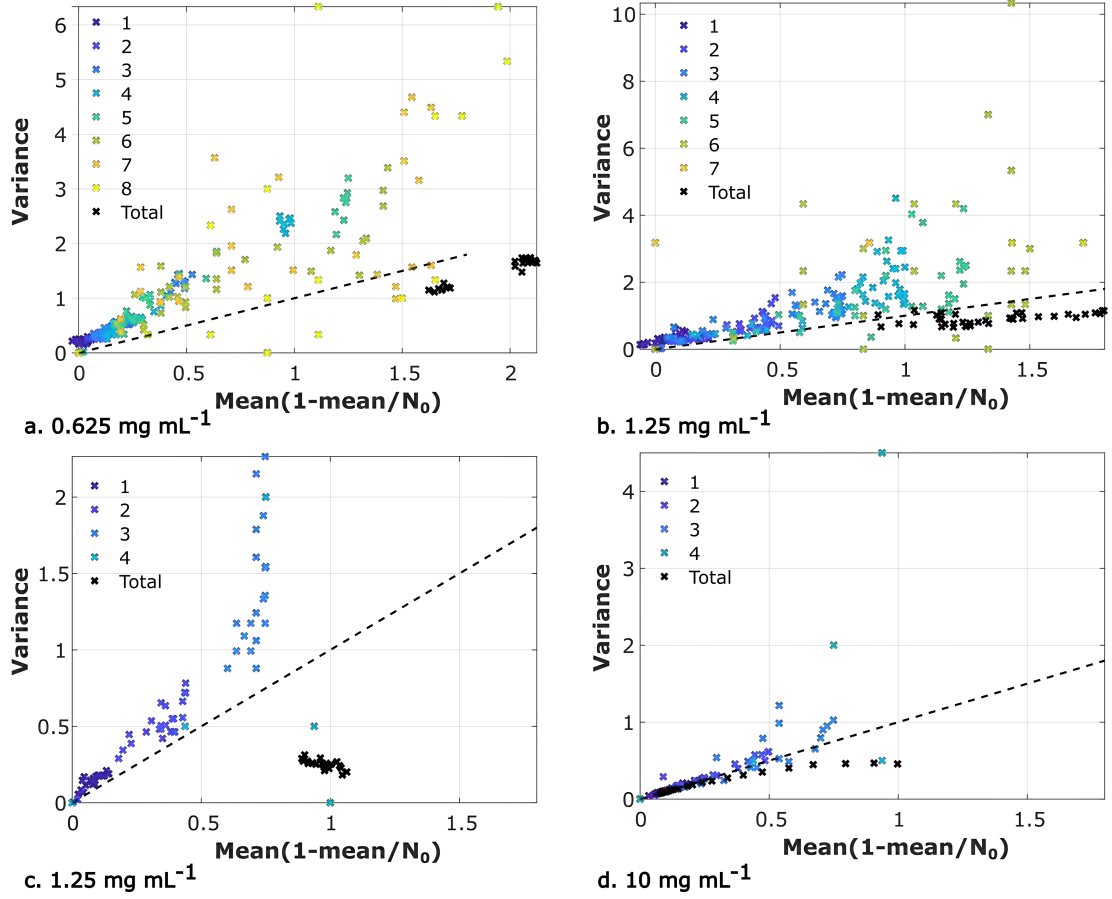


**Figure 6.15** *Test of the theoretical model for filamentation dynamics. The number of non-filamentous bacteria at time  $t$  is sampled at every time point, for all non-empty droplets. This is plotted versus  $M.(1 - \frac{M}{N_0})$ , where  $M(t)$  is the mean number of non-filamentous bacteria and  $N_0$  is the number of bacteria in the droplet at the start (each cross corresponds to a different timestep). Colours indicate the initial number of bacteria,  $N_0$  in the droplets. The calculation for the total dataset is shown in black crosses. The dotted black line indicates theoretical calculation from Eq. 6.1. Panels show data from experiments: (a)  $A(0.625)$ , (b)  $A(1.25)$ , (c)  $B(1.25)^5$  and (d)  $A(10)$ .*

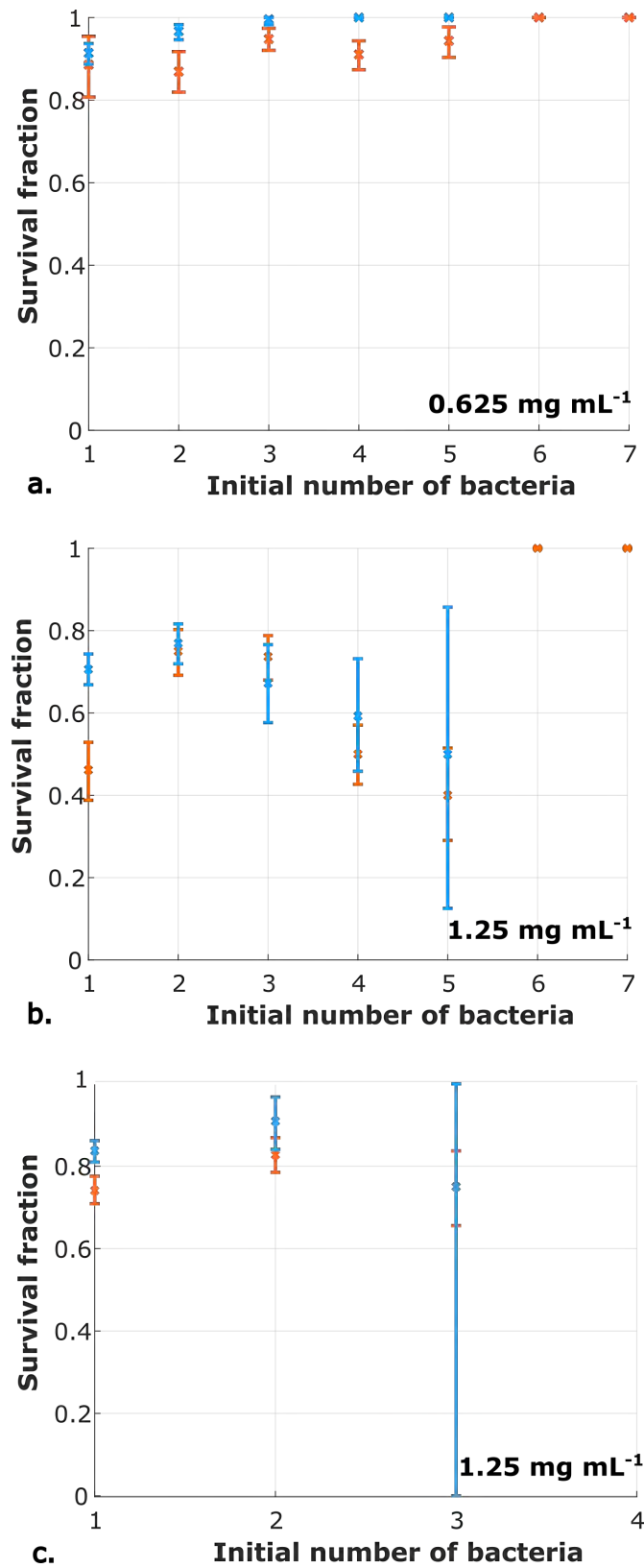


**Figure 6.16** Survival fraction for filamentous and non-filamentous droplet populations. Orange shows the survival fractions of droplets which contained filamentous bacteria, blue shows survival fractions for droplets in which no filamentation happened. The different panels show data from different experiments, with the ampicillin concentration labelled: (a) A(0.625), (b) A(1.25) and (c) B(1.25). The uncertainty represented by the error bars were calculated using bootstrap resampling.

## 6.4 Discussion

In this chapter, we presented a set of experiments with a  $\beta$ -lactamase-producing strain of *E. coli*, for a range of ampicillin concentrations. In the bulk experiments, we see a clear inoculum effect, as we expected from our simulations (Chapter 5) and from previous literature. In droplets, however, we obtained some unexpected results. Our results showed that the survival of small populations in droplets is indeed enhanced for droplets that start with more bacteria, but this can be explained with a null model where each bacterium is killed independently. Our replicate experiments show quantitatively different, but qualitatively similar, results. Moreover, our experiments revealed that bacteria tend to filament in the presence of ampicillin (in accordance with previous literature, but not accounted for in our model) [127]. Bacteria that filament continue to grow (without dividing) in the presence of antibiotic, but they do not have enhanced survival compared to non-filamentous cells. Intriguingly, our data also showed that the probability for a cell to filament appears to depend on the number of other bacteria that are in the droplet.

In our experiments, some bacteria survive to the end of the experiment without either filamenting or proliferating. These cells are apparently dormant and we might identify them as persister cells [127–130]. The droplet technology makes it very easy to identify these cells. Whilst they may also be present in the plate reader experiments, because they do not contribute to growth they remain undetected. Interestingly, non-growing cells were also detected in the uninhibited droplet experiments in Chapter 3, where we measured up to 6% of droplet populations as either no- or slow-growing. In the droplets with antibiotics the proportion of non-growers is much higher, at 8–95% depending on the conditions (survival fractions are displayed in Figure 6.6). In Chapter 3, for the uninhibited case, we hypothesised that these dormant cells could be due to stationary phase contamination of the initial bacterial suspension, but the high percentages of non-growing, surviving bacteria after antibiotic exposure imply other factors at play. For example, ampicillin might trigger a transition to a dormant state.

The possibility of a large proportion of dormant, but living cells in a population treated with a supposedly bactericidal antibiotic could be relevant for clinical treatment, especially if apparently killed infections might regrow [149]. Alternatively, growth suppression such as this could allow the natural immune response to eradicate an infection [150]. Another important point that emerges from

our results is that OD measurements do not distinguish between the increase of biomass and bacterial division [27]. In our droplet experiments, we observe no cell division but a large number of growing filamentous cells at low concentrations of ampicillin (Figures 6.5 and 6.11). The analysis of these filamentous bacteria (Section 6.3.5) is possible post-experiment because we have raw microscopy images for each droplet population. This is a major advantage of combining droplet microfluidics with microscopy.

Filamentous growth is associated with an increase in phenotypic heterogeneity; altered fluorescence levels and varying bacterial length distributions are often observed [50]. This behavior could be interpreted as part of a noise-based survival strategy. It appears from our data that the presence of other bacteria or other filaments could be a trigger for other bacteria to do the same. Alternatively, there could be environmental factors within particular droplets which caused the cells to filament in concert. For example, if these droplets were harsher micro-environments, this would perhaps explain the lower survival fractions for these droplet populations (Figure 6.16).

For the ampicillin experiments, tracking the dynamics of the total pixelated area presents a more representative picture of the response of the population than simply tracking the cell numbers—although the latter approach worked well for the uninhibited experiments in Chapter 3. In this chapter, we have assumed that cells which are still fluorescent at the end of the experiment are alive. To properly test this, we would need to see whether such cells can regrow when antibiotic is removed. However, in the current experimental setup, we can't know whether restoration of normal growth for the filamentous cells would occur if the antibiotic was removed. In the case of filaments, it is known that cells can remain metabolically active and continue with DNA replication even when division is inhibited. Upon removal of stress, filamentous *E. coli* cells have been observed to divide randomly at one of the possible division sites along the filament [151] (see Section 1.3.1). However removal of antibiotic from the droplet populations is beyond the scope of these droplet experiments.

An important confounding factor in our experiments is that replicate experiments produced quantitatively different results for the droplet population survival fraction. We determined that this was not correlated with the initial optical density of the starting culture. We suppose that it could be due to heterogeneity in the single colonies used to inoculate the overnight cultures that eventually produced our inoculating bacterial suspensions. In hindsight, more than one

starting colony could be used to start out cultures (as is standard protocol, used in our plate reader experiments). Alternatively, we could alter the experimental procedure, to carefully grow the inoculum to steady state before the start of the experiment by repeated dilution of an exponentially growing culture. This, however, would involve a significantly longer protocol, since a culture must undergo approximately 8 generations in exponential phase to achieve steady state growth [152]. Future experiments could also explore the effects of using a higher initial inoculum in the droplets. We would perhaps see a stronger inoculum effect at higher bacterial densities.

### 6.4.1 Comparing plate reader and droplet data

Bacterial response to ampicillin concentrations between 0.1 and 25 mg mL<sup>-1</sup> were tested in the plate reader, which is a larger range than the concentrations tested in droplets (0.625–10 mg mL<sup>-1</sup>). In the plate reader experiments we see growth at late times for antibiotic concentrations up to 1.25 mg mL<sup>-1</sup> for the higher bacterial densities, but not for the lower ones. This increase in the MIC with the increase of bacterial density demonstrates the inoculum effect, which is often found for  $\beta$ -lactamase-producing strains. In contrast, none of our antibiotic-treated droplet populations showed any proliferation during the course of the experiment (Figure 6.3). We do note however that our droplet experiments were considerably shorter than the plate reader experiments. The observed growth in the plate reader typically happened after 500 minutes, which is much longer than the entire duration of our droplet experiments. We could speculate therefore that growth might be observed in droplets too, if we were to observe them over a much longer time.

Comparison of the bacterial density between the plate reader and droplet experiments is not trivial. Encapsulating even one bacterium in a picolitre droplet results in a bacterial density of 10<sup>7</sup> CFU mL<sup>-1</sup> (see Table 2.2). Therefore the droplet populations are actually at higher density than the populations in most of our plate reader experiments (even when a bacterial suspension of the same density is used to generate the droplets). Figure A.5 shows the initial bacterial densities in CFU mL<sup>-1</sup> used in the plate reader experiments. The only plate reader experiment for which the bacterial density is greater than the average bacterial density in our droplet experiments is B1 in PR1 (Figure A.6). When comparing our droplet results in Figures 6.3, 6.6 and 6.13 to the plate reader

experiments, we should bear in mind that the bacterial densities in the plate reader are lower. It is interesting therefore to observe that we have higher bacterial densities in the droplets without observing the strong inoculum effect that would normally happen at these bacterial concentrations. However, the inoculum effect in the plate reader was only observed at long times (longer than the droplet experiments).

Considering, for example, the bacterial density B1, the highest density used in the plate reader experiments, we see growth at all antibiotic concentrations in the plate reader, but we do not see any proliferation in our droplet experiments. We do however, observe the growth of filaments. Therefore we can infer that the growth we observe in the plate reader is likely to be filamentous growth rather than cell division. This is a phenomenon that is well documented; for example, other studies have found the number of CFU per milliliter remains constant during the prelytic increase in OD on ampicillin exposure (Figure 2 in [143]). The turbidity measurement of optical density is not always proportional to cell number, and does not allow us to distinguish between different causes of increased absorption [27]. We can infer from the droplet experiments that any increase in OD for samples containing over  $0.625 \text{ mg mL}^{-1}$ , is likely to be solely due to filamentous growth.

An important hypothesis which arises from this data comparison is that the inoculum effect which we observe in the plate reader experiments might actually be a filamentous-inoculum effect. Indeed, in Section 6.3.5 we determine that the probability of filamentation, per bacterium, is higher in larger droplet populations than smaller populations. This suggests that we might expect more filamentation in our plate reader experiments with higher bacterial densities. In future, it would be interesting to repeat the plate reader experiments, taking regular samples for microscopy to determine the presence or absence of filaments.

Interestingly, some of the heterogeneity that we observe in our replicate droplet experiments, for example in the survival fractions for the experiments at  $2.5$  and  $5 \text{ mg mL}^{-1}$  (Figure 6.6), is also apparent in the plate reader experiments. The schematic illustrating the outcomes of our plate reader experiments (inset to Figure 6.2) is coloured yellow to indicate where there is growth in some, but not all, replicate wells at the same ampicillin concentration. In Figure 6.2 we see that only one replicate well grows at  $0.625 \text{ mg mL}^{-1}$  at bacterial concentration B4. In addition, the growth curves for the lowest bacterial density are more heterogeneous between replicate wells—even in the uninhibited case—than for



the higher bacterial densities. Perhaps because the lower concentrations, with smaller initial populations, display more stochastic behavior. This heterogeneity is also apparent in Figures A.6 and A.7.

### **6.4.2 Comparing experimental data to the simulation predictions**

There are clear differences between the outcome of our experiments and the simulation predictions made in Chapter 5. Unlike in the simulations, in our droplet experiments we do not see any cell division in the droplets with antibiotic, at least over the timescale of the experiment. The effects of temporarily nonproliferating bacteria which are tolerant of bactericidal antibiotics would be an interesting topic to explore in future simulations. It would also be very interesting to include filamentous growth in our simulations, perhaps with a density-dependent filamentation rate.

In the simulations presented in Chapter 5 we predicted that some droplet populations would survive far above the bulk (apparent) MIC. This is indeed observed in the data, with 8% of droplet populations surviving in the 10 mg mL<sup>-1</sup> experiment (which is 20× the MIC determined using the plate reader experiments). The range of antibiotic concentrations explored in the simulations were much lower than the experimentally measured MIC, however, so it is hard to make a quantitative comparison for the particular strain of *E. coli* we studied.

Our simulations provided a useful starting point for exploring what might happen in our experiments, and for informing the experimental design. However this chapter has shown that the experimental reality proved to be more complex than the simulation model.

# Chapter 7

## Simulating mixed populations of $\beta$ -lactamase producers and non-producers

### 7.1 Introduction

Using the same basic model as in Chapters 4 and 5, a model with both a sensitive and resistant strain was developed to simulate cooperative behavior. This ‘cheating’ model gives insight into cooperative dynamics by simulating the growth of two different strains in small, confined (droplet) populations. Our model is a simplified version of the model developed by Yurtev et al. [32] which predicts conditions that enable coexistence between resistant and sensitive cells. Unlike this evolutionary model, we do not give the sensitive strain a faster uninhibited growth rate (although a metabolic cost is something which could be explored in future work) and we do not include a lag time. We simply explore the dependent dynamics (without evolution) when sensitive bacteria are in the presence of  $\beta$ -lactamase-producing bacteria and are exposed to antibiotic.

The sensitive and resistant sub-populations can be interpreted as different strains of bacteria or as sensitive and resistant sub-populations of the same strain; a wild-type and a  $\beta$ -lactamase-producing mutant-type. Coexistence or cooperation between different species can be viewed in the context of social evolution theory. A sensitive strain can act as a cheater if it is protected from stress or benefits

from resource production by a different strain, but does not incur the cost of synthesising the public goods. In a well-mixed community, the cheater is sometimes able to dominate since it has a lower fitness cost [71, 153]. Under other circumstances, however, cheating behavior can promote ecological diversity and optimise resources [154].

The production and degradation of antibiotics are types of cooperative behavior and play an important role in maintaining biodiversity within natural microbial communities [155]. Many infections are polymicrobial, i.e. they contain more than one microbial strain or species. In these polymicrobial infections, interspecies interactions can influence the outcome of antibiotic treatment. In particular it has been suggested that polymicrobial interactions sometimes lead to increased antibiotic tolerance and greater spread of resistance [72, 156, 157]. The degradation of antibiotic by  $\beta$ -lactamases is one example of a resistance mechanism which can aid the surrounding species; in some cases, in detriment to the survival of the enzyme-producing bacteria [73, 158]. This protection of sensitive strains by  $\beta$ -lactamase producing strains is a well-studied phenomenon both *in vitro* and in clinical settings [56].

In this chapter we simulate mixtures of  $\beta$ -lactamase producers and non-producers, in droplets. We ask whether segregation of the population into droplets enhances cooperation or not. We also compare deterministic and stochastic models of droplet loading and birth-death dynamics (these categories of model are explained in detail in Sections 4.2 and 4.3).

## 7.2 Method

The same model presented in Chapter 4 was adapted to simulate mixtures of resistant and sensitive bacteria. As in the original model, the resistant strain degrades the antibiotic molecules (via the production of  $\beta$ -lactamase enzymes) but here we introduce a sensitive strain which does not. Therefore the antibiotic concentration is reduced in the presence of resistant bacteria, but is not affected by the presence of the sensitive bacteria. In this model, resistant and sensitive bacteria are characterised by different single-cell MIC (scMIC) values—the sensitive strain has a lower scMIC. The higher single-cell MIC of the resistant strain reflects the extra protection due to localisation of the  $\beta$ -lactamase enzymes in the periplasm [133, 159, 160], i.e. we expect the  $\beta$ -lactamase-producing cells to

be less vulnerable than the sensitive cells. Both resistant and sensitive bacteria grow when the antibiotic concentration is below their defined  $scMIC$  values, and die when the antibiotic concentration is above the  $scMIC$ .

We compare deterministic and stochastic versions of the model, represented by the schematic in Figure 4.3. As in Chapter 5, we incorporate deterministic and stochastic growth, as well as deterministic and stochastic loading of the bacterial population into droplets (see Chapter 4 for the detailed method description and justification). We assume that the two populations are independent apart from their indirect interaction via antibiotic degradation—for example, we do not simulate competition for nutrients.

### Mathematical representation

The deterministic growth and death of both the resistant ( $N_R$ ) and sensitive ( $N_S$ ) populations are modelled exponentially:

$$\frac{dN_R}{dt} = \begin{cases} \gamma_G N_R & a < scMIC_R \\ -\gamma_D N_R & a \geq scMIC_R \end{cases}, \quad (7.1)$$

$$\frac{dN_S}{dt} = \begin{cases} \gamma_G N_S & a < scMIC_S \\ -\gamma_D N_S & a \geq scMIC_S \end{cases}, \quad (7.2)$$

where  $\gamma_G$  is the growth rate,  $\gamma_D$  is the death rate,  $scMIC_R$  is the single-cell MIC of the resistant bacterial strain and  $scMIC_S$  is the single-cell MIC of the sensitive bacterial strain. Note that we use the same growth and death rates for both strains. Meanwhile, the antibiotic concentration decreases at a fixed rate, per resistant bacterium, in a manner that is identical to our earlier model, given in Section 4.2:

$$\frac{da}{dt} = -DN_R. \quad (7.3)$$

Stochastic growth and death is modelled with a tau-leaping algorithm [134], using the same rate constants as in the deterministic model. Section 4.3.2 gives details of the stochastic dynamics methodology.

Parameter	Value	Unit
$scMIC_R$	1	$\mu\text{g mL}^{-1}$
$scMIC_S$	0.1	$\mu\text{g mL}^{-1}$
Droplet volume	$1 \times 10^{-7}$	mL
$T_{end}$	300	min
Growth rate, $\gamma_G$	0.01	$\text{min}^{-1}$
Death rate, $\gamma_D$	0.045	$\text{min}^{-1}$
AB deg. rate, $D$	$1 \times 10^7$	$\text{cell}_R^{-1} \text{min}^{-1}$
Simulation timestep, $dt$	0.1	min

**Table 7.1** *Default parameters for the droplet simulations. These parameters were chosen to be comparable to experimental values or to be consistent with our resistant-only simulations. Survival of a droplet population is assessed after a simulation time of 300 minutes ( $T_{end}$ ).*

## Parameter values

Table 7.1 gives the default parameter values used in the simulations presented below. We assume that the sensitive bacteria have a single-cell MIC  $10\times$  lower than the resistant bacteria, but the same growth and death rates as the resistant strain. We assume the same growth and death rates for both the resistant and sensitive strains for simplicity. In an equivalent experimental setup, this would be a reasonable approximation if the resistant and sensitive strains differ only by the presence or absence of the ampicillin resistance cassette. The implicit modelling of the  $\beta$ -lactamase enzymes and the antibiotic degradation rate ( $D$ ) are discussed in Section 4.4. The numerical values of the parameters are the same as in Chapters 4 and 5, and are detailed in Section 4.5.3.

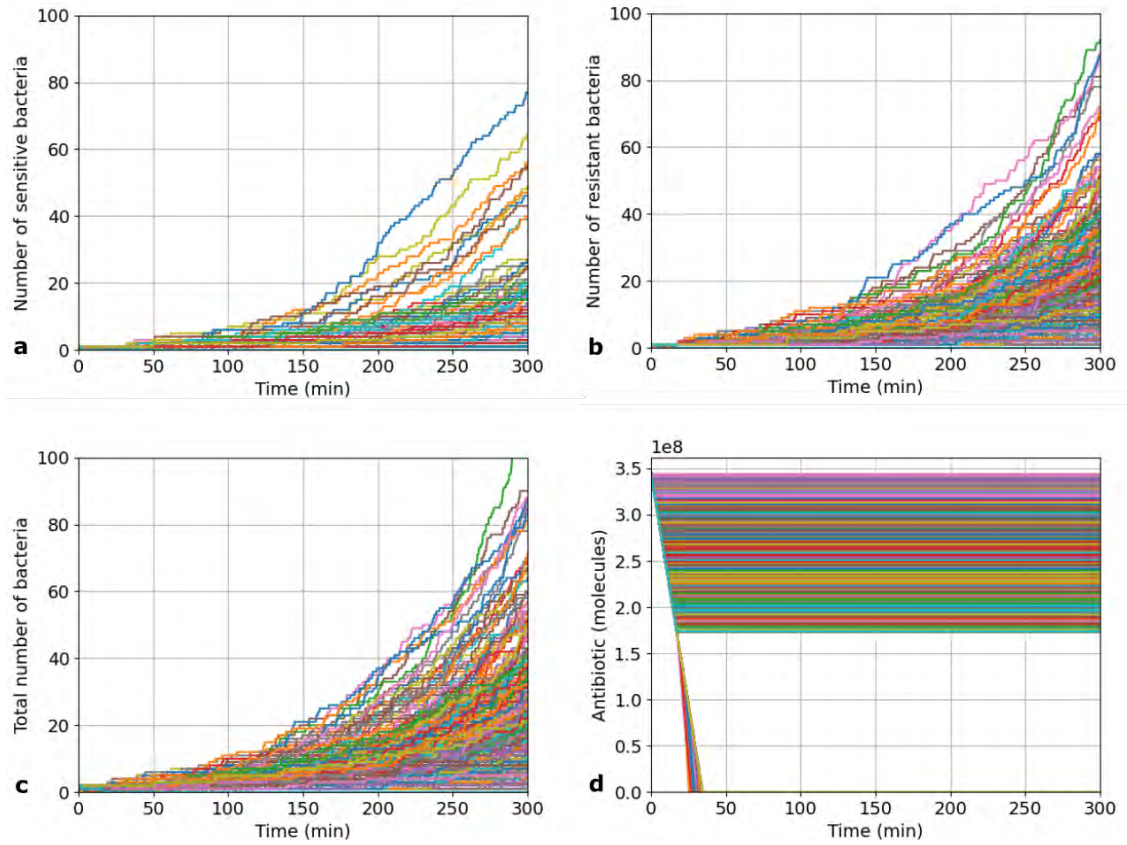


**Figure 7.1** *Dynamical trajectories for 1000 simulated droplets each with an initial population of 1 sensitive and 1 resistant bacterial cell, with an initial antibiotic concentration of  $2 \mu\text{g mL}^{-1}$ . Panels show (a) population dynamics of the sensitive strain, (b) population dynamics of the resistant strain, (c) the total growth curves, (d) the antibiotic concentration over time. In all panels, individual trajectories correspond to individual droplets. For these simulations, the fraction of droplets with surviving resistant bacteria was 0.465. The fraction of droplets with surviving sensitive bacteria was 0.102.*

## 7.3 Results

### 7.3.1 Simulations with equal starting numbers of resistant and sensitive bacteria

As an illustration, we first simulate 1000 droplet populations, with each droplet initially containing 1 sensitive bacterial cell and 1 resistant bacterial cell (i.e. we do not account for stochastic droplet filling). Trajectories from the simulations are plotted in Figure 7.1. The starting antibiotic concentration is set at  $2 \mu\text{g mL}^{-1}$ ,

which is above the single-cell MIC of both strains. The simulations are run with stochastic growth and death dynamics, so the outcome is different in replicate droplet simulations. The panels show growth curves for the sensitive strain, the resistant strain and the total population (a–c respectively) as well as the antibiotic concentration in panel (d) for each individual droplet. Panel (d) shows clearly that the antibiotic concentration plateaus at a non-zero value for a large proportion of the droplet populations; these correspond to droplets where the resistant population has been eliminated. While in droplets where resistant bacteria survive, the antibiotic concentration eventually falls to zero.

Without the resistant bacteria present, none of the sensitive strain would survive the antibiotic treatment at  $2 \mu\text{g mL}^{-1}$ , which is  $20\times$  the  $scMIC_s$ . In this example, 47% of the initial 1000 droplet populations contained surviving bacteria by  $T_{end}$ . Of these  $\approx 20\%$  contained mixtures of sensitive and resistant bacteria, while the other  $\approx 80\%$  contained only resistant bacteria. Of the 10% of the initial 1000 droplets containing surviving populations of sensitive bacteria, we see a wide range of final sensitive population size, up to 77 bacteria (see panel (a)). Figure 7.2 shows these final sensitive population numbers plotted against the final resistant population numbers. As we simulate the growth and death of each strain separately, we see that there is no correlation between the final number of resistant bacteria and the final number of sensitive bacteria. Instead, because larger population numbers are less probable, we actually see that if the population of one strain is large (e.g.  $> 30$  bacteria), the other strain is unlikely to also have a large population.

In addition, Figure 7.2 highlights the impact of the stochastic dynamics, as the deterministic version of the model results in the death of all the sensitive bacteria, under the same parameters.

### 7.3.2 Varying the initial number of resistant bacteria

Since resistant bacteria can protect sensitive bacteria by degrading the antibiotic, we expect that the survival probability for the sensitive bacteria will depend on the number of resistant bacteria that are initially present. To explore this, we ran a series of simulations, starting with 1 sensitive bacterium and a range of initial numbers of resistant bacteria. For each starting condition, we ran 1000 replicate simulations and measured the survival fractions for the resistant and sensitive bacteria. Figure 7.3 shows the results, plotted as a function of the initial number

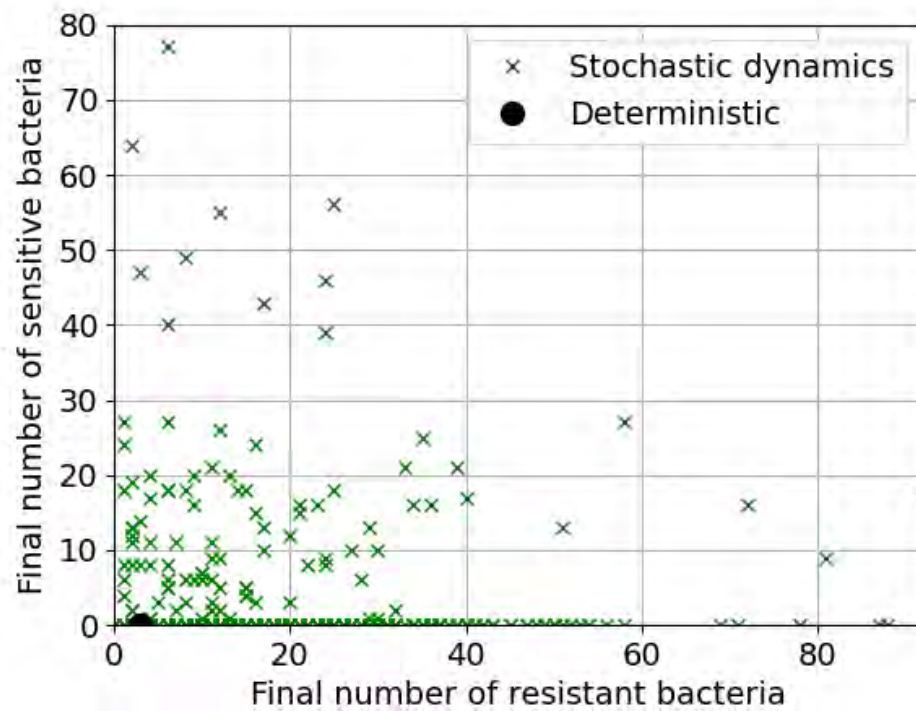


**Figure 7.2** *Plot showing the final population numbers of both strains. Each cross gives the population numbers for an individual droplet. The growth tracks for the simulations with stochastic dynamics are shown in Figure 7.1. The deterministic outcome of the simulations is given in black, where no sensitive bacteria survive.*



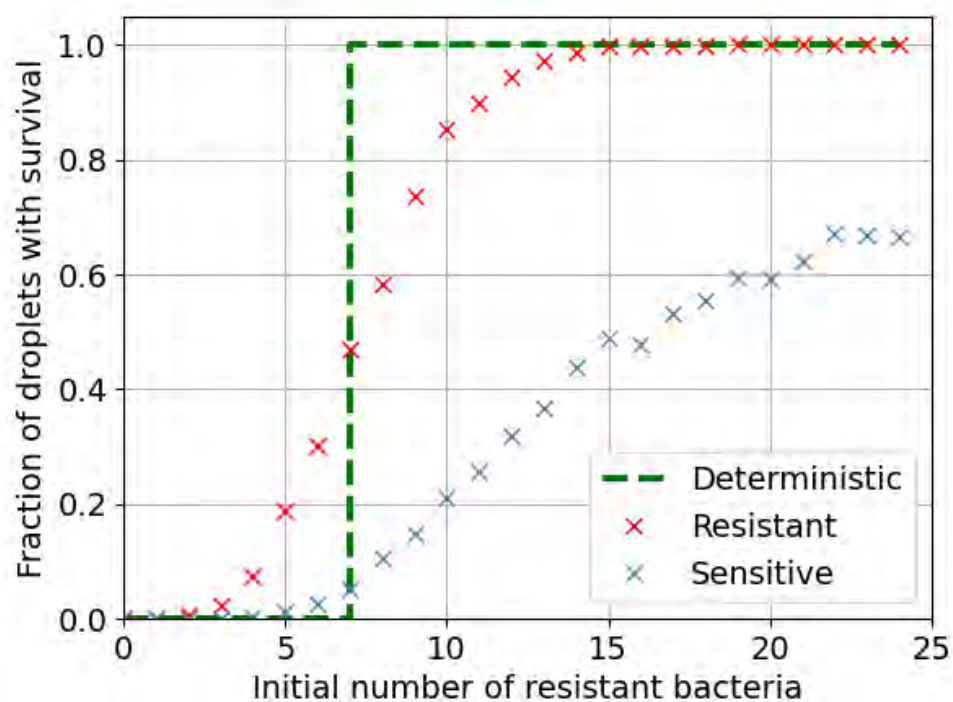


**Figure 7.3** Plot showing the fraction of droplets containing surviving resistant bacteria (red) and surviving sensitive bacteria (blue), for 1000 simulated droplet populations at a range of initial resistant bacterial numbers (1–25). All droplets began with 1 sensitive bacterium. The initial antibiotic concentration was set at  $10 \mu\text{g mL}^{-1}$ . Crosses represent the stochastic simulations and the dashed line shows the deterministic case.

of resistant bacteria.

We see the effect of increasing the population of resistant bacteria—increasing the number of enzymes and therefore protection. All droplets begin with 1 sensitive bacterial cell ( $N_{S,t=0} = 1$ ) and a set number of resistant bacteria (varied on the x-axis). For simplicity, these were fixed starting numbers (and not Poisson distributed). In Figure 7.3, the green deterministic line shows that both resistant and sensitive population survive if the initial number of resistant bacteria is greater than 7. In other words, in the deterministic model, there is never a scenario where the resistant population survives but the sensitive population dies out. This is in some sense an artefact of the deterministic model, since the sensitive population can regrow even if the ‘number’ of remaining bacteria is less than 1 (but greater than 0).

The red and blue data in Figure 7.3 show the survival fractions for the resistant and sensitive subpopulations for the simulations with stochastic (tau-leaping) birth and death dynamics. In this case we do see a difference in survival fraction between the resistant and sensitive subpopulations, partially because in the stochastic simulations the sensitive bacteria cannot regrow if their number becomes less than 1. Here we see that some droplet populations survive with  $N_{R,t=0} < 7$  but that the sensitive bacteria are only 50–70% likely to survive even when  $N_{R,t=0} > 15$ , where 100% of the resistant droplet populations survive. This is probably because the initial number of sensitive bacteria is very low ( $N_{S,0} = 1$ ), and the initial antibiotic concentration is high. Even for a high number of resistant bacteria, it takes time before the antibiotic is degraded to below the single-cell MIC of the sensitive strain. During this time there is a probability that the only sensitive bacterium will be killed.

### 7.3.3 Varying the initial number of sensitive bacteria

Increasing the number of sensitive bacteria does not cause the antibiotic to degrade more rapidly, however it can help prolong the survival of the sensitive population until the antibiotic concentration is brought to below the  $scMIC_S$ , and growth can resume.

We ran a similar set of simulations as above, but here we varied the initial number of sensitive bacteria, whilst maintaining a constant number of initial resistant bacteria. At an antibiotic concentration of  $10 \mu\text{g mL}^{-1}$ , as was used

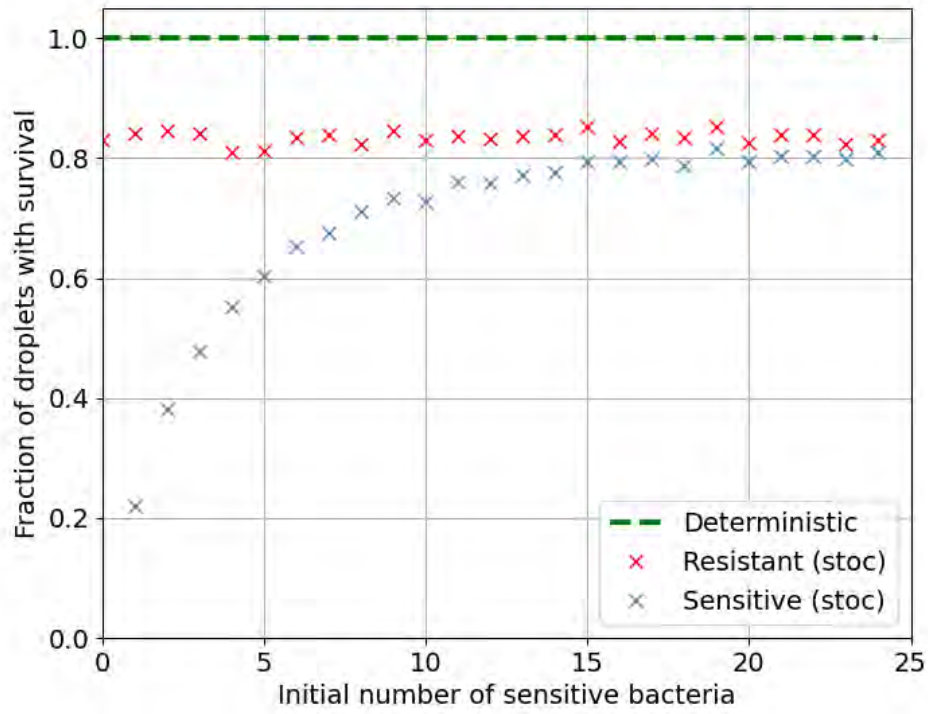


**Figure 7.4** *Survival fractions for the resistant and sensitive strains, plotted as a function of initial number of sensitive bacteria, for simulations of 1000 droplets. Each droplet started with 10 resistant bacteria. The data labelled ‘stoc’ were simulated with stochastic growth and death dynamics.*

for the simulations in Figure 7.3, droplets with only 1 initial resistant bacterial cell do not survive. Therefore we ran simulations with initial resistant bacterial populations of 10. Figure 7.4 shows that under these parameters, all droplet populations survive in the deterministic model. In the simulations with stochastic dynamics,  $\approx 0.8$  of the droplets have surviving resistant populations. The fraction of surviving sensitive populations increases as the initial number of sensitive bacteria increases, up until it reaches (but never exceeds) the survival fraction of the resistant populations.

### 7.3.4 Including stochastic droplet filling

Up to now, we did not include stochastic droplet filling in our simulations. Loading the droplets with Poisson distributed initial bacterial numbers mirrors the experimental droplet generation (see Sections 1.4.2 and 4.3). To obtain a

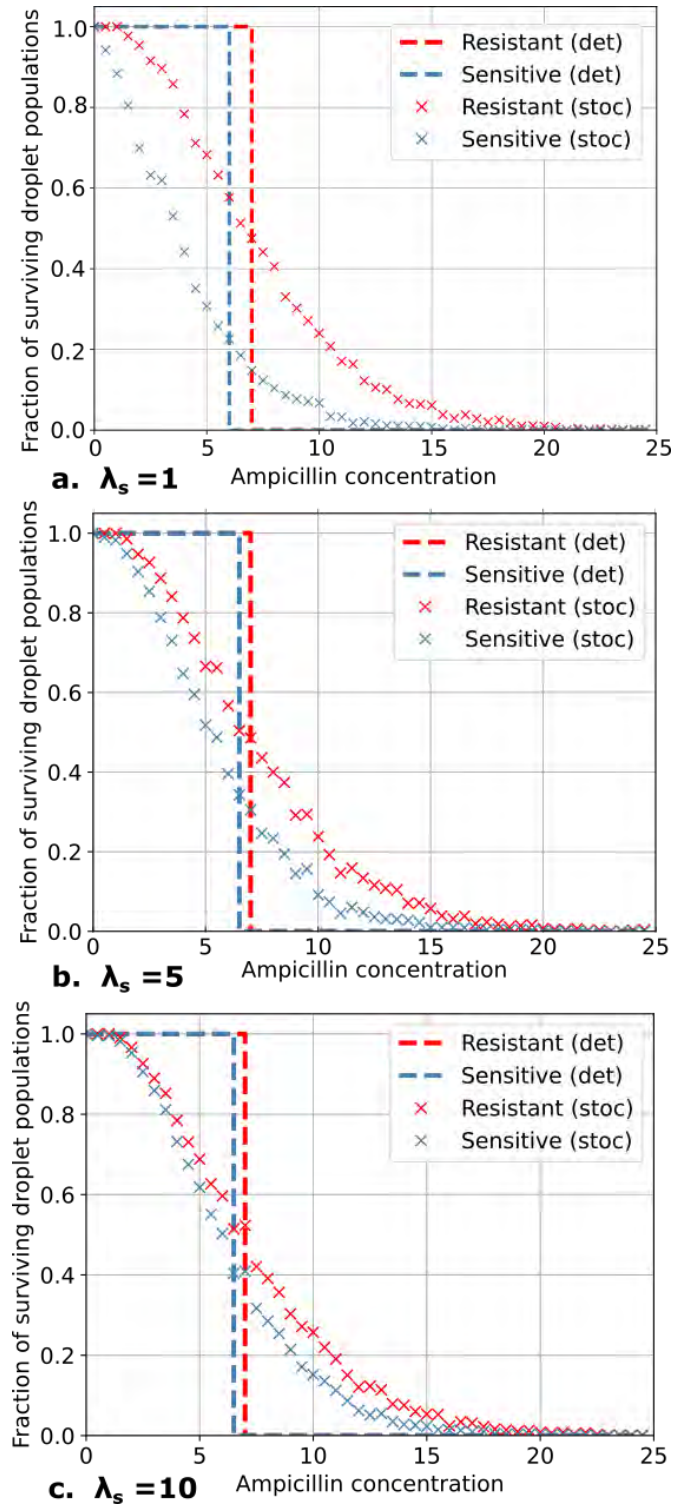


**Figure 7.5** *Survival fractions for the resistant and sensitive strains, plotted as a function of initial antibiotic concentration, for simulations of 1000 droplets. The simulations labelled ‘stoc’ include stochastic droplet filling and stochastic growth-death dynamics; the simulations labelled ‘det’ are entirely deterministic. In all simulations, the mean initial number of resistant bacteria,  $\lambda_R$ , was 5. The mean initial number of sensitive bacteria,  $\lambda_S$  was (a): 1, (b): 5 and (c): 10. Survival is greatly increased at high antibiotic concentrations in the stochastic simulations.*

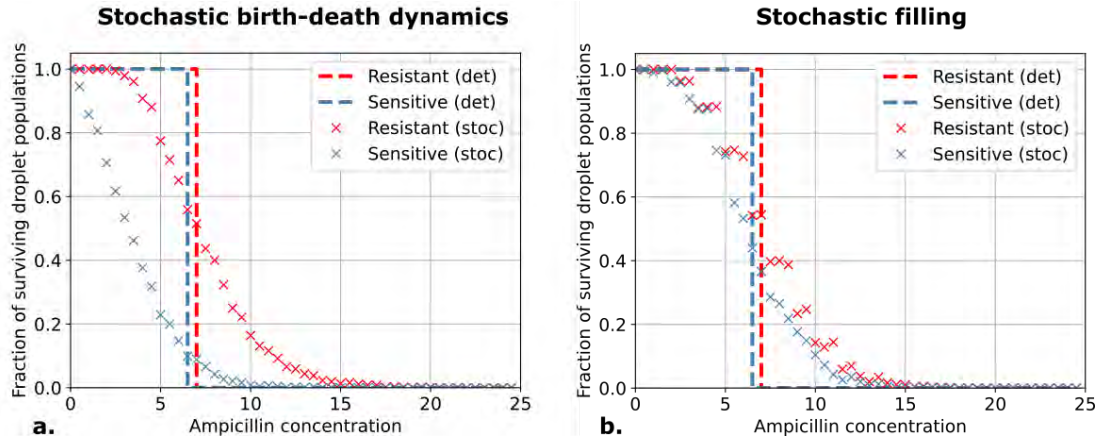
complete picture, we now simulate the mixed sensitive-resistant system, including stochastic droplet filling, for a range of initial antibiotic concentrations and a range of initial ratios of the sensitive and resistant strains.

Figure 7.5 shows the survival fractions of the sensitive and resistant strains, for 1000 simulated droplets at a range of antibiotic concentrations, for three different mean values for the starting number of sensitive bacteria ( $\lambda_S = 1$  (a), 5 (b), 10 (c)). In all cases, the mean initial number of resistant bacteria was 5 ( $\lambda_R = 5$ ; which is exactly 5 resistant cells per droplet in the deterministic case). As expected, in all ratios, the survival fraction decreases as the antibiotic concentration is increased.

The deterministic model produces step functions, for both the sensitive and resistant bacteria. However, unlike in Figures 7.3 and 7.4, the survival of the resistant strain does not guarantee the survival of the sensitive bacteria. We see surviving resistant populations at higher antibiotic concentrations, at which we do not get any surviving sensitive bacteria.

As in Chapter 5, we see that stochasticity in droplet filling and growth dynamics leads to survival at much higher antibiotic concentrations. For example, in panel (c), over 10% of sensitive populations survive at  $11 \mu\text{g mL}^{-1}$ , which is a factor of 110 greater than the  $scMIC_S$  and is a factor of 1.8 greater than the antibiotic concentration at which the deterministic model predicts no survival. Therefore we see that stochastic dynamics and Poisson-distributed encapsulation in droplets can greatly enhance survival, not only of resistant bacteria, but also of sensitive bacteria that co-exist with resistant ones.

Comparing panels (a), (b) and (c) in Figure 7.5, we see that the survival fractions for the resistant and sensitive strain differ greatly when the initial number of sensitive bacteria is small, (a), but are similar when the initial number of sensitive bacteria is large, (c). This echoes the finding of Figure 7.3, that a small sensitive population can easily die out before the antibiotic has been degraded, but a large sensitive population is more likely to survive until the resistant bacteria have degraded the antibiotic. Therefore, the protective effect of the resistant bacteria is greater when the number of sensitive bacteria is high. This is interesting, because it contrasts with the standard picture of social evolution theory, in which ‘cheating strategies’ work better for small cheater populations.



**Figure 7.6** *Results for the survival fraction of sensitive and resistant subpopulations, for simulations of 1000 droplets at varying ampicillin concentrations. All simulations start with (mean) numbers of 5 resistant and 1 sensitive bacteria. Panel (a) shows results for deterministic filling and stochastic birth-death dynamics, while panel (b) shows results for stochastic filling and deterministic birth-death dynamics. Both panels show the results from the fully deterministic simulations in dashed lines for comparison.*

### Separating the two sources of stochasticity

In Chapter 5, we found that stochastic filling and stochastic birth-death dynamics had similar effects on the survival of resistant populations in droplets. We want to investigate whether this is still the case for mixtures of sensitive and resistant bacteria. Figure 7.6 separates the effects of tau-leaping birth-death dynamics and Poisson loading on the survival of the droplet populations. Panel (a) shows the results for deterministic filling and stochastic birth-death dynamics, while panel (b) shows the results for stochastic filling and deterministic birth-death dynamics.

We start these simulations with  $\lambda$  values of 1 sensitive and 5 resistant bacterial cells per droplet, the same parameters as (a) in Figure 7.5.

Interestingly, the two sources of stochasticity have very different effects on the sensitive population—although the survival curves for the resistant population are similar in both cases. For stochastic birth-death dynamics, we see increased killing of the sensitive population. This is probably because stochastic death events lead to extinction of small sensitive populations before the resistant population has had time to degrade the antibiotic. In contrast, stochastic filling increases the range of antibiotic concentrations at which the sensitive strain can survive. This is because stochastic filling produces some droplets with large initial numbers of

resistant bacteria, that are able to protect the sensitive strain.

## 7.4 Discussion

In this chapter, I presented simulations of mixtures of resistant and sensitive bacteria, encapsulated in droplets. Resistant bacteria can protect sensitive bacteria by producing enzymes which degrade the antibiotic. Inspired by previous work on macro-scale populations [32] we were interested in how the protection of the sensitive bacteria by the resistant bacteria would play out in small droplet populations. Our results show that indeed, a small number of resistant bacteria can protect sensitive bacteria, and that this effect is greatly enhanced by stochastic encapsulation in droplets. Moreover, the protection is greatest when the initial number of sensitive bacteria is highest. This happens because having more sensitive bacteria present reduces the chances of stochastic extinction of the sensitive subpopulation before the antibiotic has been degraded.

In our model, the sensitive strain benefits from the presence of the resistant strain, but the resistant strain experiences no interaction with the sensitive strain; within a droplet, the dynamics of the resistant population is unaffected by the presence or absence of sensitive bacteria. This is of course unrealistic—in a real picolitre droplet we would expect competition for nutrients and space between the two strains. However, since competition for nutrients is mainly relevant at late times, when the droplet population becomes large, it seems unlikely that it would affect our main results, which are mostly dependent on what happens at early times<sup>1</sup>. In other words, the key event in our simulations is whether or not the sensitive population becomes extinct before the antibiotic has been degraded; this is determined while nutrients would still be abundant.

In this model, the resistant bacteria always have a better outcome than the sensitive populations. This is partially because we did not include any fitness cost for producing the  $\beta$ -lactamase enzyme. We could include such a cost by decreasing the growth rate of the resistant strain relative to that of the sensitive strain. However, in this model, a growth rate reduction of the resistant strain would not impact the survival probabilities of the resistant population (only the final population numbers). This is because the early-time dynamics, which determine

---

<sup>1</sup>Especially because we start with small numbers of bacteria and calculate survival fractions after 300 minutes of growth, which is only  $\approx 4.3$  doubling times.

survival, is dominated by death. In fact, a fitness cost such as a slower growth rate of the  $\beta$ -lactamase-producing cells could reduce the survival probabilities of the sensitive population, which is dependent on the rate at which the resistant population is able to degrade the antibiotic to below the sensitive single-cell MIC (this rate would be lower if the resistant cells took longer to reproduce). We would expect to obtain different results in a model where a second dose of antibiotic is added, after regrowth has happened; in this case, a fitness cost would be relevant. Interestingly, our model behaves quite differently to the well-known ‘cheater’ scenario of social evolution theory. Here, the sensitive bacteria do not act as cheaters, since any fitness cost for the resistant bacteria (even if it were present) would start only at late times, once survival of the resistant strain has already been determined. This distinction arises because in our model the crucial factor is survival of small populations rather than net population growth.

It would be interesting to perform a set of droplet experiments equivalent to these simulations. This would allow a quantitative investigation to assess the extent of the protection that  $\beta$ -lactamase-enzyme-producing bacteria can offer. In previous work, Yurtsev et al. investigated cooperative effects between  $\beta$ -lactamase producers and non-producers for larger populations of  $10^5$  cells [32]. A droplet experiment would not only allow us to investigate smaller populations, but also provide access to a range of population ratios, because the initial bacterial numbers will vary droplet to droplet due to the stochastic loading. Since we are able to count individual bacteria, we could correlate the fate of sensitive cells with the number of resistant cells in each droplet. This could be especially interesting as the results of these simulations have suggested that distributing the bacteria using Poisson statistics increases the chance of survival compared to the deterministic (bulk) case (see Figure 7.6). Investigating the dynamics of these small populations in a confined picolitre volume could show whether there is a critical density of resistant bacteria needed to protect sensitive cells.



# Chapter 8

## Conclusions

### 8.1 Perspectives on the work presented in the thesis

Biophysical and microbiological studies of bacterial growth and antibiotic response usually involve very large populations. However, clinical infections can start with a small number of bacteria. Individual bacteria can show strong heterogeneity in growth parameters and stress response. Therefore it is also important to study bacterial growth and death on a small population scale. The droplet methodology and image analysis techniques used in this thesis allow us to generate large datasets for statistical analysis of many identically prepared small bacterial populations. This thesis has demonstrated the validity and utility of microfluidic droplets for such studies. In particular, we can track in detail the fate of bacterial populations over many droplets, which combined with mathematical modelling, provides a way to understand how single-cell heterogeneity plays out in small populations.

This droplet-based bacterial growth approach allows us to address many questions at the intermediate scale between single cells and large populations. Do spatially separated small populations behave differently from the equivalent bulk populations? What information is lost when we study bulk populations of billions of bacteria? Faster or more resistant bacteria dominate traditional bacterial growth assays, obscuring our picture of the slow-growing bacteria within the population. Bacterial populations can sometimes survive environmental stresses

by virtue of a small subpopulation of non-growing or slowly growing cells that are not killed; these are often known as persisters. These slowly growing or non-growing bacteria provide a pool of cells from which the population can recover after the environmental conditions have improved. These bacteria are undetected in bulk experiments, but can be observed in droplet experiments (see Section 6.3.3). We note that it is important to track growth in droplet populations, rather than just looking at individual cells, since heterogeneities among cells are amplified in the exponential growth process. Therefore the distribution of traits generated in a growing population can differ than that among individual cells. It can also be argued that droplets better represent some natural environments than a well-mixed suspension in a flask. For example, droplets could mimic the interior of a host cell, or localised pockets within an infection that are exposed to a different local concentration of antibiotic. Furthermore, droplets might mimic the small niches found, e.g. in soil [15, 81].

An important feature that distinguishes our method from previous work is the use of image segmentation to identify cell counts in each droplet. Being able to count the absolute numbers of bacteria in each droplet is a great improvement over proxy methods used in previous work. For example it allows us to accurately sort our data according to initial population size. This means we can test density-dependent hypotheses, including the Bellman-Harris model predictions in much more detail than in previous work [95], and is also very useful in comparing our antibiotic data (Chapter 6) to our simulation predictions from Chapter 5.

In Chapter 3 we present the baseline heterogeneity observed for small populations undergoing uninhibited growth. This is useful for later comparison to experiments performed with antibiotic stress (Chapter 6). It also provides fundamental insights in its own right, since it allows us to test models for stochastic population growth. In particular, we showed that the data for uninhibited growth of *E. coli* populations in droplets was well fitted by the Bellman-Harris model, which assumes no inheritance of division times. This sort of data could be used in future to try to distinguish between different models for stochastic bacterial growth dynamics.

In Chapters 4–7, we focus on the effect of antibiotic on small population dynamics. In particular, we investigate populations of bacteria that produce  $\beta$ -lactamase; antibiotic degrading enzymes. Because the benefits of antibiotic degradation are collective, these populations are expected to show cooperative (density-dependent) effects. For macro-scale populations it is already known that  $\beta$ -

lactamase-producing bacteria can protect their neighbours, leading to a so-called ‘inoculum effect’, where high density populations are less susceptible to  $\beta$ -lactam antibiotics. However, we predicted using simulations that for small populations, stochasticity in droplet filling and growth-death dynamics would allow survival of antibiotic treatment at even higher concentrations.

In Chapter 6, our macro-scale experiments agreed well with the simulation predictions, showing an inoculum effect. However, our droplet experiments revealed complexity that had not been predicted in our simulations. Specifically, we observed that bacteria formed filaments in response to the ampicillin antibiotic. Moreover, we found that replicate experiments often did not give the same quantitative results (although qualitative trends were robust). Further work is needed to fully understand the effects of filamentation on bacterial survival and collective response, and to achieve fully reproducible experimental conditions.

The insights that we gained into the antibiotic response—in particular filamentation, were possible because of our use of microscopy as a method of measurement. Since we had stored images for every droplet at every time point, we could refer back to the raw images of the droplets post-experiment. This allows us to check for errors and, if required, adjust the analysis. If a growth trajectory shows unexpected dynamics, we can easily extract the image series corresponding to that droplet and inspect the images to see what has happened. This retrospective investigation also provides a useful way to confirm biological phenomena in a particular droplet, such as the onset of bacterial aggregation. Further image analysis can then be developed to investigate this, if required. The study of filamentation presented in this thesis (Sections 2.4 and 6.3.5) is an example of such post-experiment analysis. By quantifying the size, as well as the number of cells within a droplet, we were able to quantify filamentation and detect that biomass growth was occurring in the presence of antibiotic even though there was no cell division. This demonstrates the potential of this type of dynamic image-based droplet methodology.

## 8.2 Suggestions for future work

The work presented in this thesis suggests several promising avenues for future work.

## Improvements to image analysis

In this thesis, we developed image analysis methods to count bacteria in droplets automatically. However, these methods could be improved in future work. In particular a more sophisticated image analysis could be employed using machine learning techniques such as object detection, to identify bacteria and track droplets. This type of approach has been demonstrated for tracking the growth of individual *E. coli* bacteria in 2D on agar pads; identifying the cell poles and growth rates in time lapse videos taken with a 100 $\times$  objective [161]. In our experiments, improving the accuracy of the final data sets would allow us to compare our results to mathematical models with more accuracy, potentially allowing us to distinguish between alternative models, e.g. for stochastic bacterial growth.

In addition, reducing the manual optimisation steps required for every experiment would reduce the time required for the analysis.

## Regrowth of bacterial populations in the presence of antibiotic

A striking discrepancy between our simulation predictions (Chapter 5) and our experimental data (Chapter 6) is that in the simulations, droplet populations are predicted to regrow after the antibiotic is degraded below the scMIC, but in our experiments, we observe suppressed growth in droplets when ampicillin is present. Studies have shown regrowth after long times [48–50] and it is not clear whether conditions in our droplets prevent regrowth, or whether the experiment was simply too short. It would be an interesting to extend the experiments in Chapter 6 by imaging for longer than the current 4–6.5 hours. To make this possible, the frequency of imaging could be reduced from once every 10 minutes to every 30–60 minutes to give a coarser dataset which takes up less disk space. Alternatively, to determine whether bacteria are alive at the end of the experiment, we could distribute the droplets on agar plates containing fresh, antibiotic-free medium to see if colonies begin to grow. This would also provide an interesting way to independently verify our results on survival fraction (Chapter 6).

### **Closer focus on $\beta$ -lactamase producers**

Our simulation study revealed that literature values for kinetic parameters for  $\beta$ -lactamase enzymes vary widely. This made it hard to generate quantitative predictions for our experiments. Although we did observe the inoculum effect in our bulk experiments, as predicted, there were significant discrepancies between our droplet results (Chapter 6) and our simulation predictions (Chapter 5). It would be interesting to investigate further with a wider range of experimental parameters.

Adjustments could be made to the experiment, such as increasing the density of the initial bacterial suspension; changing the strain to one that produces more  $\beta$ -lactamase; testing a different  $\beta$ -lactam antibiotic; and including a colorimetric dye that directly measures  $\beta$ -lactamase activity. This would allow a more detailed investigation of the response of small populations to  $\beta$ -lactams and the possible cooperative effects of  $\beta$ -lactamase production.

### **Mixed populations of $\beta$ -lactamase producers and non-producers**

Despite their ubiquity, the dynamics of interacting microbial populations has hardly been investigated at the level of small populations. Therefore it would be very interesting to extend our clonal droplet experiments to mixed populations of  $\beta$ -lactamase producers and non-producers.

The clonal population studies in this thesis could be extended to include different strains of bacteria. This topic was investigated at a preliminary level using simulations in Chapter 7, but I did not have time to study it experimentally. Future work could include an experimental test based on the simulation predictions of Chapter 7, using microfluidic droplets. In other words, a multi-species experiment with a  $\beta$ -lactam antibiotic, to measure cooperation between a sensitive and resistant strain of bacteria. To interpret the data, the two strains would need to be distinguishable using different fluorescent proteins, for example.

## Using droplets for growth of difficult bacteria

In this thesis, I have used microfluidic droplets to study the dynamics of small populations of bacteria in the presence and absence of antibiotic. However, droplets may also provide a promising way to support the growth of bacteria or other microorganisms which are otherwise difficult to culture in laboratory conditions. This is because in the small microenvironment provided by a droplet, competitor bacteria may be absent, allowing an ‘unculturable’ species to more easily become established. Combining droplet microfluidics as used in this thesis, with traditional cell sorting systems may allow the isolation and co-cultivation of some ‘unculturable bacteria’ [125].

Using droplets to culture difficult bacteria is especially relevant for the discovery of new drugs. Natural products from bacteria account for half of all commercially available pharmaceuticals. Since 1987, no new class of antibiotics has been successfully developed (only derivatives and variations of previously discovered classes have been released for clinical use) [162]. Arguably, this is in part a result of the limited bacterial diversity we are currently able to study [125]. Employing microfluidic droplet generation methodology, could give insight into the antimicrobial properties of a range of metabolites from otherwise difficult to study species [79, 81, 83].

# Appendix A

## Extra figures

### A.1 Uninhibited droplet experiment with no growth

During the batch of uninhibited experiments, one of the overnight cultures did not grow in the droplets, despite there being no antibiotic present. Figure A.1 shows the same data on two different scales, to show the 626 individual growth tracks and the lack of growth in comparison to the other uninhibited growth plots, shown in Figure 3.1.

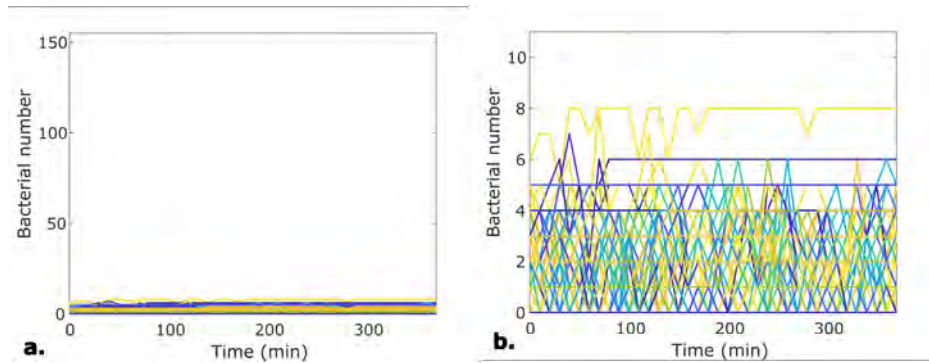


**Figure A.1** *The growth curves of the droplet populations in experiment  $E(0)$ . These are included to show that some overnight cultures simply do not grow any further whilst observed in droplets. Panels (a) and (b) show the same data on different y-axes scales.*

## A.2 Bellman–Harris analysis

The Bellman-Harris analysis for data from experiments B(0), C(0) and D(0) are shown in Figure A.2. Chapter 3, Section 3.3.4 includes a discussion of the analysis and shows the results for data from experiment A(0). Table A.1 shows the statistical test results for the  $CV(t)$  values of population size for each subset of initial bacterial number (see Figure 3.8).

$k$	1	2	3	4	5	6	7	8
Mann-Kendall	0	0	0	0	1	0	1	0
M-K p-value	0.59	0.039	0.25	0.031	0.003	0.077	0.0008	0.71
Lilliefors	0	0	0	0	0	0	0	0
Lilliefors p-value	0.029	0.24	> 0.5	> 0.5	> 0.5	0.05	0.031	0.018

**Table A.1** *Statistical test results for the  $CV(t)$  values of population size for subsets of droplet populations (with initial bacterial number,  $k$ ) from experiment A(0) (data shown in Figure 3.8). The Mann-Kendall (M-K) tests were completed using a Matlab script [124] and the Lilliefors tests were completed using an inbuilt Matlab function. A significance level,  $\alpha$  of 1% was used for both tests. There is insufficient evidence to reject the null hypothesis (of no trend) if the result is zero.*



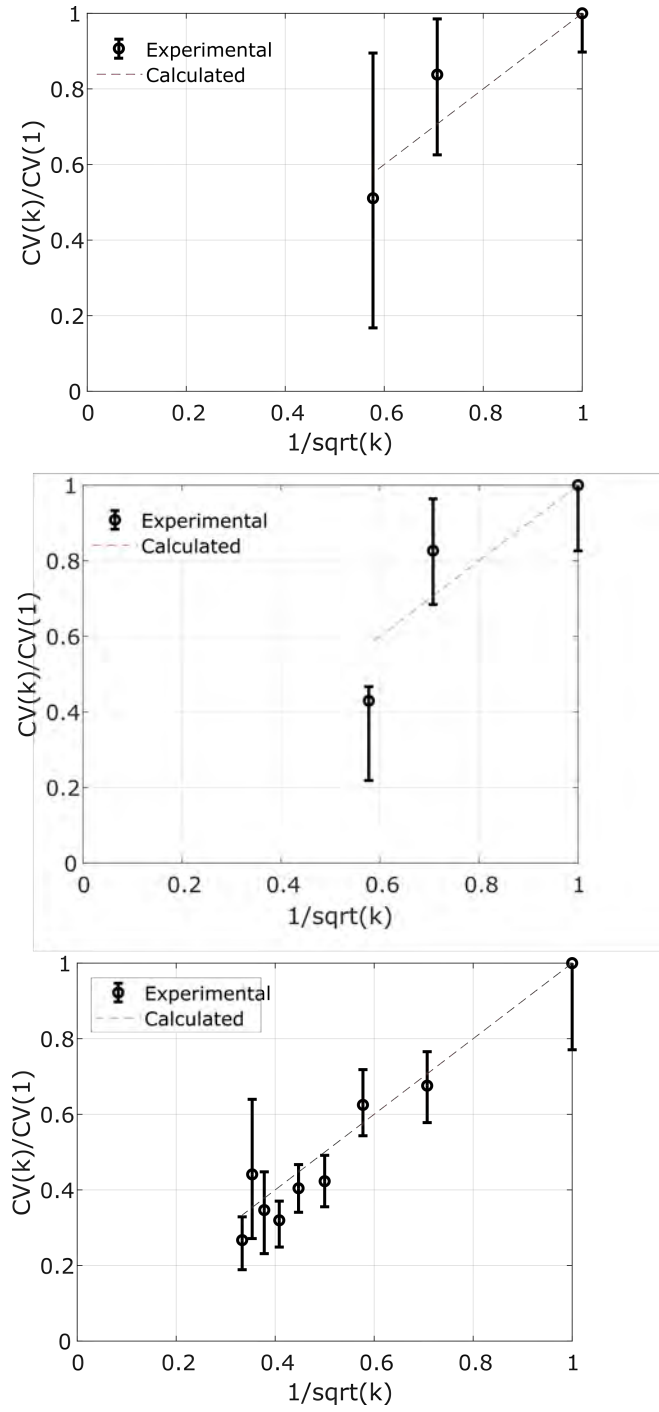


**Figure A.2** *CV of population size for droplets with initial bacterial number,  $k$ . Panels show, from top to bottom, experiments B(0), C(0), D(0). The red dotted line shows theoretical correlation. CV values were calculated using a linear fit of the standard deviation over the mean of population number, for each subset of data. Error bars were calculated using bootstrapping with 1000 resamplings.*

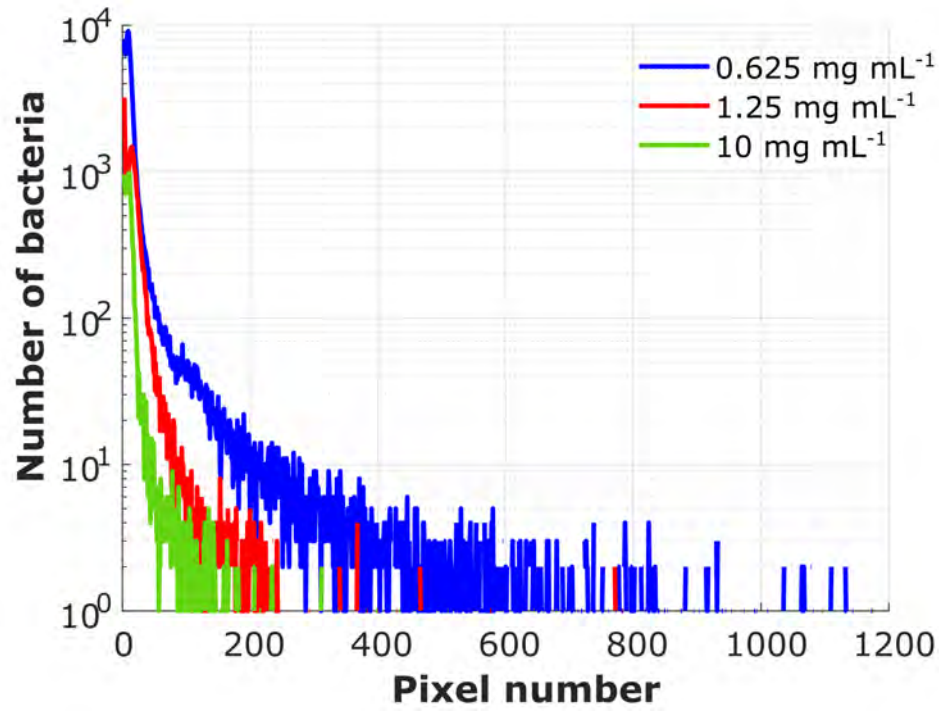


**Figure A.3** *Plot of bacterial sizes measured at all timesteps throughout the droplet experiments with initial ampicillin concentrations of  $0.625 \text{ mg mL}^{-1}$ ,  $1.25 \text{ mg mL}^{-1}$  and  $10 \text{ mg mL}^{-1}$  (data from experimental replicate A for each concentration). We see the number of filaments (cells with a pixel number above 70 px) is far higher for the  $0.625 \text{ mg mL}^{-1}$  experiment.*

### A.3 Ampicillin droplet experiments

Droplet experiments with ampicillin are presented in Chapter 6. Figure A.3 shows the bacterial sizes for three example ampicillin concentrations, to illustrate the difference in distributions. Figure A.4 shows the distribution of the droplet-population extinction times, for each concentration of ampicillin studied (see Section 6.3.4).

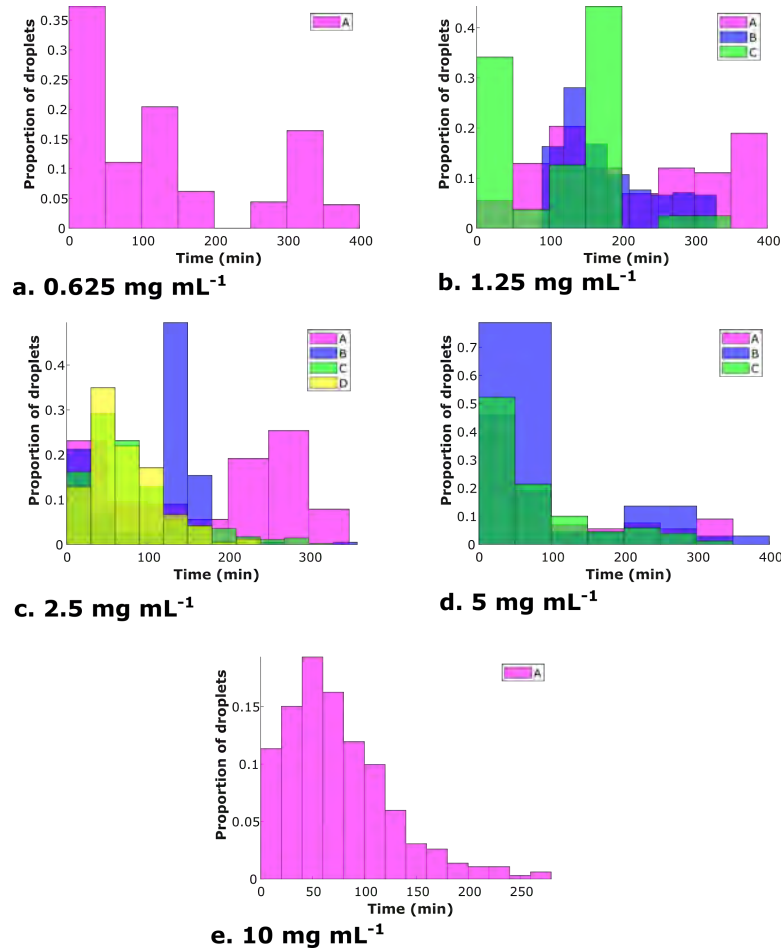


**Figure A.4** *Extinction time of droplet populations in experiments: (a) 0.625 mg mL<sup>-1</sup>, (b) 1.25 mg mL<sup>-1</sup>, (c) 2.5 mg mL<sup>-1</sup>, (d) 5 mg mL<sup>-1</sup>, and (e) 10 mg mL<sup>-1</sup>. Experimental replicates are shown in different colours. These histograms correspond to the average data shown in Figure 6.10. To reduce error caused by count fluctuations, the death of a droplet population (which was initially non-empty) was defined as when two consecutive bacterial counts were equal to zero. The time of extinction was taken as the time of the first count equal to zero which was followed by another zero count. These time values have a precision of 10 minutes due to the time required to image the whole device.*

## A.4 Bacterial density range

Before each droplet experiment, the density of the bacterial culture that was used as the aqueous phase was characterized by an  $OD_{600}$  measurement. To calibrate the measured OD in terms of CFU  $\text{mL}^{-1}$ , I followed a standard plating procedure and the results are shown in Figure A.5.

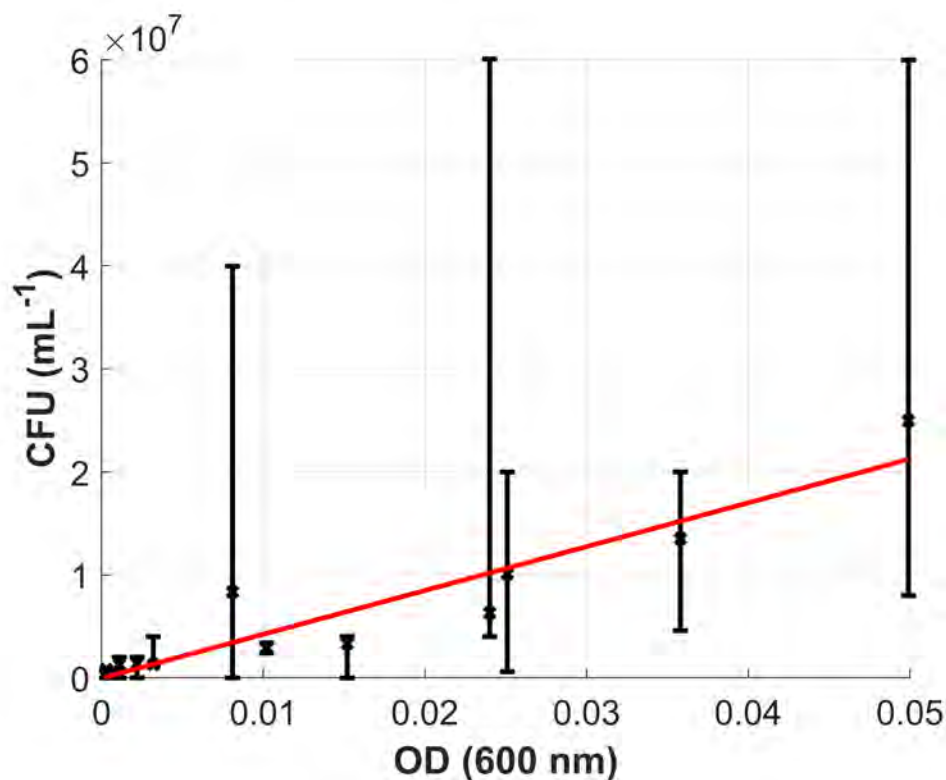


**Figure A.5** Plot of initial OD and CFU per mL, measured by plating the bacterial suspensions used in the plate reader experiments shown in Figures 6.2, A.6 and A.7. Linear fit (red) indicates the linear correlation,  $y = 4.3 \times 10^8 x - 34000$  with correlation coefficient,  $R=0.94$  and a  $p$ -value of  $6.7 \times 10^{-6}$ .

## A.5 Plate reader plots

There were three repeats of the plate reader experiment with different concentrations of RJA003 and ampicillin. Figures A.6 and A.7 are plotted below, and Figure 6.2 is shown in Chapter 6, where the results from the plate reader experiments are discussed in comparison to the droplet experiments. A schematic is shown alongside the data to help interpret the results, with each square representing the outcome of a particular combination of bacterial density (B) and antibiotic concentration (A). Growth is shown as a green square, growth at late times is shown in dark green, yellow shows growth for some, but not all, of the repeats and red indicates no growth.

Figures A.8 A.9, A.10) show the log plots of the plate reader data for PR1–3. Linear fits to the straight sections of the natural log of the data were used to get a value of growth rate in the uninhibited wells. Sections of at least 240 minutes (4 hours) or 24 data-points were used to get a representative rate. The growth rates are plotted in Figure A.11. The mean bulk growth rate for RJA003 in M9 minimal media was determined to be  $0.0066 \pm 0.002 \text{ min}^{-1}$  (the uncertainty is given from the standard deviation of the data).

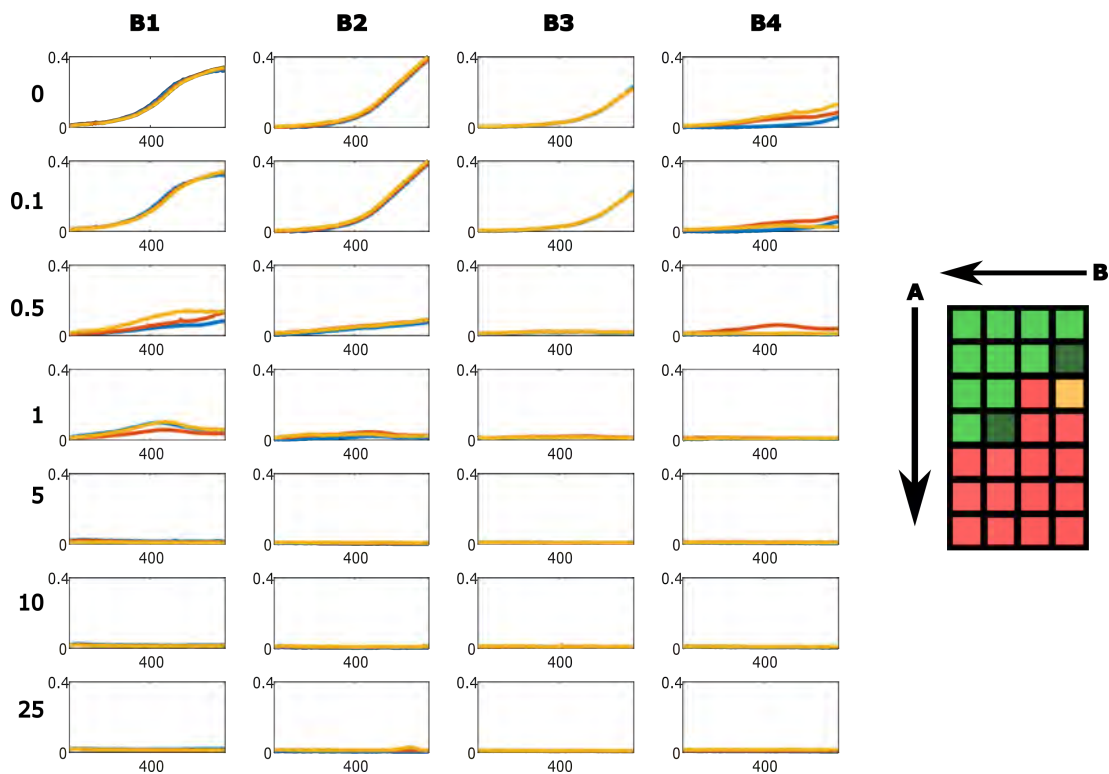


**Figure A.6** *PR1. Grid of  $OD_{600}$  (y-axis) plate reader measurements over time (x-axis, in minutes). Each plot shows 3 replicates for each combination of initial bacterial density and ampicillin concentration. Ampicillin concentration is increasing top to bottom (values given in  $\text{mg mL}^{-1}$ ). Initial bacterial density is decreasing left to right (B1 to B4). These values (from B1 to B4) are  $1.25 \times 10^7$ ,  $3.15 \times 10^6$ ,  $1.45 \times 10^6$ ,  $6.5 \times 10^5$   $\text{CFU mL}^{-1}$ . The top row shows uninhibited growth. The OD values plotted are corrected with the corresponding control subtracted as a baseline. The schematic shows growth as green, while late growth (that starts after 400 minutes) is shown in dark green. Yellow shows growth for some but not all of the replicate wells. Red indicates no growth. The arrows show increasing ampicillin concentration (A) and bacterial density (B).*

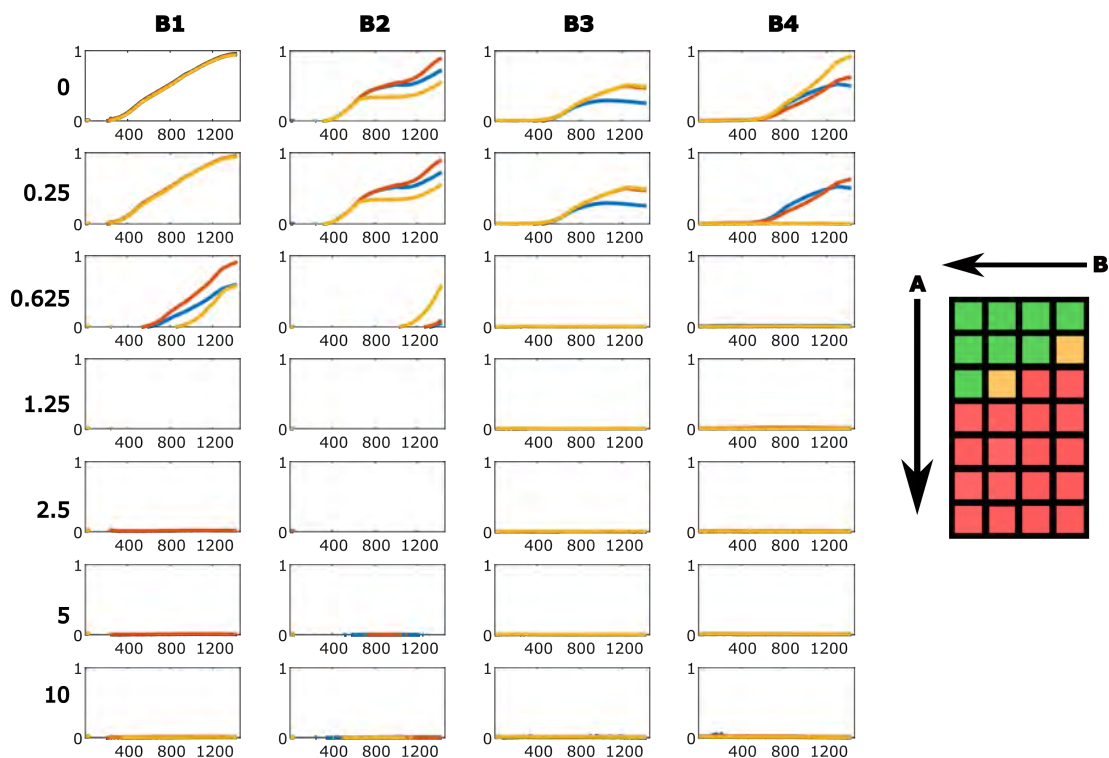


**Figure A.7** PR2. Grid of  $OD_{600}$  (y-axis) plate reader measurements over time (x-axis, in minutes). Each plot shows 3 replicates for each combination of initial bacterial density and ampicillin concentration. Ampicillin concentration is increasing top to bottom (values given in  $\text{mg mL}^{-1}$ ). Initial bacterial density is decreasing left to right (B1 to B4). These values (from B1 to B4) are  $6.77 \times 10^6$ ,  $4.17 \times 10^6$ ,  $6.50 \times 10^5$ ,  $4.00 \times 10^5$   $\text{CFU mL}^{-1}$ . The top row shows uninhibited growth. The OD values plotted are corrected with the corresponding control subtracted as a baseline. The schematic shows growth as green, yellow shows growth for some but not all of the replicate wells and red indicates no growth. The arrows show increasing ampicillin concentration (A) and bacterial density (B).

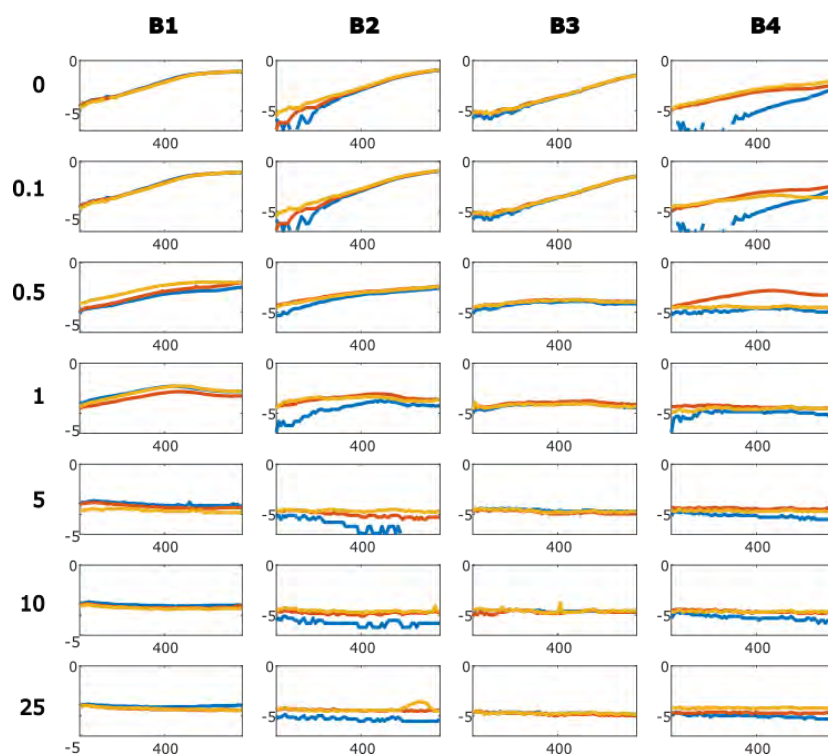


**Figure A.8** *Log plots for PR1, data shown in Figure A.6. Grid of  $OD_{600}$  (y-axis) plate reader measurements over time (x-axis, in minutes). Each plot shows 3 replicates for each combination of initial bacterial density and ampicillin concentration. Ampicillin concentration is increasing top to bottom (values given in  $\text{mg mL}^{-1}$ ). Initial bacterial density is decreasing left to right (B1 to B4).*



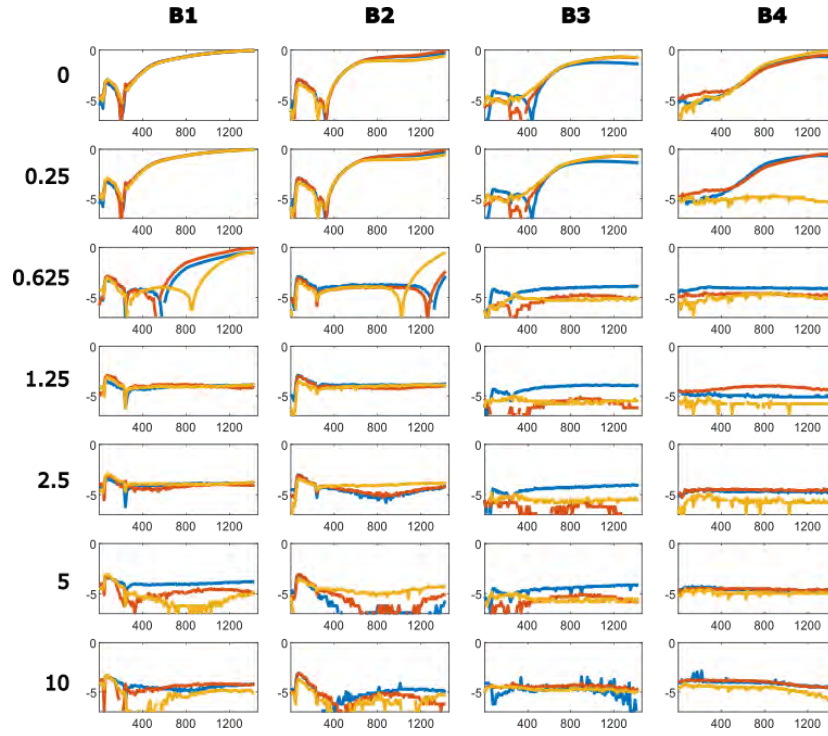


**Figure A.9** *Log plots for PR2, data shown in Figure A.7. Grid of  $OD_{600}$  ( $y$ -axis) plate reader measurements over time ( $x$ -axis, in minutes). Each plot shows 3 replicates for each combination of initial bacterial density and ampicillin concentration. Ampicillin concentration is increasing top to bottom (values given in  $\text{mg mL}^{-1}$ ). Initial bacterial density is decreasing left to right (B1 to B4).*

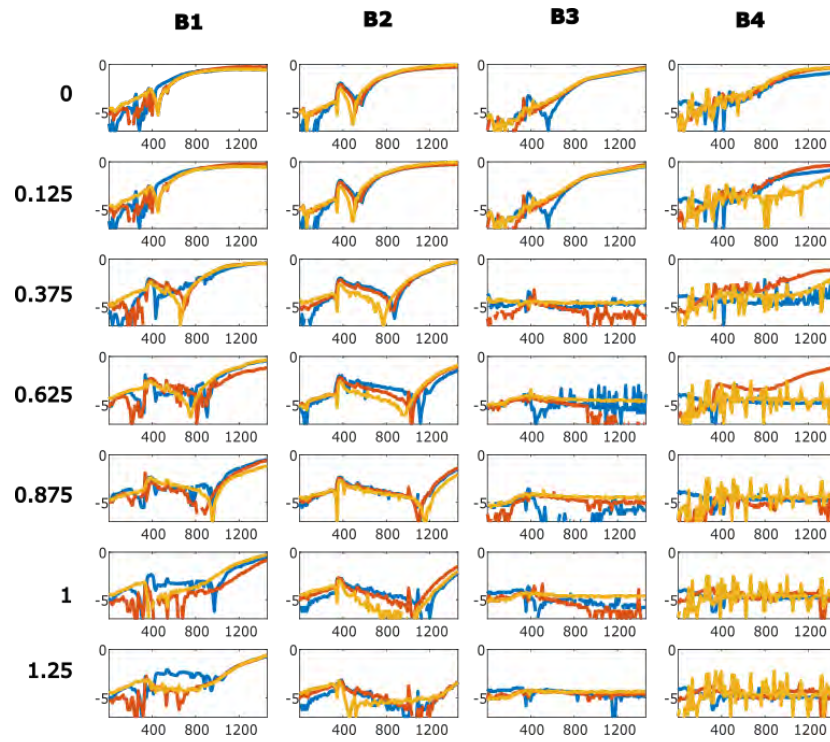


**Figure A.10** *Log plots for PR3, data shown in Figure 6.2. Grid of  $OD_{600}$  (y-axis) plate reader measurements over time (x-axis, in minutes). Each plot shows 3 replicates for each combination of initial bacterial density and ampicillin concentration. Ampicillin concentration is increasing top to bottom (values given in  $\text{mg mL}^{-1}$ ). Initial bacterial density is decreasing left to right (B1 to B4).*

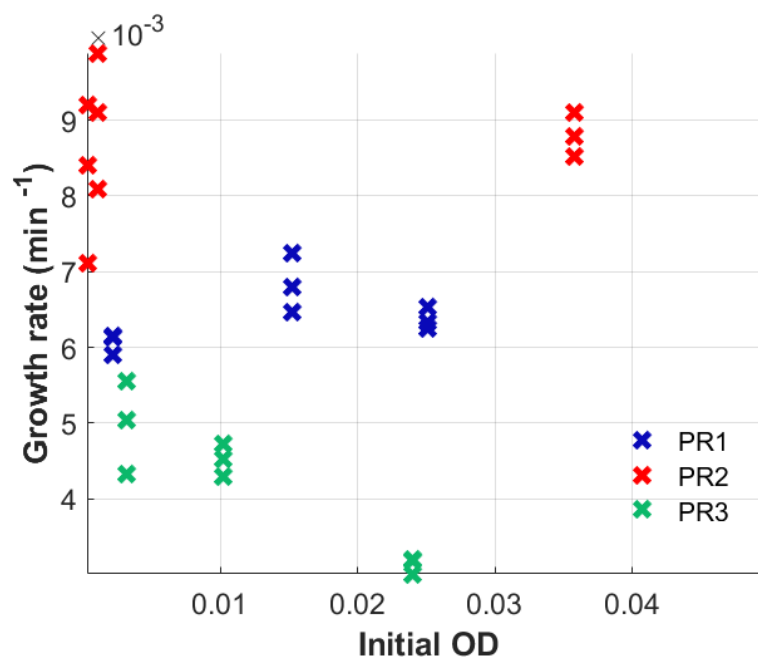


**Figure A.11** Plot of bulk growth rate of uninhibited bacteria against initial  $OD_{600}$ . Growth rates were calculated using a linear fit to the log plots of the OD curves shown in Figures 6.2, A.6 and A.7. The mean growth rate is  $0.0066 \pm 0.002 \text{ min}^{-1}$ . Colours indicate separate experimental repeats. There does not appear to be a relationship between growth rate and the initial bacterial density (measured with OD). The curves from PR1, B<sub>4</sub> and PR2, B<sub>2</sub> are excluded as this growth does not appear exponential (the log plot does not fit a linear model).

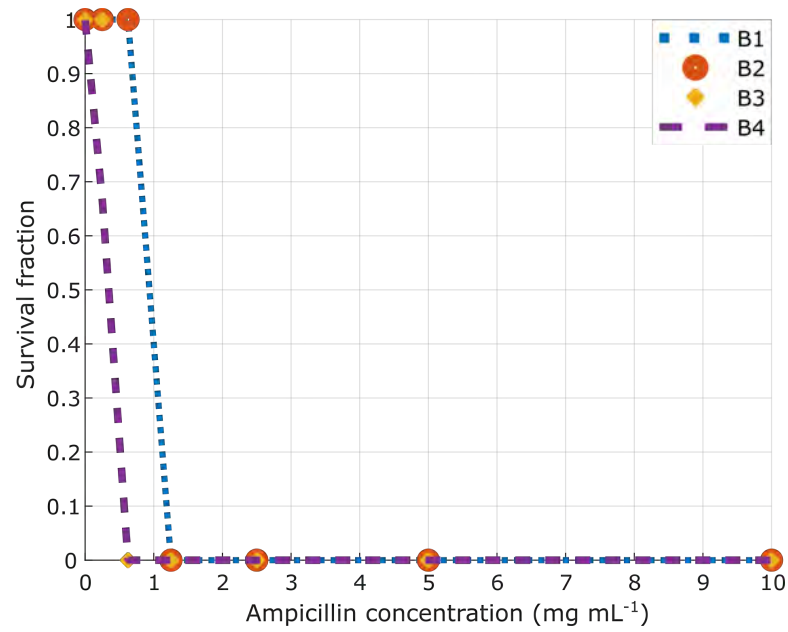


**Figure A.12** Plate reader survival fraction plot with data from experiment PR2 (see Figure A.7), showing a similar inoculum effect shape as we see in the deterministic model (Figure 5.9). Bacterial concentrations are increasing from B4 to B1.

## A.6 Droplet images

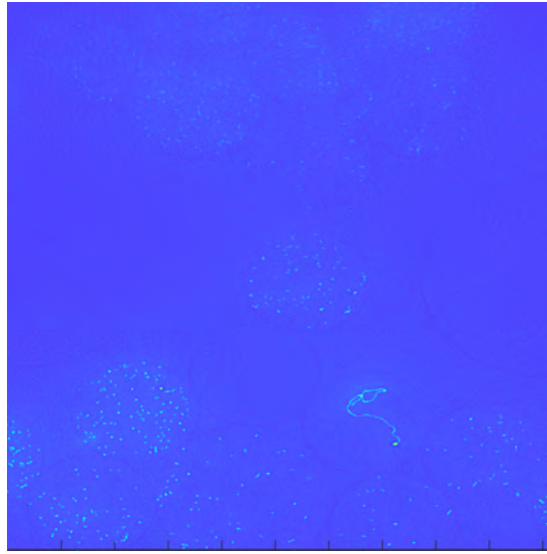


**Figure A.13** *Example CFP image of a FoV with droplet populations under uninhibited conditions after 5.5 hours of observed growth. One droplet contains a very long filament; this cell did not divide throughout the experiment. Surrounding droplets contain many bacteria (image from experiment A(0)). Adaptive thresholding is able to distinguish bacteria despite distribution of cell brightness.*

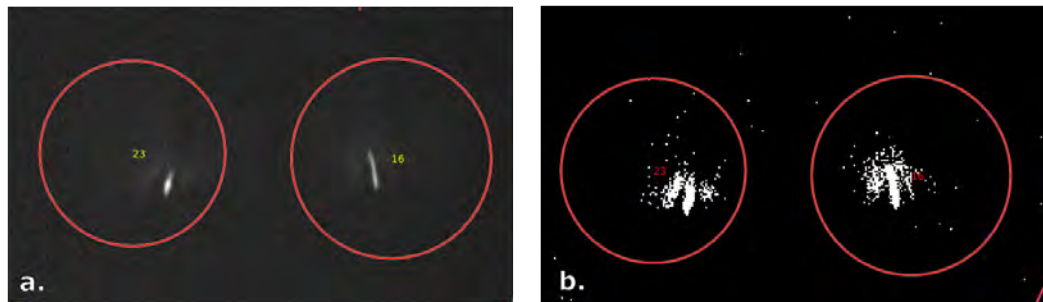


**Figure A.14** *Filamenting at later times at low antibiotic concentrations. The thresholding is inaccurate due to the ‘halo’ of fluorescence around the filaments, causing the bacteria count to be more than 1 per droplet. The population in droplet 16 dies between 270 and 280 minutes but the population in droplet 23 bacteria survives the whole experiment (image from experiment C(1.25)).*

# Appendix B

## Droplet experimental protocol

### Preparation:

#### Make device

Every droplet experiment is performed with a new microfluidic device. These are produced in-house using a master mould (see Section 1.4.1). It is important that bubbles are removed from the liquid Polydimethylsiloxane (PDMS) before it sets and that the channels are kept dust-free. The steps to make a PDMS device using a master mould are as follows:

- Clean and prepare master mould,
- Mix 10 parts elastomer to 1 part crosslinking agent to form PDMS,
- Remove bubbles (using a vacuum),
- Pour PDMS into mould and set in oven at 90°C,
- Cut device out of mould,
- Punch holes for inlets and outlets with a (1 mm) biopsy punch,
- Insert (1 mm OD, 0.75 mm ID) thin-wall single-barrel glass capillaries into the inlet and outlet holes,
- Flush inlets and outlets with compressed air to remove debris,

- Place device on clear tape to remove any debris or dust,
- Bond device to (cleaned) glass slide using a plasma oven,
- Epoxy glass capillaries to secure to the device.

### **Mount device into chamber**

Place the device into the chamber (see Section 2.2.3) and secure with the screws. Apply enough pressure to ensure water-tightness, without cracking the slide. A device in the sealed chamber is shown in Figure B.1.

### **Surface treatment**

Defrost Pico-Glide™ surface treatment. Add 0.05 mL of Pico-Glide™ to a 1 mL syringe already filled with 0.5 mL of air. Attach via tubing to the outlet of the device and slowly push through. Pico-Glide™ should be left in channels for at least 30 minutes to make them fluorophilic (see Section 2.2.5).

### **Grow bacteria overnight**

Take 3 single colonies from an M9+gl agar petri dish to make 3 separate bacterial cultures in 6 mL of M9+gl(0.4%) media. Incubate overnight with shaking at 37°C.

## **Experiment day:**

### **Dilute overnight bacterial suspension**

Dilute one of the overnight samples; 25  $\mu$ L in 10 mL of M9+gl media, or 50  $\mu$ L if using a Y-junction for the aqueous phase. Place this diluted suspension back in the 37°C incubator for 1.5 hours.

## **Start the oil phase**

Mount the chamber containing the device using the custom metal stage onto the microscope. Fill a 1 mL syringe with  $\approx 0.8$  mL of FC-40 and Pico-Surf<sup>TM</sup> mix. Remove bubbles from the syringe and then attach the tubing to the syringe. Push oil through tubing until  $\approx 2$  cm from the end. Place tubing through the chamber lid, and attach onto oil inlet. Check syringe pump settings (correct width of syringe etc.). Start syringe pump to initially fill channels (at a rate of  $40\text{--}70\ \mu\text{L hr}^{-1}$ ).

## **Set up the microscope ND acquisition scan (in NIS elements)**

Check Köhler illumination set-up; adjust position of condenser as needed. Spatially calibrate the objective. Ensure the light path is correct for scanning and stitching a large image ('Flip' selected). Check bright-field and fluorescence settings and focus. Inspect the device (especially the generator) to spot any issues (e.g. blockages in channels). Check the ND acquisition settings, ensuring the correct switching of settings between the two channels (filter, illumination, exposure, binning, capture bit number and auto-scaling). Ensure PFS (the Perfect Focus System) is selected and that the shutter is closed between time loops (to reduce fluorescence overexposure).

## **Antibiotic**

If antibiotic is being used, prepare dilution using frozen ampicillin stock (according to Table B.1). The concentration was made to be twice the desired final experimental concentration, as the ampicillin solution is introduced into the device at the same rate as the bacterial suspension, to achieve a 1:1 ratio.

## **Start the aqueous phase**

Remove bacterial suspension from incubator (after 1.5 hours). Take an initial Optical Density (OD) measurement at 600 nm (using M9 media as the baseline measurement). Fill a 1 mL syringe with the bacterial suspension, remove the air bubbles, attach tubing to syringe and insert tubing through the lid of the chamber (see Figure B.1). Start infusing at a flow rate (of  $\approx 80\ \mu\text{L hr}^{-1}$ ).



M9+gl media	Stock ampicillin	Concentration	Exp. concentration
1975	25	1.25	0.625
1950	50	2.5	1.25
1900	100	5	2.5
1800	200	10	5
1600	400	20	10

**Table B.1** *Ampicillin dilutions. Experimental (exp.) concentrations of ampicillin, made from frozen stock of 100 mg mL<sup>-1</sup> ampicillin and M9+gl media. Concentrations are given in mg mL<sup>-1</sup> and volumes in  $\mu$ L.*

If antibiotics are being used, attach two syringes, containing the bacterial suspension and the antibiotic solution (through the chamber lid) to a Y-junction, and push through both liquids. Attach the Y-junction to the aqueous inlet capillary with  $\approx 1$  cm of tubing and start the flow rates at  $\approx 40 \mu\text{L hr}^{-1}$  on a dual-syringe pump to ensure a 1:1 ratio.

### Epoxy tubing

Apply epoxy to ensure water-tightness and prevent tubing sliding off glass capillaries when water is added to the chamber. Wait for the epoxy to dry. Make sure there is flow through both the oil and aqueous inlets. Screw the lid onto the chamber; ensure that the tubing contacting the bacteria is submerged and that excess tubing does not cover the reservoir area (this would interrupt the microscope light path whilst imaging).

### Water bath

Carefully remove the chamber from the microscope, whilst the syringe pumps are still going, without pulling on the tubing. Submerge the chamber into 37°C water. Fill pump-tubing with water using the pump, starting with the outlet, and attach to create a sealed loop. Remove bubbles from the chamber, ensure it is completely filled with water, and then close the bubble-trap.

Remove excess water from the outside and re-mount onto microscope (once the chamber is warm, it is often harder to fit into the microscope mount; remove mount from the microscope and apply more force or alternatively, submerge mount and device together). Submerge tubing into the water bath to maintain

the water temperature in the chamber. Set the water bath temperature to  $\approx 40^{\circ}\text{C}$ , and adjust accordingly. Attach temperature probe to the chamber. Secure mount in place with tape to prevent movement during the scan.

### **First droplets**

Monitor the device using the microscope, and once the first droplets start to be generated, adjust the flow rates to achieve monodispersity. The rate of the oil phase should be set at  $120\ \mu\text{L hr}^{-1}$  for the device with the smaller step-width, and  $160\ \mu\text{L hr}^{-1}$  for the device with the larger step width (see Section 2.2.2 and Figure 2.3). The aqueous phase (containing the bacteria) is set at  $35\ \mu\text{L hr}^{-1}$ , if a dual-syringe pump with a Y-junction is used, or  $60\text{--}70\ \mu\text{L hr}^{-1}$  if there is only one aqueous solution. These flow rates should be adjusted as necessary.

### **Cut tubes, adjust scan settings and begin scan**

Once monodisperse droplets fill the reservoir, cut the tubing and stop both the syringe pumps. Check the focus and exposure for the bright-field and fluorescence channels and check that the PFS is working correctly. Test the area of the scan; it needs to cover all, or as much as possible of the reservoir, but not go over the limits of the chamber, and not beyond the range of the PFS. If stitching, complete a test scan, then import and stitch these images (as outlined in Section 2.3.1) to check the calibration and light path settings. Create and start the full ND acquisition (in time, channel and FoV).

### **Take OD and dilute bacterial suspension for plating**

Once the scan is successfully running, remove the bacterial suspension from the incubator and take a second OD measurement at 600 nm.

If plating, successively dilute bacteria at a ratio of 20:180  $\mu\text{L}$  in PBS. Repeat  $\times 3$ , then add 5  $\mu\text{L}$  of each dilution in a wheel to  $\times 3$  agar plates. Put the plates in an incubator to grow overnight.

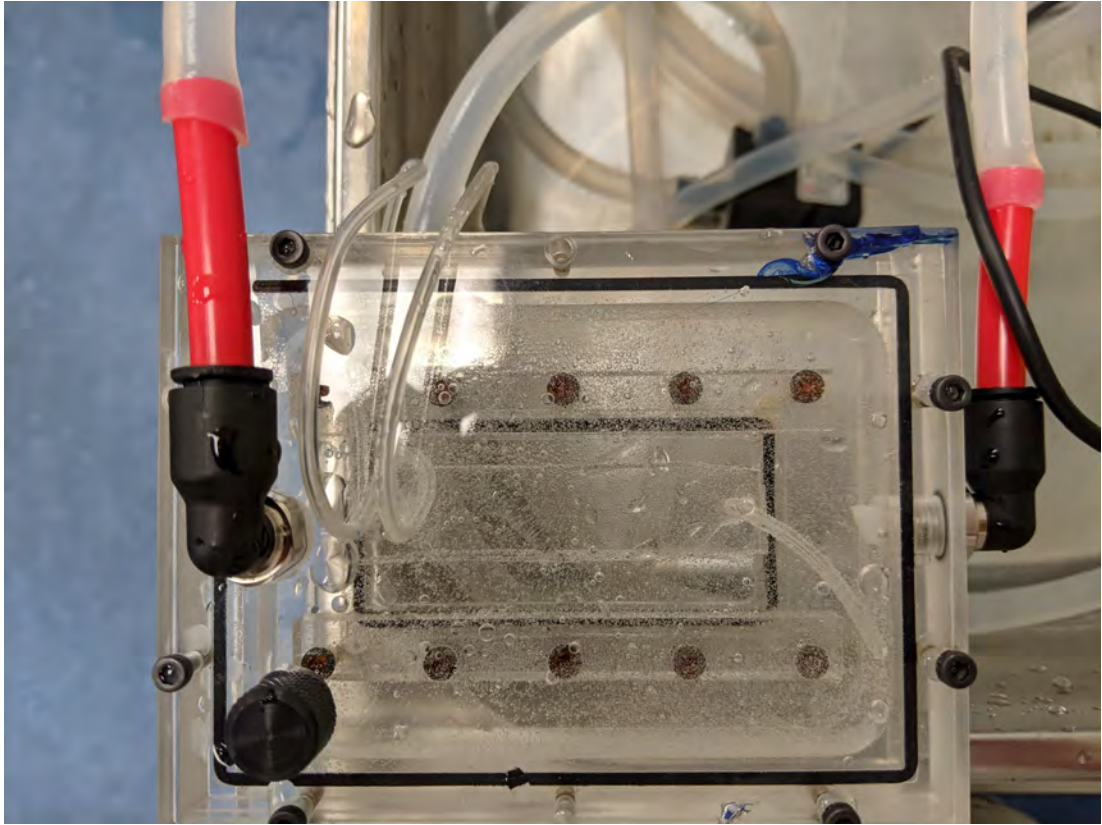


**Figure B.1** *Image of custom chamber, filled with water, containing a microfluidic device. The large slide is held in place with plastic clamps onto an O-ring. Inlet and outlet tubes pass through holes in the lid. The water pump (seen in background) is connected to the chamber through the red plastic fittings.*

**Continue to intermittently check the microscopy images from the scan, microscope focus, chamber temperature and water flow.**

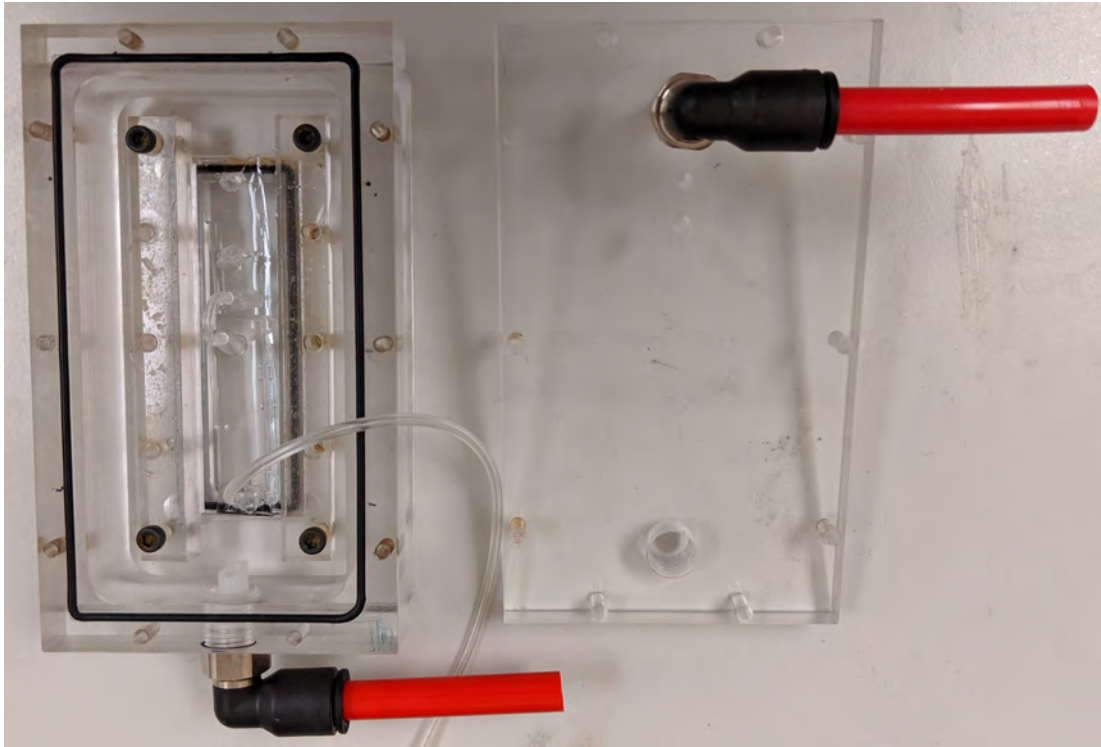


**Figure B.2** *Image of the prototype custom chamber containing the an original microfluidic device (where the generator and reservoir are made separately and connected by tubing) on a standard microscope slide. During use, all the screws are inserted before adding water.*

# Bibliography

- [1] M. Podinovskaia, W. Lee, S. Caldwell, and D. G. Russell, “Infection of macrophages with mycobacterium tuberculosis induces global modifications to phagosomal function,” *Cellular Microbiology*, vol. 15, no. 6, p. 843–859, 2013.
- [2] K. P. Koutsoumanis and A. Lianou, “Stochasticity in colonial growth dynamics of individual bacterial cells,” *Applied and Environmental Microbiology*, vol. 79, no. 7, pp. 2294–2301, 2013.
- [3] C. S. Wylie, A. D. Trout, D. A. Kessler, and H. Levine, “Optimal strategy for competence differentiation in bacteria,” *PLoS Genetics*, vol. 6, no. 9, p. e1001108, 2010.
- [4] M. Viney and S. E. Reece, “Adaptive noise,” *Proceedings of the Royal Society B: Biological Sciences*, vol. 280, no. 1767, p. 20131104, 2013.
- [5] R. Dawkins, *The selfish gene*. Oxford University Press, 1, reprint ed., 1978.
- [6] S. V. Avery, “Microbial cell individuality and the underlying sources of heterogeneity,” *Nature Reviews Microbiology*, vol. 4, no. 8, pp. 577–587, 2006.
- [7] G. Cárcamo-Oyarce, P. Lumjiaktase, R. Kümmerli, and L. Eberl, “Quorum sensing triggers the stochastic escape of individual cells from pseudomonas putida biofilms,” *Nature Communications*, vol. 6, no. 1, 2015.
- [8] K. Papenfort and B. L. Bassler, “Quorum sensing signal–response systems in gram-negative bacteria,” *Nature Reviews Microbiology*, vol. 14, no. 9, pp. 576–588, 2016.
- [9] K. Koyama, H. Hokunan, M. Hasegawa, S. Kawamura, and S. Koseki, “Do bacterial cell numbers follow a theoretical Poisson distribution? Comparison of experimentally obtained numbers of single cells with random number generation via computer simulation,” *Food Microbiology*, vol. 60, pp. 49–53, 2016.
- [10] Y. Hara-Kudo and K. Takatori, “Contamination level and ingestion dose of foodborne pathogens associated with infections,” *Epidemiology and Infection*, vol. 139, no. 10, pp. 1505–1510, 2011.

- [11] A. R. Rachael M Jones, Mark Nicas, Alan Hubbard, Matthew D. Sylvester, “The Infectious Dose of *Francisella Tularensis* (Tularemia),” *Applied Biosafety*, vol. 10, no. 4, pp. 227–239, 2005.
- [12] T. C. Z. Roger D. Pechous, Travis R. McCarthy, “Working toward the Future: Insights into *Francisella tularensis* Pathogenesis and Vaccine Development,” *Microbiology and Molecular Biology Reviews*, 2009.
- [13] R. M. Jones, M. Nicas, A. E. Hubbard, and A. L. Reingold, “The Infectious Dose of *Coxiella Burnetii* (Q Fever),” *Applied Biosafety*, vol. 11, no. 1, p. 32–41, 2006.
- [14] D. Saini, G. W. Hopkins, S. A. Seay, C.-J. Chen, C. C. Perley, E. M. Click, and R. Frothingham, “Ultra-low dose of mycobacterium tuberculosis aerosol creates partial infection in mice,” *Tuberculosis*, vol. 92, no. 2, p. 160–165, 2012.
- [15] P. Greulich, B. Waclaw, and R. J. Allen, “Mutational pathway determines whether drug gradients accelerate evolution of drug-resistant cells,” *Physical Review Letters*, vol. 109, no. 8, 2012.
- [16] N. M. Vega and J. Gore, “Collective antibiotic resistance: Mechanisms and implications,” *Current Opinion in Microbiology*, vol. 21, p. 28–34, 2014.
- [17] C. van Boxtel, J. H. van Heerden, N. Nordholt, P. Schmidt, and F. J. Bruggeman, “Taking chances and making mistakes: non-genetic phenotypic heterogeneity and its consequences for surviving in dynamic environments,” *Journal of The Royal Society Interface*, vol. 14, no. 132, p. 20170141, 2017.
- [18] P. Patra and S. Klumpp, “Population dynamics of bacterial persistence,” *PLoS ONE*, vol. 8, no. 5, 2013.
- [19] S. Klumpp, Z. Zhang, and T. Hwa, “Growth rate-dependent global effects on gene expression in bacteria,” *Cell*, vol. 139, no. 7, pp. 1366–1375, 2009.
- [20] F. Lyu, M. Pan, S. Patil, J.-H. Wang, A. Matin, J. R. Andrews, and S. K. Tang, “Phenotyping antibiotic resistance with single-cell resolution for the detection of heteroresistance,” *Sensors and Actuators B: Chemical*, vol. 270, pp. 396–404, 2018.
- [21] P. S. Ocampo, V. Lázár, B. Papp, M. Arnoldini, P. A. Zur Wiesch, R. Busa-Fekete, G. Fekete, C. Pál, M. Ackermann, and S. Bonhoeffer, “Antagonism between bacteriostatic and bactericidal antibiotics is prevalent,” *Antimicrobial Agents and Chemotherapy*, vol. 58, no. 8, pp. 4573–4582, 2014.
- [22] J. Coates, B. R. Park, D. Le, E. Simsek, W. Chaudhry, and M. Kim, “Antibiotic-induced population fluctuations and stochastic clearance of bacteria,” *eLife*, vol. 7, p. e32976, 2018.

- [23] H. K. Alexander and R. C. MacLean, “Stochastic bacterial population dynamics restrict the establishment of antibiotic resistance from single cells,” *Proceedings of the National Academy of Sciences*, vol. 117, no. 32, pp. 19455–19464, 2020.
- [24] I. El Meouche and M. J. Dunlop, “Heterogeneity in efflux pump expression predisposes antibiotic-resistant cells to mutation,” *Science*, vol. 362, no. 6415, pp. 686–690, 2018.
- [25] A. S. Kennard, M. Osella, A. Javer, J. Grilli, P. Nghe, S. J. Tans, P. Cicuta, and M. Cosentino Lagomarsino, “Individuality and universality in the growth-division laws of single e. coli cells,” *Physical Review E*, vol. 93, no. 1, 2016.
- [26] G. N. Rolinson, “Effect of beta-lactam antibiotics on bacterial cell growth rate,” *Microbiology*, vol. 120, no. 2, pp. 317–323, 1980.
- [27] K. Stevenson, A. F. McVey, I. B. N. Clark, P. S. Swain, and T. Pilizota, “General calibration of microbial growth in microplate readers,” *Scientific Reports*, vol. 6, no. 1, 2016.
- [28] J. Kayser, C. F. Schreck, M. Gralka, D. Fusco, and O. Hallatschek, “Collective motion conceals fitness differences in crowded cellular populations,” *Nature Ecology amp; Evolution*, vol. 3, no. 1, pp. 125–134, 2018.
- [29] K. M. Davis and R. R. Isberg, “Defining heterogeneity within bacterial populations via single cell approaches,” *BioEssays*, vol. 38, no. 8, pp. 782–790, 2016.
- [30] E. J. Stewart, R. Madden, G. Paul, and F. Taddei, “Aging and death in an organism that reproduces by morphologically symmetric division,” *PLoS Biology*, vol. 3, no. 2, p. e45, 2005.
- [31] K. M. McKinnon, “Flow cytometry: An overview,” *Current Protocols in Immunology*, vol. 120, no. 1, 2018.
- [32] E. A. Yurtsev, H. X. Chao, M. S. Datta, T. Artemova, and J. Gore, “Bacterial cheating drives the population dynamics of cooperative antibiotic resistance plasmids,” *Molecular Systems Biology*, 2013.
- [33] P. Wang, L. Robert, J. Pelletier, W. L. Dang, F. Taddei, A. Wright, and S. Jun, “Robust growth of escherichia coli,” *Current Biology*, vol. 20, no. 12, pp. 1099–1103, 2010.
- [34] J. Mannik, R. Driessen, P. Galajda, J. E. Keymer, and C. Dekker, “Bacterial growth and motility in sub-micron constrictions,” *Proceedings of the National Academy of Sciences*, vol. 106, no. 35, pp. 14861–14866, 2009.

- [35] Yang D, Jennings AD, Borrego E, Retterer ST and Mannik J, “Analysis of Factors Limiting Bacterial Growth in PDMS Mother Machine Devices,” *Front. Microbiol.*, vol. 9, 2018.
- [36] G. Kapoor, S. Saigal, and A. Elongavan, “Action and resistance mechanisms of antibiotics: A guide for clinicians,” *Journal of Anaesthesiology Clinical Pharmacology*, vol. 33, no. 3, p. 300, 2017.
- [37] A. Fleming, “On the antibacterial action of cultures of a penicillium, with special reference to their use in the isolation of b. influenzæ,” *British journal of experimental pathology*, vol. 10, pp. 226–236, 1929.
- [38] D. J. Abraham, F. L. Lewis, A. Burger, D. Andreotti, S. Biondi, and E. Di Modugno, *Beta-Lactam Antibiotics*, p. 607–736. Wiley, 2003.
- [39] N. Pandey and M. Cascella, *Beta Lactam Antibiotics*. Treasure Island (FL, USA): StatPearls Publishing LLC., 2021.
- [40] European Centre for Disease Prevention and Control (ECDC), “Country overview of antimicrobial consumption.” [www.ecdc.europa.eu/en/antimicrobial-consumption/database/country-overview](http://www.ecdc.europa.eu/en/antimicrobial-consumption/database/country-overview), 2022.
- [41] K. L. Bhaskar Thakuria, “The Beta Lactam Antibiotics as an Empirical Therapy in a Developing Country: An Update on Their Current Status and Recommendations to Counter the Resistance against Them,” *J Clin Diagn Res.*, 2013.
- [42] E. Y. Klein, T. P. Van Boeckel, E. M. Martinez, S. Pant, S. Gandra, S. A. Levin, H. Goossens, and R. Laxminarayan, “Global increase and geographic convergence in antibiotic consumption between 2000 and 2015,” *Proceedings of the National Academy of Sciences*, vol. 115, no. 15, pp. E3463–E3470, 2018.
- [43] World Health Organisation, *WHO report on surveillance of antibiotic consumption: 2016–2018 early implementation.*, pp. 102–113. 2018.
- [44] European Centre for Disease Prevention and Control, “Antimicrobial consumption in the eu/eea.” [www.ecdc.europa.eu/sites/default/files/documents/Antimicrobial-consumption-in-the-EU-Annual-Epidemiological-Report-2019.pdf](http://www.ecdc.europa.eu/sites/default/files/documents/Antimicrobial-consumption-in-the-EU-Annual-Epidemiological-Report-2019.pdf), 2019.
- [45] The 2021 Expert Committee on Selection and Use of Essential Medicines, “Who model lists of essential medicines.” [www.who.int/groups/expert-committee-on-selection-and-use-of-essential-medicines/essential-medicines-lists](http://www.who.int/groups/expert-committee-on-selection-and-use-of-essential-medicines/essential-medicines-lists), 2021.
- [46] S. S. Castle, “Ampicillin,” in *xPharm: The Comprehensive Pharmacology Reference* (S. Enna and D. B. Bylund, eds.), pp. 1–6, New York: Elsevier, 2007.



- [47] Z. W. El-Hajj and E. B. Newman, “How much territory can a single *E. coli* cell control?,” *Frontiers in Microbiology*, vol. 6, 2015.
- [48] J. E. Sulaiman and H. Lam, “Proteomic study of the survival and resuscitation mechanisms of filamentous persisters in an evolved *Escherichia coli* population from cyclic ampicillin treatment,” *mSystems*, vol. 5, no. 4, 2020.
- [49] Z. W. El-Hajj and E. B. Newman, “An *Escherichia coli* Mutant That Makes Exceptionally Long Cells,” *Journal of Bacteriology*, vol. 197, no. 8, pp. 1507–1514, 2015.
- [50] A. Mückl, M. Schwarz-Schilling, K. Fischer, and F. C. Simmel, “Filamentation and restoration of normal growth in *Escherichia coli* using a combined CRISPRi sgRNA/antisense RNA approach,” *PLOS ONE*, vol. 13, no. 9, 2018.
- [51] N. Mahfouz, I. Ferreira, S. Beisken, A. von Haeseler, and A. E. Posch, “Large-scale assessment of antimicrobial resistance marker databases for genetic phenotype prediction: a systematic review,” *Journal of Antimicrobial Chemotherapy*, vol. 75, no. 11, pp. 3099–3108, 2020.
- [52] Barreto, B. Guimarães, H. Radhouani, C. Araújo, A. Gonçalves, E. Gaspar, J. Rodrigues, G. Igrejas, and P. Poeta, “Detection of antibiotic resistant *E. coli* and *enterococcus* spp. in stool of healthy growing children in Portugal,” *Journal of Basic Microbiology*, vol. 49, no. 6, pp. 503–512, 2009.
- [53] C. L. Tooke, P. Hinchliffe, E. C. Bragginton, C. K. Colenso, V. H. Hirvonen, Y. Takebayashi, and J. Spencer, “ $\beta$ -Lactamases and  $\beta$ -Lactamase Inhibitors in the 21st Century,” *Journal of Molecular Biology*, vol. 431, no. 18, p. 3472–3500, 2019.
- [54] R. J. Worthington and C. Melander, “Overcoming resistance to  $\beta$ -Lactam antibiotics,” *Journal of Organic Chemistry*, vol. 78, no. 9, p. 4207–4213, 2013.
- [55] G. Masuda and S. Tomioka, “Possible beta-lactamase activities detectable in infective clinical specimens,” *The Journal of Antibiotics*, vol. 30, no. 12, pp. 1093–1097, 1977.
- [56] I. Brook, “The role of beta-lactamase-producing-bacteria in mixed infections,” *BMC Infectious Diseases*, vol. 9, 2009.
- [57] E. C. for Antimicrobial Susceptibility Testing (EUCAST) of the European Society of Clinical Microbiology and I. D. (ESCMID), “Determination of minimum inhibitory concentrations (MICs) of antibacterial agents by broth dilution,” *Clinical Microbiology and Infection*, vol. 9, no. 8, pp. ix–xv, 2003.
- [58] I. Wiegand, K. Hilpert, and R. E. W. Hancock, “Agar and broth dilution methods to determine the minimal inhibitory concentration (MIC) of

- antimicrobial substances,” *Nature Protocols*, vol. 3, no. 2, pp. 163–175, 2008.
- [59] J. W. Mouton, A. E. Muller, R. Canton, C. G. Giske, G. Kahlmeter, and J. Turnidge, “MIC-based dose adjustment: facts and fables,” *Journal of Antimicrobial Chemotherapy*, vol. 73, pp. 564–568, 2018.
  - [60] M. Abdul-Aziz, J. Lipman, J. Mouton, W. Hope, and J. Roberts, “Applying pharmacokinetic/pharmacodynamic principles in critically ill patients: Optimizing efficacy and reducing resistance development,” *Seminars in Respiratory and Critical Care Medicine*, vol. 36, no. 01, p. 136–153, 2015.
  - [61] B. Kowalska-Krochmal and R. Dudek-Wicher, “The minimum inhibitory concentration of antibiotics: Methods, interpretation, clinical relevance,” *Pathogens*, vol. 10, no. 2, p. 165, 2021.
  - [62] U. Ullmann, “Correlation of minimum inhibitory concentration and beta-lactamase activity,” *Infection*, vol. 5, no. 4, pp. 261–262, 1977.
  - [63] J. W. Mouton and A. A. Vinks, “Relationship between minimum inhibitory concentration and stationary concentration revisited,” *Clinical Pharmacokinetics*, vol. 44, no. 7, pp. 767–768, 2005.
  - [64] K. P. Smith and J. E. Kirby, “The inoculum effect in the era of multidrug resistance: Minor differences in inoculum have dramatic effect on mic determination,” *Antimicrobial Agents and Chemotherapy*, vol. 62, no. 8, 2018.
  - [65] T. Artemova, Y. Gerardin, C. Dudley, N. M. Vega, and J. Gore, “Isolated cell behavior drives the evolution of antibiotic resistance,” *Molecular Systems Biology*, vol. 11, no. 7, pp. 822–822, 2015.
  - [66] O. Scheler, K. Makuch, P. R. Debski, M. Horka, A. Ruszczak, N. Pacocha, K. Sozański, O. P. Smolander, W. Postek, and P. Garstecki, “Droplet-based digital antibiotic susceptibility screen reveals single-cell clonal heteroresistance in an isogenic bacterial population,” *Scientific Reports*, vol. 10, no. 1, 2020.
  - [67] R. Mitchell, P. Bellamy, C. Ellis, R. Hewison, N. Hodgetts, G. Iason, N. Littlewood, S. Newey, J. Stockan, and A. Taylor, “Collapsing foundations: The ecology of the British oak, implications of its decline and mitigation options,” *Biological Conservation*, vol. 233, pp. 316–327, 2019.
  - [68] V. Nava and B. Leoni, “A critical review of interactions between microplastics, microalgae and aquatic ecosystem function,” *Water Research*, vol. 188, p. 116476, 2021.
  - [69] D. Kalenitchenko, N. Le Bris, L. Dadaglio, E. Peru, A. Besserer, and P. E. Galand, “Bacteria alone establish the chemical basis of the wood-fall chemosynthetic ecosystem in the deep-sea,” *The ISME Journal*, vol. 12, no. 2, pp. 367–379, 2017.

- [70] B. J. Enagbonma and O. O. Babalola, “Potentials of termite mound soil bacteria in ecosystem engineering for sustainable agriculture,” *Annals of Microbiology*, vol. 69, no. 3, pp. 211–219, 2019.
- [71] A. S. Griffin, S. A. West, and A. Buckling, “Cooperation and competition in pathogenic bacteria,” *Nature*, vol. 430, no. 7003, pp. 1024–1027, 2004.
- [72] G. Orazi and G. A. O’Toole, ““It Takes a Village”: Mechanisms Underlying Antimicrobial Recalcitrance of Polymicrobial Biofilms,” *Journal of Bacteriology*, vol. 202, no. 1, 2019.
- [73] L. Galera-Laporta and J. Garcia-Ojalvo, “Antithetic population response to antibiotics in a polybacterial community,” *Science Advances*, vol. 6, no. 10, 2020.
- [74] O. J. Dressler, X. Casadevall i Solvas, and A. J. DeMello, “Chemical and Biological Dynamics Using Droplet-Based Microfluidics,” *Annual Review of Analytical Chemistry*, vol. 10, no. 1, pp. 1–24, 2017.
- [75] R. Ramji, M. Wang, A. A. S. Bhagat, D. Tan Shao Weng, N. V. Thakor, C. Teck Lim, and C.-H. Chen, “Single cell kinase signaling assay using pinched flow coupled droplet microfluidics,” *Biomicrofluidics*, vol. 8, no. 3, 2014.
- [76] A. B. Theberge, F. Courtois, Y. Schaerli, M. Fischlechner, C. Abell, F. Hollfelder, and W. T. Huck, “Microdroplets in microfluidics: An evolving platform for discoveries in chemistry and biology,” *Angewandte Chemie - International Edition*, vol. 49, no. 34, pp. 5846–5868, 2010.
- [77] J. Ma, Y. Wang, and J. Liu, “Biomaterials meet microfluidics: from synthesis technologies to biological applications,” *Micromachines*, vol. 8, no. 8, 2017.
- [78] O. J. Miller, A. El, T. Mangeat, J.-c. Baret, L. Frenz, B. El, E. Mayot, M. L. Samuels, E. K. Rooney, P. Dieu, M. Galvan, D. R. Link, and A. D. Griffiths, “High-resolution dose, response screening using droplet-based microfluidics,” *Proceedings of the National Academy of Sciences*, vol. 109, no. 2, pp. 378–83, 2012.
- [79] J. Pan, A. L. Stephenson, E. Kazamia, W. T. S. Huck, J. S. Dennis, A. G. Smith, and C. Abell, “Quantitative tracking of the growth of individual algal cells in microdroplet compartments,” *Integrative Biology*, p. 1043, 2011.
- [80] S. Huang, J. K. Srimani, A. J. Lee, Y. Zhang, A. J. Lopatkin, K. W. Leong, and L. You, “Dynamic control and quantification of bacterial population dynamics in droplets,” *Biomaterials*, vol. 61, pp. 239–245, 2015.
- [81] L. Mahler, K. Wink, R. J. Beulig, K. Scherlach, M. Tovar, E. Zang, K. Martin, C. Hertweck, D. Belder, and M. Roth, “Detection of antibiotics

- synthetized in microfluidic picolitre-droplets by various actinobacteria,” *Scientific Reports*, vol. 8, no. 1, p. 13087, 2018.
- [82] L. Mazutis, J. Gilbert, W. L. Ung, D. A. Weitz, A. D. Griffiths, and J. A. Heyman, “Single-cell analysis and sorting using droplet-based microfluidics,” *Nature Protocols*, vol. 8, no. 5, p. 870–891, 2013.
  - [83] J. Park, A. Kerner, M. A. Burns, and X. N. Lin, “Microdroplet-enabled highly parallel co-cultivation of Microbial Communities,” *PLoS ONE*, vol. 6, no. 2, 2011.
  - [84] I. D. Vladescu, E. J. Marsden, J. Schwarz-Linek, V. A. Martinez, J. Arlt, A. N. Morozov, D. Marenduzzo, M. E. Cates, and W. C. Poon, “Filling an emulsion drop with motile bacteria,” *Physical Review Letters*, vol. 113, no. 26, pp. 1–5, 2014.
  - [85] C. B. Chang, J. N. Wilking, S. H. Kim, H. C. Shum, and D. A. Weitz, “Monodisperse Emulsion Drop Microenvironments for Bacterial Biofilm Growth,” *Small*, vol. 11, no. 32, pp. 3954–3961, 2015.
  - [86] H. H. Jeong, S. H. Jin, B. J. Lee, T. Kim, and C. S. Lee, “Microfluidic static droplet array for analyzing microbial communication on a population gradient,” *Lab on a Chip*, vol. 15, no. 3, pp. 889–899, 2015.
  - [87] R. Seemann, M. Brinkmann, T. Pfohl, and S. Herminghaus, “Droplet based microfluidics,” *Reports on Progress in Physics*, vol. 75, no. 1, 2011.
  - [88] D. J. Collins, A. Neild, A. DeMello, A. Q. Liu, and Y. Ai, “The Poisson distribution and beyond: Methods for microfluidic droplet production and single cell encapsulation,” vol. 15, no. 17, pp. 3439–3459, 2015.
  - [89] A. K. Price and B. M. Paegel, “Discovery in Droplets,” *Analytical Chemistry*, vol. 88, 2016.
  - [90] L. A. Bawazer, C. S. McNally, C. J. Empson, W. J. Marchant, T. P. Comyn, X. Niu, S. Cho, M. J. Mcpherson, B. P. Binks, A. Demello, and F. C. Meldrum, “Combinatorial microfluidic droplet engineering for biomimetic material synthesis,” *Science Advances*, 2016.
  - [91] G. F. Christopher and S. L. Anna, “Microfluidic methods for generating continuous droplet streams,” *Journal of Physics D: Applied Physics*, vol. 40, Sep 2007.
  - [92] X. Niu, F. Gielen, J. B. Edel, and A. J. DeMello, “A microdroplet dilutor for high-throughput screening,” *Nature Chemistry*, vol. 3, no. 6, pp. 437–442, 2011.
  - [93] J. C. Baret, O. J. Miller, V. Taly, M. Ryckelynck, A. El-Harrak, L. Frenz, C. Rick, M. L. Samuels, J. B. Hutchison, J. J. Agresti, D. R. Link, D. A. Weitz, and A. D. Griffiths, “Fluorescence-activated droplet sorting (FADS):

- Efficient microfluidic cell sorting based on enzymatic activity,” *Lab on a Chip*, vol. 9, no. 13, pp. 1850–1858, 2009.
- [94] R. J. Best, J. J. Lyczakowski, S. Abalde-Cela, Z. Yu, C. Abell, and A. G. Smith, “Label-Free Analysis and Sorting of Microalgae and Cyanobacteria in Microdroplets by Intrinsic Chlorophyll Fluorescence for the Identification of Fast Growing Strains,” *Analytical Chemistry*, vol. 88, no. 21, pp. 10445–10451, 2016.
  - [95] A. Barizien, M. S. Suryateja Jammalamadaka, G. Amselem, and C. N. Baroud, “Growing from a few cells: combined effects of initial stochasticity and cell-to-cell variability,” *Journal of The Royal Society Interface*, vol. 16, no. 153, p. 20180935, 2019.
  - [96] D. Taylor, N. Verdon, P. Lomax, R. J. Allen, and S. Titmuss, “Tracking the stochastic growth of bacterial populations in microfluidic droplets,” *Physical Biology*, vol. 19, no. 2, p. 026003, 2022.
  - [97] S. Scott and Z. Ali, “Fabrication methods for microfluidic devices: An overview,” *Micromachines*, vol. 12, no. 3, p. 319, 2021.
  - [98] A. San-Miguel and H. Lu, “Microfluidics as a tool for *C. elegans* research.” School of Chemical Biomolecular Engineering, Georgia Institute of Technology, Atlanta GA, 30332, USA, 2013.
  - [99] D. Taylor, *Bacterial Confinement in Microfluidic Micro-Environments*. PhD thesis, The University of Edinburgh, 2019.
  - [100] J. Q. Boedicker, L. Li, T. R. Kline, and R. F. Ismagilov, “Detecting bacteria and determining their susceptibility to antibiotics by stochastic confinement in nanoliter droplets using plug-based microfluidics,” *Lab on a Chip*, vol. 8, no. 8, p. 1265, 2008.
  - [101] J. F. Edd, D. Di Carlo, K. J. Humphry, S. Köster, D. Irimia, D. A. Weitz, and M. Toner, “Controlled encapsulation of single-cells into monodisperse picolitre drops,” *Lab on a Chip*, vol. 8, no. 8, pp. 1262–1264, 2008.
  - [102] M. B. Elowitz, “Stochastic gene expression in a single cell,” *Science*, vol. 297, no. 5584, pp. 1183–1186, 2002.
  - [103] D. P. Lloyd and R. J. Allen, “Competition for space during bacterial colonization of a surface,” *Journal of The Royal Society Interface*, vol. 12, no. 110, p. 20150608, 2015.
  - [104] E. Ivashkiv, “Ampicillin,” vol. 2 of *Analytical Profiles of Drug Substances*, pp. 1–61, Academic Press, 1973.
  - [105] J. P. Hou and J. W. Poole, “Kinetics and mechanism of degradation of ampicillin in solution,” *Journal of Pharmaceutical Sciences*, vol. 58, no. 4, p. 447–454, 1969.

- [106] G. M. Pacifici, “Clinical pharmacology of morphine in infants and children,” *Pharmaceutics and Pharmacology Research*, vol. 4, no. 5, p. 01–08, 2021.
- [107] Nikon, *NIS-Elements AR (Advanced Research) User’s Guide (Ver.4.50)*. Laboratory Imaging, 2015.
- [108] Micrux Technologies. [www.micruxfluidic.com](http://www.micruxfluidic.com), 2022.
- [109] Sphere Fluidics Limited, *Pico-Surf™*. Novel biocompatible surfactants for the generation of stable picodroplets, 2022.
- [110] Sphere Fluidics Limited, *Pico-Glide™*. A novel surface coating agent for enhanced picodroplet performance and stability, 2022.
- [111] IAPWS, “Viscosity of water.” [www.wiki.anton-paar.com/uk-en/water/](http://www.wiki.anton-paar.com/uk-en/water/), 2008.
- [112] H. Yuen, J. Princen, J. Illingworth, and J. Kittler, “Comparative study of hough transform methods for circle finding,” *Image and Vision Computing*, vol. 8, no. 1, pp. 71–77, 1989.
- [113] N. Otsu, “A threshold selection method from gray-level histograms,” *IEEE Trans Syst Man Cybern*, vol. 9, no. 1, pp. 62–66, 1979.
- [114] D. Bradley and G. Roth, “Adaptive thresholding using the integral image,” *Journal of Graphics Tools*, vol. 12, no. 2, pp. 13–21, 2007.
- [115] J. C. Crocker, “track.m (2007 update),” *Lewis Lab, Harvard University*, 2007.
- [116] R. M. Haralick and L. G. Shapiro, *Computer and robot vision*, pp. 28–48. Addison-Wesley Publishing Company, 1992.
- [117] S. Takeuchi, W. R. DiLuzio, D. B. Weibel, and G. M. Whitesides, “Controlling the shape of filamentous cells of escherichia coli,” *Nano Letters*, vol. 5, no. 9, pp. 1819–1823, 2005.
- [118] T. Trunk, H. S. Khalil, and J. C. Leo, “Bacterial autoaggregation,” *AIMS Microbiology*, vol. 4, no. 1, pp. 140–164, 2018.
- [119] K. Leung, H. Zahn, T. Leaver, K. M. Konwar, N. W. Hanson, A. P. Pagé, C.-C. Lo, P. S. Chain, S. J. Hallam, and C. L. Hansen, “A programmable droplet-based microfluidic device applied to multiparameter analysis of single microbes and microbial communities,” *Proceedings of the National Academy of Sciences*, vol. 109, no. 20, pp. 7665–7670, 2012.
- [120] J. C. Waters, “Accuracy and precision in quantitative fluorescence microscopy,” *J Cell Biol.*, vol. 185, no. 7, pp. 1135–1148, 2009.
- [121] S. Taheri-Araghi, S. Bradde, J. T. Sauls, N. S. Hill, P. A. Levin, J. Paulsson, M. Vergassola, and S. Jun, “Cell-size control and homeostasis in bacteria,” *Current Biology*, vol. 25, no. 3, pp. 385–391, 2015.

- [122] J. Lin and A. Amir, “The Effects of Stochasticity at the Single-Cell Level and Cell Size Control on the Population Growth,” *Cell Systems*, vol. 5, no. 4, pp. 358–367, 2017.
- [123] R. Bellman and T. Harris, “On age-dependent binary branching processes,” *Ann. Math.*, vol. 55, pp. 385–391, 1952.
- [124] S. Fatichi, “Mann-Kendall Test,” *MATLAB Central File Exchange*, 2009.
- [125] E. J. Stewart, “Growing unculturable bacteria,” *Journal of Bacteriology*, vol. 194, pp. 4151–4160, 2012.
- [126] M. Wallden, D. Fange, E. G. Lundius, Baltekin, and J. Elf, “The Synchronization of Replication and Division Cycles in Individual *E. coli* Cells,” *Cell*, vol. 166, no. 3, pp. 729–739, 2016.
- [127] H. Luidalepp, A. Jõers, N. Kaldalu, and T. Tenson, “Age of inoculum strongly influences persister frequency and can mask effects of mutations implicated in altered persistence,” *Journal of Bacteriology*, vol. 193, no. 14, pp. 3598–3605, 2011.
- [128] A. Harms, C. Fino, M. A. Sørensen, S. Semsey, and K. Gerdes, “Prophages and growth dynamics confound experimental results with antibiotic-tolerant persister cells,” *mBio*, vol. 8, no. 6, 2017.
- [129] N. Q. Balaban, J. Merrin, R. Chait, L. Kowalik, and S. Leibler, “Bacterial persistence as a phenotypic switch,” *Science*, vol. 305, no. 5690, pp. 1622–1625, 2004.
- [130] D. Hughes and D. I. Andersson, “Environmental and genetic modulation of the phenotypic expression of antibiotic resistance,” *FEMS Microbiology Reviews*, vol. 41, no. 3, pp. 374–391, 2017.
- [131] J. Grilli, C. Cadart, G. Micali, M. Osella, and M. Cosentino Lagomarsino, “The Empirical Fluctuation Pattern of *E. coli* Division Control,” *Frontiers in Microbiology*, vol. 9, 2018.
- [132] A. Cassini, L. D. Högberg, D. Plachouras, A. Quattrocchi, A. Hoxha, G. S. Simonsen, M. Colomb-Cotinat, M. E. Kretzschmar, B. Devleesschauwer, and M. e. a. Cecchini, “Attributable deaths and disability-adjusted life-years caused by infections with antibiotic-resistant bacteria in the EU and the European Economic Area in 2015: a population-level modelling analysis,” *The Lancet Infectious Diseases*, vol. 19, no. 1, pp. 56–66, 2019.
- [133] A. J. Lee, S. Wang, H. R. Meredith, B. Zhuang, Z. Dai, and L. You, “Robust, linear correlations between growth rates and  $\beta$ -lactam-mediated lysis rates,” *Proceedings of the National Academy of Sciences*, vol. 115, no. 16, pp. 4069–4074, 2018.

- [134] D. T. Gillespie, "Approximate accelerated stochastic simulation of chemically reacting systems," *The Journal of Chemical Physics*, vol. 115, no. 4, p. 1716–1733, 2001.
- [135] M. A. Pinsky and S. Karlin, *An introduction to stochastic modeling*. Burlington, MA: Academic Press: Elsevier, 4 ed., 2011.
- [136] S. M. Ross, "CHAPTER 6: Continuous-Time Markov Chains," in *Introduction to Probability Models (Tenth Edition)* (S. M. Ross, ed.), pp. 371–419, Boston: Academic Press, tenth edition ed., 2010.
- [137] C. Danelon, E. M. Nestorovich, M. Winterhalter, M. Ceccarelli, and S. M. Bezrukov, "Interaction of zwitterionic penicillins with the OmpF channel facilitates their translocation," *Biophysical Journal*, 2006.
- [138] R. Chang and J. Thoman Jr., *Physical chemistry for the biosciences*, pp. 717–723. University Science Books, 2005.
- [139] H. Nikaido and S. Normark, "Sensitivity of escherichia coli to various beta-lactams is determined by the interplay of outer membrane permeability and degradation by periplasmic beta-lactamases: a quantitative predictive treatment," *Molecular Microbiology*, vol. 1, no. 3, pp. 29–36, 1987.
- [140] M. S. Helfand, C. R. Bethel, A. M. Hujer, K. M. Hujer, V. E. Anderson, and R. A. Bonomo, "Understanding resistance to -lactams and -lactamase inhibitors in the shv -lactamase," *Journal of Biological Chemistry*, vol. 278, no. 52, pp. 52724–52729, 2003.
- [141] D. J. Zygmunt, C. W. Stratton, and D. S. Kernodle, "Characterization of four beta-lactamases produced by staphylococcus aureus," *Antimicrobial Agents and Chemotherapy*, vol. 36, no. 2, pp. 440–445, 1992.
- [142] B. Soufi, K. Krug, A. Harst, and B. Macek, "Characterization of the E. coli proteome and its modifications during growth and ethanol stress, volume=6, doi=10.3389/fmicb.2015.00103," *Frontiers in Microbiology*, 2015.
- [143] E. Yourassowsky, M. P. Van der Linden, M. J. Lismont, F. Crokaert, and Y. Glupczynski, "Correlation between growth curve and killing curve of Escherichia coli after a brief exposure to suprainhibitory concentrations of ampicillin and piperacillin," *Antimicrobial Agents and Chemotherapy*, vol. 28, no. 6, pp. 756–760, 1985.
- [144] I. P. Thonus, P. Fontijne, and M. F. Michel, "Ampicillin susceptibility and ampicillin-induced killing rate of Escherichia coli.," *Antimicrobial Agents and Chemotherapy*, vol. 22, no. 3, pp. 386–390, 1982.
- [145] National Library of Medicine, "Compound Summary for CID 6249, Ampicillin," *PubChem*, 2022.



- [146] K. Brudzynski and C. Sjaarda, “Antibacterial compounds of Canadian honeys target bacterial cell wall inducing phenotype changes, growth inhibition and cell lysis that resemble action of  $\beta$ -lactam antibiotics,” *PLoS ONE*, vol. 9, no. 9, 2014.
- [147] M. de Boer, C. Heuer, H. Hussein, and S. McDougall, “Minimum inhibitory concentrations of selected antimicrobials against *Escherichia coli* and *Trueperella pyogenes* of bovine uterine origin,” *Journal of Dairy Science*, vol. 98, no. 7, pp. 4427–4438, 2015.
- [148] Ö. Baltekin, A. Boucharin, E. Tano, D. I. Andersson, and J. Elf, “Antibiotic susceptibility testing in less than 30 min using direct single-cell imaging,” *Proceedings of the National Academy of Sciences*, vol. 114, no. 34, pp. 9170–9175, 2017.
- [149] E. S. Pshennikova and A. S. Voronina, “Dormancy: There and back again,” *Molecular Biology*, vol. 56, no. 5, p. 735–755, 2022.
- [150] K. Lewis, “Persister cells, dormancy and infectious disease,” *Nature Reviews Microbiology*, vol. 5, no. 1, p. 48–56, 2006.
- [151] M. Wehrens, D. Ershov, R. Rozendaal, N. Walker, D. Schultz, R. Kishony, P. A. Levin, and S. J. Tans, “Size laws and division ring dynamics in filamentous *Escherichia coli* cells,” *Current Biology*, vol. 28, no. 6, pp. 972–979.e5, 2018.
- [152] N. Ziv, N. J. Brandt, and D. Gresham, “The use of Chemostats in Microbial Systems Biology,” *Journal of Visualized Experiments*, no. 80, 2013.
- [153] P. Smith and M. Schuster, “Public goods and cheating in microbes,” *Current Biology*, vol. 29, no. 11, 2019.
- [154] R. García-Contreras and D. Loarca, “The bright side of social cheaters: Potential beneficial roles of “social cheaters” in microbial communities,” *FEMS Microbiology Ecology*, vol. 97, no. 1, 2020.
- [155] E. D. Kelsic, J. Zhao, K. Vetsigian, and R. Kishony, “Counteraction of antibiotic production and degradation stabilizes microbial communities,” *Nature*, vol. 521, no. 7553, pp. 516–519, 2015.
- [156] S. Estrela and S. P. Brown, “Community interactions and spatial structure shape selection on antibiotic resistant lineages,” *PLOS Computational Biology*, vol. 14, no. 6, p. e1006179, 2018.
- [157] S. P. Bernier and M. G. Surette, “Concentration-dependent activity in natural environments,” *Frontiers in Microbiology*, vol. 4, 2013.
- [158] R. A. Sorg, L. Lin, G. S. van Doorn, M. Sorg, J. Olson, V. Nizet, and J.-W. Veening, “Collective resistance in microbial communities by intracellular antibiotic deactivation,” *PLOS Biology*, vol. 14, no. 12, p. e2000631, 2016.

- [159] T. Farmer, “Penetration of  $\beta$ -lactamase inhibitors into the periplasm of gram-negative bacteria,” *FEMS Microbiology Letters*, vol. 176, no. 1, p. 11–15, 1999.
- [160] N. Matsumura, S. Minami, H. Araki, R. Hori, N. Ogake, and Y. Watanabe, “Determination of intracellular and extracellular  $\beta$ -lactamase activities of *pseudomonas aeruginosa* after exposure to  $\beta$ -lactams in vitro and in vivo,” *Journal of Infection and Chemotherapy*, vol. 6, no. 4, p. 200–205, 2000.
- [161] O. M. O’Connor, R. N. Alnahhas, J.-B. Lugagne, and M. J. Dunlop, “Delta 2.0: A deep learning pipeline for quantifying single-cell spatial and temporal dynamics,” *PLOS Computational Biology*, vol. 18, no. 1, p. e1009797, 2022.
- [162] L. L. Silver, “Challenges of antibacterial discovery,” *Clinical Microbiology Reviews*, vol. 24, no. 1, p. 71–109, 2011.